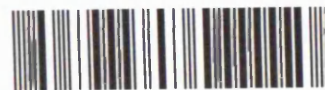


REFERENCE ONLY



280951032X

UNIVERSITY OF LONDON THESIS

Degree

Year

Name of Author JUAN FELIPE

PEREZ JUSTE ABASCAL

COPYRIGHT

This is a thesis accepted for a Higher Degree of the University of London. It is an unpublished typescript and the copyright is held by the author. All persons consulting the thesis must read and abide by the Copyright Declaration below.

COPYRIGHT DECLARATION

I recognise that the copyright of the above-described thesis rests with the author and that no quotation from it or information derived from it may be published without the prior written consent of the author.

LOAN

Theses may not be lent to individuals, but the University Library may lend a copy to approved libraries within the United Kingdom, for consultation solely on the premises of those libraries. Application should be made to: The Theses Section, University of London Library, Senate House, Malet Street, London WC1E 7HU.

REPRODUCTION

University of London theses may not be reproduced without explicit written permission from the University of London Library. Enquiries should be addressed to the Theses Section of the Library. Regulations concerning reproduction vary according to the date of acceptance of the thesis and are listed below as guidelines.

- A. Before 1962. Permission granted only upon the prior written consent of the author. (The University Library will provide addresses where possible).
- B. 1962 - 1974. In many cases the author has agreed to permit copying upon completion of a Copyright Declaration.
- C. 1975 - 1988. Most theses may be copied upon completion of a Copyright Declaration.
- D. 1989 onwards. Most theses may be copied.

This thesis comes within category D.

This copy has been deposited in the Library of

UCL

This copy has been deposited in the University of London Library, Senate House, Malet Street, London WC1E 7HU.

Improvements in reconstruction algorithms for Electrical Impedance Tomography of brain function

Juan Felipe Pérez-Juste Abascal

A dissertation submitted for the degree of
Doctor of Philosophy
of the
University of London.

Department of Medical Physics
University College London

2007

UMI Number: U593107

All rights reserved

INFORMATION TO ALL USERS

The quality of this reproduction is dependent upon the quality of the copy submitted.

In the unlikely event that the author did not send a complete manuscript and there are missing pages, these will be noted. Also, if material had to be removed, a note will indicate the deletion.



UMI U593107

Published by ProQuest LLC 2013. Copyright in the Dissertation held by the Author.
Microform Edition © ProQuest LLC.

All rights reserved. This work is protected against
unauthorized copying under Title 17, United States Code.



ProQuest LLC
789 East Eisenhower Parkway
P.O. Box 1346
Ann Arbor, MI 48106-1346

Declaration of authorship

The tank and the neonatal data, used in chapters five and six, was collected and pre-processed by Tom Tidswell. The neonatal head-shaped FEM mesh, used in chapters five and six, was provided by Andrew Tizzard. MATLAB routines for modelling of the head and linear solvers for the forward problem, used in chapters five, six, and nine were provided by Lior Horesh. The epilepsy changes simulated in chapter nine were done by Lorenzo Fabrizi.

The rest of the work in this thesis has been done by me with the suggestions and help as indicated in the acknowledgements section.

Abstract

Electrical Impedance Tomography (EIT) is a relatively new medical imaging method which, by injecting current and measuring voltage, estimates a volume conductivity map of the subject. It has the potential to become a portable noninvasive imaging technique of particular use in imaging brain function. A good estimate of the modelling parameters is essential for absolute image reconstruction. While biological tissue like bone and white matter is anisotropic, clinical applications have assumed isotropic conductivity and adopted linear reconstruction of time difference data, as this is less affected by systematic errors. In previous studies, measured scalp impedance changes during evoked response on adults and on neonates were consistent, yet data had a low signal-to-noise ratio and image localisation using truncated singular-value-decomposition and a fixed truncation level was unsuccessful. There were four main goals in this thesis. The first goal was to examine ways of optimising linear reconstruction. This was attempted by comparison of standard methods for selecting the truncation level with modelling of the covariance of the noise. When examined on data from simulation, a head-shaped saline tank, and scalp neonatal evoked responses, there was no significant difference among selection methods, yet modelling a general covariance of the noise led to a significant improvement for simulated data. The second goal was to reduce the noise by applying Principal Component Analysis (PCA), for the case of EIT images collected during cortical evoked responses in the neonate. PCA significantly improved the SNR by 15dB on both tank and neonatal data. The third goal was to study the possibility of the recovery of a piecewise linear anisotropic tensor with known eigenvectors. It was possible to recover three smooth eigenvalues for simulated conductivity distributions with eigenvectors generally orientated and for a conductivity tensor estimated from diffusion weighted MRI. The fourth goal was to develop a method for incorporating anisotropy in a forward numerical model for EIT of the head and assess the resulting improvement in image quality. Neglecting anisotropy of the scalp, skull, and brain, yielded a 50% error in the forward solution and 24mm localisation error for a linearised inverse solution. This suggests that use of anisotropy is likely to improve EIT image quality.

Acknowledgements

I wish to thank my supervisors Simon Arridge, David Holder, and Richard Bayford who provided me with great guidance and support throughout my thesis.

I am also grateful to the EIT and OT groups, at UCL, for their valuable suggestions, challenges, and enjoyable discussions. Members of the OT group were Martin Schweiger, Athanasios Zacharopoulos, Jason Riley, Abdel Douiri, and Christos Panagiotou; linked with this group belonging to the Computer Science department at UCL were Daniel Alexander, Phil Cook, Jason Kastanis, and Kathleen Curran. Members of the EIT group were Gershon Ahadzi, Marzia De Lucia, Lorenzo Fabrizi, Juan Fritschy, Alistair McEwan, Lior Horesh, Rebeca Yerworth, Raya Schindmes, and Andrea Romsauerova. I specially acknowledge Lior Horesh for his helpful and supportive comments and innumerable conversations.

Among other advisors with who I had the opportunity to discuss about inverse problems, I thank Bill Lionheart and Manuchehr Solemaini, at the University of Manchester; Oliver Dorn, at Universidad Carlos III in Madrid. I also thank the M.Phil. to Ph.D. transfer examiner Derek Hill and the Ph.D. examiners Will Penny and Mike Pidcock for their suggestions and comments.

Some collaborations were essential to accomplish this work. I would like to thank Tom Tidswell for collecting and pre-processing tank and the neonatal data, for chapters five and six; Andrew Tizzard for providing me with the neonatal head-shaped FEM mesh, for chapters five and six; Lior Horesh for the use of routines on the meshing and head modelling and linear solvers, for chapters five, six, and nine; Bill Lionheart for his suggestions and comments for chapter seven, and advice and help for the design and development of chapter eight, that was initiated after the 2005 AIP meeting, hosting me for a week in Manchester University and following the work that I started during my M.Sc. at Manchester University under his supervision, which was also used for chapter nine; Martin Schweiger for helping with the numerical integration, for chapter eight; Marzia De Lucia for discussions and comments regarding the estimation and finite element modelling of the diffusion tensor and registration of the T1- and DT-MRI, for chapter nine; Damien Buie for his support when using the VTK toolkit; Mathew Browne for his support with the maintenance of the IXI web site; Raya Schindmes for her dedication

explaining the procedure for the segmentation and meshing from MRI data, for chapter nine; David Atkinson for providing me with the necessary tools for reconstructing and visualising the diffusion tensor, and for his dedication and comments that made possible to develop the work on DTI, for chapter nine; and Lorenzo Fabrizi for contributing with suggestions and the routines to simulate the epilepsy changes, for chapter nine.

I also express my gratitude to those responsible of the computing facilities at UCL, in special, Davide Poccecai at the Medical Physics department, and Neil Daeche at the Computer Science department, who provided me with supportive assistance; the administrative secretary Karen Cardy; the head of the Medical Physics department Andrew Todd-Pokropek; and Ph.D. tutor Roger Ordidge.

I am thankful to the University London Union (ULU), especially to the sports committee, that sponsored the ULU Canoe Polo Club of which I have been member, providing us with great facilities for training and travelling and making it inexpensive; in particular, Angela Jelfs who was in charge of the travelling assistance; and the London Paddington Basin that let us training and organising tournaments in the canal. We were the best club at BUSA in 2006 winning two out of four divisions, and where my team, ULU B, finished second; I am grateful to all the team members with who I shared such a good moments.

Personally, I thank, my collaborators and friends Lorenzo Fabrizi and Lior Horesh for their advice and support and for sharing with me all those moments that made this work even more fun; my friends, Daniele Savi, Miok Han, Ricky Savi, Konstantinos Pappidas, and Dominique Arpino, for their unconditional support and friendship; my home friends Alejandro P.-J. Valero, Angel Caballero, and Gerardo Santos; my classmates Eva Ferreiro, Jesus Iravedra, Laura Sanz, and Sergio Torres; and my family, in special, my parents, for giving me support and incentive during my studies, to whom I dedicate this thesis.

Finally, I would like to thank The Epilepsy Research Foundation who supported this study.

To my parents

Contents

1	Introduction	33
1.1	Overview of imaging	35
1.1.1	Imaging and inverse problems	35
1.1.2	Medical imaging	37
1.1.3	Imaging of brain function	42
1.2	Electrical impedance tomography	45
1.2.1	History and background	45
1.2.2	Applications	46
1.2.3	EIT systems for medical applications	46
1.2.4	EIT of brain function	50
1.2.5	EIT algorithms	52
1.3	Thesis goals	54
1.4	Thesis outline	55
2	Forward problem theory	56
2.1	Physical model	56
2.1.1	Maxwell's and the generalized Laplace's equations	56
2.1.2	Boundary conditions: the Complete Electrode Model	58
2.2	Methods for solving the forward problem	59
2.2.1	FEM formulation	60
2.2.2	Implementation and computation	62
2.2.3	Resistor network	64
2.3	Summary	65
3	Inverse problem theory	66
3.1	The inverse conductivity problem	66
3.1.1	The Dirichlet-to-Neumann map	67

3.1.2	Uniqueness	67
3.1.3	Anisotropic mediums	68
3.1.4	Incomplete data	69
3.1.5	Sensitivity matrix	70
3.2	Solving the inverse problem	70
3.2.1	Ill-posedness	71
3.2.2	Regularisation	71
3.2.3	Statistical framework	72
3.2.4	Optimisation	73
3.3	Summary	76
4	The linear inverse problem	77
4.1	Review of Methods	78
4.1.1	Linear model	78
4.1.2	Generalised least squares solution for well-posed problems	79
4.1.3	Ill-posedness for linear problems	79
4.1.4	Regularisation	80
4.1.5	Modelling a general covariance matrix	83
4.1.6	Regularisation parameter selection	84
4.1.7	Computing regularisation schemes for EIT of brain function	86
4.2	Summary	88
5	Selecting the regularisation parameter	90
5.1	Introduction	90
5.2	Methods	92
5.2.1	Model and forward solution	92
5.2.2	Image reconstruction	93
5.2.3	Computation of the selection methods functionals	93
5.2.4	Comparison of methods	95
5.2.5	Data sets	95
5.3	Results	98
5.3.1	Preliminaries	98
5.3.2	Simulated data	99
5.3.3	Tank data	99
5.3.4	Neonatal data	102

5.4	Discussion	103
6	Principal Component Analysis	107
6.1	Introduction	107
6.2	Methods	108
6.2.1	Data sets	108
6.2.2	Analysis of the data correlations	108
6.2.3	Principal components	109
6.2.4	Image reconstruction	110
6.2.5	Comparison of results	110
6.3	Results	111
6.3.1	Analysis of data correlations	111
6.3.2	Principal components	111
6.3.3	Data and image comparison	114
6.4	Discussion	119
7	Validation of an anisotropic FEM solution	121
7.1	Introduction	121
7.2	Methods	122
7.2.1	Model	122
7.2.2	Analytical solution	123
7.2.3	Finite element solution	124
7.2.4	Convergence of the anisotropic FEM solution	125
7.2.5	FEM mesh	127
7.3	Results	127
7.3.1	Convergence of the analytical solution	127
7.3.2	Comparison between the FEM isotropic and anisotropic solutions	127
7.3.3	Comparison of analytical and FEM solutions	128
7.4	Discussion	128
8	Anisotropic EIT with known eigenvectors	132
8.1	Introduction	132
8.2	Methods	134
8.2.1	Forward solution	134
8.2.2	Sensitivity matrix	137

8.2.3	Finite element mesh	138
8.2.4	Rank analysis	138
8.2.5	Simulated tensor distributions	140
8.2.6	Inverse Problem	151
8.3	Results	151
8.3.1	Rank analysis	151
8.3.2	Recovery of eigenvalues	152
8.4	Discussion	154
9	Influence of anisotropy for EIT of the head	164
9.1	Introduction	164
9.1.1	Background	164
9.1.2	Objective and experimental design	165
9.2	Methods	167
9.2.1	Preliminaries: Voltage and current density in an anisotropic domain . .	167
9.2.2	Head model: geometry and mesh	168
9.2.3	Head model: conductivity tensor estimate	169
9.2.4	Forward solution	180
9.2.5	Inverse problem	180
9.2.6	Comparison of the forward solutions	181
9.2.7	Comparison of the reconstructed images	182
9.2.8	Simulation of conductivity changes	183
9.3	Results	183
9.3.1	Preliminaries: Voltage and current density in an anisotropic domain . .	183
9.3.2	Qualitative comparison of the forward isotropic and anisotropic solutions	187
9.3.3	Quantitative comparison of the forward isotropic and anisotropic solutions	189
9.3.4	Effect of anisotropy on the linear image reconstruction of difference data	191
9.4	Discussion	199
9.4.1	Summary of results	199
9.4.2	Technical issues	207
9.4.3	Comparison with previous results	208
9.4.4	Conclusion and further work	209
10	Conclusions	210
10.1	Introduction	210

10.1.1	EIT of brain function	210
10.1.2	Forward and inverse problem theory	211
10.2	Summary of findings	212
10.3	Suggestions for further research	214
Appendices		214
A Miscellaneous mathematical definitions		215
A.1	Vector spaces	215
A.1.1	Convex function	215
A.1.2	Lipschitz continuity	215
A.1.3	Lebesgue integrable	215
A.1.4	Generalised weak derivative	215
A.1.5	Sobolev space	216
A.1.6	Hilbert space	216
A.1.7	G-norm	216
A.1.8	Compact operators	216
A.1.9	Kernel	216
A.1.10	Symmetric positive definite matrix	217
A.2	Numerical tools	217
A.2.1	Eigenvalue decomposition	217
A.2.2	SVD	218
A.2.3	Rank	219
A.2.4	Pseudo-inverse	220
A.2.5	Condition number	220
A.2.6	Differentiation	220
B Statistical background		222
B.1	General concepts	222
B.1.1	First and second moments	223
B.1.2	Bayes theorem	223
B.1.3	Gaussian distribution	224
B.2	Maximum Likelihood Estimate	224
B.3	Estimation of the first and second moments	224
B.3.1	Mean estimation	224

B.3.2	Unbiased estimate of the covariance	225
B.4	Best linear predictors	225
B.4.1	Principal Component Analysis	225
C	Derivation of linear approaches	227
C.1	Nonlinear least squares problem	227
C.2	Linear least squares problem	228
C.3	Row normalisation	228
D	Concepts of differential geometry	231
D.1	Diffeomorphism on manifolds	231
D.2	Invariance up to a diffeomorphism	231
D.3	Curves and surfaces in 3D manifolds	232
D.4	Tensors and transformation of coordinates	233
D.4.1	Rank one tensor: Vector components	234
D.4.2	Two rank tensor: Conductivity tensor	235
D.4.3	Two tensor: Riemannian metric tensor	235
D.4.4	Riemannian metric tensor	235
D.4.5	Relation conductivity-metric	236
D.4.6	Example: spherical coordinates	237
D.4.7	Tangent and cotangent space	238
E	Conductivity tensor scaling	240
	Bibliography	241

List of Figures

- 1.1 Anatomical brain images by different modalities: a) MRI (Wipro GE Healthcare, http://www.gehealthcare.com/inen/rad/mri/products/openspeed/os_neuro6.html), b) CT image (Casey Hospital CT Department, Southern Health Diagnostic Imaging, http://www.southernhealth.org.au/imaging/ct_casey_equip.htm), c) DTMRI image where colors specify diffusion directions (Beth Meyerand, Applied Neuro MRI Lab, <http://128.104.229.200/fmri/dti.html>), d) US image of a normal brain in an infant in the NICU (Ultrasound division, Children's Hospital Boston, <http://www.childrenshospital.org/clinicalservices/Site1867/mainpageS1867P0.html>).

38

- 1.2 Functional brain images by different modalities: a) PET image (WNEM TV5, Your Health: Spotlight On Alzheimer's Disease, http://www.wnem.com/Global/story.asp?S=1935894&nav=menu97_6), and for functional imaging: b) SPECT image (PET imaging at the UCI Brain Imaging Center (BIC), http://www.bic.uci.edu/PET_Imaging.htm), c) FMRI image of visual cortex stimulation (<http://www.imaging.robarts.ca/~jgati/Pages/fMRI.html>), d) PET image of a subject while thinking (Crump Institute for molecular imaging, from Michael E. Phelps, Dept. of Molecular and Medical Pharmacology, UCLA School of Medicine <http://www.crump.ucla.edu/software/lpp/clinpetneuro/function.html#Function>).

39

1.3	Functional brain images by different modalities: a) OT transverse, coronal, and sagittal images of an infant (Biomedical Optics Research Laboratory, UCL, http://www.medphys.ucl.ac.uk/research/borl/research/monstir/neonatal.htm , [67]), b) EIT image during left motor stimulation (Med. Phys. Dep., UCL).	40
1.4	Map of functional regions of the brain (BBC News, Monday, 7 June, 1999, 18:39 GMT 19:39 UK, http://news.bbc.co.uk/2/hi/health/medical_notes/363368.stm)	43
1.5	31-electrode positions designed for the human head at UCL based on the 10-20 EEG electrode localisation protocol.	49
2.1	A resistor network in 2D where resistors are placed at the finite element edges is equivalent to the discrete finite element mesh for piecewise linear voltage and constant conductivity, such that the contribution from the element conductivity to the resistor conductance is given by $\sigma \cot \alpha$ where σ is the element conductivity and α is the opposite angle. Both formulations lead to the same system matrix. (Image taken from [75], thanks to Bill Lionheart at the University of Manchester and David Holder at UCL).	64
5.1	A realistic neonatal head shaped FEM mesh created from a structural MRI of a neonate; segmented and meshed using IDEAS. Thanks to A Tizzard, Middlesex University	93
5.2	Mark 1b UCLH EIT system whose components are 1) headbox that contains the current source and multiplexer; 2) base unit, consisted of the power supply, measurement circuits, and 8-bit microprocessor; 3) notebook; 4) connector box between the notebook card and the UCLH system.	98
5.3	Example of the different functionals for a simulation under the influence of 100% white noise.	100
5.4	Example of the different functionals for a simulation under the influence of 100% white noise.	101
5.5	Sagittal view, through the middle of the neonatal head, of the simulated conductivity change (first column) and the reconstructed conductivity images (rest of columns) from its simulated scalp data under the influence of correlated noise. This is a single example out of the 25 corresponding to SNR of 1.8dB. In the first row, I assumed white noise ($C = I$), and in the second, I provided the covariance used for simulating correlated noise (true C).	101

- 5.6 Axial view of the reconstructed conductivity images of a Perspex in a saline head-shaped tank positioned on the front (Column 1 and 2), right (Column 3 and 4), back (Column 5 and 6), and left (Column 7 and 8). In the first row, I assumed white noise ($C = I$), and in the second, I estimated a diagonal covariance from the data. Data was reconstructed by the two predictors the LC and GCV since the UPRE and DP did not converge. 102
- 5.7 Sagittal view, throughout the middle of the neonatal head, of four neonatal data sets (in rows) where the other six data sets were discarded because images were very noisy, lacking of a localised change. Columns correspond to the four predictors: the LC, GCV, DP, and UPRE; and where, for the first four columns, I assumed white noise ($C = I$), and for the last four, I estimated a diagonal covariance of the noise. 104
- 6.1 a) Time covariance and b) channels covariance matrices, for a data set of perspex in a saline head-shaped tank. a) Time correlations had a pattern that was easier to interpret than b) channels correlations, suggesting a possible dimensionality reduction. 111
- 6.2 Time covariance matrix of a synthetic pseudo-random data set, of the same dimensions as tank data. It did not contain large off-diagonal elements, which illustrate the lack of correlation of random data in comparison with tank data. . 112
- 6.3 Eigenvectors of the covariance matrix across time for a data set of perspex in a saline head-shaped tank. Axes are % change (y-axis) and time in seconds (x-axis). Eigenvectors of the covariance matrix, from top to bottom and from left to right: 1st, 2nd, 3rd, 4th, 5th, 6th, 7th, (m-1)th, mth. Their corresponding eigenvalues are 57.9835, 0.5386, 0.1282, 0.1128, 0.0703, 0.0443, 0.03, $0.2 \cdot 10^{-4}$, $0.1 \cdot 10^{-4}$. The first PC had most of the weight (high eigenvalue) and best represented the experimental paradigm. 113
- 6.4 Neonatal data set 1 with SNR of around 10dB. a) Covariance matrix in time frames, where there were four frames a second; and b) PCs of the covariance with corresponding eigenvalues 1.5619, 0.0821, 0.0582, 0.0494, 0.0413, 0.0306, 0.0277, 0.0001, 0.0001. The first PC had most of the weight (high eigenvalue) and best represented the experimental paradigm while higher PCs represented other time courses that differ from it (red and blue correspond to high and low correlation, respectively). 114

- 6.5 Neonatal data set 2 with SNR of around -5dB. a) Covariance matrix in time frames, where there were four frames a second; and b) PCs of the covariance with corresponding eigenvalues 0.3131, 0.1163, 0.0260, 0.0194, 0.0141, 0.0119, 0.0088, $0.9 \cdot 10^{-5}$, $0.5 \cdot 10^{-5}$. The first PC had three times more weight (eigenvalue) than the second, however, it consisted of noise only. On the other hand, the 2nd PC best represented the experimental paradigm, and higher PCs corresponded to other time courses that differ from it (red and blue correspond to high and low correlation, respectively). 115
- 6.6 Data set of impedance measurements, of perspex in a saline head-shaped tank, for all 187 channels, measured four times a second following a paradigm of twenty seconds stimulus between two baselines of ten seconds each with no perspex on the tank. a) Raw data and b) data projected onto the 1st PC, which best represented the experimental paradigm, neglecting higher PCs. 116
- 6.7 Neonatal data set 1 with SNR of around 10dB. a) Raw data and b) data projected onto the 1st PC, which best represented the experimental paradigm, neglecting higher PCs (stimulus from 15 to 40s). 116
- 6.8 Neonatal data set 2 with SNR of around -5dB. a) Raw data and b) data projected onto the 2nd PC, which best represented the experimental paradigm, neglecting other PCs (stimulus from 15 to 40s). 117
- 6.9 Sagittal view, through the middle of the head, of normalised reconstructed conductivity of perspex in a saline head-shaped tank where the stimulus was from 11 to 20s. Rows correspond to with (2nd row) and without (1st row) projecting onto the 1st PC 117
- 6.10 Sagittal view, through the middle of the head, of normalised reconstructed conductivity, for neonatal data set 1 (stimulus from 15 to 40s). Rows correspond to with (2nd row) and without (1st row) projecting onto the 1st PC 118
- 6.11 Sagittal view, through the middle of the head, of normalised reconstructed conductivity, for neonatal data set 2 (stimulus from 15 to 40s). Data has been reconstructed with Tikhonov and the GCV. First row are images corresponding to the raw data, where the truncation level was predicted to be 24 dof; second row are images corresponding to the data projected onto the 2nd PC, where the truncation level was predicted to be 60 dof since the SNR is now higher; and third row are images corresponding to the data projected onto the 2nd PC, reconstructed with a truncation level of 24 dof. 118

- 7.1 Imposed Dirichlet boundary condition: voltage $u = 1$ on the plane $z = 0$ for $|x| < 1, |y| < 1$ (grey), and $u = 0$ on the rest of the boundary (black), for the isotropic domain (mesh of 98843 elements). 123
- 7.2 Convergence of the analytical solution (7.19), u , to the imposed boundary conditions $u(x, y, z) = 1$, for $z = 0, |x| < 1, |y| < 1$ (7.5), versus the maximum number of terms μ and ν equal to n used to approximate the infinite series, where the three different curves correspond to several points at the specified region of the boundary for a mesh of 384 elements. 127
- 7.3 Percentage relative voltage difference e^{ani} (7.25), for the interior vertices, where $\text{vtx}\#$ is the number of interior vertices, between the FEM isotropic solution $u(x)$ in Ω for $\sigma = 1$, and the anisotropic FEM solution $u(\tilde{x})$ in the transformed domain $\tilde{\Omega}$ for $\tilde{\sigma}(\tilde{x}) = \hat{\Psi}\sigma(x)\hat{\Psi}^T / |\det(\hat{\Psi})|$ (7.1) under two nonlinear transformations given by a-b) (7.26), and c-d) (7.27), where $\det(\hat{\Psi})$ is the determinant of the Jacobian of the transformation (dash line, which was scaled as $|\det(\hat{\Psi})|(\max(e^{\text{ani}}) / \max(|\det(\hat{\Psi})|))$ to be plotted together with the relative error). 129
- 7.4 Loglog plot of the FEM error norm $\|e\|_{\Omega}$ (7.31) versus the element size h (the same as in table 7.1) and a linear fit $\|e\|_{\Omega} \propto h^{1.1}$ with correlation coefficient $r = 0.98$ 130
- 8.1 Representation of a current injection by a vector with value 1 at a given node and value $-1/(N - 1)$ on the rest of nodes, on the boundary, that is, $e_i = (-1/(N - 1), \dots, 1, \dots, -1/(N - 1))$, where N is the number of exterior nodes. 136
- 8.2 Mesh connectivity, in 2D, such that the system matrix is zero when nodes are not connected, that is, in this example the nonzero entries for node one are two to seven but not eight. 140
- 8.3 Example of two anisotropic domains, whose anisotropic structure is given at each point by the three orthonormal eigenvectors that form a local coordinate system \hat{O} whose axes did not coincide with axes in the global coordinate system O , where eigenvectors a) eigenvectors were constant in the domain, b) changed throughout the domain. 141
- 8.4 Main biological eigenvector orientation: a) oblate, of flattened structure like bone tissue; b) prolate, resembling fibre structure like brain white matter. 142

- 8.5 Model 1A: anisotropy structure with eigenvectors aligned with the axes in the given global coordinates such that conductivity is favoured in the x-direction resembling a fibre type material aligned with the x-axis. Since eigenvectors coincide with the axes, the conductivity tensor is diagonal, where diagonal elements weight the conductivity along each axis; the simulated conductivity was $\sigma = \text{diag}(\sqrt{3}, 1/\sqrt{3}, 1/\sqrt{3})$, constant in a cubical domain. 145
- 8.6 Model 2A for which eigenvectors are defined locally coinciding with the axes in spherical coordinates where the most important direction, the gradient direction, is shown. 146
- 8.7 Model 3: anisotropic cubical domain (mesh of 495 elements) with eigenvectors changing along the y-direction, such that a) the first and second eigenvectors are the velocity and normal vectors to the curve $(x, y, z) = (x, t, at^2)$, for $a = 1/8$, that is, $v_1 = (0, 1, 2ay)$, $v_2 = (0, -2ay, 1)$, and $v_3 = (1, 0, 0)$ for the whole domain. Model 3A: eigenvalues weighting the conductivity along eigenvectors were $D = \text{diag}(\sqrt{3}, 1/\sqrt{3}, \sqrt{3})$, so that each plane $y = \text{const.}$ given by b) v_1 or v_3 defined a plane of preferred current flow, changing smoothly with y , and penalised the direction perpendicular to that plane given by v_2 148
- 8.8 Model 4: anisotropic structure with preferred current flow along a helix and penalised along its perpendicular plane, defined in a spherical domain. a) Helix function, $(x, y, z) = (R \cos(\theta), R \sin(\theta), P\theta/\pi)$, along which the first eigenvector v_θ is defined as the velocity vector for every point of the domain being the predominant direction. b) Spring surface that represents the volume from defining a helix at each point, weighted with maximum weight in its center. Model 5(1B & 4): the conductivity was simulated by $\sigma = \text{diag}(0.5, 1.7, 0.5) + 1.3 \exp(-2r^2) V \text{diag}(1.7, 0.5, 0.5) V^T$ where r is the perpendicular distance from a point to the helix, where $V = [v_\theta, a_\theta, b_\theta]$, and $v_\theta = (-R \sin \theta, R \cos \theta, P/\pi)$, $a_\theta = (-R \cos(\theta), -R \sin(\theta), 0)$, $b_\theta = (0, 0, 1)$. 149
- 8.9 Model 4: Helix model where the first eigenvector is defined to be tangent to the helix. It is shown, here, projected in the plane $z = 0$ and $z = 1$ being constant for each plane $z = \text{const.}$ and varying smoothly with z 150
- 8.10 Weighting function $f(z) = 0.5(1 + \cos(2\pi z))$ used for adding up to tensor distributions in Model 5(1B & 4). 150

8.11 Rank analysis of the Jacobian with respect to the diagonal elements where a) is a comparison between the Jacobian computed by FD and product of fields, $(J^{\text{direct}} - J^{\text{FD}})$, and b) is the SV spectrum. The direct and finite difference Jacobians agreed up to the FD incremental step length $\Delta\sigma \simeq 10^{-8}$. It was full rank with conditioning $\text{cond}(J) = 59$. It corresponded to a sphere mesh of 148 elements with 2916 measurements and diagonal conductivity with sinusoidal diagonal elements. 152

8.12 Rank analysis of the Jacobian with respect to the six coefficients for piecewise constant conductivity, for the complete NtoD and current and measurement pattern given by vectors perpendicular to one (the only thing that changes with respect to the rest of the chapter is that the conductivity is piecewise constant instead of linear). SV spectrums for a) a spherical mesh (148 elements), and for b) a cubical mesh (384 elements). 153

8.13 Model 1A. Results of the recovery of the eigenvalues for Model 1A, for which eigenvectors coincide with axis and conductivity was a constant distribution $\sigma = \text{diag}(\sqrt{3}, 1/\sqrt{3}, 1/\sqrt{3})$ in a cube of 495 elements. Objective function (top left), objective gradient (top right), relative error norm (bottom left), and max relative error (bottom right), versus the iteration number. 154

8.14 Model 1B. Results of the recovery of the eigenvalues for Model 1B for a spherical mesh of 807 elements, for which eigenvectors coincide with axes and conductivity eigenvalues were three linear distributions. The simulated linear distributions were $\sigma_{xx} = 3 + x + y + z$, $\sigma_{yy} = 3.2 + x + y + z$, $\sigma_{zz} = 3 + 1.2x + 1.4y + 0.8z$, for a conductivity estimate $\sigma_{\text{estimate}} = \text{diag}(3, 3, 3)$. Cross sections centered at the origin for simulated (left) a) σ_{xx} , c) σ_{yy} , e) σ_{zz} and reconstructed (right) b) σ_{xx} , d) σ_{yy} , f) σ_{zz} eigenvalues. 155

8.15 Model 1C. Results of the recovery of the eigenvalues for Model 1C for a spherical mesh of 807 elements, for which eigenvectors coincide with axis and conductivity was a cosine distribution for the first eigenvalue and constant for the other two. Simulated distributions were $\sigma_{xx} = 3 + \cos(\pi x) + \cos(\pi y) + \cos(\pi z)$, $\sigma_{yy} = 3$, $\sigma_{zz} = 3$, for a conductivity estimate $\sigma_{\text{estimate}} = 3$. Surface plot of the a) simulated and b) reconstructed σ_{xx} , cross sections of the c) simulated and d) reconstructed σ_{xx} , f) σ_{yy} , and e) objective function (left) and its gradient (right) are given versus the iteration number. 156

- 8.16 Model 2A. Results of the recovery of the eigenvalues for Model 2A for a spherical mesh of 148 elements, for which eigenvectors are defined locally coinciding with axes in spherical coordinates, and eigenvalues were constant in the domain. The conductivity tensor was given by $\sigma = VDV^T$, where $V = [v_\theta, v_\phi, v_r]$ and eigenvalues $D = \text{diag}(1, 1, 4)$, such that the radial was the preferred direction for current flow. a) Objective function (left) and its gradient (right), and b) the recovered eigenvalues are given. 157
- 8.17 Model 2D. Results of the recovery of the eigenvalues for Model 2D for a spherical mesh of 148 elements, for which eigenvectors are defined locally coinciding with axes in spherical coordinates, and the first two eigenvalues were constant in the domain and the third one was exponentially decreasing towards the center. The conductivity tensor was given by $\sigma = VDV^T$, where $V = [v_\theta, v_\phi, v_r]$ and eigenvalues $D = \text{diag}(1, 1, \exp(-2(x^2 + y^2 + z^2)))$. Objective function (top left), objective gradient (top right), maximum relative error in percentage (bottom) are given versus the iteration number. 158
- 8.18 Model 2D. Results of the recovery of the eigenvalues for Model 2D for a spherical mesh of 309 elements, for which eigenvectors are defined locally coinciding with axes in spherical coordinates, and the first two conductivity eigenvalues were constant in the domain and the third one was exponentially decreasing towards the center. The conductivity tensor was given by $\sigma = VDV^T$, where $V = [v_\theta, v_\phi, v_r]$ and eigenvalues $D = \text{diag}(1, 1, \exp(-2(x^2 + y^2 + z^2)))$. a) Objective function (top left), objective gradient (top right), maximum relative error in percentage (bottom) versus the iteration number; cross sections of the b) simulated and c) reconstructed third eigenvalue σ_{zz} 159
- 8.19 Model 3A. Results of the recovery of the eigenvalues for Model 3A for a cubical mesh of 495 elements, for which eigenvectors are defined locally parallel and perpendicular to a polynomial plane. Objective function (top left), objective gradient (top right), maximum percentage relative error norm (low left), and maximum percentage relative error (low right) versus the iteration number. . . . 160

8.20 Model 5(1A & 3A). Results of the recovery of the eigenvalues for Model 5 (1A & 3A) for a cubical mesh of 495 elements, from a mix of two tensors that yield a smooth overlap between a tensor with eigenvectors defined locally parallel and perpendicular to a polynomial plane, and an isotropic background. Objective function (top left), objective gradient (top right), maximum percentage relative error norm (bottom left), and maximum percentage relative error (bottom right) are given versus the iteration number. 160

8.21 Model 5(1B & 4). Results of the recovery of the eigenvalues for Model 5 (1B & 4), (spherical mesh of 309 elements), from a mix of two tensors that yield a smooth overlap between a tensor with eigenvectors defined locally parallel and plane perpendicular to a helix function, and an isotropic background, and with eigenvalues exponentially decaying towards the center of the helix. a) Objective function (top left), objective gradient (top right), maximum percentage relative error norm (bottom left), and maximum percentage relative error (bottom right) are given versus the iteration number, with cross sections of the b) simulated and c) reconstructed third eigenvalue σ_{zz} 161

8.22 Model 6. Results of the recovery of the eigenvalues for Model 6 for a cubical mesh of 495 elements, for which eigenvectors were computed from a Diffusion Tensor (DT) detail, of resolution 8-8-8 (2mm voxels), by interpolating the tensor elements and extrapolating them in the mesh vertices. DT details at a) $z = 0$ and c) $z = 0.38$ and b,d) their projections into the mesh, respectively. e) Objective function (top) and objective gradient (bottom) are given versus the iteration number. 162

9.1 T1-MRI of a 24 year old male, acquired at 3T. 168

9.2 B0 of the DT-MRI and the coregistered T1, from which the FE mesh was obtained. 169

9.3 Results of the coregistration of T1-MRI to the B0 of the DT-MRI. Top) initial (left) and final (right) histograms, and bottom) target B0 (left) and coregistered T1 (right). 170

9.4 Second view of the results of the coregistration of T1-MRI to the B0 of the DT-MRI. Top) initial (left) and final (right) histograms, and bottom) target B0 (left) and coregistered T1 (right). 171

- 9.5 Mesh from the coregistered T1-MRI, of 311,727 tetrahedral. a) Brain mesh, b) scalp mesh, c) conductivity model with isotropic conductivity values (S/m): brain 0.30, CSF 1.79, skull 0.018, scalp 0.44. 172
- 9.6 Cross section of the fractional anisotropy of the diffusion tensor estimated from the DT-MRI, on a grey scale where white correspond to $FA = 1$ (white matter) and black correspond to $FA = 0$ (grey matter). 173
- 9.7 Conductivity trace a) surface and b-c) cross section (CS) of the brain conductivity tensor σ obtained from the diffusion tensor T by the linear relation $\sigma/T = 0.844 \pm 0.0545 Ss/mm^3$ 174
- 9.8 a) Surface and b-f) cross sections (CS) of fraction anisotropy of the conductivity tensor interpolated from the diffusion tensor by the linear relation in the brain finite elements. 176
- 9.9 Cross sections (CS) of the direction of the eigenvector with largest eigenvalue on a tree colour scale indicating the most important direction among x (light blue, value 1), y (yellow, value 2), z (red, 3), where isotropic conductivity (blue, zero value) was defined as having FA less than 0.4. 177
- 9.10 Radial eigenvector approximated for each triangular element on the skull surface as a unit vector perpendicular to the surface element. Then tetrahedra were assigned the direction of the closest surface element. 178
- 9.11 Three cross sections of the conductivity tensor trace for all head. 179
- 9.12 Electrode positions. 180
- 9.13 Locations of the simulated conductivity changes, placed in the grey matter, within FA in the background, in A) the occipital lobe to simulate stimulation of the visual cortex, and in B) the temporal lobe and C) the hippocampus to simulate changes in epilepsy. 184
- 9.14 (Continuation) Locations of the simulated conductivity changes, placed in the grey matter, within FA in the background. 185
- 9.15 Comparison of the surface potential (left) and current density norm (right) cross section (CS) at $z = 0.08$ (right), for a-b) an isotropic domain with $\sigma = \text{diag}(1, 1, 1)$ and c-d) an anisotropic domain with $\sigma = \text{diag}(10, 1, 1)$, for a current injection with value one at $(0, 0, 0)$ and zero elsewhere (current perpendicular to ones), using the nodal based conductivity model. 186

- 9.16 Sketch of the expected isopotential voltage in 2D for i) an isotropic domain and ii) anisotropic domain with ten times higher conductivity in the x-direction. While in the isotropic domain the isopotential is expected to be a semicircle centered at the injection point, in the anisotropic domain it is expected to become parallel to the main direction. 187
- 9.17 Cross sections, at $z = 0.08$, of the electrical field $E = -\nabla u$ (left) and normalised current density $J = \sigma E$ (right), for a-b) an isotropic domain with $\sigma = \text{diag}(1, 1, 1)$, and c-d) an anisotropic domain with $\sigma = \text{diag}(10, 1, 1)$ 188
- 9.18 Concentric three spheres model with interior shell radius $0.4 \leq r \leq 0.6$, where a) the middle sphere (red) was anisotropic and inner and outer shells (blue) were isotropic, and b) mesh. 189
- 9.19 Cross section (left), at $z = 0$, and contour plot (right), for the current density of a-b) an isotropic domain with $\sigma = \text{diag}(1, 1, 1)$, and c-d) an anisotropic sphere with $\sigma = VDV^T$, where $D = \text{diag}(1.493, 1.493, 0.15)$ such that $\text{trace}(D) = 3$, in between inner and outer isotropic concentric spheres, for a nodal based conductivity and current pattern perpendicular to one. 190
- 9.20 Current density norm for the a) isotropic head model with $\sigma = \text{diag}(1, 1, 1)$ everywhere and b) head model with anisotropic skull with $\sigma = VDV^T$ with eigenvalues $D = \text{diag}(1.43, 1.43, 0.14)$, such that $\text{trace}(\sigma) = 3$ for both the isotropic and the anisotropic head model. 191
- 9.21 Cross sections (CS) of the current density norm $\|J\|$ for head model with anisotropic tensor for the brain estimated from DTI and scaled to $\text{trace}(\sigma) = 3$, where a) covers the whole range of values and b-e) covers a small range between two and three order of magnitude less for the current decrease because of the volume effect. 192
- 9.22 Current norm cross section for the a) isotropic and b) anisotropic head models. c-d) Same as a-b) but as contour maps. 193
- 9.23 Cross sections of the voltage for the a) isotropic and b) anisotropic models, and c) Measurement voltage percentage error produced by considering the isotropic instead of the anisotropic model, $100|(V^{\text{ani}} - V^{\text{iso}})/V^{\text{ani}}|$ where V are the simulated measurement voltages with both models. 194
- 9.24 Conductivity trace in the anisotropic model for a local perturbation of 10% in the occipital lobe. 195

- 9.25 Cross section (CS) ($z = -4$) of the absolute voltage difference between the a) anisotropic models with and without perturbation, and b) anisotropic with perturbation and isotropic model, for one current injection. 195
- 9.26 Percentage change of scalp voltages for a local perturbation in the brain of 10% in the a) anisotropic model, b) isotropic model. Thus a local change of conductivity of 10% led to 0.02% change on the scalp for the anisotropic case and 0.1% in the isotropic case. 197
- 9.27 (SIM 1, location A) Cross sections (CS) (column 1 and 2) and isosurface (column 3) for linear reconstruction of isotropic data with d-f) an isotropic model for a-c) a local perturbation of 10% change in conductivity and of 16% diameter with respect to head size. 198
- 9.28 (SIM 2, location A) Cross sections (CS) (column 1 and 2) and isosurface (column 3) for linear reconstruction of anisotropic data with a-c) an isotropic (ISO) model and d-f) an anisotropic (ANI) model, for a local perturbation of 10% change in conductivity and of 16% diameter with respect to head size. 200
- 9.29 (SIM 3, location A) Cross sections (CS) (column 1 and 2) and isosurface (column 3) for linear reconstruction of anisotropic data with a-c) an isotropic (ISO) model and d-f) an anisotropic (ANI) model, for a local perturbation of 10% change in conductivity and of 8% diameter with respect to head size. 201
- 9.30 (SIM 4, location A) Cross sections (CS) (column 1 and 2) and isosurface (column 3) for linear reconstruction of anisotropic data with a-c) an isotropic (ISO) model and d-f) an anisotropic (ANI) model, for a local perturbation in the occipital lobe of 1% change in conductivity and of 16% diameter with respect to head size. 202
- 9.31 (SIM 5, location B) Cross sections (CS) (column 1 and 2) and isosurface (column 3) for linear reconstruction of anisotropic data corresponding to a-c) a simulated 9% decrease in conductivity on the temporal lobe, reconstructed with d-f) an isotropic (ISO) model and g-i) an anisotropic (ANI) model 203
- 9.32 (SIM 6, location C) Cross sections (CS) (column 1 and 2) and isosurface (column 3) for linear reconstruction of anisotropic data corresponding to a-c) a simulated 9% decrease in conductivity on the hippocampus, reconstructed with d-f) an isotropic (ISO) model and g-i) an anisotropic (ANI) model 204

- 9.33 (SIM 7, location D) Cross sections (CS) (column 1 and 2) and isosurface (column 3) for linear reconstruction of anisotropic data with a-c) an isotropic (ISO) model and d-f) an anisotropic (ANI) model, for a local perturbation of 10% change in conductivity and of 8% diameter with respect to head size. 205
- 9.34 (SIM 8, location E) Cross sections (CS) (column 1 and 2) and isosurface (column 3) for linear reconstruction of anisotropic data with a-c) an isotropic (ISO) model and d-f) an anisotropic (ANI) model, for a local perturbation of 10% change in conductivity and of 8% diameter with respect to head size. 206
- A.1 A 2-by-2 symmetric matrix A (A.18) maps the unit circle onto an ellipse where the main axes are given by the eigenvectors v_i and the semiaxes length given by the eigenvalues $\lambda_1 = 4$, $\lambda_2 = 2$ 219
- C.1 Relative singular values of the Jacobian with and without row normalisation. . . 230

List of Tables

4.1	Linear inverse problem approaches comparison in terms of modelling the covariance of the solution, C_x , and the covariance of the noise, C_η , inverting C_η , and feasibility for Large Scale Problems (LSP).	88
5.1	Means and standard error (SE) ($p < 0.05$) of the solution error norm, for simulated data, reconstructed by the LC, DP, GCV and UPRE, with (true C) and without ($C = I$) providing the covariance used for simulating correlated noise.	99
5.2	Means and standard error (SE) ($p < 0.05$) of the SNR of the largest change in the reconstructed images of a Perspex in four positions inside a saline head-shaped tank. Images were reconstructed by the two predictors the LC and GCV, where the UPRE and DP did not converge, and with (diagonal C) and without ($C = I$) estimating a diagonal covariance of the noise.	102
5.3	Means and standard error (SE) ($p < 0.05$) of the SNR of the largest change in the reconstructed images of four neonatal data sets where the other six data sets were discarded because images were very noise lacking of a localised change. Images were reconstructed by the four predictors and with (diagonal C) and without ($C = I$) estimating a diagonal covariance of the noise.	103
6.1	Data d and images x SNR, in decibels, before and after projecting the impedance measurements data onto the first principal components (PC), for perspex in a saline head-shaped tank and neonatal data during visual stimulation.	117
7.1	FEM error norm $\% \ e\ _\Omega$ (7.31) by increasing the number of elements N , which yielded a relation $\ e\ _\Omega \propto h^\alpha$ (Figure 7.4), where h is the element size; and the maximum percentage relative vertex error $\max e_i $ (7.30).	128

- 8.1 Summary of simulations. Simulations are grouped regarding their purpose, the eigenvector (eigvec.) orientation and eigenvalue distribution type (eigvals.); they are labelled to be easily found in the text. Also the geometry (geom.) and number of elements of the mesh are given. 144
- 8.2 Mesh parameters and rank results for the Jacobian J with respect to piecewise constant conductivity, for a general anisotropic tensor constant in the domain, where $J \in \mathbb{R}^{N^2 \times 6n_s}$ for # meas. = N^2 , the dof(E) is the number of nonzeros in the upper triangular part of the system matrix E , n_s is the number of elements, n is the number of nodes, N is the number of exterior nodes, and geom. is the geometry. 153
- 9.1 Tissues isotropic value σ^{iso} and tangential:normal conductivity ratio such that $\text{trace}(\sigma) = 3\sigma^{\text{iso}}$ 179
- 9.2 Percentage current density norm at each shell, e.g. $100 \sum_{i \in \text{shell}} \|J_i\| / \sum_{i \in \text{head}} \|J_i\|$, where i corresponded to the tetrahedral elements, for both the isotropic and anisotropic models. 189
- 9.3 Summary of scalp voltage comparisons between the isotropic and anisotropic models with and without a perturbation in the occipital lobe. First row - absolute relative difference (RD) between the anisotropic and isotropic boundary voltages for the reference conductivity: $RD = 100|(F(\sigma^{\text{ani}}) - F(\sigma^{\text{iso}}))/F(\sigma^{\text{ani}})|$, i.e. the error by neglecting anisotropy. Remaining rows - the relative difference between the boundary voltages with and without a conductivity perturbation, $RD = 100|(F(\sigma^{\text{inh}}) - F(\sigma^{\text{ref}}))/F(\sigma^{\text{ref}})|$, giving the mean (\bar{RD}) and standard error (SE), for the isotropic model and the anisotropic models, for a local perturbation where location, % change and size are specified. 192
- 9.4 Results of the linear reconstruction of difference data for the isotropic (ISO) and anisotropic (ANI) data and models, for simulated conductivity changes in different locations, in terms of the localisation error (LE) and maximum reconstructed conductivity value (peak). Also the size (1 diameter, high) in millimeters is given, where the size of the head of the y-direction was 218mm. ²In this data there were two maximums. The LE was 15 ± 3 for the isotropic reconstruction and 13 ± 2 for the anisotropic reconstruction. 196

Special Note

**Page 20 missing from
the original**

List of symbols

A	System matrix (Other times S)
B	Cholesky factor of C
base	Baseline
C	Covariance matrix
C^k	Set of functions with continuous derivatives up to the k -order
$\text{cond}(\cdot)$	Condition of a matrix
d	Data (potential) for the nonlinear problem or difference data and relative difference data for the linear case
$\det(\cdot)$	Determinant of a matrix
$\text{diag}(a_1, \dots, a_n)$	Diagonal matrix with diagonal elements a_i
$E[y], \bar{y}$	Estimation (mean) of variable y
η	Noise
F	Forward problem operator
ϕ	Shape functions
\mathbb{I}	Unit matrix
I	Electrical current
inh	Inhomogeneity
J	Jacobian or electrical current density (few cases)
\mathcal{K}	Null space or kernel
Λ	Dirichlet to Neumann map
m	Number of measurements
meas	Measurements
\mathcal{N}	Normal distribution
$x \sim \mathcal{N}(x_0, C_x)$	Normally distributed variable x with mean x_0 and covariance C_x
n	Number of elements
...	...

...	...
Ω	Domain
$\partial\Omega$	Domain's boundary
$\partial\Omega^\perp$	Domain's interior
σ	Standard deviation or Conductivity (few cases)
σ^2	Variance
Ψ	Diffeomorphism
$\mathcal{R}(\cdot)$	Range of an operator
$r = \text{rank}$	Rank
s	Singular value
stim	Stimulus
U, V	Left and right singular vectors matrix respectively
ref	Reference
sup	supremum
x	Conductivity, difference conductivity or independent variable
$x_1 \cdot x_2 = \langle x_1, x_2 \rangle$	Scalar product of vectors x_1 and x_2
V	Matrix of potential on the electrodes or vector of boundary voltages (Appendix C)

List of abbreviations and notations

ANI	Anisotropic
ANOVA	ANalysis Of VAriance
BEM	Boundary Element Method
CEM	Complete Electrode Model
CS	Cross section
CT	Computerised Tomography
CT	Computerised Tensor
dof	Degrees of freedom
DP	Discrepancy Principle
DT	Diffusion Tensor
DTI	Diffusion Tensor Imaging
DTMRI	Diffusion Tensor MRI
DtN	Dirichlet-to-Neumann
DWI	Difussion Weighted Images
EIT	Electrical Impedance Tomography
EITS	EIT Spectroscopy
EEG	Electroencephalogram
EP	Evoked Potential
FA	Fractional Anisotropy
FE	Finite Element
FEM	Finite Element Method
FMRI	Functional MRI
FWHM	Full Width at Half Maximum
GCV	Generalised Cross Validation
GLS	Generalised LS
ISO	Isotropic
...	...

...	...
LC	L-curve
LE	Localisation Error
LHS	Left Hand Side
LS	Least Squares
MAP	Maximum A Posteriori
MLE	Maximum Likelihood Estimate
MRI	Magnetic Resonance Imaging
NtD	Neumann-to-Dirichlet
PC	Principal Component
PCA	Principal Component Analysis
PET	Positron Emission Tomography
rCBF	Regional Cerebral Blood Flow
rCBV	Regional Cerebral Blood Volume
RD	Relative Difference
RHS	Right Hand Side
RN	Resistor Network
RN	Row Normalisation
SE	Standard Error
SIM	Simulation
SNR	Signal-to-Noise Ratio
SPM	Statistical Parametric Mapping
STD	STandard Deviation
SV	Singular Value
SVD	Singular Value Decomposition
TSVD	Truncated SVD
TV	Total Variation
UPRE	Unbiased Predictive Risk Estimator

Chapter 1

Introduction

There have been great advances in medical imaging in the past two decades. It has now been widely and routinely adopted as a diagnostic tool. For example, brain function is imaged in normal and abnormal brain by measuring mechanism associated with neuronal activity like cell swelling during epilepsy [109] and changes in blood flow, blood volume, and blood oxygenation level during normal brain activity [68].

For imaging brain function, the techniques of Functional Magnetic Resonance Imaging (F-MRI) [133] and Positron Emission Tomography (PET) [137] are able to supply most of the demands and have made a huge improvement in patient management and cognitive neuroscience. The group in which I have been working at University College London has been pioneering the use of Electrical Impedance Tomography (EIT) for imaging brain function. EIT is a relatively new medical imaging method, which has the advantages that it is small, portable safe and noninvasive. Set against this is a relatively poor spatial resolution. Nevertheless, there are several applications in imaging brain function where it has the potential to yield images not possible or practical with other methods. These include imaging in an emergency situation in acute stroke, where the portability of EIT could confer an advantage in deciding whether clot-busting treatments could be used. Acute stroke can be treated with clotbusting drugs if they are administered within 3-6 hours of the stroke onset, but imaging is previously required to eliminate the possibility of haemorrhage, as the clotbusting treatment would make this worse. Thus, EIT could be used in the casualty department and in ambulances [115, 145]. Another possible application is the use of EIT at low frequencies to image neuronal, depolarisation during normal activity. It could also be used in cognitive neuroscience to provide a low cost portable system for imaging blood flow changes related to functional activity.

My PhD work was funded by the Epilepsy Research Foundation and so I have had a particular interest in the possible application of EIT to imaging in epilepsy. Many epileptic patients can be treated with drugs, but some continue to have seizures and these may be

treated surgically. Before operation, they are intensively investigated on a ward, where Electro-Encephalography (EEG) and video are collected over days while they have several seizures. This is termed video-EEG telemetry. Although this has been effective, neither scalp EEG or structural MRI used can give direct information about the local part of the brain where the seizure starts. This can only be obtained with invasive depth electrodes, which is expensive and hazardous procedure. In addition, surgery fails in fourth of cases, which may be caused by inaccurate localisation or the existence of several foci [45]. Thus, EIT could be used in continuous non-invasive monitoring for imaging conductivity changes related to epilepsy.

Inverse source modelling of the EEG has a unique inverse solution under ideal circumstances where the nature and number of sources are known and there are 6 independent measurements for each reconstructed source. Unfortunately, in vivo recordings in the brain, these requirements are not met and so the inverse solution is non-unique. In order to produce a unique solution, the inverse is constrained, for example by imposing a criterion for smoothness [134] or for the likelihood of activation of the different parts of the brain [171]. In practice, good results are achieved for simple sources near the surface of the brain, such as cortical evoked responses, but deeper responses may also be accurately modelled, especially if simple such as deep evoked responses such as those coming from the brainstem in brain stem evoked potentials.

The main drawback of EIT is its low spatial resolution. This is mainly because the image reconstruction problem is not well-posed, being more sensitive to modelling and experimental errors than to body electrical properties, and data sampling is usually incomplete. In the last two decades, a large number of papers have been published, which deal with non well-posed problems. They have mainly addressed numerical methods and optimisation methods, but there is a scarcity of testing with real clinical data. The objective of this thesis was to develop methods which would build on existing work with linear reconstruction algorithms for EIT of the head, and to try and develop improved methods for image reconstruction.

This introductory chapter is divided into four sections. The first section covers, first, imaging terminology, applications, modalities, and the relation between imaging and inverse problems; and then focuses on medical imaging and imaging of brain function. The second section is dedicated to EIT starting with its history, applications, characteristics, and EIT of brain function, and finalising with EIT algorithms. The last two sections set up the goals and outline of this thesis.

1.1 Overview of imaging

In this section, an introduction to brain functional imaging and its relation to other imaging applications is presented. First, imaging in general is introduced. This includes other related imaging applications and terminology. One of the most important concepts in this thesis, namely inverse problems, is introduced. Second, a historical introduction to medical imaging is provided, followed by a presentation of the modalities, divided into structural and functional, that, today, are applied clinically as well as those still in research. Then, an introduction to imaging of brain function is presented.

1.1.1 Imaging and inverse problems

Imaging, meaning ‘to form an image’, has been used to explore astral objects, to probe microscopic tissue, to depict a picture of the inside of the body or deep underground, to forecast the weather, to detect moving objects using radar, to track movement, to find patterns on the earth surface or in a picture, among many others. They all aim to gather and to reveal information in varied areas such as medical diagnosis, astronomy, finance, and so on.

Tomography, which comes from the Greek meaning ‘slice’, was born in radiology where different modalities were employed in an attempt to image slices of the body. Following the precedent set by Computerised Tomography (CT), many imaging techniques have since adopted this term, e.g.: PET, Single Photon Emission Computerised Tomography (SPECT), Optical Tomography (OT) [8], and EIT. Electromagnetic tomography techniques, as well as EIT, are Electrical Capacitance Tomography (ECT), Magnetic Induction Tomography (MIT) and Magnetostatic Permeability Tomography (MPT) [159].

The concepts of Forward Problem (FP) and Inverse Problem (IP) appear in imaging, specifically in tomography, when one attempts a mathematical explanation of the procedures. For imaging, basically, one measures a type of data and aims to image a parameterised property of an object. For this purpose, first, the FP, or mathematical model of how the data depends on the model parameters, is obtained. Let F be the forward operator that maps the parameters $x \in \mathcal{S}_x$, where \mathcal{S}_x is the volume parameter space, into the boundary data $d \in \mathcal{S}_d$, where \mathcal{S}_d is the boundary data space, that is,

$$F : \mathcal{S}_x \mapsto \mathcal{S}_d. \quad (1.1)$$

Then the IP, which is the inverse of the FP, aims to estimate the object parameters from the experimental data. Thus, an inverse operator can be defined as the inverse of the forward operator (1.1) as

$$F^{-1} : \mathcal{S}_d \mapsto \mathcal{S}_x. \quad (1.2)$$

In the case of tomography, for example, experimental data that has interacted with the object is mapped by the IP into a two or three-dimensional distribution of a specific property of the object. In the statistical framework, the deterministic concept of IP is called inference, estimation, or regression; yet it seeks the same goal [43], [176, Chapter 4].

An example of a number of IP applications are presented below. In elastodynamics, one may seek the elasticity parameter, cracks, or inclusions inside an object, by providing mechanic, thermal, or electromagnetic excitations, which are modelled by Poisson's equations with some boundary conditions. Similar models appear for other inverse problems in electromagnetics or acoustics [23].

The EIT problem, whose FP is modelled by the generalized Laplace's equation, aims to recover the conductivity inside an object by injecting current and measuring voltage on the boundary [24].

The Resistor Network (RN) problem aims to detect a failure in a resistor by injecting current and measuring voltages at the external nodes of the network. Its FP is modelled by the generalized Laplace's equation where a 2D EIT problem has a RN equivalent, but the opposite is not always true. While the RN and the EIT forward problems are similar, the IP approach to the RN problem is more unstable, and thus it is not considered in this thesis [100, 37]; besides; uniqueness holds only for special planar rectangular design [35].

Other IP applications include financial markets [28], microwave imaging, and astronomical imaging. The IP in quantum mechanics, for example, provides insight and understanding of the change in energy corresponding to an specific perturbed potential [186]. In radar, which was invented in the 30s, an attempt was made to solve the scattering IP for civil and military aviation [25].

Two common characteristics among these IPs are the lack of existence and uniqueness of a solution, and the non-linear relation between the data and the solution. These make the IP ill-posed and very sensitive to noise in the data. Moreover, IPs have as common goal estimation of the parameters that yield the model data that best fits the experimental data up to the noise level. Besides, IPs share this goal with many areas of sciences where applied mathematics and statistics are needed for minimising the discrepancy between the predicted and the experimental data. For example, computer vision, which extracts information from an image, is applied to medical image analysis, image restoration, gesture analysis, surveillance, among others. In medical image registration, one attempts to find a mapping between two images across modalities or patients.

1.1.2 Medical imaging

1.1.2.1 A brief history

A brief history of imaging as one of the most significant inventions of the century can be found in [125]; a brief summary is as follows.

The discovery of X-rays was a pioneering development in medical imaging. In the late 1920s, imaging as a diagnostic tool was introduced for early diagnosis of breast cancer by using X-rays. In the early 50s, different applications using x-ray technology were developed: X-ray crystallography, which revealed DNA structure and yielded a Nobel Prize, in the early 60s, for solving the structure of proteins myoglobin and haemoglobin; and fluoroscopy that reduced the exposure to the x-rays radiation.

In the 60s, new techniques were introduced for diagnosis: PET, for tumour detection; Ultra Sound (US), for obstetrics and gynaecology; and Nuclear Medicine Imaging (NMR), which used gamma rays, for tumour detection.

The last decades were dominated by the development of computers. In the 70s, Computerised Axial Tomography (CAT) provided several slices and 3D images and was used for brain and spinal disorders; SPECT, for tumour detection. Also, MRI appeared in the medical scene with the development of computers and provided an improvement with respect to CAT although it was not ready till the 80s. The 90s brought fMRI for imaging brain activity after thought and motor stimulation.

1.1.2.2 Imaging modalities

Medical imaging can be divided into two type of modalities with respect to their purpose: anatomical and functional. Anatomical imaging techniques that resolve tissue structure are X-ray, CT, MRI, US, among others (Figure 1.1). Functional modalities, which image body activity, are fMRI, SPECT, PET (Figure 1.2); still at research level: the source localisation techniques EEG and Magneto-Encelography (MEG); EIT, OT, functional CT, Magnetic Resonance Elastography (MRE) (Figure 1.3). Some imaging techniques are based on the previous ones like Magnetic Resonance EIT (MR-EIT) [126].

Hard field modalities, like CT or MRI, are characterised by the value of the field at one point being independent of any other point, which makes it easier to track the field path and leads to high resolution images. In contrast, soft field modalities, like EIT or OT, are characterised by the field at a point being a function of all points where it spreads, which leads to very low spatial resolution and an image reconstruction problem that is not well-conditioned [119, 139]. Thus, soft field modalities are mainly used for functional imaging, for which resolution does not need to be as high as for hard field modalities.

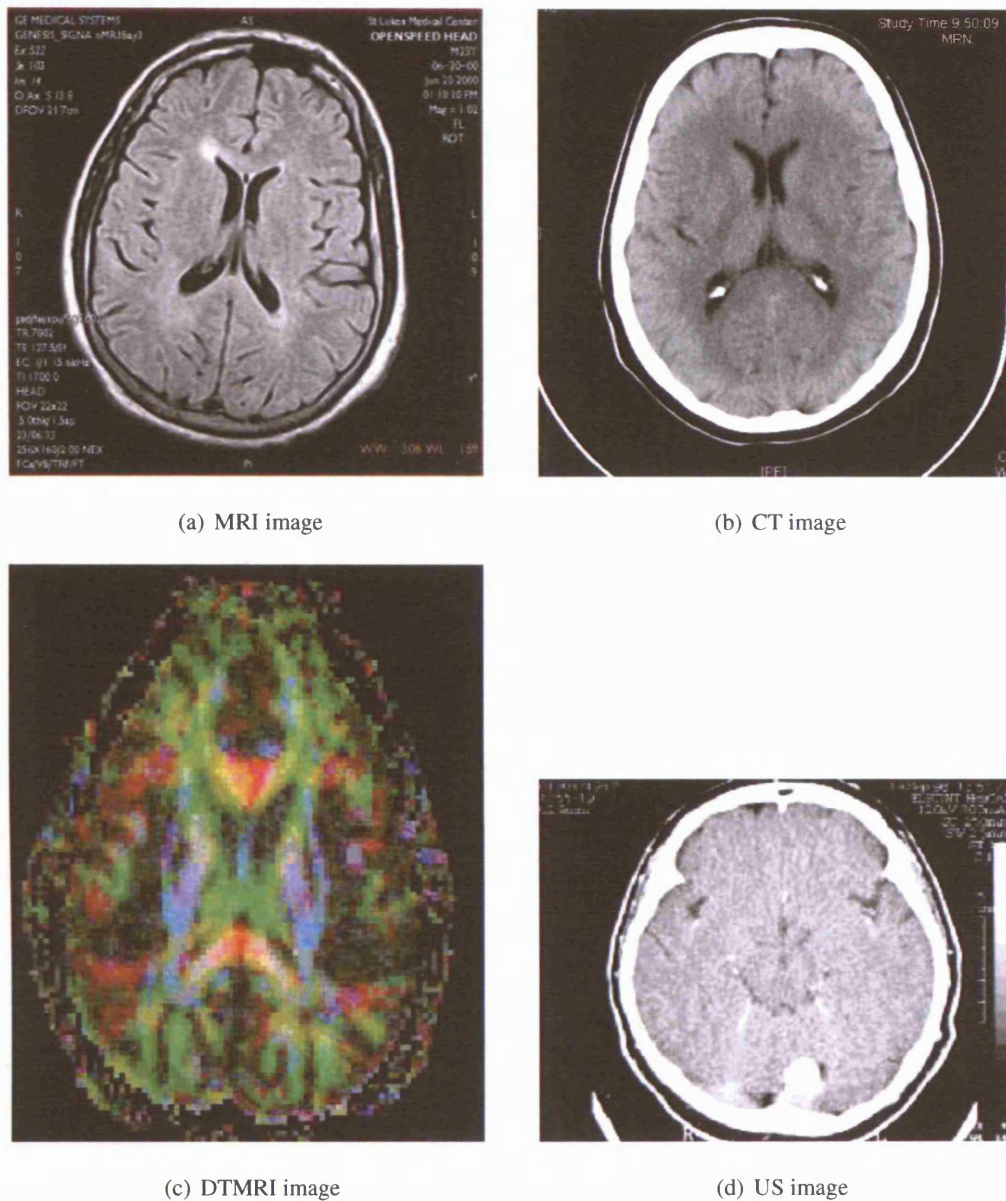


Figure 1.1: Anatomical brain images by different modalities: a) MRI (Wipro GE Healthcare, http://www.gehealthcare.com/inen/rad/mri/products/openspeed/os_neuro6.html), b) CT image (Casey Hospital CT Department, Southern Health Diagnostic Imaging, http://www.southernhealth.org.au/imaging/ct_casey equip.htm), c) DTMRI image where colors specify diffusion directions (Beth Meyerand, Applied Neuro MRI Lab, <http://128.104.229.200/fmri/dti.html>), d) US image of a normal brain in an infant in the NICU (Ultrasound division, Children's Hospital Boston, <http://www.childrenshospital.org/clinicalservices/Site1867/mainpageS1867P0.html>).

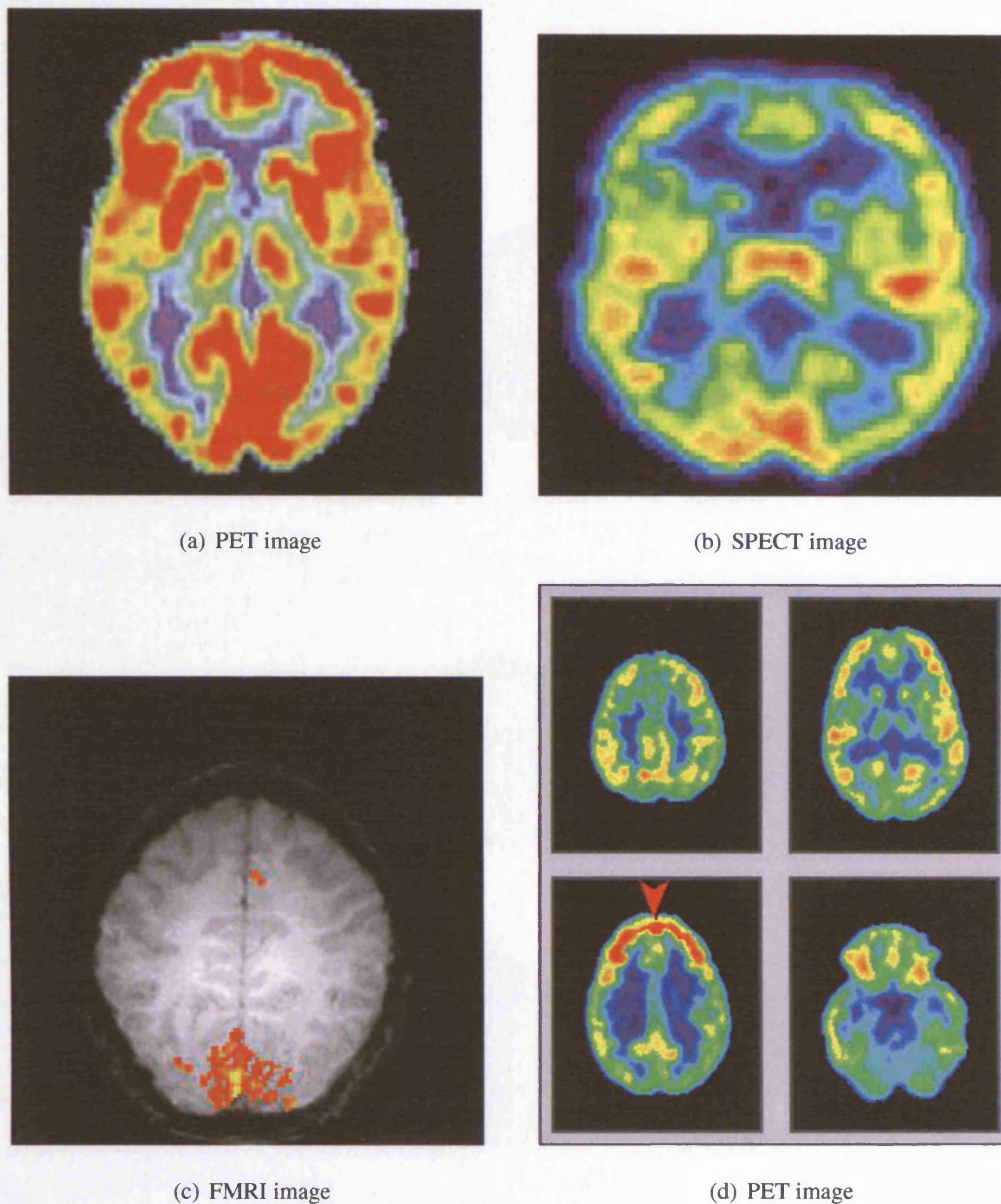
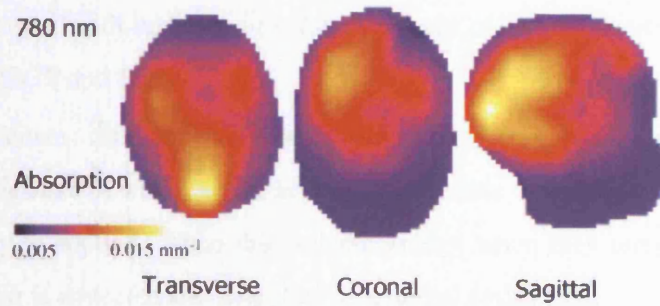
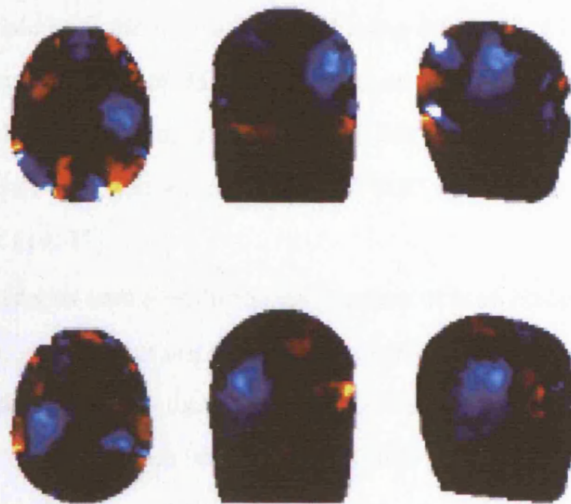


Figure 1.2: Functional brain images by different modalities: a) PET image (WNEM TV5, Your Health: Spotlight On Alzheimer's Disease, http://www.wnem.com/Global/story.asp? S=1935894&nav=menu97_6), and for functional imaging: b) SPECT image (PET imaging at the UCI Brain Imaging Center (BIC), http://www.bic.uci.edu/PET_Imaging.htm), c) FMRI image of visual cortex stimulation (<http://www.imaging.robarts.ca/~jgati/Pages/ fMRI.html>), d) PET image of a subject while thinking (Crump Institute for molecular imaging, from Michael E. Phelps, Dept. of Molecular and Medical Pharmacology, UCLA School of Medicine <http://www.crump.ucla.edu/software/lpp/clinpetneuro/function.html#Function>).



(a) OT image



(b) EIT image

Figure 1.3: Functional brain images by different modalities: a) OT transverse, coronal, and sagittal images of an infant (Biomedical Optics Research Laboratory, UCL, <http://www.medphys.ucl.ac.uk/research/borl/research/monstir/neonatal.htm>, [67]), b) EIT image during left motor stimulation (Med. Phys. Dep., UCL).

CT was the first modality used clinically. It denotes those modalities that seek the recovery of a function by means of line integrals [119]. The leading technique is Transmission CT where X-rays are sent from several sources and their intensity is measured after having interacted with the object of study. By covering a plane with line integrals and assuming that there is no scattering, a cross-section of the body is imaged by inverting the Radon transform, which relates the line integral with surfaces; or volumes, in case of covering a volume. Other CT-type modalities are SPECT and PET,

MRI discriminates different tissues with respect to their amount of water. Atoms of hydrogen in the molecules of water, which act as tiny magnetic dipoles, get aligned when a pulse of radiofrequency is applied. Then they release energy when they return to the position of equilibrium, which is collected and amplified by external coils [133].

For anisotropic materials, like muscle tissue or white matter, which present an aligned microstructure providing a preferred direction on the diffusion of water molecules, DT-MRI relates the microscopic with the macroscopic diffusion tensor [3, 172]. For this purpose, DT-MRI is required to apply diffusion MRI, at least seven directions so as to characterise the six components of the diffusion tensor and a constant. MR has been applied mainly to the brain; other applications are breast, kidney, and liver; DT-MRI outside the brain has been applied to the tongue and heart [19, 17].

In PET, radioisotopes emit a positron that interacts with an electron, and as a consequence of their annihilation, two photons are emitted 180 degrees apart which are detected by the system. It was developed in the 50s, but initial images were blurred. Image quality improved in the 70s, due to improved hardware which allowed more photon counts per image, iterative algorithms and, filtered back projection and Fourier based methods [137]. PET may be applied to diagnosis of Alzheimer's disease, cardiovascular diseases, and cancer; it can image cancer lesions and discriminate benign and malignant lesions in cases where CT or MRI cannot. Moreover, PET can be also applied for imaging brain activity.

Two areas of relevant interest for us are medical image registration and multimodality. Medical image registration is used to compare images, for example, for diagnosis before epilepsy surgery where images correspond to different modalities; it also allows inter-subject comparison [110]. The registration procedure requires several criteria where the most relevant are the feature to be compared, whether based on segmentation or based on information content, the transformation type mapping between images, and the optimisation procedure [103, 110]. Special care needs to be taken when applying transformations on tensors; tensors have different transformation rules than vectors, which have been studied for DT-MRI [4, 34]. In contrast to

the comparison of images from different modalities in medical image registration, multimodality imaging combines the advantages of two modalities by solving both problems simultaneously, e.g. PET and x-ray CT [137].

In EIT, low frequency electrical fields propagating throughout the subject can be modelled by the generalized Laplace's equation, which is equivalent to the propagation of heat in a room where an external source may be a heating system. In this situation, the temperature at one point of the room far from the source depends on the conductive properties at all points the heat flow has travelled up to there. In a more complex medium, one may also consider anisotropic properties of the medium, which favours special directions at each point.

Some biological tissue especially bone, muscle, and brain white matter - is highly anisotropic. In principle it might seem desirable to model anisotropy for EIT, but there have not been many attempts because the image reconstruction problem is more complicated and, in the past, there has been a lack of anisotropic conductivity tensor estimates. The first studies contemplating numerical simulations of anisotropy in EIT are reviewed in the next section. An estimate of the anisotropic conductivity tensor can be obtained from the diffusion tensor by using the cross-property relation. This is a relationship between different transport tensors, that, for the case of the diffusion and conductivity tensors, is given in terms of the intra- and extracellular space, such that, both tensors share eigenvectors, and, for low frequencies, their eigenvalues are linearly proportional [66][172, Chapter 5].

A combination of MRI and EIT, MR-EIT, in which one injects electrical current using EIT and measures the magnetic flux density with MRI, has taken the first steps to provide numerical anisotropic conductivity images based on the MR-EIT model, assuming symmetry in the z-direction [156].

1.1.3 Imaging of brain function

How the brain works has been a mystery. A brief review of the history of brain function and physiology is presented below [133].

In the mid of the 19th century, some studies related brain and mind by associating physiological disorders, like aphasia or problems with speech, with damages in specific parts of the left hemisphere of the brain. This allowed creation of a map for several functional regions of the brain [148] (Figure 1.4). Quoting the neurologist Sacks regarding one of his patient who suffered a massive tumour in the visual cortex:

Sometimes a student would present himself, and Dr. P. would not recognise him;
... The moment the student spoke, he would be recognised by his voice.

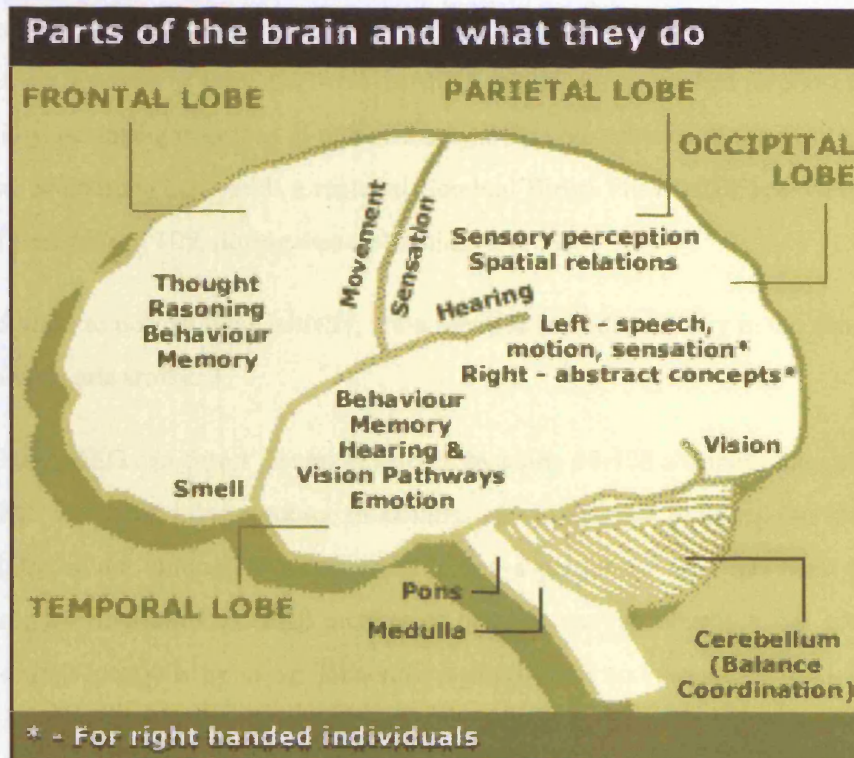


Figure 1.4: Map of functional regions of the brain (BBC News, Monday, 7 June, 1999, 18:39 GMT 19:39 UK, http://news.bbc.co.uk/2/hi/health/medical_notes/363368.stm)

Mapping of functional regions was developed through animal studies where provoking brain lesions produced functional disorders. However, Freud soon realised that this identification was rather simplistic and focused only on the most specialised regions [148]. Besides, lesions can damage more than the provoked region, complicating the diagnosis.

In the late 1970s, imaging innovated clinical diagnosis by localising brain tumours using x-ray CT. At present, fMRI and PET can be used to identify *in vivo* activated regions of the brain while it carries out a specific activity - they teach us how the brain works. Also, EEG has been widely used by neurophysiologists treating epilepsy.

What happens in the brain when it gets activated? Some excitation encoded as an electric impulse reaches the axon of a neuron, which releases chemical transmitters when the impulse exceeds a threshold, and then it is transferred onto the synapse and from there onto the dendrites of other neurons. When this process continues, a region is activated. This activation that is accompanied by energy consumption demands an increase of oxygen, and so it yields an increase of blood flow, which is known as the haemodynamic response.

Consequently, there are two types of physiological effects related to brain activity. Fast

brain activity occurs over tens of milliseconds, and a transfer of ions during neuronal depolarisation yields a decrease of local electrical resistivity of 1% during evoked responses [52]. Slow brain activity, occurring over tens of milliseconds, is the consequence of the overlapping effect of millions of neurons that yields a regional Cerebral Blood Flow (rCBF) or Volume (rCBV) change of the order of 10% during visual stimulation [168].

In addition to normal brain activity, brain function includes activity in the abnormal brain due to epilepsy and stroke.

EEG and MEG can detect fast brain activity by using 64-128 channels and sampling rates up to 8KHz. However, inverse source modelling, which attempts to image the sources of the brain activity, is not uniquely determined. Finding a unique solution has been achieved by constraining the solution to a small number of dipoles; another approach has considered all possible source locations by using Tikhonov regularisation and assuming MRI-based priors [138].

EIT measuring hundred times a second could be used for imaging fast neuronal activity, as an alternative to EEG with similar temporal and spatial resolution, but in contrast with EEG, in EIT the source is known; yet EIT data SNR on the present-day is very low for those tiny signals [51, 52].

fMRI and PET have been used for imaging changes in rCBF. fMRI can measure changes in blood flow and blood oxygenation level [68]; it obtains, first, an structural image and then statistically maps a change of rCBF. fMRI measured changes of 1.8% in rCBF and blood oxygenation in the visual cortex under 8Hz flash stimulation [99]. These results are in agreement with PET studies where increases of rCBF were seen during different brain stimulations [113].

The standard structural imaging techniques fMRI and PET have high spatial resolution, of millimetre accuracy, but low temporal resolution, of a few seconds, limited by changes in blood flow. In contrast, EEG/MEG source localisation techniques have a high temporal resolution, of milliseconds, measuring fast neuronal activity, but they have a low spatial resolution, of ten millimetres or so. EIT belongs with EEG/MEG to the group of functional imaging techniques of low spatial resolution but high temporal resolution [75].

Although fMRI and PET are the leading techniques for imaging slow brain activity, new modalities like EIT and OT are being developed and, may in time provide an alternative since they are portable, non-invasive, and cheaper.

1.2 Electrical impedance tomography

1.2.1 History and background

Different materials have dissimilar electrical conductivity; therefore, conductivity can be exploited for providing a volume map that differentiates materials of different electrical properties, for example, for detecting water in the lung.

In 1980, Calderón proposed the problem of determining under what conditions a unique conductivity could be recovered from boundary voltage [81]. Uniqueness for isotropic conductivities has been proved [92, 93, 165]. Nevertheless, anisotropic conductivities cannot be uniquely determined by boundary voltages [101], unless, some a-priori information is provided [104]. Providing uniqueness for an inverse problem is analogous to assuming stability under certain constraints [83], where stability can be studied by looking at the conditioning of a given mapping. Stability for EIT algorithms has been reviewed in [24].

EIT refers the imaging technique that, by applying current and measuring voltage at the boundary, or vice versa, provides a volume complex conductivity. In principle, under a perfect knowledge of the boundary shape, this current-to-voltage map depends uniquely on the conductivity. In practice, one does not have a full knowledge of this map; in addition, the measured voltage strongly depends on the electrode contact impedance, position of the electrodes, and boundary shape.

This dependence has yielded three different modalities of EIT: static, dynamical, and multifrequency. Static imaging aims to reconstruct an absolute conductivity [31, 120], and is the most difficult of the three because there is a strong dependency of the measured boundary impedance on external parameters [97]. In dynamical imaging, a change of conductivity is recovered from a small change of boundary impedance; it requires a reference, and enables a reduction of the errors. EIT Spectroscopy (EITS), also called multifrequency EIT, takes advantage of differences in conductivity between different tissues over a frequency range [57].

In the early years, EIT was limited to the 2D case where a cross-section of the body, delimited by a ring of electrodes, was imaged. In the 1980s, a back projection reconstruction algorithm for EIT was suggested by Barber and Brown [13] and explained numerically in [151]. This approach assumed a 2-D linear version of Poisson's equation and that the initial conductivity was homogeneous. Although it was widely used, these assumptions were proved to be crude. Nowadays, a 3D nonlinear model of the electrical fields is widely used [117, 120], with modelling of the electrodes [31], and in real-time [22]. The Electrical Impedance and Diffuse Optical Reconstruction Software (EIDORS), a MATLAB toolbox for the 3D EIT problem with modelling of the electrodes, is freely available [140].

Clinically, EIT could provide a non-invasive, safe, portable, and cheap imaging technique, by measuring electrical impedance on electrodes placed on the skin of the subject; it permits estimation a volume conductivity map of the body. History and general references can be found in [75]. In the early 80s, clinical EIT was born at Sheffield with a system that was suitable for humans, the Sheffield Mark I, which became commercially available. At this early stage, most clinical studies were carried out with that system, which provided difference imaging only and was successfully applied to gastric emptying and ventilation [74].

So far, the EIT community has been divided into groups dealing with algorithm development, where diverse nonlinear reconstruction methods have been used; and groups that seek success experimentally, for which linear reconstruction methods have been adopted. At the moment, EIT is being developed and modelling and other specific issues must be addressed [106].

1.2.2 Applications

Most of EIT applications are in Geophysics [132], medical imaging, and process tomography. Process tomography has applied Electrical Resistivity Tomography (ERT) for imaging particle transportation through pipes [178]. EIT for medical applications has been successfully applied to imaging gastric emptying [111], gastric acid secretion, and lung ventilation [117, 65]. Other possible applications which are under development are lung water detection; hyperthermia; imaging breast cancer with EITS [128]; detecting intraperitoneal fluid [149]; imaging brain functional activity: epilepsy, discerning between cerebral ischaemia and haemorrhage [73, 72], detecting intraventricular haemorrhage in neonates, and normal brain functional activity [168]. A review can be found in [30, 74, 75].

As for other applications, for instance, EIT has been proposed for crack detection where experiments have been done in 2D by using a resistor network approach [100].

1.2.3 EIT systems for medical applications

EIT systems for medical applications have been used, now, for nearly three decades. A review of EIT systems and instrumentation can be found in [30].

1.2.3.1 Systems for medical applications

The first system used clinically was the Sheffield Mark I, which, developed in 1987, injected current at 5mA at 50KHz, had 104 independent adjacent measurements, and took a measurement every 40ms. An improved system, the Sheffield MK3.5, measured both the real and imaginary part of the impedance, injecting a current, at 30 frequencies in the range $2KHz-1.6MHz$, using an adjacent drive and 8 electrodes [180].

A modified version of the Sheffield system, at UCL, the UCLH Mark-II/Sheffield MK3.5 system, was designed for multifrequency with a frequency range 20 – 500KHz [116].

An adaptive current system, the ACT3 system, injected a sinusoidal current pattern which was proved to optimise the current injection pattern. It injected 0.5mA peak of sinusoidal current at 29KHz, using 32 electrodes and taking an image in 133ms [53, 33].

Below 100kHz, the resistive component of biological tissue is predominant over the capacitive one. Almost all clinical applications have worked at around 50KHz and have neglected the imaginary part of the complex impedance. However, for pathologies like stroke, for which a reference is not available, one may use multifrequency EIT, compensating for the lack of a time reference by using a large range of frequencies [116].

EIT systems for medical applications as any other electrical equipment must follow safety regulations that limit the maximum power dissipated in the body. It is common to limit the total current than can be injected into the patient and the leakage currents [50]. The maximum current that can be used depends on the frequency used. The IEC 610-1 regulations for current applied to the skin permit 100 μ A at 1KHz which scales linearly with applied current in KHz up to a maximum of 5mA at 50KHz and above. A limit in the leakage currents that flow from the patient to the ground protects the patient in case of malfunctioning. This limit corresponds to about 10% of the threshold at which sensation occurs. EIT systems apply less than this - a typical figure would be 5mA at 50KHz.

1.2.3.2 Resolution

A high temporal resolution is one of the advantages of EIT. For example, a measurement is acquired every 40ms with the Sheffield Mark I.

Spatial resolution is the main disadvantage. It depends on the number of electrodes, type of current pattern, which electrode combinations are selected from among all possible ones - this is termed the electrode protocol, and noise. Early studies, summarised in [74], showed spatial resolution of 12 – 20% of the diameter of a ring of electrodes, where spatial resolution is defined as the smallest distance to separate two objects. The smallest values were obtained near the edge, for radially moved perturbations; the largest values were near the centre, for tangentially moved perturbations.

1.2.3.3 Current injection protocol

The type of current pattern and electrode combinations used for injecting the current determine the information content in the data, which can be quantified by the number of independent measurements. While an optimum sinusoidal current pattern can be applied using all electrodes [31, 53], less computationally and instrumentationally demanding current patterns have been

preferred: an adjacent injection has been applied to cylindrical objects, and a diametric injection has been used for providing deeper sensitivity.

For an adjacent protocol, given N electrodes, there are N adjacent pairs for the injection and $N - 1$ pairs for the measurement; therefore, the number of independent measurements is given by $N(N - 1)/2$ [12]. Thus, the number of independent measurements is 120 with 16 electrodes, acquired in 0.5s, and 8128 with 128 electrodes, acquired in 20s where measurements were taken in serial, and acquisition time could be improved by measuring in parallel [12]. If one excludes the drive electrodes used for measuring, then there are $N(N - 3)/2$ independent measurements for the adjacent protocol.

The adjacent protocol has been used for rings of electrodes placed on cylindrical bodies. However, for some applications, like EIT of the brain, since electrodes are not equally spaced throughout the head surface, one may consider other electrode combinations. In practice, it is impractical to use all possible combinations where the total number of combinations is given by $C_{N,2}C_{N-2,2} = N(N - 1)(N - 2)(N - 3)/4$, which is over two hundred thousand for 32 electrodes. Since an adjacent injection provides more sensitivity near the boundary, diametric injection has been used for EIT of brain function, as this provides deeper sensitivity [15]. However, this required the selection of a set of electrode combinations.

Thus, use of an arbitrary protocol requires selection of a small number of measurements among all possible ones. A complete search across all possibilities is computationally impossible [107]; for example, for 32 electrodes, even fixing the length of a protocol to 200 measurements and constraining the searching space to 1000 possible combinations, the selection yields $C_{1000,200} \simeq 10^{208}$ comparisons. Thus, the problem of obtaining an optimum protocol for a general combination of electrodes, for which one must constrain the searching space, remains open.

1.2.3.4 Electrodes

The number, location, and contact impedance of electrodes influences the image resolution. How many electrodes should be used? In principle, adding more electrodes will improve the spatial resolution up to some limit since it augments the number of independent measurements. Nevertheless, it has been pointed out that as one increases the number of electrodes, noise appears more significant because the potential gradient is proportional to N^{-2} [12]. Thus, it was reported that going from 32 to 128 electrodes, using adjacent measurements at 1mA on a human arm, led the smallest measured potential to go from $80\mu V$ to $5\mu V$. As a measure of the electrode noise, it was reported that Johnson noise, for an electrode impedance of $1K\Omega$ and electrode surface of $4mm^2$, at 50KHz was $0.9\mu V$.

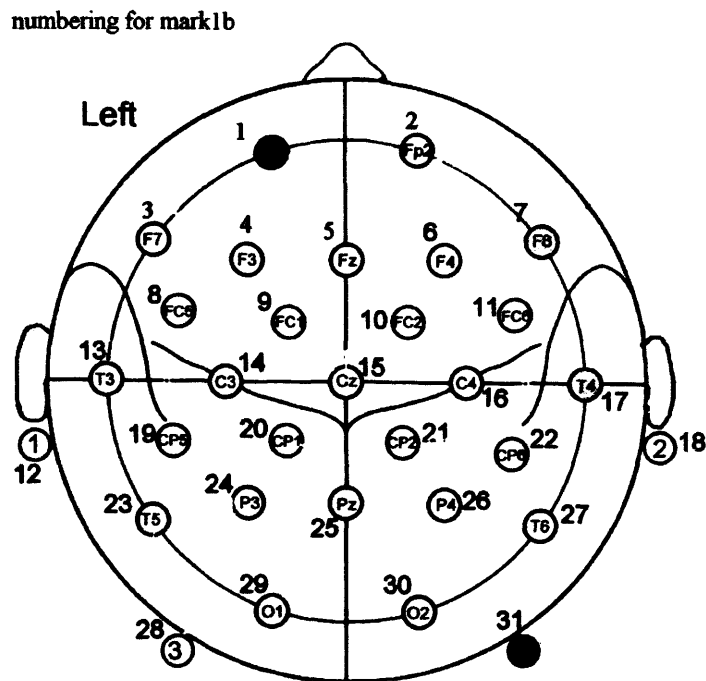


Figure 1.5: 31-electrode positions designed for the human head at UCL based on the 10-20 EEG electrode localisation protocol.

An optimum position for electrodes for general 3D objects is not clear. The UCL group has used, for EIT of brain function, 31 electrode positions (Figure 1.5) based on the 10-20 EEG electrode location protocol [20].

It is essential to model the contact impedance of the skin-electrode interface because there is a potential drop, explained by Ohm's law as ZI , when a current I passes through the contact impedance Z [82, 135]. For medical applications, Z could be described in parallel as the resistive part of the gel, skin, and electrode added in serial and the impedance part corresponding to the phase [74, Chapter 8][114].

1.2.3.5 Noise and experimental sources of error

Source of errors have been classified into random noise, systematic changes, and physiological noise [74, Chapter 1]. Discrepancies between the model and the subject include boundary shape, conductivity values, and anisotropy. Instrumentation issues are electrode contact impedance, phase changing across electrodes, and stray capacitance in the electronic and leads.

Although calibration in saline tanks account for some sources of error, like discrepancies between the model and the tank and some instrumental errors, validations in vivo test for electrode location and movement, isotropy and homogeneity assumption, and physiological

noise. It was concluded that correction for those errors was difficult unless they were clearly identified or random noise that could be averaged out. As a general figure, noise could be decreased below 1%. For example, for animal experiments, slow drifts in the cerebral cortex were of 0.5% [73]; for neonates scalp measurements, physiological and movement errors were of 0.1 – 1%, and baseline drift in the upper abdomen was of 5%, as summarised in [74, Chapter 1].

1.2.4 EIT of brain function

EIT may be applied to imaging brain function, where changes of cortical impedance measured on the scalp are related to changes in local brain impedance. EIT of brain function has two major applications: imaging fast brain activity, which occurs over milliseconds, due to action potentials [51]; and imaging the slow brain activity, which occurs over seconds or minutes, in epilepsy, ischaemia and haemorrhage, and normal brain activity. In this work, the focus is the slow brain activity.

During epileptic activity there is a dominant local impedance increase due to cell swelling and reduction of the extracellular space [109]. In cat and rabbits, using intracortical electrodes, a predominant increase in impedance was explained as the effect of the electrolyte transport into the cellular elements; yet a smaller decrease in impedance was explained by an increase of metabolism and local vasodilatation [64]. Similar studies, in cats, found impedance increases of 3.5 – 5% dominant to impedance decreases; and, for the long and strongest seizures, found impedance increases of up to 10 – 12% [42]. Other studies found an increase in 85% of cases, a decrease in 9%, and mixed in the rest [157]. An increase of 10 – 12% was found in most activated regions [41]; specifically, they found an increase in the resistive part and a decrease in the capacitive part of the impedance. Using the Sheffield Mark 1 EIT system, impedance increases of 5 – 12% were imaged with a spatial resolution error of 7 – 12% of the imaging field [143]. An attempt for imaging epilepsy with scalp electrodes and an accurate head model has been done where changes were excessively large compared to the reported animal experiments and the model prediction; a more controlled baseline and less movement were reported as essential for future studies [45].

During normal brain activity, a decrease of cortical impedance is related to an increase of rCBV in the stimulated cortical area [49]. Using the Sheffield Mark 1 EIT system, impedance decreases of 4.5% have been imaged, in rabbits using cortical electrodes, during sensory evoked responses [76]. A similar study found impedance decreases of 2 – 5% [143].

One may expect a decrease of one or two orders of magnitude on scalp electrodes, due to the fact that the skull, which is hundreds times more resistive than the brain, diverts applied

current. During visual stimulation, an impedance decrease of the order of 0.5% was found in scalp electrodes [168]. Although scalp impedance changes were consistent, localisation of conductivity changes in the reconstructed images was unsuccessful. In neonates, an impedance decrease of 1%, larger than on adults, was explained on the basis that neonates have a smaller volume response to the stimulation, yet present a smaller attenuation by the skull, which is not calcified and mainly formed by cartilaginous tissue [166]. However, those impedance changes meant a decrease of one order of magnitude with respect to local changes, contradicting new model predictions that forecasted a decrease of 50 – 100 times because of the shunting effect of the skull [78].

For discerning haemorrhage from ischaemia in acute stroke, a feasibility study has been undertaken which compared modelled scalp impedance changes with several modelling errors. It concluded that EIT multifrequency could be an alternative to absolute imaging if electrode positions were measured with millimetre accuracy and better estimates of tissue conductivity were provided [78]. Simulated local resistivity changes up to 75% due to ischemic tissue and –750% due to haemorrhage tissue led to 2% and –7% changes on the scalp [78].

In the last five years, some efforts have been made to produce an accurate model of the head for EIT of brain function: the influence of the skull on localisation [167]; the influence of a shell model versus a sphere model and numerical finite element method (FEM) versus analytical formulation [108]; an accurate model of the head in which layers representing scalp, CSF, skull, and brain obtained from MRI scan were incorporated [16, 11, 170].

The variability of tissue conductivity values published in the literature, many taken under different conditions, and anisotropy makes accurate simulation in the forward problem difficult. An extensive review of both pathological and healthy tissue of the head has been recently done [79]. White matter in the brain and the skull are highly anisotropic. The skull is comprised of different layers with diverse conductivity, making local inhomogeneity relevant and hardening the estimation of a generic conductivity for the skull. For example, the resistivity of the tibia was found to be $1.55K\Omega cm^{-1}$ in the axial direction, $15.79K\Omega cm^{-1}$ in the circumferential direction, and $21.5K\Omega cm^{-1}$ in the radial direction [150]. For the white matter, the anisotropic conductivity tensor can be estimated from DT-MRI since the diffusion and conductivity tensors share eigenvectors and eigenvalues are linearly proportional at low frequencies [172].

Influence of anisotropy of both white matter and skull and skull thickness have been studied for the EEG and EMG forward problem and inverse source localisation [127, 66, 182, 181]. It was found that the effect of anisotropy was most relevant for white matter when the source was close to the cortex. Anisotropy of the skull gained importance for a deeper source in the

brain; neglecting anisotropy yielded 10% error on the forward solution. There does not appear to have been any equivalent work for EIT.

1.2.5 EIT algorithms

The theory used in this thesis for the forward and inverse problems is given in the next three chapters, but main issues from a general point of view are reviewed below. A review on EIT algorithms can be found in [106, 24].

1.2.5.1 Forward problem

Reconstructing the conductivity requires, first, solution of the forward problem, that is, obtaining the electrical potential in the whole domain for an estimate of the conductivity. There are several methods for solving the forward problem, which are introduced in the next chapter. Here, main difficulties and modelling issues that make the forward mapping influence the inverse problem are presented.

The estimated boundary potential is a nonlinear function of the conductivity estimate, external geometry, and modelling of the electrodes. As a result of the nonlinearity, accurate exterior shape and electrode position are essential for the forward model to fit the boundary measurements. In fact, there is not a unique isotropic conductivity that satisfies the boundary voltages without a perfect knowledge of those quantities [105].

When an accurate value for those figures is not available, there are ways around it. For instance, it has been proved that one can reconstruct both the boundary shape and conductivity from impedance boundary measurements [104]; a study checked its feasibility in a numerical example [160]. The idea behind the last point is to include into the inverse problem those parameters that cannot be accurately measured. Although this makes the reconstruction harder, the converted problem has a higher chance of being solved. For example, one may recover simultaneously the electrode contact impedance and interior conductivity [175], which has been successful in tank experiments [69]. While, for EIT of brain function, contact impedance of the skin-electrode interface has been pointed out as an important source of error [78] which varies across subjects and time, it is not usually measured [74].

Introducing all uncertainties into the reconstruction is appealing; nevertheless, real applications must prove, first, the feasibility of their problem by providing the true values of the electrode position, external geometry, and electrode contact impedance. A simulation study for EIT of the head concluded errors in electrode position had more effect than electrode contact impedance and conductivity estimate. Moreover, electrode positions can be accurately obtained with a precision of a millimetre using photogrammetry [147]. An irregular and complicated ge-

ometry, such as that of the human head, must be modelled accurately to achieve a good forward solution - model. This has been done for a generic subject in EIT of brain function [11] where an accurate model of the head was obtained from a structural imaging technique, like MRI or CT [16, 170].

Another option is to compensate for the geometric mismodelling with anisotropy, which has been accomplished in both OT and EIT [70, 96].

1.2.5.2 Inverse problem

Once there is a mathematical forward problem that predicts boundary voltages for given model parameters, the inverse problem estimates some of those parameters, usually the conductivity, from measured boundary voltages. In the following chapters I present the theory employed in this thesis; below I introduce the nonlinearity of the problem and a few of the most popular reconstruction algorithms, regularisation approaches, and uniqueness.

The recovery of interior conductivity from boundary measurements is a nonlinear problem where boundary measurements are much more sensitive to external shape, electrode position, and skin-electrode impedance than to internal conductivity. The nonlinearity has been explained as a consequence of the fact that large changes in conductivity may provide small changes in voltage since potential redistributions tend to be minimised; therefore, small perturbations in voltage can lead to large errors in the reconstructed conductivity [74, Chapter 3].

Nonlinearity has influenced EIT to be divided into three approaches: static imaging, for which one attempts to obtain the real conductivity values; difference imaging, for which a change in conductivity is estimated from a change in boundary voltages; and multifrequency imaging, for which one seeks conductivity changes across frequency instead of across time.

Difference imaging, using linear reconstruction algorithms has been preferred in most clinical applications because it is less sensitive to errors than static imaging. The linear back-projection algorithm, proposed by Barber and Brown as a linear version of the EIT problem and explained with the Radon transform in [151], was proved to be unstable [18]. As a result, most of the clinical applications have hitherto adopted a direct linear reconstruction of difference data, for example, Truncated SVD, which can get rid of some of the consistent errors [13, 11], and single-step reconstruction methods like Newton's One Step Error Reconstructor (NOSER) [80, 31] and the three-dimensional linearised reconstruction (ToDLER) [22] were implemented in the early years. Normalised data has been suggested for reduction of the influence of shape and electrode position errors [74].

Static imaging aims to recover absolute conductivity and appears to be feasible if the boundary voltages can be predicted with an error of 0.1% [161], however, an accurate model

of the electrodes and the boundary shape is also required [97]. In the last two decades, a large number of reconstruction algorithms have been proposed; a review can be found in [8, 24, 106].

Solving an ill-posed problem can be done by regularising the solution by penalising high frequency components; common approaches are Tikhonov and Total Variation (TV) regularisation. The Tikhonov type is associated to L_2 norms and is characterised by smoothing edges on the image. The TV type corresponds to L_1 norms and penalises variations while preserving sharp profiles [38, 26, 176].

Theoretically, while the problem of recovering isotropic conductivity from boundary voltages has an unique solution [92, 93, 165], recovering anisotropic conductivity is not unique [93, 101]. Nevertheless, uniqueness for the anisotropic case can be recovered by providing a priori information, which could be taken from another modality [104].

1.3 Thesis goals

In last two decades or so, the EIT algorithm community has developed a large number of methods to deal with the ill-posedness of the problem by using optimisation, priors, and statistical methods; EIT applications have been successful because simplified approaches to the reconstruction problem have been used and efforts have been made to focus on the forward modelling and instrumental issues.

This thesis is an attempt to incorporate those novel approaches into improving image reconstruction in EIT of brain function: implementation of optimisation algorithms, statistical methods, improvement of the head model, and use of priors that could be a first stage towards multimodality.

There were four main goals: to optimise linear reconstruction, improving SNR of raw data, the recovery of a piecewise linear anisotropic conductivity tensor with known eigenvectors, and to include anisotropy in a realistic forward model of the head. The objective of optimisation of the linear inverse problem was to develop a method that could cope with the requirements of our problem: handling large scale problems; model a realistic distribution of the data where diverse variances and correlations could be modelled; and optimisation of regularisation up to the noise level for each data set. Improvement of the SNR in the raw data prior to reconstruction was a major goal since the skull shunts applied current and this reduces the signal that is measured on the scalp just to the limit of being detectable. The last two goals, which modelled a conductivity tensor in anisotropic media, were to verify numerically the feasibility of the recovery of a piecewise linear anisotropic conductivity tensor with known eigenvectors; and to study the influence of anisotropic tissue, such as the skull and white matter, on the boundary voltages and

the reconstructed conductivity.

1.4 Thesis outline

General theory for the forward and inverse problem is covered in chapters 2 and 3. In chapter 4, the goal was to summarise the most important methods for solving the linear inverse problem with the intention of determining which one satisfies the requirements for linear EIT of brain function to be used during the rest of the thesis. These include methods that deal with ill-posedness for linear inverse problems, modelling the covariance of the noise, and computational issues for large scale problems.

Chapters 5 and 6 are the results chapters for the method developed for optimising linear EIT of brain function. These were tested in saline filled tanks and human neonatal data acquired during visual stimulation. In chapter 5, the goal was to develop a methodology for selecting an optimum regularisation parameter and modelling the covariance of the noise. In chapter 6, the goal was to improve the SNR of the data and the reconstructed images by applying Principal Component Analysis.

Chapter 7, 8, and 9 form the final major project of the thesis with the aim of analysing the influence of anisotropy for EIT of the head. In chapter 7, a FEM forward solution for anisotropic media was validated with an analytical solution for a cubical domain with a Dirichlet boundary condition. In Chapter 8, the aim was to verify uniqueness for the recovery of a piecewise linear conductivity tensor with known eigenvectors from the complete NtoD data, that is, all possible boundary data, using a numerical approach; which is an important usable constraint for EIT of medical applications. Chapter 9 is a feasibility study of anisotropy for EIT of the head. The purpose of this was to study the influence on the forward and inverse problems of inclusion of an anisotropic conductivity estimate in the model.

Chapter 10 presents conclusions of the thesis, a summary of findings, and suggestions for further research.

Chapter 2

Forward problem theory

Reconstruction of the conductivity distribution inside an object requires, first, solution of the forward problem. This means solution of the voltage in the whole domain, given a physical model for the applied current injection and conductivity estimate, and then obtaining the boundary voltages. Thus, the forward operator F as defined in (1.1) maps the volume conductivity x into the boundary voltages d (section 1.1.1). The physical system is modelled by combining Maxwell's equations of electromagnetism, which for the quasi-static approximation leads to the generalised Laplace's equation, with a choice of some boundary conditions. The system of equations can be solved analytically for simple geometries or numerically for geometrically complicated objects where FEM formulation is the most widespread.

2.1 Physical model

In EIT, an electrical current is injected, generally, through a pair of boundary electrodes, and the voltage is measured at a different pair. Thus, one requires both a good electrical model for estimating the current flow in the object, which is solved by Maxwell's equations, and a realistic model of the electrodes, which can be approximated by the Complete Electrode Model (CEM).

2.1.1 Maxwell's and the generalized Laplace's equations

James Clerk Maxwell, a Scottish lord from the Victorian times, who was greatly amazed by the revelation of the equivalence between light and electromagnetic waves, stated a set of equations that solves all classical electromagnetic problems [46, 169]. Those are

$$\nabla \cdot E = \frac{\rho}{\epsilon_0} \quad (2.1a)$$

$$\nabla \times E = -\frac{\partial B}{\partial t} \quad (2.1b)$$

$$\nabla \cdot B = 0 \quad (2.1c)$$

$$c^2 \nabla \times B = -\frac{J}{\epsilon_0} + \frac{\partial E}{\partial t} c^2, \quad (2.1d)$$

where E is the electrical field, B the magnetic field, both twice differentiable in the domain Ω ; J is the current density; ρ is the charge density; and ε_0 is the electrical permittivity in vacuum.

For pursuing the mathematical model for EIT, we take the divergence upon equation (2.1d), that is, Faraday's theorem with the displacement current $\varepsilon_0 E$ introduced by Maxwell, which relates the magnetic field with its sources: electrical current and fluctuating electrical fields. Since the divergence of the rotational is zero, that is, $\nabla \cdot (\nabla \times B) = 0$, then (2.1d) leads by using (2.1a) to the well known conservation charge law

$$\nabla \cdot J = -\frac{\partial \rho}{\partial t}. \quad (2.2)$$

The previous equation states that the flux across a closed surface is justified by a loss of charge in the volume enclosed by the surface. Since there are not any electrical sources in the interior and giving the total interior charge Q and the charge density ρ related by $\rho = \int_{\Omega} Q$, then (2.2) becomes

$$\nabla \cdot J = 0. \quad (2.3)$$

The presence of an electrical field E in a medium provides excitation and reorganisation of charges that is quantified by the conductivity σ and permittivity ε , which can be coupled by a general admittivity γ as $\gamma = \sigma + i\omega\varepsilon$. Thus, the admittivity is function of the frequency as well as the position, that is, $\gamma = \gamma(x, w)$. This induces a current density J that, under the assumption that the medium has a linear response, is given by $J = \gamma E$. If the medium is anisotropic, then, in general, γ is a 2-rank tensor form, which is represented in some coordinates by a 3-by-3 positive definite matrix (Section A.1.10)

$$\gamma = \begin{pmatrix} \gamma_{11} & \gamma_{12} & \gamma_{13} \\ \gamma_{12} & \gamma_{22} & \gamma_{23} \\ \gamma_{13} & \gamma_{23} & \gamma_{33} \end{pmatrix}, \quad (2.4)$$

such that the electrical field and current density may not be parallel in general since in presence of an electrical field, γ induces a current density vector with i th-coordinate J_i given by

$$J_i = \sum_{j=1}^3 \gamma_{ij} E_j. \quad (2.5)$$

Hence, γ maps electrical fields E onto current density vectors J , and since it is symmetric, the transformation can be explained by the eigenvalue decomposition as a map of the unit sphere onto an ellipsoid, whose semiaxes direction and length are given by σ eigenvectors and eigenvalues, respectively (A.2.1). In an isotropic medium, γ can be treated as a scalar value α ,

that is, a scalar multiplying the unit matrix.

$$\gamma = \alpha \begin{pmatrix} 1 & 0 & 0 \\ 0 & 1 & 0 \\ 0 & 0 & 1 \end{pmatrix}, \quad (2.6)$$

where in this case E and J are always parallel.

EIT applications usually operate at low frequency assuming the quasi-static approximation, in which the imaginary part of the admittivity is neglected, that is, the response of the material is instant and frequency independent, which yields $J = \sigma E$, where the conductivity is in general the 2-rank tensor

$$\sigma = \begin{pmatrix} \sigma_{11} & \sigma_{12} & \sigma_{13} \\ \sigma_{12} & \sigma_{22} & \sigma_{23} \\ \sigma_{13} & \sigma_{23} & \sigma_{33} \end{pmatrix}. \quad (2.7)$$

It has been shown that, for harmonic electromagnetic fields at a fixed frequency, the previous approximation is valid when $\omega\mu\sigma x^2$ is negligible, where μ is the magnetic permeability and x is the length of the object [31]. Providing some numbers, for example, σ in the range 0.1 to $0.01\Omega^{-1}m$, ω in the range 0.1 to $0.01KHz$, and $x = 0.2m$, the previous figure is around $5 \cdot 10^{-8}$, which shows the tiny contribution of the complex part of the admittivity at low frequencies.

Substituting J in (2.3) and using the relation $E = -\nabla u$, where u is the electrical potential in Ω , the mathematical model for EIT is given by the generalised Laplace's equation

$$\nabla \cdot (\sigma \nabla u) = 0, \quad (2.8)$$

where the conductivity σ is generally a 2-rank tensor.

2.1.2 Boundary conditions: the Complete Electrode Model

Several boundary conditions have been proposed to enhance the modelling of the electrodes based on the continuum Neumann condition [31] that reads as

$$\sigma \frac{\partial u}{\partial \nu} = J \quad \text{on} \quad \partial\Omega, \quad (2.9)$$

where ν is the outward normal to the surface. This was modified by the Gap Model that considered the current density to be zero where there are not electrodes and to be constant at the electrodes. Because the known quantity is the current injected at each electrode rather than the current density, the Gap Shunt proposed the total current to be constant at the l th-electrode E_l , that is

$$\int_{E_l} \sigma \frac{\partial u}{\partial \nu} ds = I_l. \quad (2.10)$$

Due to the high conductivity of the electrodes, a constraint was added to force the potential to be constant on each electrode, that is, $u = V_i$, where u is the potential solved by the forward problem.

The Complete Electrode Model [135], used in this thesis, models the effect between the electrode and the skin by adding the contact impedance. The CEM is given by the generalized Laplace's equation (2.8) together with

$$u + z_l \sigma \frac{\partial u}{\partial \nu} = V_i \quad \text{on } \partial\Omega, \quad (2.11)$$

$$\sum I_i = 0 \quad \text{conservation of charge,} \quad (2.12)$$

$$\sum V_i = 0 \quad \text{ground selection,} \quad (2.13)$$

where (2.11) accounts for the contact impedance of the skin-electrode interface z_l ; (2.12) forces the total current, in and out, for each injection to sum zero; (2.13) provides uniqueness to the FP by selecting a ground point (electrode). The CEM has been proved to have an unique solution and to fit the experimental settings with less than 0.1% error [161].

2.2 Methods for solving the forward problem

Solving the Forward Problem (FP) implies finding a solution, u , to the boundary value problem given by the generalised Laplace's equation with some boundary conditions. A straight forward solution to this problem in the continuous case, called a classical solution, is required to be sufficiently smooth: for the generalized Laplace's equation (2.8), the solution must be twice differentiable, that is, $u \in \mathbb{C}^2$. Also, the boundary must be Lipschitz continuous (A.2) for the solution to exist and to be unique.

The previous conditions are too strong, being only valid for very simple geometries, for which analytical solutions may be available; for general geometries, the classical problem can be converted onto a less restrictive weak formulation.

To solve numerically the weak formulation the domain is discretised. Among all numerical methods the most commonly used are Finite Differences (FD), for simple geometries; FEM, for general geometries and non-homogeneous medium; and Boundary Element Method (BEM), for homogeneous medium, being computationally less expensive than FEM though more difficult to implement.

In the next section I look, first, at the possibility of converting the problem to a less restrictive one, by applying the weak formulation. Then the weak formulation is discretised by partitioning the domain, which leads to a discrete linear system of equations. Some computational aspects regarding the implementation are crucial in practice and are seen here: generating

the partition and solving the linear system for a large number of unknowns.

2.2.1 FEM formulation

For solving the problem numerically, the domain must be discretised in a finite number of sub-domains, called finite elements. Then, the system of equations can be built up independently for each finite element and then all pieces gathered together in a large sparse system matrix.

Before the discretisation, the strong smoothness condition that is required by the classical problem must be loosened. Thus, a weak formulation to the generalized Laplace's equation relaxes the continuity requirements leading to a more general weak solution, which complies also with non-smooth domains.

2.2.1.1 Weak formulation

If the domain Ω is non-smooth, then a smooth solution to the problem may not exist. Thus, the problem must be converted onto a less restrictive one, so that the solution, hopefully, lies in a more general subspace. Multiplying the generalized Laplace's equation (2.8) by a set of test functions, v , and integrating over the whole domain Ω ,

$$\int_{\Omega} v \nabla \cdot (\sigma \nabla u) = 0. \quad (2.14)$$

Then, applying the Divergence theorem

$$-\int_{\Omega} v \nabla \cdot (\sigma \nabla u) = \int_{\Omega} \nabla v \cdot (\sigma \nabla u) - \int_{\partial\Omega} v (\sigma \frac{\partial u}{\partial \nu}), \quad (2.15)$$

where ν is the outer unit normal to the surface, the problem (2.14) becomes

$$\int_{\Omega} \nabla v \cdot (\sigma \nabla u) = \int_{\partial\Omega} v \sigma \frac{\partial u}{\partial \nu}, \quad (2.16)$$

which is the weak formulation that corresponds to the generalized Laplace's equation.

Now, by looking into the type of subspace of the weak solution and test function in (2.16), one infers that the test function v and its first derivatives ∂v must be integrable, which defines a Sobolev space H^1 (sections A.1.5 and A.1.6); the same refers to the solution u , that is, $u \in H^1(\Omega)$.

It is easy to prove that the weak formulation (2.16) with Dirichlet boundary condition has a unique solution and with Neumann boundary condition (2.9) has a unique solution up to a constant, which in practice is solved by defining a ground point (2.13).

For the complete electrode model, the RHS of the weak equation (2.16) representing Neumann boundary condition, is given in terms of the CEM (2.11) as

$$\sum_{l=1}^L \frac{1}{z_l} \int_{E_l} v (V_l - u), \quad (2.17)$$

where E_l symbolises the contribution of each electrode, being zero away from the electrodes. Existence and uniqueness of the complete electrode model has been proved in [161], with predicted voltage errors of 0.1%, which was less than with the previous models.

The total current (2.10) at the l th-electrode E_l is obtained by substituting the CEM boundary condition (2.11)

$$I_l = \int_{E_l} \frac{1}{z_l} (V_l - u_l). \quad (2.18)$$

2.2.1.2 Galerkin FEM

In FEM, the domain is partitioned in what is called a mesh: elements cover the whole domain and do not intersect, and neighbouring vertices coincide [29]. For the discretisation, nodes are labelled, and a set of basis functions ϕ is defined for each node such that the i -th vector ϕ_i follows

$$\phi_i = \begin{cases} 1 & \text{on the node } i, \\ 0 & \text{on the rest.} \end{cases} \quad (2.19)$$

Given N nodes, one can introduce a N -dimensional discrete subspace S that belongs to the Sobolev space H^1 , which is called conforming FE, such that the potential can be interpolated as

$$u = \sum_j u_j \phi_j, \quad (2.20)$$

where u_j is a vector of scalar coefficients.

In the Galerkin FEM formulation, N equations are obtained by replacing the test function v by all basis functions ϕ_i , where $i = 1, \dots, N$. Then, by substituting the test function and the solution in terms of the basis functions, the LHS of the weak equation (2.16) becomes

$$\sum_{i=1}^N u_j \int_{\Omega} \nabla \phi_i \cdot \nabla (\sigma \phi_j). \quad (2.21)$$

Combining the RHS and LHS, and reordering their terms, the weak equation becomes

$$\sum_{j=1}^N u_j \left(\underbrace{\int_{\Omega} \nabla \phi_i \cdot \nabla (\sigma \phi_j)}_{(A_M)_{ij}} + \underbrace{\sum_{l=1}^L \frac{1}{z_l} \int_{E_l} \phi_i \phi_j}_{(A_Z)_{ij}} \right) + \sum_{l=1}^L V_l \left(\underbrace{-\frac{1}{z_l} \int_{E_l} \phi_i}_{(A_W)_{il}} \right) = 0, \quad (2.22)$$

where the first term, A_M , $N \times N$ symmetric matrix, is the main part of the system matrix; the second term, A_Z , $N \times N$ matrix, corresponds to the Neumann boundary condition; and the third term, A_W , $N \times L$ matrix, constrains the electrode voltage to V_l .

An advantage of FE is that one can write the conductivity distribution as an interpolation of basis functions φ_k , that is

$$\sigma = \sum_{k=1}^K \sigma_k \varphi_k, \quad (2.23)$$

which allows the system matrix to be computed for each element and then assembled together at the end. Generally, the conductivity is chosen to be constant in each element, by making φ_k one in the k th-element and zero elsewhere. This permits the conductivity to be taken outside the integral of the main part of the system matrix, A_M , as

$$(A_M)_{ij} = \sum_{k=1}^K \sigma_k \int_{\Omega_k} \nabla \phi_i \cdot \nabla \phi_j, \quad (2.24)$$

where the integral can be computed off-site.

Substituting u (2.20) onto the total current through E_l (2.18) becomes

$$I_l = V_l \underbrace{\frac{|E_l|}{z_l}}_{(A_D)_{ll}} + \sum_{j=1}^N u_j \underbrace{\left(-\frac{1}{z_l} \int_{E_l} \phi_j \right)}_{(A_W)_{lj}}, \quad (2.25)$$

where the first term, A_D , $L \times L$ diagonal matrix, explains the CEM boundary condition, and $|E_l|$ is the area of E_l .

Combining the weak equation (2.22) with the current equation (2.25), the forward problem is given by the linear system [75, Chapter 1]

$$\begin{bmatrix} A_M + A_Z & A_W \\ A_W^T & A_D \end{bmatrix} \begin{bmatrix} u \\ V \end{bmatrix} = \begin{bmatrix} 0 \\ I \end{bmatrix}, \quad (2.26)$$

where u is the solution vector, $u = (u_1, \dots, u_N)^T$; V is the electrodes potential vector, $V = (V_1, \dots, V_L)^T$; and I is the electrodes electrical current vector, $I = (I_1, \dots, I_L)^T$. The linear system (2.26), which can be written as $A\tilde{u} = \tilde{I}$, is only for one current injection; several current injections are solved simultaneously by adding as many columns to \tilde{u} and \tilde{I} as the total number of current injections, that is,

$$A[\tilde{u}_1, \dots, \tilde{u}_G] = [\tilde{I}_1, \dots, \tilde{I}_G], \quad (2.27)$$

where G is the total number of current injections, and all columns \tilde{u} and \tilde{I} sum zero as given in (2.12) (2.13).

2.2.2 Implementation and computation

Several decisions must be taken when implementing the numerical forward problem: the type and size of the mesh, the method for solving the linear system, and the software used for generating the mesh and building up the system matrix.

2.2.2.1 Partition and mesh generator

Three possible choices that influence the accuracy of the approximated FE solution are the kind of partition, the degree of the polynomial, and the density of the mesh.

Regarding the type of partition, in 3D, tetrahedral finite elements are usually adopted since it can fill the domain better for irregular boundaries; cubic is more regular; other polyhedrons are also possible. Also, a combination of them is feasible, for example, cubes in the interior of the domain and tetrahedra at the boundary.

The degree of the polynomials for the potential determines the order of the approximation. In this work, linear tetrahedra, \mathbb{P}_1 approximation, were adopted for simplifying the computation. Cubes are described by bilinear basis functions, \mathbb{Q}_1 approximation, which approximate better the potential than linear functions since they can model non-zero curvature by a cross product term. Higher order polynomials, for example, the quadratic \mathbb{P}_2 approximation, provide better accuracy though they are more difficult to integrate and computationally more expensive.

Another way to improve the accuracy of the forward solution is to increase the mesh density.

Considering the mesh generator, some free-software is available like Netgen [154], for simple geometries, while more complicated geometries and non-homogenous domains require a more advanced software. The meshes generated for this work were done by using the Integrated Design Engineering Analysis Software (IDEAS) [170]. A realistic neonatal head shaped FEM mesh was produced by segmenting the outer surface of a neonatal MRI scan and by meshing using IDEAS. First, a Delaunay triangulation algorithm was applied on the surface and then grown inwards with linear tetrahedral elements. Keeping elements to a similar size achieved a high quality mesh [170].

2.2.2.2 Constructing the system matrix

The system matrix A in (2.26) was here computed by using the Three-Dimensional Electrical Impedance and Diffuse Optical Reconstruction Software (EIDORS-3D), a toolkit that builds up the system matrix for the CEM on linear tetrahedra with isotropic piecewise constant conductivity [140, 139]. A modified version of 3D-EIDORS for modelling anisotropic media has been implemented by modification of the system matrix [1].

2.2.2.3 Solving the linear system

There are several methods to solve the linear symmetric positive definite system (2.26). Medical applications give rise to thousands of unknowns, making linear solvers like Gaussian elimination impractical; therefore, iterative solvers are preferred [29]. Two flourishing methods have been popular in the last decade: Preconditioned Conjugate Gradient (PCG) and multigrid, which converge in less than n steps, where n is the number of unknowns. They also permit parallel computation where parallel multigrid has been applied for EEG of the human head [182]. In this thesis both PCG and multigrid are applied.

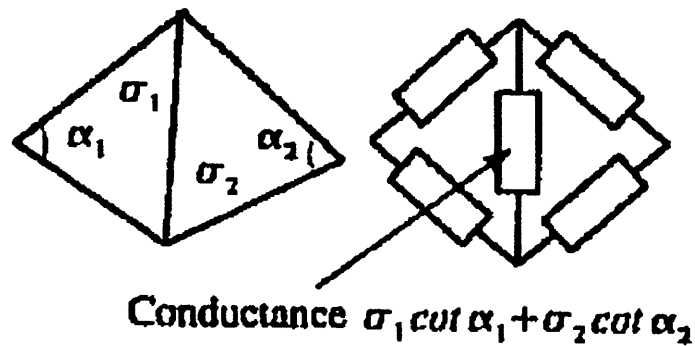


Figure 2.1: A resistor network in 2D where resistors are placed at the finite element edges is equivalent to the discrete finite element mesh for piecewise linear voltage and constant conductivity, such that the contribution from the element conductivity to the resistor conductance is given by $\sigma \cot \alpha$ where σ is the element conductivity and α is the opposite angle. Both formulations lead to the same system matrix. (Image taken from [75], thanks to Bill Lionheart at the University of Manchester and David Holder at UCL).

The accuracy of the linear solution depends on the condition number of the system matrix, which, for the CEM, can be ill-conditioned for tiny electrical impedance; if this is the case the shunt model should be used instead. An advantage of iterative methods is that the solution can be obtained more efficiently, in less number of steps, by reducing its accuracy to that of the measurements.

2.2.3 Resistor network

The aim of the Resistor Network (RN) problem, [37, 35, 100], is to detect a failure in a resistor by injecting current and measuring voltages at the external nodes of the network. Its FP is also modelled by the generalized Laplace's equation such that the finite element 2D EIT problem with piecewise constant conductivity has a RN equivalent, but the opposite is not always true [106]. Thus, placing resistors at the edges of the finite element mesh and defining the resistor conductance in terms of the element conductivity, such that the contribution of an element conductivity σ to the resistor conductance is given by $\sigma \cot(\alpha)$ where α is the angle opposite to the edge (Figure 2.1), leads to the same system matrix. It can be generalised for the 3D case.

2.3 Summary

Solving the forward problem implies modelling the physical system and obtaining the predicted boundary voltages for a conductivity estimate. From Maxwell's equations, at low frequency, the quasi-static approximation yields the generalized Laplace's equation, which models the electrical voltage in the given domain. Boundary conditions, for the injected current and the measured voltage, must account for the voltage drop because of the contact impedance of the skin-electrode interface, which is modelled by the CEM with an error of less than 0.1%. Although some simple geometries have analytical solutions, for general irregular geometries one must solve the forward problem numerically by using a discrete formulation. The FEM formulation is well established within the EIT community and is easy to implement. It can be used for general geometries, and can model anisotropic conductivities. The RN problem is equivalent to the EIT problem for a finite element formulation with piecewise linear voltage and constant conductivity.

In this thesis, MATLAB toolkit 3D-EIDORS was used to built up the system matrix for the CEM for linear basis functions and piece-wise constant conductivity, for isotropic media (Chapters 5 and 6); a modified version of 3D-EIDORS was used for anisotropic media (Chapters 7, 8, and 9). A realistic homogeneous neonatal head-shaped FEM mesh used was created by using IDEAS. The linear system was solved by using both PCG and multigrid.

Chapter 3

Inverse problem theory

This chapter is an introduction to definitions, theoretical results, and methods that are needed for analysing and solving inverse problems. Section 3.1 is dedicated to the conductivity inverse problem, defining the inverse conductivity problem, the Dirichlet-to-Neumann (DtN) map, most relevant uniqueness and stability results, specifically an explanation of non-uniqueness for anisotropic conductivity and theoretical results of the recovery of uniqueness by redefining the problem, and the Jacobian as the operator that contains the information of how sensitive the voltages are with respect to the conductivity. Section 3.2 is dedicated to a review of the theory for solving inverse problems: ill-posedness as given by Hadamard's definition; regularisation as a strategy for recovering numerical uniqueness by providing extra information; prior information is justified by revealing the statistical approach equivalent to deterministic regularisation; and optimisation as a numerical methodology for solving inverse problems that provides recipes for both unconstrained and constrained optimisation.

3.1 The inverse conductivity problem

The aim of the inverse conductivity problem is to estimate the conductivity inside an object from the current-to-voltage map (section 3.1.1). In practice, as it has been previously introduced (section 1.1.1), the inverse conductivity problem can be described as a mapping F^{-1} (1.2) from boundary voltages d into volume conductivity x^1 , and is obtained as an approximated inverse to the forward mapping F (1.2) that provides boundary voltages after solving the voltages in all the domain for a given conductivity (2.26). Theoretical and numerical results for EIT can be found in [24].

¹While in chapter 2 the boundary voltage was indicated with the symbol V and the conductivity with σ , in this chapter and in parts of the thesis dealing with inverse problem definitions, the boundary voltage (data) was indicated with the symbol d and the conductivity (solution) with x .

3.1.1 The Dirichlet-to-Neumann map

In practice, one injects electrical current (Neumann data) and measures voltage (Dirichlet data) at the boundary; therefore, all the information one possesses about the conductivity is given by the current-to-voltage map, or its opposite, the voltage-to-current map known as the Dirichlet-to-Neumann (DtN) map.

In 1980, Calderón [81] proposed the inverse problem of determining under what conditions the conductivity σ could be uniquely reconstructed from the DtN map Λ_σ defined as

$$\Lambda_\sigma : u \mapsto \sigma \nabla u \cdot \nu, \quad u \in \partial\Omega, \quad (3.1)$$

such that all the information for recovering σ , by applying a voltage and measuring current, is contained in the mapping Λ_σ , which depends in the conductivity.

Let $\Lambda_\sigma u|_{\delta\Omega}$ be the flux, an inner product involving the DtN map explains the generalised Laplace's weak formulation (2.16) by the bilinear function S_σ [118]

$$S_\sigma(u, v) = \langle v|_{\delta\Omega}, \Lambda_\sigma u|_{\delta\Omega} \rangle = \int_{\delta\Omega} v|_{\delta\Omega} \sigma \nabla u \cdot \nu = \int_{\Omega} \sigma \nabla u \cdot \nabla v. \quad (3.2)$$

Now, by assuming $v = u$, the inner product (3.2) is zero if and only if $\nabla u = 0$; hence, the kernel of the DtN map, $\mathcal{K}(\Lambda_\sigma)$ (section A.1.9), is constant voltages [24]. In real applications, one uses the Neumann-to-Dirichlet (NtD) map, $(\Lambda_\sigma)^{-1} : H^{-1/2} \mapsto H^{1/2}$ (section A.1.5), because it is easier and more accurate to measure a voltage ($H^{1/2}$) than a current ($H^{-1/2}$). It satisfies the variational form

$$\langle I, (\Lambda_\sigma)^{-1} I \rangle = \int_{\Omega} \frac{1}{\sigma} |J|^2, \quad (3.3)$$

where the kernel of $(\Lambda_\sigma)^{-1}$ is given by constant currents, that is, measured voltages are nonzero when the applied current I is not a constant function.

3.1.2 Uniqueness

A review of uniqueness and stability results for the recovery of coefficients of partial differential equations can be found in [83]; uniqueness results for EIT can be found in [24]. A brief summary is given as follows.

3.1.2.1 Two dimensional domains

For the 2D case, which is a special case, global uniqueness has been proved for conductivities in W_p^2 (A.1.5), for $p > 1$, in a Lipschitz bounded domain [118].

3.1.2.2 Isotropic mediums

In the isotropic case, for dimensions larger or equal to three, uniqueness has been proved for piecewise analytical conductivities from $\partial\Omega \in C^\infty$ [92, 93]. Global uniqueness has been

proved for continuously differentiable conductivities in $\bar{\Omega}$, that is, $\sigma \in C^\infty(\bar{\Omega})$, where $\bar{\Omega}$ is the domain including the boundary [165].

3.1.3 Anisotropic mediums

In an anisotropic medium, Λ_σ determines σ uniquely up to a diffeomorphism $\Psi : \tilde{\Omega} \mapsto \Omega$ (D.1) that fixes the boundary, $\Psi = \mathbb{I}$ on $\partial\Omega$, that is,

$$\begin{aligned} x &= \Psi(\tilde{x}) \quad \text{in } \Omega \\ x &= \tilde{x} \quad \text{on } \partial\Omega. \end{aligned}$$

Thus, the anisotropic inverse conductivity problem is not unique, which can be explained by the non-injectivity of the DtoN map [101]. However, it is possible to recover uniqueness by constraining the solution [104].

3.1.3.1 Non-injectivity

Non-uniqueness can be explained by showing the non-injectivity of Λ_σ , that is, there are two different conductivity tensors related by Ψ that satisfy the same boundary data Λ_σ [174]. Given the potentials $u(x)$ and $v(x)$ and the conductivity $\sigma^{ij}(x)$ ² in the domain Ω , the bilinear function S_σ (3.2) in terms of the partial derivatives

$$S_\sigma(u, v) = \int_{\Omega} \left(\frac{\partial v}{\partial x^i} \right) \sigma^{ij}(x) \left(\frac{\partial u}{\partial x^j} \right) dx^1 dx^2 dx^3, \quad (3.4)$$

and rewriting the partial derivatives after applying the diffeomorphism Ψ in terms of the old ones as (D.22)

$$\frac{\partial}{\partial x^i} = \frac{\partial \tilde{x}^j}{\partial x^i} \frac{\partial}{\partial \tilde{x}^j} = B_i^j \frac{\partial}{\partial \tilde{x}^j}, \quad (3.5)$$

where $B = (\Psi')^{-1}$ is the Jacobian inverse of Ψ , S_σ becomes

$$\int_{\tilde{\Omega}} \left(B_i^l \frac{\partial \tilde{v}}{\partial \tilde{x}^l} \right) \sigma^{ij}(x) \left(B_j^k \frac{\partial \tilde{u}}{\partial \tilde{x}^k} \right) |B^{-1}| d\tilde{x}^1 d\tilde{x}^2 d\tilde{x}^3 = \quad (3.6)$$

$$\int_{\tilde{\Omega}} \frac{\partial \tilde{v}}{\partial \tilde{x}^l} \tilde{\sigma}^{lk}(\tilde{x}) \frac{\partial \tilde{u}}{\partial \tilde{x}^k} d\tilde{x}^1 d\tilde{x}^2 d\tilde{x}^3 = S_{\tilde{\sigma}}(\tilde{u}, \tilde{v}), \quad (3.7)$$

where $|B^{-1}|$ measures the change in volume (D.16), $\tilde{u} = \tilde{u}(\tilde{x})$ and $\tilde{v} = \tilde{v}(\tilde{x})$ are the potentials evaluated in $\tilde{\Omega}$, and $\tilde{\sigma}(x)$ is given by

$$\tilde{\sigma}(\tilde{x}) = \left(\frac{B\sigma B^T}{|B|} \right) (\Psi(\tilde{x})), \quad (3.8)$$

which can be explained by the transformation rule for two rank tensors and a change of the element volume B^{-1} (D.28). Hence,

$$S_\sigma(u(x), v(x)) = S_{\tilde{\sigma}}(u(\tilde{x}), v(\tilde{x})). \quad (3.9)$$

²Only in this section and in the appendix D.1 a distinction between upper and lower indices is made to define transformations of coordinates for two-rank tensors.

Now, substituting the DtoN map Λ_σ in the bilinear function S_σ (3.2),

$$S_\sigma(u(x), v(x)) = \int_{\partial\Omega} v\nu \cdot \sigma \nabla u = \int_{\partial\Omega} v \Lambda_\sigma u, \quad (3.10)$$

then

$$\int_{\partial\Omega} v \Lambda_\sigma u = \int_{\partial\tilde{\Omega}} \tilde{v} \Lambda_{\tilde{\sigma}} \tilde{u}, \quad (3.11)$$

and since $\Psi = \mathbb{I}$ on $\partial\Omega$, and $\tilde{u}(\tilde{x}) = u(x)$ and $\tilde{v}(\tilde{x}) = v(x)$, then

$$\Lambda_{\tilde{\sigma}} = \Lambda_\sigma. \quad (3.12)$$

As a consequence, the two conductivities σ and $\tilde{\sigma}$ yield the same DtoN map, that is, the same boundary conditions. In fact, there are an infinite number of $\tilde{\sigma}$ for an infinite number of diffeomorphism Ψ that satisfy the same boundary conditions.

The non-injectivity can be verified numerically by comparing the boundary data $\Lambda_\sigma u$ in Ω with the boundary data $\Lambda_{\tilde{\sigma}} \tilde{u}$ in $\tilde{\Omega}$, where $\tilde{\sigma}$ (3.8) is given in terms of the Jacobian of the diffeomorphism Ψ' , which can be computed elementwise [1].

3.1.3.2 Recovery of uniqueness

A physical interpretation of the non-uniqueness (Appendix D.2) explains the uniqueness up to a diffeomorphism as a theoretical choice such that the measured boundary voltages do not depend on the selected reference system. An analogy of the conductivity with the metric in Riemmanian manifolds explains the conductivity inverse problem as the problem of recovering the metric in a manifold, which can be done in two steps, the first one provides the manifold structure, and the second, which is non unique selects the coordinate system (Appendix D.2). However, it is indicated that providing extra information that selects the diffeomorphism yields a unique solution. Uniqueness holds under few constraints: recovery of one eigenvalue [92, 93], where eigenvectors and two of the three eigenvalues are known; a multiple scalar to the tensor [104], extended to a function [2, 48], where eigenvalue ratios and eigenvectors are known. Accordingly, providing uniqueness for an inverse problem can be understood as assuming stability under certain constraints [83].

3.1.4 Incomplete data

Uniqueness results suppose that there is complete boundary data [81]. However, in practice there is incomplete data, for which uniqueness is still open [83]. A possibility is to constrain the problem so that the solution can be uniquely determined by incomplete data; for example, to assume there are two mediums of known conductivity [81].

3.1.5 Sensitivity matrix

The Sensitivity matrix, known as the Jacobian, is the sensitivity of the boundary voltages with respect to the conductivity, that is, first derivatives or Jacobian of the forward operator (1.1). At a first order approximation, it can be computed for each conductivity element as the integral over the volume element of the product of the driven and the measurements fields

$$\frac{\delta V_{dm}}{\delta \sigma_k} = - \int_{\Omega_k} \nabla u(I^d) \cdot \nabla u(I^m), \quad (3.13)$$

where $u(I^d)$ is the voltage corresponding to the driven current, and $u(I^m)$ is the voltage for the fictional measurement current [140]. Redefining V as a vector for all current injections and all measurements, such that V_i is the voltage for the i th-measurement accounting for both indices d and m , the Jacobian (3.13) can be represented as the sensitivity of the i th-measurement to the k th-element conductivity as

$$J_{ik} = \frac{\partial V_i}{\partial \sigma_k}, \quad (3.14)$$

which can be also computed by finite differences by calculating the voltage difference for a perturbation in the conductivity (A.25).

Since the Jacobian corresponds to the first derivatives of the forward mapping, it contains information about the ill-posedness of the problem. It is also used mainly in optimisation algorithms for solving the inverse problem, since it appears in computation of the gradient of the functional to be optimised. In conclusion, it is one of the most important tools because it represents how sensitive the current-to-voltage map is to a change of conductivity, which is the aim.

3.2 Solving the inverse problem

Given the forward operator F (1.1), solving the inverse conductivity problem implies finding a solution to the nonlinear system of equations

$$F(x) - d = 0, \quad (3.15)$$

where $d \in \mathbb{R}^{m \times 1}$ is a vector of measured boundary voltages, for m boundary voltages, $F(x) \in \mathbb{R}^{m \times 1}$ is a vector of predicted boundary voltages by the model, and $x \in \mathbb{R}^{n \times 1}$ is a vector of element conductivities, for n finite elements. In practise, m is few hundreds and n is few thousands.

A characteristic of the inverse problem is the lack of a well defined inverse F^{-1} and high sensitivity to measurement errors and modelling errors; therefore, an approximation to the inverse is needed.

3.2.1 Ill-posedness

Given two Hilbert vector spaces (section A.1.6), H_1 and H_2 , where $x \in H_1$ and $d \in H_2$, and an operator $F : H_1 \mapsto H_2$, such that $F(x) = d$, Hadamard defined F to be well posed if [176]:

- i) For all d , there is x , such that $F(x) = d$. That is, H_2 is in the range of F .
- ii) The solution x is unique for each d .
- iii) The solution is stable with respect to perturbations on the data.

Thus, well-posedness implies that there is a well-defined inverse $F^{-1} : H_2 \mapsto H_1$; otherwise, if any of the three conditions does not hold, F is ill-posed.

3.2.2 Regularisation

Inverse problems are usually ill-posed; therefore, there is a necessity to transform the problem to a well-posed one, which can be done by regularisation. Since there is not an exact solution to the nonlinear system (3.15), one seeks an approximated solution by minimising some functional

$$\|F(x) - d\|_A^2, \quad (3.16)$$

in a given A -norm (A.9), up to the noise level $\|\eta\|_A^2$, where η represents the noise. A possible way to control the level of minimisation in (3.16) is by adding a regularisation term $\Psi(x)$ to the previous functional, so that the new problem has unique solution; it becomes

$$\min_x \frac{1}{2} \{ \|F(x) - d\|_A^2 + \alpha \Psi(x) \}, \quad (3.17)$$

where α is the regularisation term that controls the amount of regularisation, such that when α increases, the optimisation routine would concentrate in minimising $\Psi(x)$. The idea is that the new problem becomes well-posed, having unique solution, when

$$\mathcal{K}(\Psi(x)) \cap \mathcal{K}(\|F(x) - d\|_A^2) = \emptyset, \quad (3.18)$$

where \mathcal{K} represents the kernel (section A.1.9) and \emptyset the empty set.

The type of regularisation is selected in relation with some knowledge of the solution. The standard is Tikhonov regularisation, which corresponds to a \mathcal{L}_2 -norm, that is,

$$\Psi(x) = \Psi(\|x\|^2), \quad (3.19)$$

penalising solutions with large norm and yielding smooth solutions. Other common penalisation term is TV, which corresponds to a \mathcal{L}_1 -norm, that is,

$$\Psi(x) = \Psi(|\nabla x|), \quad (3.20)$$

penalising high frequency components but allowing sharp profiles of the image [38, 26, 176]. The difficulty with TV in the deterministic approach is the non-differentiability of (3.20); nevertheless, non-differentiable complex prior densities can be applied in the statistical framework [85].

3.2.3 Statistical framework

The statistical approach where inverse problems are considered as statistical inference explains the Least Squares (LS) solution as a Maximum Likelihood Estimate (MLE), regularisation as prior information, and Tikhonov regularisation as the Maximum A Posteriori (MAP) estimate.

A statistical approach to EIT considers the boundary data d to be a function of the unknown quantities conductivity x and noise η as

$$d = F(x, \eta), \quad (3.21)$$

and defines a joint probability $P(d, x, \eta)$ (B.2) [85].

Assuming additive noise and x and η being independent, the model becomes

$$d = F(x) + \eta. \quad (3.22)$$

A Bayesian approach computes the posterior probability $P(x|d)$ (B.10) as

$$P(x|d) = \frac{P(d|x)}{P(d)} P(x), \quad (3.23)$$

explaining the forward problem as the likelihood density $P(d|x)$ and regularisation as the prior density $P(x)$.

An estimate of the conductivity can be then obtained by the MAP, that is, by maximising (3.23), which implies an optimisation problem. Other possibility is to compute the conditional expectation of (3.23), that is, $E[x|d]$, which is an integration problem that can be solved by Monte Carlo methods [85].

A linear approximation to the nonlinear problem (3.22) can be considered by assuming J to be the Jacobian of F and x and d to be small changes in the solution and boundary voltages respectively as described in (4.5).

Statistical inference can be easily determined by assuming the data to be a random variable that follows a Gaussian distribution, $d \sim \mathcal{N}(Jx, C_\eta)$, read as d follows a Gaussian distribution of mean Jx and covariance C_η (Appendix B.1.3). In this case, the likelihood is proportional to

$$\exp\left(-\frac{1}{2}(d - Jx)^T C_\eta^{-1}(d - Jx)\right). \quad (3.24)$$

Taking then the conductivity as parameters, the MLE maximises (3.24)[176, Chapter 4], which is equivalent to the minimisation of

$$\min_x \{\Phi_{MLE}\} = \min_x \left\{ \frac{1}{2} (d - Jx)^T C_\eta^{-1} (d - Jx) \right\}, \quad (3.25)$$

whose solution is given by

$$x_{MLE} = J^\dagger d, \quad (3.26)$$

where J^\dagger is the pseudo-inverse (section A.2.4). In fact, the problem (3.25) is equivalent to the Generalised LS (GLS) problem (4.8).

Since (4.8) is unstable for ill-posed problems, the solution must be also considered a random variable as $x \sim \mathcal{N}(0, C_x)$. Therefore, a linear model in which the variables x and d are jointly distributed, the posterior probability $P(x|d)$ (3.23) is proportional to

$$\exp\left(-\frac{1}{2}\|Jx - d\|_{C_\eta^{-1}}^2\right) \exp\left(-\frac{1}{2}\|x\|_{C_x^{-1}}^2\right). \quad (3.27)$$

The MAP estimate [176, Chapter 4] that maximises (3.27) is given by

$$x_{MAP} = (J^T C_\eta^{-1} J + C_x^{-1})^{-1} J^T C_\eta^{-1} d = C_x J^T (J C_x J^T + C_\eta)^{-1} d, \quad (3.28)$$

which agrees with Tikhonov regularisation, where the first version of (3.28) is ideal for underdetermined systems since it inverts a $n \times n$ matrix, and the second one is better for overdetermined systems since it inverts a $m \times m$ matrix with $n \gg m$.

3.2.4 Optimisation

Optimisation allows one to find the value of some unknown property of the system under study that minimises (maximises) some objective functional. It is referred to as constrained optimisation when variables are restricted to certain values, and otherwise as unconstrained optimisation. There are a large number of methods available ranked in terms of robustness, efficiency, and accuracy.

Let $f : \mathbb{R}^n \mapsto \mathbb{R}$ be the objective that is a function of the unknown variable x constrained to a domain Ω , the optimisation problem is

$$\min_{x \in \Omega} f(x). \quad (3.29)$$

If f and Ω are convex (A.1), then (3.29) converges to a global minimiser [122] defined as

$$f(x^*) \leq f(x) \quad \text{for all } x. \quad (3.30)$$

Since convexity is hardly satisfied, methods converge to a local minimiser defined as

$$f(x^*) \leq f(x) \quad \text{for } x \text{ in neighbourhood of } x^*. \quad (3.31)$$

Here, the focus is on unconstrained optimisation where optimality conditions impose requirements to the local minimiser and objective function.

3.2.4.1 Unconstrained optimality conditions

Optimality conditions are divided into necessary conditions, imposed to the local minimiser, and sufficient conditions, imposed to the objective function; they can be found in [122].

First-order necessary conditions provide information about the first derivatives at the minimiser. If x^* is a local minimiser (3.29) and f is continuously differentiable in a neighbourhood of x^* , then

$$\nabla f(x^*) = 0. \quad (3.32)$$

Second-order necessary conditions provide information about the second derivatives. If x^* is a local minimiser and $\nabla^2 f$ is locally continuous, then

$$\nabla f(x^*) = 0 \quad \text{and} \quad \nabla^2 f(x^*) \quad \text{is positive semidefinite.} \quad (3.33)$$

Second-order sufficient conditions guarantee a local minimiser. If $\nabla f(x^*) = 0$ and $\nabla^2 f(x^*)$ is positive definite, then x^* is a local minimiser of f .

In fact, a continuous and twice differentiable function is convex in a convex domain if and only if its Hessian is positive semidefinite on the interior of the domain (http://en.wikipedia.org/wiki/Convex_function).

3.2.4.2 Unconstrained optimisation strategies

Unconstrained optimisation methods iteratively minimise the objective function f , following one of the two strategies line search or trust region. Here, I focus only on the line search where Newton's step is the most important [122].

At each step k , line search selects a direction p_k along which the solution x_k moves, minimising the objective $f(x_{k+1})$ for the updated solution

$$x_{k+1} = x_k + \alpha_k p_k, \quad (3.34)$$

where α is the step length. Once p_k is determined, α is obtained by solving the problem

$$\min_{\alpha > 0} f(x_k + \alpha p_k). \quad (3.35)$$

Newton's step is obtained by approximating $f(x_k + p_k)$ using second-order Taylor series, that is,

$$f(x_k + p_k) \simeq f(x_k) + p_k^T \nabla f(x_k) + \frac{1}{2} p_k^T \nabla^2 f(x_k) p_k. \quad (3.36)$$

Imposing condition (3.32) onto (3.36) yields Newton's step

$$p_k = -\nabla^2 f(x_k)^{-1} \nabla f(x_k), \quad (3.37)$$

which is accurate when the difference between the model and the quadratic approximation (3.36) is small.

Finding an optimum α is needed since an extremely large step may go far from the minimum. This can be done by using Armijo's condition

$$f(x_k + \alpha p_k) \leq f(x_k) + c\alpha \nabla f_k^T p_k, \quad (3.38)$$

for which sufficient decrease is considered by decreasing the objective function more than a linear function. The constant $c \in (0, 1)$ was chosen as $c = 10^{-4}$.

In practice, the Hessian or second derivative is not available or it is computationally very expensive; therefore, Quasi Newton's methods approximate the Hessian using only first derivatives. The Quasi-Newton method BFGS, applied in this thesis, has superlinear convergence, robustness, and a cost of $O(n^2)$. It was implemented as given in [122]

$$\begin{aligned} H_0 &= \mathbb{I}, \quad \alpha = 1 \\ \text{while } \|\nabla f_k\| &> \epsilon \\ p_k &= -H_k^{-1} \nabla f_k \\ x_{k+1} &= x_k + \alpha_k p_k \quad \text{using Armijo's condition} \\ s_k &= x_{k+1} - x_k, \quad y_k = \nabla f_{k+1} - \nabla f_k, \quad \rho_k = \frac{1}{y_k^T s_k} \\ H_{k+1} &= (\mathbb{I} - \rho_k s_k y_k^T) H_k (\mathbb{I} - \rho_k s_k y_k^T) + \rho_k s_k s_k^T \\ \text{end} \end{aligned} \quad (3.39)$$

where the Hessian was initialised as $H_0 = y_k^T s_k / (y_k^T y_k) \mathbb{I}$ after computing the descent direction.

3.2.4.3 Reconstruction methods

Optimisation deals with the conditions and methods for minimising an objective function, however, it is common to divide the type of methods in linear and nonlinear and direct and iterative [24, 106].

Linear inversion methods are divided into direct methods like TSVD and Tikhonov [176] and iterative ones like Conjugate Gradients [71].

Nonlinear direct methods, such as the layer stripping algorithm, recovered the conductivity in two steps: first, it estimated the conductivity in the boundary by assuming most of the current did not penetrate deeply in the domain; second, it approximated nonlinearly the conductivity in a thin layer near the domain. Then, it proceeded layer by layer. Although it was attractive compared to computationally expensive iterative methods, it may become very unstable when the inhomogeneity is near the boundary [162].

An overview of nonlinear iterative methods for inverse problems can be found in [8]. Because Newton-type methods compute second derivatives or Hessian (3.37), which is com-

putationally expensive for large scale problems, Krylov-space methods avoid the necessity of forming and inverting the Hessian [141, 155]: CG has been analysed in [9]; recently a Newton-Krylov method has been applied to OT [155].

A shape reconstruction approach assumes regions of constant material properties and seeks to recover regional boundaries from boundary data. Assuming the material coefficients are known, recovering shape, size, and location of boundaries for several regions been done for general elliptic partial differential equations [95]. The proposed method presented convergence and stability problems when initial estimates were far from the target boundary, and a previous recovery of the location and size of the different region was suggested. Recovery of region boundaries using level set functions has been done in a two step-reconstruction: first, by approximating shape and location of boundaries, and second, by recovering the shape represented by level set functions [40].

3.3 Summary

The aim of the inverse conductivity problem is to determine conductivity inside an object from the DtN map. A uniqueness result has been proved for isotropic conductivity while anisotropic conductivity cannot be uniquely recovered unless prior information is provided. Furthermore, uniqueness from uncompleted data is still open. Information about the sensitivity of boundary voltages with respect to the conductivity is given by the Jacobian, which can be computed as the product of the driven and measurements fields for each element.

Solving inverse problems, which are usually ill-posed as given by Hadamard's conditions, implies applying some type of regularisation. Regularisation can be explained from the statistical framework where a common choice is to assume that the solution follows a Gaussian distribution, which corresponds to Tikhonov regularisation. An inverse problem can be solved by minimising the difference between the experimental and the predicted data where optimisation provides different recipes for both unconstrained and constrained solution. Reconstruction methods can be divided into linear and nonlinear and direct and iterative. Linear direct methods like TSVD and Tikhonov and nonlinear iterative methods like Newton's type are related to this thesis.

Chapter 4

The linear inverse problem

The linear inverse conductivity problem is ill-posed; therefore, regularisation is needed to convert the problem to a better-posed one. There is a large variety of regularisation methods that differ from each other in the assumptions about the type of distributions of the solution and the data, and the numerical scheme used to find an approximate solution.

The usual statistical assumption is to consider the data and the solution to follow a Gaussian distribution, whose inverse solution is given by the MAP estimator for which prior knowledge can be easily included. Other types of regularisation adopt a different distribution. Regularisation methods can be computed using different schemes where some of them cannot be implemented because they are computationally very expensive.

Truncated SVD has been previously used for linear EIT of brain function [11]. However, Tikhonov regularisation is more widely used in the inverse problem community since it is equivalent to the MAP estimator and allows the inclusion of data and solution priors explicitly.

The goal of this chapter is to summarise the most important methods for solving the linear inverse problem and to decide which best satisfies the requirements of linear EIT of brain function.

To achieve this goal, the first assumption is a linear model in which Gaussian additive noise is assumed. An approximate solution to this model is given by the generalised least square solution in the case of over-determined and well-posed problems; however, linear EIT is ill-posed as given by Hadamard's conditions. As a result, linear regularisation, which can be explained as a linear filter, is required. Assuming EIT has white noise, TSVD and Phillips-Tikhonov are discussed as linear filters. With the intention of modelling the covariance matrix of the noise, generalised Tikhonov is adopted as the general formulation for the EIT problem. Finally, one of the possible schemes to compute Generalised-Tikhonov regularisation that is not computationally very expensive for solving large scale problems and modelling the covariance matrix is selected. This scheme will be used for the following chapters.

4.1 Review of Methods

4.1.1 Linear model

For small changes of conductivity, the relation between changes in conductivity and changes in boundary voltages can be approximated by a linear mapping given by the Jacobian (3.14) of the nonlinear forward mapping. The inverse of this mapping would then map a change in boundary voltages onto a conductivity change, for which a measured reference voltage and estimated conductivity reference are required.

Let $F(x)$ be the model predicted voltages, or forward solution, for a given conductivity distribution x ; and $F(x_{\text{ref}})$ be the predicted reference voltage, for a reference conductivity x_{ref} . For a small conductivity change $\Delta x = x - x_0$ around x_0 , the predicted voltage $F(x)$ can be approximated around the predicted reference voltage $F(x_0)$ using Taylor's expansion as

$$F(x) \simeq F(x_0) + J(x_0)\Delta x, \quad (4.1)$$

where changes of order $(\Delta x)^2$ are neglected, and $J(x_0)$ is the Jacobian of the forward mapping F at x_0 .

Now, by defining difference data as

$$d = F(x) - F(x_0), \quad (4.2)$$

the linear problem becomes

$$d = J\Delta x. \quad (4.3)$$

For simplicity on the notation, from here onwards, unless mentioned explicitly, x represents a conductivity change, that is,

$$x \leftarrow \Delta x. \quad (4.4)$$

For the additive noise in the nonlinear problem (3.22), the linear additive noise problem can be similarly derived. Thus, let $d \in \mathbb{R}^m$ be a vector of the voltage changes and $J \in \mathbb{R}^{m \times n}$ be the Jacobian of the mapping of conductivity changes $x \in \mathbb{R}^n$ into d . A linear relation of impedance and conductivity, assuming Gaussian additive noise η with mean zero and covariance C_η , that is, $\eta \sim \mathcal{N}(0, C_\eta)$ (B.1.3), is given by the linear system

$$d = Jx + \eta, \quad (4.5)$$

where C_η allows variables η_i to have different variance and to be correlated. The noise vector η can be understood as the transformation of a vector $e \sim \mathcal{N}(0, I)$ by the Cholesky factor $B \in \mathbb{R}^{m \times r}$ of rank r , that is,

$$\eta = Be, \quad (4.6)$$

where the Cholesky factor is related to the covariance as

$$C_\eta = BB^T. \quad (4.7)$$

A simplified experimental paradigm for difference imaging comprises periods with and without stimulation. Let $V(t)$ be the absolute voltage acquired in time t , and V_{ref} be the reference voltage, averaged across the period without stimulation, the difference data is defined as $d(t) = V(t) - V_{\text{ref}}$. Thus, the data d comprises two different periods, the stimulation period, which represents a voltage change, and the period without stimulation, also called baseline, which is the fluctuations around the reference, that is, the noise η .

4.1.2 Generalised least squares solution for well-posed problems

A solution to (4.5) cannot be found exactly since, in general, the data does not belong to the range of the Jacobian, which will be explained in more detail in section 4.1.3. Thus, one must look for an approximate solution that can be achieved by considering the problem

$$\min_x \{\Phi_{\text{GLS}}\} = \min_x \left\{ \frac{1}{2} \|Jx - d\|_{C_\eta^{-1}}^2 \right\} = \min_x \left\{ \frac{1}{2} (Jx - d)^T C_\eta^{-1} (Jx - d) \right\}, \quad (4.8)$$

whose minimiser is the Generalised Least Squares solution, existing for over-determined and full-rank systems, that is, $m \geq n$ and $\text{rank}(J) = n$. It can be found by making zero the first derivative of the functional (4.8) with respect to x , that is

$$J^T C_\eta^{-1} (Jx - d) = 0, \quad (4.9)$$

thus the GLS solution is given by

$$x_{\text{GLS}} = (J^T C_\eta^{-1} J)^{-1} J^T C_\eta^{-1} d, \quad (4.10)$$

which exists only when J^{-1} and C_η^{-1} are well defined.

The GLS solution (4.10) can be also expressed in terms of the pseudo-inverse (section A.2.4) if one multiplies J by the Cholesky factor B (4.7) as

$$\tilde{J} = B^\dagger J, \quad (4.11)$$

where B is assumed to be nonsingular and C_η well-posed. Then the GLS solution is given by

$$x_{\text{GLS}} = \tilde{J}^\dagger d. \quad (4.12)$$

4.1.3 Ill-posedness for linear problems

In general both J and C_η can be rank-deficient and even ill-conditioned. In addition, the system (4.5) is usually under-determined as the discretisation of the solution x becomes very large;

therefore, an approximated solution to (4.5) cannot be found by the GLS method (4.8). Before looking for an alternative solution to the linear system, Hadamard's considerations of ill-posedness are highlighted (section 3.2.1):

a) There is not an exact solution to the linear system $Jx = d$ since d may not belong to $\mathcal{R}(J)$. In this case, the GLS problem (4.8) provides an approximate solution (4.10) for overdetermined well-conditioned J as long as $d \in \mathcal{R}(J)^\perp$.

b) In practice, the system of equations is highly under-determined, $n \gg m$, and numerically rank-deficient, $r = \text{rank}(J) < m$. Then, considering the pseudo-inverse $J^\dagger = V \text{diag}(s_i^{-1}) U^T$ (A.21) to solve the LS problem, implies inverting all s_i where

$$s_i \sim 0 \quad \text{for all} \quad r < i \leq m. \quad (4.13)$$

Thus, the inversion of (4.13) must be somehow penalised.

c) The ill-conditioning of J makes small perturbations in the data provide very large errors in the solution. In real applications where the data is noisy, the smallest singular values are highly sensitive to noise and their inversion will amplify the errors.

These three conditions make the inverse problem ill-posed. To account for the three conditions one must a) seek an approximate solution; b) convert the problem to a well-posed one, that is, full-rank; and c) better conditioning.

4.1.4 Regularisation

Regularisation is needed to make the problem well-posed (section 3.2.2) by providing prior information about the solution that constrains the previous set of possible solutions and leads to a unique one (section 3.2.3).

Often regularising implies adding a penalisation to the GLS objective function where Tikhonov regularisation (3.19) yields

$$\min_x \frac{1}{2} \left\{ \|Jx - d\|_{C_n^{-1}}^2 + \alpha \|x - x_0\|_{C_x^{-1}}^2 \right\}, \quad (4.14)$$

where α is the regularisation term controlling the penalisation term.

4.1.4.1 Regularisation by filtering

Regularisation methods for a linear inverse problem can be always described as a linear filter [61]. For example, the Truncated SVD solution, which can be derived from the SVD (section A.2.2), is expressed as a filter as

$$x_{\text{TSVD}} = \sum_{s_i^2 \leq \alpha} \frac{1}{s_i} (u_i^T d) v_i, \quad (4.15)$$

where u_i and v_i are the left and right singular vectors of J , respectively. It can be also given as

$$x_{\text{TSVD}} = V \Lambda_{\text{TSVD}} U^T d, \quad (4.16)$$

where U and V are defined in section A.2.4 and Λ_{TSVD} corresponds to the low pass filter

$$\Lambda_{\text{TSVD}} = \text{diag}(s_1^{-1}, \dots, s_w^{-1}, 0, \dots, 0), \quad (4.17)$$

for a truncation level w such that $w \leq r$, where $r = \text{rank}(J)$.

Phillips-Tikhonov regularisation seeks a minimiser to

$$\min_x \{\Phi_{\text{Phi-Tik}}\} = \min_x \frac{1}{2} \{ \|Jx - d\|_2^2 + \alpha \|x\|_2^2 \}, \quad (4.18)$$

which penalises large solution norms. A solution to (4.18) can be obtained by differentiating $\Phi_{\text{Phi-Tik}}$ with respect to x and making it equal to zero [94], that is,

$$\frac{\partial \Phi_{\text{Phi-Tik}}}{\partial x} = J^T Jx - J^T d + \alpha x = 0. \quad (4.19)$$

Thus, a minimiser to (4.18) is given by

$$x_{\text{Phi-Tik}} = (J^T J + \alpha I)^{-1} J^T d. \quad (4.20)$$

The same result can be obtained from the nonlinear iterative Newton's method, by converting the updated solution $x_{k+1} = x_k + p_k$ to a direct approach by $k = 0$, $x_0 = 0$ and $x_1 = p_0$, where p_0 is Newton's step (3.37) and the Hessian is given by $H = JJ^T + \alpha$, and the gradient by $G = J^T(Jx_0 - d^T) + \alpha x_0$. This yields the same solution (4.20).

By substituting J by its SVD, (4.20) is given in filter form as

$$x_{\text{Phi-Tik}} = \sum_{i=1}^m \frac{s_i}{s_i^2 + \alpha} (u_i^T d) v_i, \quad (4.21)$$

or in compact form as

$$x_{\text{Phi-Tik}} = V \Lambda_{\text{Phi-Tik}} U^T d, \quad (4.22)$$

where Phillips-Tikhonov's filter $\Lambda_{\text{Phi-Tik}}$ is given by

$$\Lambda_{\text{Phi-Tik}} = \text{diag}\left(\frac{s_i}{s_i^2 + \alpha}\right). \quad (4.23)$$

While the TSVD filter (4.15) corresponds to a low-pass filter providing a jump function, Phillips-Tikhonov's filter (4.23) is smooth. Examples of other filters can be found in [62]. Anisotropic-smoothness filters have been studied in [27].

4.1.4.2 Generalised-Tikhonov regularisation

TSVD and Phillips-Tikhonov assume the covariance of the noise and solution to be the unit matrix, yet the matched filtering theorem says that the smoothing should match the signal to maximise the SNR [183]. Thus, spatial smoothing for neighbouring elements improves the SNR when the smoothing of the filter matches the dimensions of the object to be detected [183]. Modelling the covariance matrix of the noise is essential if data variables have different variance and are correlated, and it has been proved to decrease image error for EIT of experimental tank data [69].

A more general model of the problem is Generalised-Tikhonov regularisation, which is equivalent to the MAP estimator. Statistically, it assumes the solution and the data random vectors are normally distributed, that is, $x \sim N(x_0, C_x)$ and $\eta \sim N(0, C_\eta)$ [176]. It seeks a minimiser of

$$\min_x \{\Phi_{\text{Gen-Tik}}\} = \min_x \frac{1}{2} \left\{ \|Jx - d\|_{C_\eta^{-1}}^2 + \alpha \|x - x_0\|_{C_x^{-1}}^2 \right\}, \quad (4.24)$$

whose solution can be obtained as in (4.19) by differentiating as (4.24)

$$\frac{\partial \Phi_{\text{Gen-Tik}}}{\partial x} = 0. \quad (4.25)$$

Thus, the solution to (4.24) is given by

$$x_{\text{Gen-Tik}} = [J^T C_\eta^{-1} J + \alpha C_x^{-1}]^{-1} J^T C_\eta^{-1} d, \quad (4.26)$$

which is more suitable for overdetermined systems ($J^T J$ is a n-by-n matrix where J is a m-by-n matrix) than the equivalent form for large scale problems

$$x_{\text{MAP}} = C_x J^T (J C_x J^T + \alpha C_\eta)^{-1} d, \quad (4.27)$$

which is more suitable for underdetermined systems ($J J^T$ is a m-by-m matrix).

A deterministic approach, as in [139, 26], defines a differential operator L , such that $L^T L = C^{-1}$. Then, the problem (4.24) becomes

$$\min_x \{\Phi_{\text{Gen-Tik}}\} = \min_x \frac{1}{2} \left\{ \|L_\eta(Jx - d)\|_2^2 + \alpha \|L_x(x - x_0)\|_2^2 \right\}, \quad (4.28)$$

which can be solved by doing a Generalised SVD (GSVD) [56] or by minimising the equivalent augmented system

$$\min_x \frac{1}{2} \left\{ \left\| \begin{pmatrix} L_\eta J \\ \sqrt{\alpha} L_x \end{pmatrix} x - \begin{pmatrix} L_\eta d \\ \sqrt{\alpha} L_x x_0 \end{pmatrix} \right\|^2 \right\} \quad (4.29)$$

$$= \min_x \frac{1}{2} \left\{ \|\tilde{J}x - \tilde{d}\|^2 \right\}, \quad (4.30)$$

where now \tilde{J} has a well defined inverse as long as $\mathcal{K}(L_\eta J) \cap \mathcal{K}(L_x) = \emptyset$. If this is the case, then the augmented system (4.29) has now full rank and can be solved using the pseudo-inverse as

$$x = \tilde{J}^\dagger \tilde{d}. \quad (4.31)$$

4.1.5 Modelling a general covariance matrix

So far, the reviewed methods assumed the covariance matrix of the noise C_η to have a well-defined inverse. While most approaches have considered $C_\eta = I$, modelling data errors as white noise, this is not the case for EIT data where data variables may have different variance and be correlated [106, 69].

A first approximation to the data covariance is to allow the variance to differ for different channels while neglecting correlations among channels, that is, assuming the covariance of the noise to be a diagonal matrix

$$C_\eta = \text{diag}(\sigma_1^2, \dots, \sigma_m^2), \quad (4.32)$$

where σ_i^2 is the variance of the i th-channel. The main advantage is that C_η^{-1} is well-defined making the Generalised-Tikhonov solution (4.26) stable. Then, by substituting the Cholesky factor B defined in (4.7) into (4.24), the problem can be computed as

$$\min_x \frac{1}{2} \left\{ \|B^\dagger(Jx - d)\|_2^2 + \alpha \|x - x_0\|_{C_x^{-1}}^2 \right\}, \quad (4.33)$$

where $B^\dagger = \text{diag}(\sigma_1^{-1}, \dots, \sigma_m^{-1})$. This is also known as whitening, with which the data space becomes an equal variance domain, and it is a good approximation as long as the correlations are small enough.

A more general covariance matrix would model error correlations in the data and would allow its decorrelation; unfortunately, its implementation is non trivial since C_η can be rank deficient and even ill-conditioned. A generalised LS can be solved by applying the Gauss-Markov linear model introduced by Paige [129], which can be computed as indicated in [130] or by using GSVD [131]. Bjork [21] dealt with the case when J and C_η are rank deficient. Hansen, in [187], assumed J to be ill-conditioned and C_η well-conditioned, and he suggested a better understanding was needed when C_η is ill-conditioned. They adopted Tikhonov regularisation on the constrained LS problem on the form

$$\min_{u,x} \left\{ \|u\|_2^2 + \alpha \|L_x x\|_2^2 \right\} \quad \text{subject to} \quad Jx + Bu = d, \quad (4.34)$$

where $B \in \mathbb{R}^{m \times p}$ has rank p , such that $C_\eta = BB^T$. Moreover, the case when B is ill-conditioned seemed to be unstable and not completely solved.

The ill-posedness of C_η usually comes from the number of observations q being much smaller than the number of unknowns to estimate, which for a full covariance matrix is given by [98]

$$\frac{1}{2}m(m-1). \quad (4.35)$$

In practice, if the number of measurements m is two hundred, then the number of unknowns (4.35) required to produce a covariance estimate is twenty thousand; which would require over eighty minutes of baseline if measurements are taken four times a second. In the case where the number of observations is much smaller than the number of unknowns (4.35), C_η is ill-conditioned.

An alternative to increase the baseline time can be to constrain the covariance matrix. The easiest constraint is a diagonal matrix that neglects correlations between measurements. However, it may be unrealistic when measurements are taking in parallel or acquisition time is twice faster than possible correlations. An appealing method to constrain the covariance is to use the concept of conditional independence from multivariate normal distributions [98]. This procedure assigns conditional independence for indirectly connected variables d_i and d_j by making $W_{ij} = 0$, where $W = C^{-1}$ is known as the concentration matrix. Unfortunately, defining conditional independence does not seem straightforward for EIT of the head, where data variables correspond to measurements on pairs of electrodes far apart from each other. Different approaches to tackle this issue can be found in [98, 32].

4.1.6 Regularisation parameter selection

Regularising is important, so errors in the model and the data are not amplified by the inversion; however, excessive regularisation yields larger spatial regularisation than the target dimensions losing vital information in the data. A collection of methods that guarantee convergence for selecting an optimum regularisation parameter regularisation parameter is presented in [176, Chapter 7]. The aim is to find a minimiser α to the solution error norm

$$\|x_\alpha - x_{\text{true}}\|_2^2, \quad (4.36)$$

where obviously the solution x_{true} is only known in simulations. Instead of minimising (5.8) some of those methods are based on minimising an approximation to the mean squared norm of the predictive error

$$\frac{1}{m} \|Jx_{\text{true}} - Jx_\alpha\|^2. \quad (4.37)$$

Some of the selection methods require prior knowledge of the noise as the Discrepancy Principle (DP) due to Morozov, which seeks a minimiser of the functional

$$\Phi_{\text{DP}} = \|Jx_\alpha - d\|_2 - \|\eta\|_2, \quad (4.38)$$

assuming white noisy and $\|\eta\|_2 < \|d\|_2$. Its solution appears right at the L-curve "corner" [60], where for white noise, σ , can be estimated from a plot of the functional ϑ

$$\vartheta = \frac{\|Jx_\alpha - d\|_2^2}{\text{trace}(I - JR_\alpha)}, \quad (4.39)$$

where σ^2 can be estimated as the plateau when ϑ is plotted against α^{-1} . It can be estimated also from experimental data.

The Unbiased Predictive Risk Estimator (UPRE) is based on minimising (4.37). Assuming white noisy a minimiser to (4.37) is proved to be close to the minimiser of the UPRE functional

$$\Phi_{\text{UPRE}} = \frac{1}{m} \|x_\alpha - d\|_2^2 + \frac{2\sigma^2}{m} \text{trace}(JR_\alpha) - \sigma^2, \quad (4.40)$$

where R_α is the regularisation operator defined as

$$x = R_\alpha d. \quad (4.41)$$

The Generalised Cross Validation (GCV) [177] does not need a priori knowledge of the noise but it assumes white noise and the existence of a smooth solution. It aims to minimise

$$\Phi_{\text{GCV}} = \frac{\frac{1}{m} \|Jx_\alpha - d\|_2^2}{\left[\frac{1}{m} \text{trace}(I - JR_\alpha)\right]^2}. \quad (4.42)$$

The L-curve is based on a plot of the squared seminorm of the solution $\|Lx_\alpha\|_2$ versus the residual norm $\|Jx_\alpha - d\|_2$. The idea is that a trade off between fitting the data and regularising the solution provides a L-curve shaped graph where the "corner" corresponds to the optimum regularisation parameter. It was first suggested by Lawson and Hanson, in 1974, regarding LS problems. Hansen proposed, after fitting a 2D-cubic spline, the point of maximum curvature for selecting the point in the corner [63]; refer to [176, p. 107] for the computation of the L-curve curvature.

Although, Hanke proved nonconvergence for the L-curve [58], Hansen [61] suggested three conditions for a better distinguishability of the "corner": i) Picard condition so that regularised solution exists; ii) the noise follows a distribution $N(0, \sigma^2 I)$, otherwise he suggested to implement the general Gauss-Markov linear model for general covariance matrices, as in [187] where C is assumed to be a well conditioned general covariance matrix; iii) $\|\eta\| < \|d\|$, that is, an optimum SNR.

Another method is the quasi-optimality criterion [61] which looks at changes of the regularised solution. For TSVD, recent method based on the mean squared error (MSE) claimed to provide better estimator in terms of the MSE and biases than the L-curve, which over-stabilised the solution [184]. There are iterative methods that simultaneously converges to an optimum

regularisation parameter and regularised solution, in few steps, avoiding these selection methods; for instance, a method proposed in image restoration converged to a unique solution assuming white noise [86], it is yet to be shown that it can be used in our area.

The existence of correlated errors in the data was showed to make the GCV fail [60], where the GCV did not have a minimum or was too flat to be estimated while the L-curve gave good results. It was explained that while the GCV is based on the residual norm, the L-curve does take on account both the fitting of the data and the solution norm, and it identified correlated errors which do not satisfy the discrete Picard condition.

4.1.7 Computing regularisation schemes for EIT of brain function

Optimising linear EIT of brain function requires a decision for a regularisation scheme that is computationally cheap, for large scale problems, and stable enough, to model the general covariance matrix. Different methods to compute TSVD and Generalised Tikhonov regularisation are compared below to achieve these goals.

A Generalised-Tikhonov approach (4.24), equivalent to the MAP estimator, implies modelling the data covariance C_η , spatial covariance C_x , initial estimate x_0 , and, considering the dimensions of the Jacobian, which are given by the number of measurements by the number of conductivity elements. Regarding the size of the Jacobian, for example, a typical paradigm comprises around $m = 200$ channels and $n \sim 4 \cdot 10^4$ conductivity unknowns. For evoked potentials, the estimate of the conductivity change has been taken as $x_0 = 0$ since no better knowledge of the solution is available. For spatial regularisation, the covariance of the solution has been assumed to be the unit matrix, $C_x = I$, that is, the solution variables have the same variance and are uncorrelated.

For the size of the problem, the conventional Generalised-Tikhonov method as given in (4.26) or (4.29) are computationally too expensive since they imply inverting $n \times n$ and $(m + n) \times n$ matrices, respectively.

4.1.7.1 TSVD

TSVD has been previously applied to EIT of brain function avoiding the computation of the SVD of J , which is too expensive. Since $J = USV^T$, then U is a matrix of eigenvectors of the operator JJ^T with a matrix of eigenvalues S^2 , and

$$(JJ^T)U = US^2, \quad (4.43)$$

such that the Jacobian inverse can be obtained by inverting JJ^T of dimensions $m \times m$ instead of J of dimensions $m \times n$, that is.

$$J^{-1} = J^T(JJ^T)^{-1}. \quad (4.44)$$

Then, the idea is to compute the SVD of JJ^T , $JJ^T = \bar{U}\bar{S}\bar{V}^T$, and then to calculate its truncated inverse as

$$x_{TSVD} = J^T \bar{V} \Lambda \bar{U}^T d, \quad (4.45)$$

where $\Lambda = \text{diag}(\bar{s}_1^{-1}, \dots, \bar{s}_w^{-1}, 0, \dots, 0)$ is the truncated filter of truncation level w singular values. The idea is feasible because the ranges of the operators J and JJ^T are both equal to U_r .

However, computing the SVD of JJ^T implies an inevitable loss of information in the cross product. One can see that for a given J , the conditioning of JJ^T increases, $\text{cond}(JJ^T) > \text{cond}(J)$; consequently, then the eigenvalues of JJ^T decay much faster than those of J .

A more direct method of computing TSVD avoiding the cross product JJ^T is to compute the reduced SVD of J , $J = \tilde{U}\tilde{S}\tilde{V}^T$, where $U = [\tilde{U}, \tilde{U}^\perp]$, $\tilde{U} \in \mathbb{R}^{m \times r}$, $V = [\tilde{V}, \tilde{V}^\perp]$, $\tilde{V} \in \mathbb{R}^{n \times r}$, $\tilde{S} = \text{diag}(s_1^{-1}, \dots, s_r^{-1})$, and $r = \text{rank}(J)$. Then the TSVD solution can be obtained as

$$x = \tilde{V} \Lambda \tilde{U}^T d, \quad (4.46)$$

where $\Lambda = \tilde{S}$, such that, $s_i^{-1} = 0$ for $i > w$. Thus, the previous equation is equivalent to the low pass filter as defined in (4.15).

4.1.7.2 Generalised Tikhonov

The Generalised Tikhonov for under-determined and over-determined systems is given by the MAP estimate (3.28) where the regularisation parameter α defined previously in (4.26) can be absorbed by the covariance matrices.

Two realistic assumptions can be taken: $x_0 = 0$, where the conductivity change has mean zero; and $C_x = I$, where elements in x are uncorrelated. Spatial regularisation considering neighbouring finite elements has been proved to increase the image SNR as given by the matched filter theorem; however, in this work the aim is to model the effect of C_η . From here onwards, the terminology $C = C_\eta$ is adopted. Thus, the problem (4.26) becomes

$$\min_x \{\Phi\} = \min_x \frac{1}{2} \{ \|Jx - d\|_{C^{-1}}^2 + \alpha \|x\|_2^2 \}. \quad (4.47)$$

The solution to (4.47) can be derived by

$$\frac{\partial \Phi}{\partial x} = 0, \quad (4.48)$$

that is,

$$J^T C^{-1} (Jx - d) + \alpha x = 0, \quad (4.49)$$

Table 4.1: Linear inverse problem approaches comparison in terms of modelling the covariance of the solution, C_x , and the covariance of the noise, C_η , inverting C_η , and feasibility for Large Scale Problems (LSP).

approach	eq. #	C_x	C_η	avoid C_η^{-1}	LSP	comments
GLS	(4.10,4.12)	↓	↑	↓	↓	no for IP
TSVD	(4.16)	↓	↓	–	↓	–
“	(4.45)	↓	↓	–	↑	–
“	(4.46)	↓	↓	–	↑	avoids JJ^T
Phi-Tik	(4.20)	↓	↓	–	↓	–
“	(4.22)	↓	↓	↓	↓	–
Gauss-Markov	(4.34)	↑	↑	↑	–	constrained method
Gen-Tik	(4.26,4.29)	↑	↑	↓	↓	MAP
“	(4.27)	↑	↑	↑	↑	“
“	(4.51)	↓	↑	↑	↑	“

then by re-ordering

$$\begin{aligned}
J^T C^{-1} J x - J^T C^{-1} d + \alpha x &= \\
J x - d + C J^{-T} \alpha x &= \\
(J + \alpha C J^{-T}) x - d &= \\
(J J^T + \alpha C) J^{-T} x - d &= 0,
\end{aligned} \tag{4.50}$$

then a solution (4.47) is given by

$$x = J^T (J J^T + \alpha C)^{-1} d. \tag{4.51}$$

Among all linear inversion approaches (Table 4.1) the solution (4.51), which is suitable for large scale problems, models the covariance, and avoid the inversion of the covariance, will be used, in this thesis, for linear EIT of brain function.

4.2 Summary

The aim of this chapter is to select a linear inversion method that can handle large scale problems and can model the covariance of the data. Linear EIT is ill-posed; therefore, it needs regularisation. Linear regularisation can be explained as a linear filter where the most common ones are

TSVD and Phillips-Tikhonov. While they assume the solution and the data to be standard normally distributed variables, in practice variables have different variance and are correlated. The Generalised-Tikhonov problem models general normally distributed variables and agrees with the MAP estimator. The most generally used version of Tikhonov for overdetermined systems inverts the covariance of the data, which can be unstable when the number of observations is not larger than (4.35), where m is the number of measurements. From the different flavours of the Generalised-Tikhonov solution, the one selected to be used in this thesis is the method for underdetermined systems (4.51) that avoids the inversion of the covariance of the data.

Chapter 5

Selecting the regularisation parameter

5.1 Introduction

EIT is severely ill-posed, so it needs regularisation to find a unique solution. Insufficient regularisation leads to images with artefacts, yet excessive regularisation yields excessively smooth images. Thus, selecting the regularisation parameter is needed to obtain an optimum solution. There are different methods (section 4.1.6) that converge to an optimum parameter under the assumption that the noise of the data follows a standard normal distribution - white noise; however, EIT noise is not white as given by the Lilliefors or Jarque-Bera tests of normality.

So what happens when the noise is not white? A better approximation is to model a general Gaussian distribution, which allows the data variables to have diverse variances and correlations (section 4.1.5). Correlations may exist when measurements are acquired simultaneously or at least twice as fast as the correlated signal, and can be modelled by a general covariance matrix that allows de-correlation, also known as whitening. Unfortunately, whitening is non trivial since C_η can be rank-deficient and ill-conditioned; therefore, it cannot be inverted. A generalised Least Squares (LS) problem, which accounts for a general covariance matrix, can be solved by applying the Gauss-Markov linear method [129, 130], which can be computed using the generalised SVD [131]. Although the cases when J and C_η are rank deficient [21] and J is ill-conditioned while C_η is assumed to be well-conditioned [187] have been analysed, in a general case C_η can be ill-conditioned. Other imaging techniques have included a weighted LS approach, in [136, 6] for PET, or have iteratively predicted the covariance matrix, in [164] for SPECT.

As the number of measurements, m , increases, the estimation of C_η becomes impracticable since it requires as many observations as number of parameters (4.35) to be determined [98]. Otherwise, an estimate from a low number of observations may be rank-deficient and ill-posed if no constraint is imposed to it. There are several ways for constraining the covariance

where the most explicit is applying conditional independence to variables that are not directly dependent [98]. This is employed in Geophysics for spatial data where entries for the concentration matrix, C_η^{-1} , are set to zero for conditional independent variables that are, for example, far apart. For EIT of the head, it is not obvious how to define conditional independence where channel variables correspond to injection from two diametric positions. A simple constraint for a low number of observations is to assume C_η to be diagonal.

Contemplating the possibility that C_η can be ill-conditioned, a method that is both easy to implement and does not invert the covariance matrix is the MAP estimate for under-determined systems (3.28), which agrees with the solution to the Generalised-Tikhonov problem (4.24). Two realistic assumptions can be taken: $x_0 = 0$, where the conductivity change has mean zero; and $C_x = I$, where elements in x are uncorrelated. Thus, under the two previous assumptions, the solution to the problem (4.24) becomes (3.28).

Whatever the linearised filter is, one needs to select the filter truncation or its corresponding regularisation parameter.

Previously, applications for EIT of brain function have chosen the truncation level by means of localisation in phantom data [168] [11], and it has been recommended an objective way of finding an optimum truncation [11]. From a different perspective, although Hanke proved nonconvergence for the L-curve [63], Hansen and O'Leary [61] suggested a distinguishable corner could be identified objectively for the L-curve, providing the noise followed a standard normal distribution. Otherwise, he suggested a general Gauss-Markov linear model for modelling a general covariance matrix of the noise; which was done in [187], where C was assumed to be well conditioned.

Standard methods are divided into two types: those that require prior knowledge of the noise as the Discrepancy Principle, due to Morozov, and the Unbiased Predictive Risk Estimator; others do not need a-priori information as the L-curve and Generalised Cross Validation (section 4.1.6). Other standard methods as the quasi-optimality criterion can be found in [61]. For TSVD, a new method based on the mean squared error (MSE) claimed to provide better estimator in terms of the MSE and biases than the L-curve, which (over)stabilised ill-posed problems [184]. There are iterative methods applied in other applications, which simultaneously converge to an optimum regularisation parameter and regularised solution in a few steps: in image restoration, assuming white noise [86]; in PET, based on iterative approximated computations of the L-curve [88]. A comparison of several regularisation methods, for inverse helioseismology and 2D deconvolution, gave the best results, in decreasing order, for the LC, GCV, quasi-optimality, and DP [59]. Nevertheless, it was emphasized that those results were

optimised for specific models, and are likely to differ for different inverse problems. Similarly, it was suggested the comparison of selection methods for a specific application [176, Chapter 7].

As previously mentioned, one possible area of application for EIT is to image brain function. Impedance changes have been measured from scalp electrodes during adult motor and visual stimulations [168]. However, localisation was not successfully achieved and SNR was low due to the fact that brain impedance change is decreased between one or two orders of magnitude because of the skull. This motivated EIT of brain function on neonates where although the signal is smaller, the effect of the skull is smaller too [166] [114]. Neonatal skull is less calcified and mainly formed by cartilaginous tissue. Using FMRI [5], it has been verified that blood flow and volume changes in neonates during sensory stimulation.

There are two goals in this chapter: to establish the best choice for selecting the regularisation parameter for EIT of brain function, and to study whether modelling a general covariance matrix instead of assuming white noise improves image quality.

Thus, I compared four methods LC, GCV, UPRE and DP; with and without modelling the covariance matrix of the noise, in simulated, saline filled tank and human neonatal data during a visual stimulus paradigm.

5.2 Methods

5.2.1 Model and forward solution

Obtaining a realistic neonatal head shaped FEM mesh was done by segmenting the outer surface of a neonatal MRI scan and by meshing using IDEAS [170], which provided an accurate mesh made of thirty-six thousands tetrahedra. A Delaunay triangulation algorithm was applied on the surface and then linear tetrahedral elements were grown inwards, where keeping elements to a similar size achieved a high quality mesh [170].

Previous studies in EIT have modelled the internal geometry for the adult head; however, the neonatal skull is less calcified and mainly formed by cartilaginous tissue, which makes the effect of the skull less important [166]. Thus, in this work, the neonatal mesh was considered as homogeneous and so the same conductivity estimate was provided for the whole head. Since the surface under the electrodes was essential for modelling the contact impedance, for this mesh, electrodes were modelled by two surface elements (Figures 5.1(a) and 5.1(b)).

The forward solution was solved using a modified version of EIDORS-3D toolkit [140], which modelling the CEM for first order tetrahedral finite elements, provided boundary voltages and the Jacobian, given a conductivity estimate.

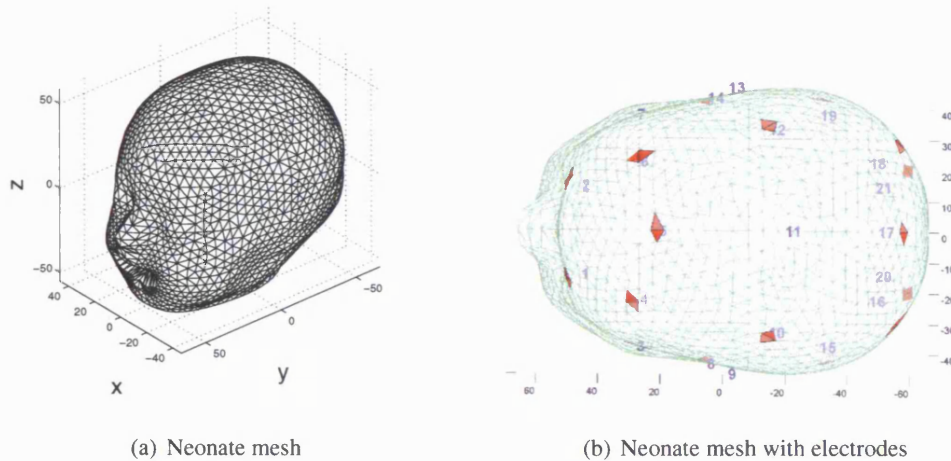


Figure 5.1: A realistic neonatal head shaped FEM mesh created from a structural MRI of a neonate; segmented and meshed using IDEAS. Thanks to A Tizzard, Middlesex University

5.2.2 Image reconstruction

The reconstruction strategy was done in two steps: normalisation of the Jacobian and inverse reconstruction for a range of regularisation parameters. Jacobian row normalisation was needed for reconstructing relative difference data. Details of row normalisation are given in appendix C. The Jacobian, rescaled by the row normalisation matrix R , was inverted using the Generalised-Tikhonov solution (4.51) for twenty logarithmically equally spaced parameters α , in the range 10^{-5} to 10^2 , that corresponded to a truncation level of 120 and 1 singular values.

5.2.3 Computation of the selection methods functionals

The selection parameter functionals were modified from those given in (section 4.1.6), which assumed noise to be additive and white, for which the covariance of the noise, C , is the unit matrix. Nevertheless, in this work, noise vector elements were allowed to have different variance and to have correlations, which can be modelled by a General Gaussian distribution. This is equivalent to compute vector norms in the data space as C^{-1} -norms (A.9), where C is a general covariance matrix of the noise of the data inverted by using the truncated pseudo-inverse.

Selection methods functionals were computed as follows. The GCV estimator minimised

$$\Phi_{\text{GCV}} = \frac{\frac{1}{m} \|Jx_{\alpha} - d\|_{C^{-1}}^2}{\left[\frac{1}{m} \text{trace}(I - JJ_{\alpha}^{-1})\right]^2}. \quad (5.1)$$

The LC is based on a plot of the solution norm $\|x_{\alpha}\|$ versus the residual norm $\|Jx_{\alpha} - d\|_{C^{-1}}$. The idea is that a trade off between fitting the data and regularising the solution provides a L-curve shaped graph whose corner corresponds to the optimum regularisation parameter. First implemented for LS problems, the L-curve optimum corner can be obtained as the point on the curve with maximum curvature, computed here as given in [176, Chapter 7].

The DP estimator minimised

$$\Phi_{\text{DP}} = \|Jx_\alpha - d\|_{C^{-1}} - \|\eta\|_{C^{-1}}, \quad (5.2)$$

where $\|\eta\|_{C^{-1}}$ is the norm of the noise vector η .

The UPRE estimator minimised

$$\Phi_{\text{UPRE}} = \frac{1}{m} \|Jx_\alpha - d\|_{C^{-1}}^2 + \frac{2\sigma^2}{m} \text{trace}(JJ_\alpha^{-1}) - \sigma^2, \quad (5.3)$$

where σ^2 is the variance of the noise.

Estimates of the noise norm, for DP, and of the noise variance, for UPRE, are required. Let $\eta \sim \mathcal{N}(0, C_\eta)$ be the noise vector and σ_i^2 be the variance of the i th-measurement, the estimation of the 2-norm $\|\eta\|^2$ is related to the measurement variance as

$$E[\|\eta\|^2] = E[\eta_1^2 + \dots + \eta_m^2] = \sum_{i=1}^m \sigma_i^2. \quad (5.4)$$

In the case of assuming white noise, for simulated data, where η was known, the noise norm was directly computed as $\|\eta\|^2 = \eta_1^2 + \dots + \eta_m^2$; the noise variance was approximated from the noise norm, using (5.4), as the mean of the measurement variance

$$\sigma^2 = \frac{1}{m} \sum_{i=1}^m \sigma_i^2 \simeq \frac{1}{m} \|\eta\|^2. \quad (5.5)$$

For real data, firstly, the variance of the i -th measurement σ_i^2 was estimated from the baseline period, and then the variance was approximated as the mean of the measurement variance; the noise norm was estimated from the variance by using the previous relation (5.5).

In the case of modelling a general covariance, for simulated data, where η was known, the noise norm was directly computed as $\|\eta\|_{C^{-1}}^2 = \eta^T C^{-1} \eta$; the noise variance was approximated from the noise norm, generalising (5.4), as in (5.5) by

$$\sigma^2 = \frac{1}{m} \sum_{i=1}^m \sigma_i^2 \simeq \frac{1}{m} \|\eta\|_{C^{-1}}^2. \quad (5.6)$$

For real data, where C was assumed to be diagonal, the noise norm $\|\eta\|_{C^{-1}}^2 = \|C^{-1/2} \eta\|^2$ in (5.6) can be approximated by

$$E[\|\eta\|_{C^{-1}}^2] = \sum_{i=1}^m \frac{1}{\sigma_i^2} E[\eta_i^2] = m, \quad (5.7)$$

which shows the effect of whitening, where the variance estimate in (5.6) becomes $\sigma^2 \simeq 1$, that is, a white noise distribution.

5.2.4 Comparison of methods

Comparison of methods was done in terms of the solution error norm, for simulated data, and in terms of the SNR of the largest change in the image, for tank and neonatal data.

The solution error norm was computed as

$$\|x_\alpha - x_{\text{true}}\|^2, \quad (5.8)$$

where x_{true} was the simulated conductivity change and x_α was the reconstructed conductivity change for each regularisation parameter.

Image SNR was computed as the ratio between mean conductivity at Full Width at Half Maximum (FWHM), x_{FWHM} , and the standard deviation of the background conductivity, $\sigma(x_{\text{background}})$, that is,

$$SNR_{\text{image}} = \frac{E[x_{FWHM}] - E[x_{\text{background}}]}{\sigma(x_{\text{background}})}. \quad (5.9)$$

For the statistical comparison, ANalysis Of VAriance (ANOVA) and a multi-comparison test were applied. Employed on the dependent variable, here the solution error norm for simulated data and the image SNR for tank or neonatal data, ANOVA revealed if there were significant differences among the eight groups corresponding to the combination of the four predictors: the LC, GCV, DP, and UPRE; and the two type of covariance: a unit matrix, and general matrix. ANOVA was used to compare means of the eight groups by analysis of group of variances, for a set of observations assumed to be independent and normally distributed with equal variance. The set of observations were twenty-five different noise vectors, for simulated data; four locations of a Perspex inside a saline filled head-shaped tank, for tank data; and ten different subjects, for neonatal data.

Because ANOVA tests for the null hypothesis that all means are equal, for comparing any pair means, I applied a multicomparison test whose outcome was the group means and the Standard Error (SE) or 95% interval of confidence. The multicomparison function was Tukey's honestly significant difference criterion, 'multcompare' function in MATLAB (<http://www.mathworks.com>).

Some data was discarded before the statistical comparison following two criteria: selection methods that did not converge for all data sets, and data sets that yielded images with artefacts.

5.2.5 Data sets

5.2.5.1 Simulated data

Simulated difference data was employed for testing methods in the ideal case where the only difference between data and the model was additive noise. Difference data was the subtraction

between the data corresponding to a local conductivity perturbation and the data corresponding to homogeneous conductivity. A change in conductivity of 1% was simulated in the Region of Interest (RoI), here the visual cortex region, with radius 14% of the neonatal head axial diameter. The primary visual cortex, as fMRI predicts, has a volume in the range eight to fourteen cubic centimetres [7], which roughly corresponds to a range between twelve and thirteen percent of the axial diameter of the adult head. It is located in the occipital part of the brain cortex at the height of the eyes.

Correlated noise was simulated by computing white noise and then by correlating it with a covariance matrix, estimated from a neonatal data set. White noise was computed by changing two parameters: five different states of the pseudo-random generator; and five different SNR in the range 20 to 2 dB, for each of the previous state. In total, there were 25 data sets. All noise vectors were correlated by a general covariance matrix estimated from a specific neonatal data set baseline of one thousand five hundreds points, where the number of parameters to be estimated (4.35) was seventeen thousands, which yielded to an ill-posed covariance matrix. Thus, given a covariance matrix C and a pseudo-random vector e , the correlated noise vector η (4.5), was simulated as $\eta = Be$, where B , such that $C = \text{cov}(\eta) = B^T B$, was determined here using the eigenvalue decomposition.

5.2.5.2 Tank data

Impedance measurements were acquired using the Mark 1b UCLH EIT system (Figure 5.2) [185]. This was specially designed for taking head measurements and current applied complied with safety standards. It comprised a head box, set of electrodes, base unit, and notebook. The headbox containing the current source and multiplexer was connected by a 3m lead to the base unit, which consisted of the power supply, measurement circuits, and 8-bit microprocessor. The head box was attached to the tank by a set of 21 silver/silver chloride EEG electrodes, of 1cm diameter, whose positions were based on 10-20 EEG electrode location protocol [20].

A four-electrode measurement was used: two electrodes to inject an alternating current of 38.4KHz and two different ones to measure electrical impedance. Measurements, of tens of millivolts, were amplified to a range of $\pm 5V$, and then converted to a 12-bit digital signal by an analogue to digital converter.

A new injection-measurement electrode protocol, consisting of 187 measurements [166], had to be adapted, from the 31-electrode protocol previously used [15], for allocating a smaller number of electrodes on a neonatal head.

Tank data comprised a Perspex rod placed at four different locations - at the front, back, left, and right - inside a saline filled head-shaped tank. This produced an infinite local decrease

in conductivity with respect to the saline background conductivity. A set of 187 impedance measurements was taken four times a second for over two minutes. Four repetitions of the same experiment were undertaken; an experiment paradigm consisted of ten seconds of baseline, ten seconds of stimulus, and ten seconds of baseline.

Pre-processing was performed by data segmentation on experiment repetitions, drift correction, data normalisation, and removal of very noisy electrodes. Each data set, after having been segmented into different experiment repetitions, was subtracted to a linear fit of the baseline and represented as percentage change from the mean baseline. Measurements were eliminated when their STD during the baseline exceeded the mean of the ten largest measurements during the stimulus period. Experiment repetitions were removed when the mean STD of all measurements during baseline was larger than 1%.

Before the reconstruction, each data set was averaged across experiment repetitions, in order to remove white noise, and then averaged across the stimulus period for obtaining consistent changes. Consequently, the data for the reconstruction consisted of four data sets, where each one was a vector $d \in \mathbb{R}^m$ with m electrode measurements corresponding to the normalised impedance averaged across experiments and stimulus period.

A covariance matrix of the noise, C , was estimated and included into the reconstruction algorithm (4.20), where noise was considered as the baseline data after averaging across experiment repetitions to be consistent with the averaged data. Because after averaging across experiments, the baseline had only one hundred points, less than the number of variables, a general covariance matrix would have been rank-deficient and unreliable; therefore, for this case, the covariance matrix was constrained to be a diagonal matrix, that is, $C = \text{diag}(\sigma_1^2, \dots, \sigma_m^2)$. This accounted for measurements having different variance, but being uncorrelated.

5.2.5.3 Neonatal data

Visual stimulation was performed using a flash at $8Hz$, using LED goggles, as this gives higher EEG potential than checkboard stimulation, and this frequency is optimum [166].

Continuous recording during twelve minutes allowed fifteen repetitions of the same experiment, where an experiment consisted of a stimulus period of $25s$ in between two baseline periods of $20s$ each. In comparison with tank data, a longer baseline was needed to enable more time for the recovery from the stimulation.

For this study, I used 10 neonatal data sets, corresponding to 4 infants, who followed the paradigm described above. EIT system, hardware, data pre-processing, and estimation of a covariance matrix were done as in section 5.2.5.2.

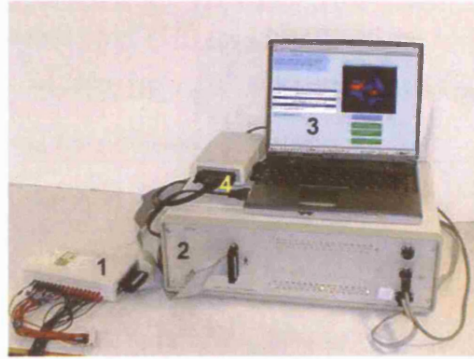


Figure 5.2: Mark 1b UCLH EIT system whose components are 1) headbox that contains the current source and multiplexer; 2) base unit, consisted of the power supply, measurement circuits, and 8-bit microprocessor; 3) notebook; 4) connector box between the notebook card and the UCLH system.

5.3 Results

First, for simulated data, I compared the solution error norm verifying that the selection methods converged to the optimum solution, under the influence of white noise. Then, I carried out a statistical comparison of the different methods for simulated, tank, and neonatal data.

5.3.1 Preliminaries

I present a specific simulation as an example of the selection methods functionals and norms of the solution, residual, and solution error. This also verifies that the selection methods converged to the optimum solution, under the influence of white noise.

Under the influence of 100% white noise, the effect of regularisation is illustrated as α is increased from $1 \cdot 10^{-8}$ to 1. For small α , that is, little regularisation, the residual norm took the smallest values since the model fitted best the data (Figure 5.3(b)). Nevertheless, lack of regularisation implied the model was also fitting the noise, which yielded the largest values of the solution norm, with the solution being amplified by high frequency components (Figure 5.3(a)). On the contrary, for very large α , the solution was excessively smooth, and the model gave a poor fit to the data.

The four predictors were computed as an estimate of an optimum trade off between fitting the noise and smoothing the solution. The LC, GCV, and UPRE agreed on the prediction of the regularisation parameter that corresponded to 37 singular values (Figures 5.3(d), 5.3(e) and 5.3(f)), similar to the DP that estimated a cut off of 25 singular values (Figure 5.4(a)). Note that the LC curvature had a local maximum (Figure 5.3(d)), which in other examples was also global maximum misleading the solution. The solution error norm was minimised for

Table 5.1: Means and standard error (SE) ($p < 0.05$) of the solution error norm, for simulated data, reconstructed by the LC, DP, GCV and UPRE, with (true C) and without ($C = I$) providing the covariance used for simulating correlated noise.

method	$C = I$	true C	SE
LC	0.0898	0.0857	0.0001
GCV	0.0898	0.0858	0.0001
DP	0.0905	0.0859	0.0001
UPRE	0.0898	0.0874	0.0001

25 singular values (Figure 5.4(b)), which, in this particular case, agreed with the DP and was closed to the LC, GCV, and UPRE prediction.

Consequently, the four selection methods successfully predicted an optimum regularisation parameter, among the given twenty, in terms of minimising the solution error norm. In contrast, since the optimum parameter depended on the amount of white noise, a fixed truncation level would not yield an optimum solution.

5.3.2 Simulated data

From twenty five simulated data sets reconstructed with and without modelling the covariance, results were reported by the solution error norm means and SE for the four predictors and for the two covariance types (Table 5.1). Providing the covariance used for simulating the data (true covariance) decreased the solution error norm significantly for all methods where the UPRE had significantly larger error norm than the other three (2nd column in Table 5.1). Assuming white noise, the DP had a larger error while no difference was found among the other three methods (1st column in Table 5.1).

A qualitative comparison of the images for a particular simulated data set presented a significant improvement when providing the true covariance matrix, however, no significant differences among selection methods were found (Figure 5.5).

5.3.3 Tank data

From the four tank data sets, results were reported by image SNR means and SE for the two predictors, the DP and GCV, and the two covariance types, unit matrix and diagonal matrix (Table 5.2). Estimations with the DP and UPRE underestimated noise and failed to converge, leading to noisy images; therefore, they were discarded before the statistical comparison. Between the LC and the GCV there were no significant differences, nor between estimating a diagonal

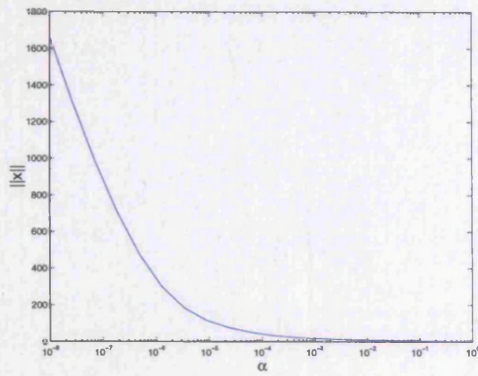
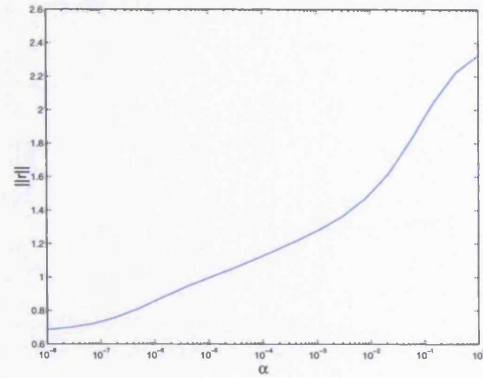
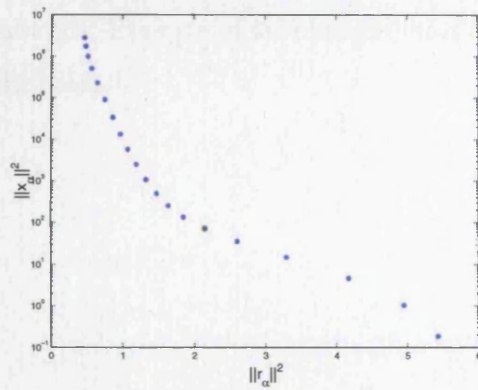
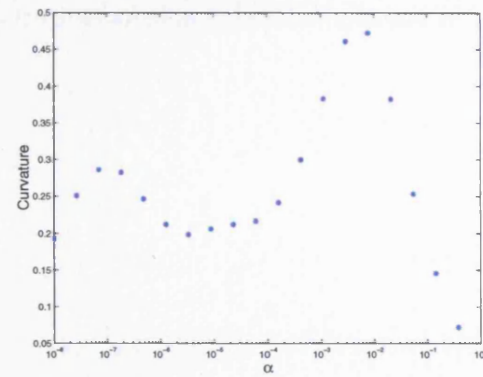
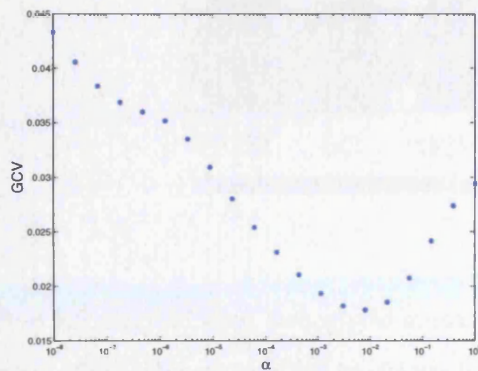
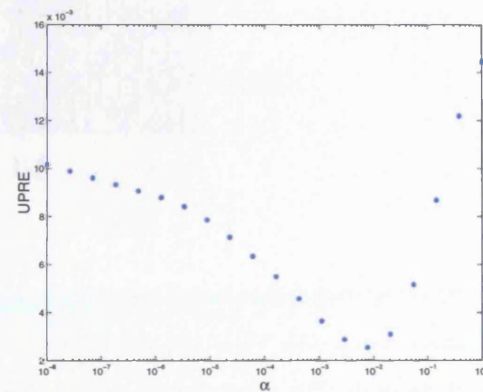
(a) Solution norm $\|x(\alpha)\|$ (b) Residual norm $\|Jx(\alpha) - d\|$ (c) L-curve (α)(d) L-curve (α) curvature(e) GCV(α) functional(f) UPRE (α) functional

Figure 5.3: Example of the different functionals for a simulation under the influence of 100% white noise.

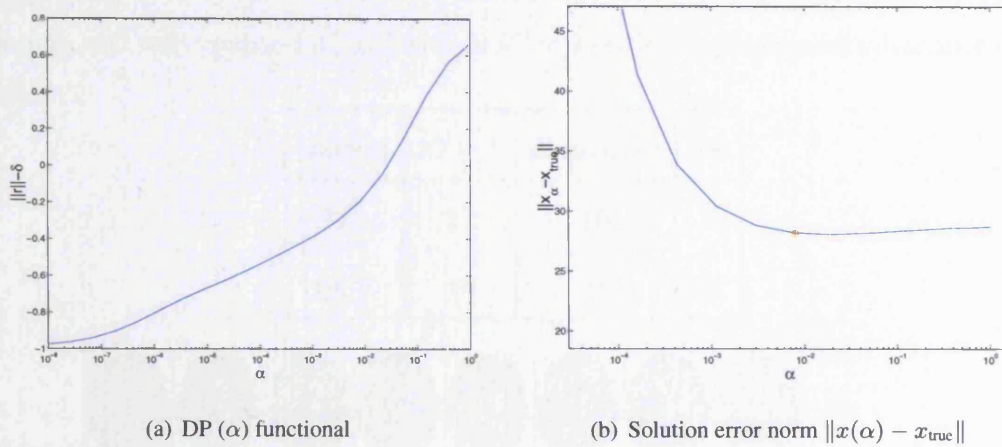


Figure 5.4: Example of the different functionals for a simulation under the influence of 100% white noise.

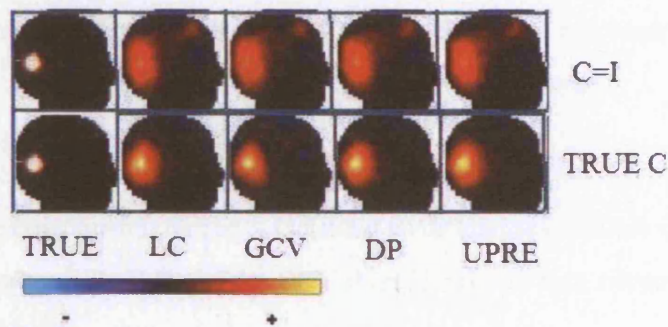


Figure 5.5: Sagittal view, through the middle of the neonatal head, of the simulated conductivity change (first column) and the reconstructed conductivity images (rest of columns) from its simulated scalp data under the influence of correlated noise. This is a single example out of the 25 corresponding to SNR of 1.8dB . In the first row, I assumed white noise ($C = I$), and in the second, I provided the covariance used for simulating correlated noise (true C).

Table 5.2: Means and standard error (SE) ($p < 0.05$) of the SNR of the largest change in the reconstructed images of a Perspex in four positions inside a saline head-shaped tank. Images were reconstructed by the two predictors the LC and GCV, where the UPRE and DP did not converge, and with (diagonal C) and without ($C = I$) estimating a diagonal covariance of the noise.

method	$C = I$	diagonal C	SE
LC	11	10	2
GCV	10	9	2

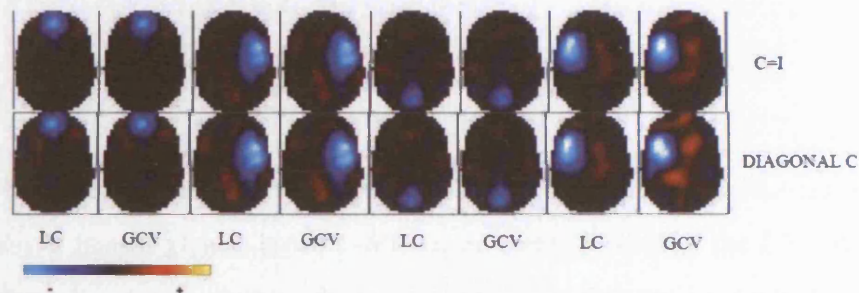


Figure 5.6: Axial view of the reconstructed conductivity images of a Perspex in a saline head-shaped tank positioned on the front (Column 1 and 2), right (Column 3 and 4), back (Column 5 and 6), and left (Column 7 and 8). In the first row, I assumed white noise ($C = I$), and in the second, I estimated a diagonal covariance from the data. Data was reconstructed by the two predictors the LC and GCV since the UPRE and DP did not converge.

covariance matrix and assuming white noise (Table 5.2).

A qualitative comparison of images indicated no differences whether or not modelling the covariance, nor between the LC and the GCV (Figure 5.6). In fact, because the high SNR of the data, $20dB$, no large variations were expected.

5.3.4 Neonatal data

From ten neonatal data sets, six that presented noisy images with a non-localised conductivity change were rejected before the statistical comparison. Out of the remaining four data sets, only one set presented the highest change in the RoI, the visual cortex (back of the head); for the rest the dominant change was on the front (Figure 5.7). Results were reported as a statistical comparison by image SNR means and SE for the four predictors and for the two covariance types, unit matrix and diagonal matrix (Table 5.3).

No significant differences were found among methods for the four neonatal data sets be-

Table 5.3: Means and standard error (SE) ($p < 0.05$) of the SNR of the largest change in the reconstructed images of four neonatal data sets where the other six data sets were discarded because images were very noisy lacking a localised change. Images were reconstructed by the four predictors and with (diagonal C) and without ($C = I$) estimating a diagonal covariance of the noise.

method	$C = I$	diagonal C	SE
LC	3.4	3.4	0.7
GCV	3.1	2.7	0.7
DP	4.4	4.4	0.7
UPRE	3.9	4.2	0.7

cause of the high variability across neonatal data sets (Table 5.3). Nevertheless, a qualitative comparison of images yielded specific differences among methods. The DP and UPRE provided excessively smooth images where modelling the covariance increased the image SNR (Columns 3,4,7, and 8 in Figure 5.7). LC and the GCV with modelling the covariance were best for the data set with a change in the RoI (Subject 2 in Figure 5.7), however, they converged to a small regularisation parameter, yielding images with artefacts, for two data sets (Columns 1,2,5, and 6 in Figure 5.7). Consequently, modelling the covariance consistently improved image quality.

5.4 Discussion

For simulated data, including the true covariance matrix of the noise into the reconstruction significantly decreased the solution error norm, compared to the white noise assumption. However, for either of these methods, no one selection method was clearly better than others. On the other hand, for tank data where the data SNR was very high, estimating a diagonal covariance did not have a remarkable effect. For selection methods, the LC and GCV were equally the best, as the DP and UPRE failed to converge. For real human neonatal data, there was no significant difference among any of the methods because of the variability across subjects. However, estimating a diagonal covariance consistently increased image quality. Overall, therefore, modelling the covariance of the noise improved image quality, but it was not possible to determine the best selection method from human data, whereas from tank and simulated data the best methods were the LC and GCV.

There are some limitations for generalising this study since the feasibility of optimising

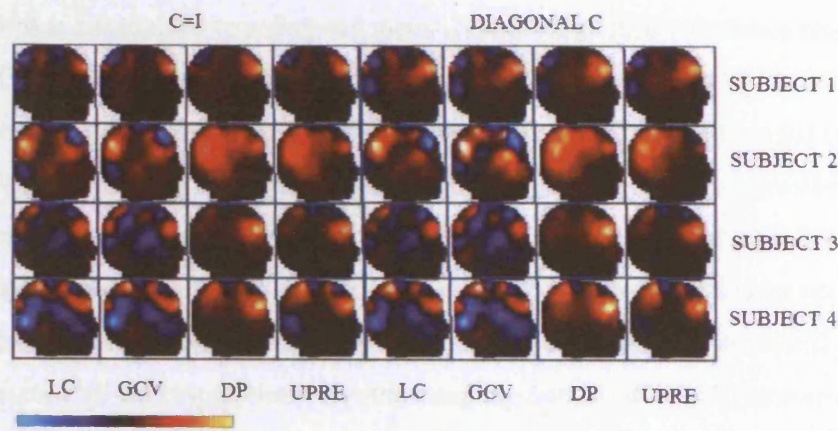


Figure 5.7: Sagittal view, throughout the middle of the neonatal head, of four neonatal data sets (in rows) where the other six data sets were discarded because images were very noisy, lacking of a localised change. Columns correspond to the four predictors: the LC, GCV, DP, and UPRE; and where, for the first four columns, I assumed white noise ($C = I$), and for the last four, I estimated a diagonal covariance of the noise.

the solution of a linear ill-posed system by selecting the regularisation parameter relies on the assumption that the only difference between the model prediction and the data can be explained by a white noise distribution. Because of those limitations, I aimed to test the methods against modelling errors, deviation from a white distribution, and real data, where other physiological activity is present. First, for simulated data, I tested that all methods converged under the appropriate assumptions, and coped with correlated noise. However, simulated correlated noise may have been biased to a specific correlation matrix, which was estimated from a particular neonatal data set. For the tank study, I analysed the effect of shape and electrodes position errors, although it did not explain for inaccuracies of the different layers in the head and anisotropy conductivity. The fact that the DP and UPRE did not converge, underestimating the noise, may be caused by larger modelling errors than accounted for by a Gaussian distribution.

In relation to modelling the covariance of the noise, simulations presented the improvement that can be achieved by modelling the covariance employed for correlating the noise. Modelling a diagonal covariance matrix, for tank data, did not have a large influence, which indicates that no large improvement can be made for high SNR data, and a wrong estimation of the covariance may yield poorer results; for neonatal data, it increased the SNR in one data set though no significant improvement was found over all data sets, what may be due to large variations of some of the selection methods across the different subjects. For real data, the

covariance was constrained to a diagonal matrix because a general covariance required larger number of observations than those of the baseline, which could be solved by increasing the data acquisition during the baseline period. In cases where this is impractical from the experimental point of view, imposing more realistic constraints to the covariance matrix is possible and would allow its estimation from a lower number of points [32] [98], but does not seem straightforward for our application. Moreover, if considering a general covariance of the noise accounting for correlations when measurements have not been acquired in parallel, one would account for only those correlations twice slower than the sampling rate; in this work, measurements were acquired four times a second.

Concerning physiological noise, the neonatal study showed that more than half of the data sets presented excessively noisy images, and all but one data set had the largest changes outside the RoI.

Other technical issues: a more efficient way of estimation of the LC curvature can be done by fitting a 2D-cubic spline before its calculation [63].

Theoretically, selection methods converge under the assumption of white noise, as the only source of error, and positive SNR, where the UPRE has the best convergence and the LC lacks of convergence.

Others found the LC to be more robust to correlated errors than the GCV, while in this work the GCV and LC showed no differences. It was found that the GCV did not converge for correlated data [177]; similar results were found for a low number of data sets [87]. Moreover, a comparison of several regularisation methods, for inverse helioseismology and 2D deconvolution, gave best results, in decreasing order, for the LC, GCV, quasi-optimality, and DP [59]; where the performance of the DP agreed with our simulated study. Nevertheless, it was emphasized those results to be best for that specific models, yet likely to differ for different inverse problems.

EIT of brain function has previously selected a fixed truncation level empirically. Objective selection using one of these methods is superior since the regularisation parameter was optimised for each data set. This has been corroborated for simulated data where the solution error norm was optimised by the four methods. Nevertheless, for tank and neonatal data, the methods failed in a few cases, which suggests that a fixed truncation level could be chosen when the applied selection method fails.

Although no large differences were found among selection methods, I prefer the GCV, because it is simpler to implement than the LC and the latter lacks theoretical convergence [58], and the DP and UPRE require an estimate of the noise, which could be more difficult to

estimate in case of modelling errors or a low number of observations; a truncation level obtained experimentally could be also used, in case the selection methods do not converge. Modelling a general covariance of the noise significantly improved the solution for simulation studies while modelling a diagonal covariance for neonatal data provided a small change and had not effect for high SNR tank data.

Our recommendation for human scalp data in general, therefore is to use the GCV with covariance modelling, and empirical truncation if this does not converge. However, this is based on this limited testing for neonatal visual evoked responses and needs verification in other situations of current interest, such as in epilepsy or adult evoked response EIT.

Chapter 6

Principal Component Analysis

6.1 Introduction

EIT data SNR during evoked responses has been reported in the range 0.76 to 1.34 on adults [168], and 2 on neonates, where experiments were repeated between six and twelve times to increase the SNR by averaging [166].

Principal Component Analysis (PCA), which yields the best linear predictor of the data [32], can be used to reduce the dimensionality of the data set to a small number of Principal Components (PCs), the eigenvectors of the covariance of the data, that are uncorrelated and best preserve the variation in the data [84]. One can then represent the data by its first PCs and neglect higher PCs, such that the first PCs best represent the data and the discarded PCs correspond to noise.

How to select the right number of first PCs that best represents the data is not clear; one approach is to assess the percentage of variation accounted for by the chosen number of PCs, which is given by the Maximum Predictive Error [84].

Estimation of the covariance from a small number of data sets may yield an ill-posed covariance matrix; unless some constraints are imposed (section 4.1.5).

PCA has been used to find a single evoked potential signal for EEG, and it was found that using the covariance of the data (second moment) is rather more accurate than averaging (first moment) since averaging looks only at the first moment and a Gaussian distribution is completely determined by the first and the second moment [87].

The goal of this chapter was to apply PCA for improving the SNR on EIT data collected in a saline head shaped tank with a Perspex rod as test object and visual evoked responses recorded with scalp electrodes at 50 kHz in two neonates. Thus, I projected the data sets onto the first PCs that had the most significant part of the signal and neglected higher order PCs. Data and reconstructed images SNR of raw data and the selected first PCs were compared before and after

reconstruction using Tikhonov-Phillips as the linear regularisation scheme and the Generalised Cross Validation as the selection of the regularisation parameter.

6.2 Methods

6.2.1 Data sets

Data comprised recordings from saline head-shaped tank with a Perspex rod as target and two data sets of visual stimulation in neonates. Only two of the neonatal data sets have been used in this chapter because the localisation of the conductivity changes of the evoked responses was unsuccessful (chapter 5); only one had a reasonable change in the occipital cortex. The data acquisition and pre-processing has been described previously (chapter 5).

6.2.2 Analysis of the data correlations

For tank data, I computed the covariance matrices across time and channels and visualised them as a 2D-plot to identify possible correlations. Also, I computed the covariance of a synthetic pseudo-random data set to support the comparison. The goal was to find whether time or channel correlations were easy to identify.

Data comprised a set of 187 scalp impedance measurements acquired four times a second (Figure 6.6(a)). Let $d_i(t_k)$ represent the data for the i -th channel at time t_k , where $i = 1, \dots, m$ and $k = 1, \dots, q$, and m is the number of channels and q the number of time frames; then the data can be represented as $d \in \mathbb{R}^{m \times q}$.

6.2.2.1 Time covariance

To study time correlations, the covariance matrix $C \in \mathbb{R}^{q \times q}$, whose entries $\text{cov}(d(t_k), d(t_{k'}))$ measured the correlation between the data at time t_k and the data at time $t_{k'}$, was estimated as

$$C_{kk'} = \text{cov}(d(t_k), d(t_{k'})) = \frac{1}{m} \sum_{i=1}^m [(d_i(t_k) - E[d(t_k)])^T (d_i(t_{k'}) - E[d(t_{k'})])], \quad (6.1)$$

where $E[d(t_k)]$ is the estimation across channels for the time frame t_k , that is,

$$E[d(t_k)] = \frac{1}{m} \sum_{i=1}^m d_i(t_k). \quad (6.2)$$

6.2.2.2 Channel covariance

To study channel correlations, the covariance matrix a $C \in \mathbb{R}^{m \times m}$, whose entries $\text{cov}(d_i, d_j)$ measured the correlation between the i th-channel and the j th-channel, was estimated as

$$C_{ij} = \text{cov}(d_i, d_j) = \frac{1}{q} \sum_{k=1}^q [(d_i(t_k) - E[d_i])^T (d_j(t_k) - E[d_j])], \quad (6.3)$$

where $E[d_i]$ is the estimation across time for the i th-channel, that is,

$$E[d_i] = \frac{1}{q} \sum_{k=1}^q d_i(t_k). \quad (6.4)$$

6.2.3 Principal components

Having estimated the time covariance (6.1), I computed its eigenvectors, plotted the first six and last three, and selected those that correlated with the stimulus paradigm assuming therefore the initial and end time frames as prior knowledge. Then the data was projected onto the selected eigenvectors yielding the selected PCs.

6.2.3.1 Computation of the eigenvectors of the covariance

Let C be the time covariance (6.1), its eigenvalue decomposition is given by

$$CP = PS, \quad (6.5)$$

where $S = \text{diag}(s_1, \dots, s_q)$ is the matrix of eigenvalues of C such that

$$s_1 \geq \dots \geq s_q, \quad (6.6)$$

and columns of $P \in \mathbb{R}^{q \times q}$ are the eigenvectors a of C , that is,

$$P = [a_1, \dots, a_q]. \quad (6.7)$$

6.2.3.2 Computation of the principal components

Let d be the matrix of the data where rows are channels and columns time frames, then the i -th channel can be represented as the row vector

$$d_i(t)^T = (d_i(t_1), \dots, d_i(t_q))^T, \quad (6.8)$$

where $i = 1 \dots, m$. Now, let e_k be the basis vector for the k th-time frame, the data $d_i(t)$ can be expressed as a function of this basis as

$$d_i(t)^T = (d_i(t)^T e_1) e_1^T + \dots + (d_i(t)^T e_q) e_q^T. \quad (6.9)$$

Defining a new basis, whose vectors a are the eigenvectors (6.7), then in the new basis the data is given by

$$d_i(t)^T = (d_i(t)^T a_1) a_1^T + \dots + (d_i(t)^T a_q) a_q^T. \quad (6.10)$$

The approximation of the i -th channel data with r basis vectors, such that $r \ll q$, is

$$(d_i(t)^T a_1) a_1^T + \dots + (d_i(t)^T a_r) a_r^T, \quad (6.11)$$

where the r terms in (6.11) are the r -first PCs, which maximise the linear prediction of the original data d_i by using r terms [32, 84]. The rest of PCs were neglected, which implied an inevitable loss of information; however, it agreed with our motivation of neglecting the irrelevant part of the data. In addition, it has been shown that approximating the data by the first PCs is appealing since the discarded PCs correspond to measurements with worse precision [84].

After projecting the data onto the r -first PCs, the percentage of information remaining of the original data, also called Maximum Predictive Error [32], which accounts for the eigenvalues (6.6) percentage weight of the selected PCs, was computed as

$$\text{MPE} = 100 \frac{\sum_{j=1}^r s_j}{\sum_{i=1}^q s_i}. \quad (6.12)$$

6.2.4 Image reconstruction

The reconstruction strategy was done by row normalising the Jacobian before the reconstruction, reconstructing the data for a range of regularisation parameters, and selecting the optimum solution using the GCV criterion. Jacobian row normalisation was implemented as in appendix C. The row normalised Jacobian was inverted using the Generalised-Tikhonov solution (4.51) for twenty logarithmically equally spaced parameters α , in the range 10^{-5} to 10^2 , that corresponded to a truncation level of 120 and 1 singular values. The optimum regularisation parameter was the minimiser of the GCV functional (5.1).

6.2.5 Comparison of results

I compared the raw data d and reconstructed images x SNR with and without projecting the data onto the selected PCs.

6.2.5.1 Comparison of data SNR

I compared the raw and the projected data SNR computed in dB as

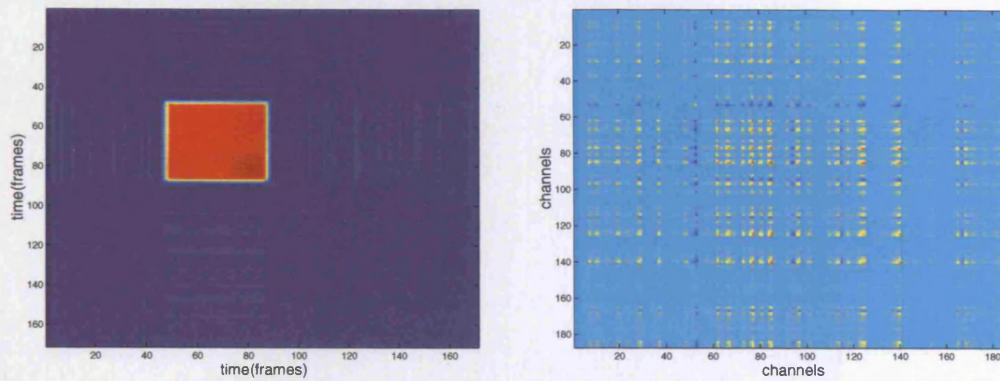
$$\text{SNR} = 20 \log_{10} \left(E \left[\frac{|E[d_i(t_{stim})]|}{\sigma(d_i(t_{base}))} \right] \right), \quad (6.13)$$

where $E[d_i(t_{stim})]$ is estimation of the data across the stimulus period and $\sigma(d_i(t_{base}))$ is the standard deviation during the baseline period, for the i th channel, where $i = 1, \dots, m$ and m is the number of channels.

6.2.5.2 Comparison of images SNR

I compared the raw and the projected data SNR computed in dB as

$$\text{SNR} = 20 \log_{10} \left(E \left[\frac{|E[x_i(t_{stim})]|}{\sigma(x_i(d_{base}))} \right] \right), \quad (6.14)$$



(a) Covariance matrix for time frames, four frames
a second

(b) Covariance matrix for 187 channels

Figure 6.1: a) Time covariance and b) channels covariance matrices, for a data set of perspex in a saline head-shaped tank. a) Time correlations had a pattern that was easier to interpret than b) channels correlations, suggesting a possible dimensionality reduction.

where $E[x_i(d_{stim})]$ is estimation of the reconstructed data across the stimulus period and $\sigma(x_i(d_{base}))$ is the standard deviation during the baseline period, for the i th finite element, where $i = 1, \dots, n$ and n is the number finite elements.

6.3 Results

6.3.1 Analysis of data correlations

For tank data I computed the time and channel covariance matrices. The time covariance had a high correlation during the stimulus period and low correlation during the baseline. On the contrary, the channels covariance had a correlation pattern that was less clear to interpret (Figure 6.1). In comparison, the covariance of a synthetic data set made of pseudo-random numbers of the same dimensions as tank data did not exhibit large off-diagonal elements, which demonstrated that no pattern exists in the covariance for white noise only (Figure 6.2).

Although both time and channels were correlated, I preferred time correlations because they were easier to identify by visualization than channel correlations. Thus, only time covariance was considered for the rest of the study.

6.3.2 Principal components

I computed the time covariance matrix, its eigenvectors (6.7), the maximum predictive error (6.12), and selected the eigenvectors that correlated with the stimulus period for tank and neonatal data.

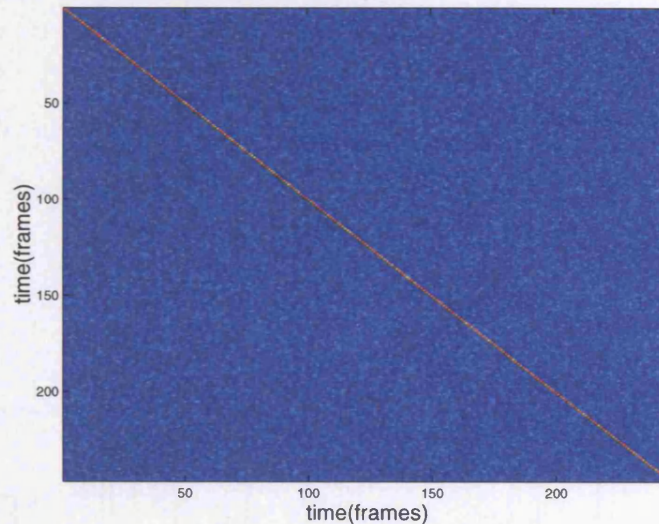


Figure 6.2: Time covariance matrix of a synthetic pseudo-random data set, of the same dimensions as tank data. It did not contain large off-diagonal elements, which illustrate the lack of correlation of random data in comparison with tank data.

6.3.2.1 Tank data

High correlations during the stimulus period and no correlations during the baseline were found by visualising the time covariance (Figure 6.1(a)) where the first eigenvector had MPE (6.12) of 98% and best represented the time response (Figure 6.3). From the second to the sixth eigenvectors, weights were more than hundred times smaller, and signals did not correspond to the expected square wave signal, and from the seventh upwards, eigenvectors corresponded to high frequency signals. Thus, raw data (Figure 6.6(a)) was projected onto the first eigenvector and the rest of eigenvectors were neglected; this led to use of the first PC (Figure 6.6(b)).

6.3.2.2 Neonatal data

For the first data set, a high correlation was found during the stimulus period, smaller during the recovery, and negligible during the baseline (Figure 6.4(a)), as expected from the experimental paradigm. While the first eigenvector best represented this time response where MPE was 87%, the second to the sixth eigenvectors represented signals that did not correspond to the experimental paradigm. Thus, raw data (Figure 6.7(a)) was projected only onto the first eigenvector and the rest of eigenvectors were neglected; this led to use of the first PC (Figure 6.7(b)).

For the second data set, a higher correlation was found during the stimulus and recovery periods than during the baseline period, however, other correlations were found during the baseline (Figure 6.5(a)). The first eigenvector corresponded to high frequency noise, and therefore was discarded; the second eigenvector best correlated with the experimental paradigm (Fig-

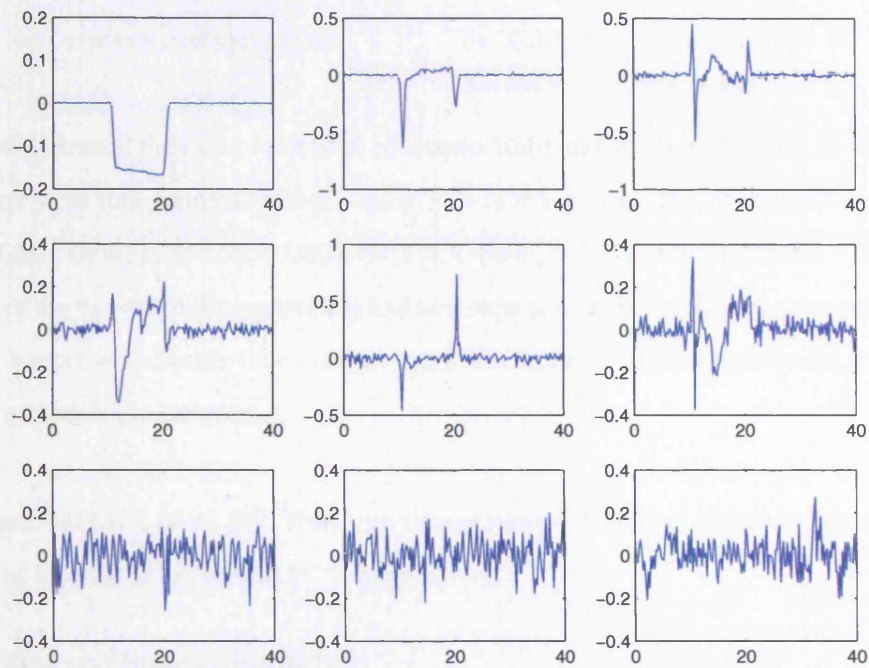


Figure 6.3: Eigenvectors of the covariance matrix across time for a data set of perspex in a saline head-shaped tank. Axes are % change (y-axis) and time in seconds (x-axis). Eigenvectors of the covariance matrix, from top to bottom and from left to right: 1st, 2nd, 3rd, 4th, 5th, 6th, 7th, (m-1)th, mth. Their corresponding eigenvalues are 57.9835, 0.5386, 0.1282, 0.1128, 0.0703, 0.0443, 0.03, $0.2 \cdot 10^{-4}$, $0.1 \cdot 10^{-4}$. The first PC had most of the weight (high eigenvalue) and best represented the experimental paradigm.

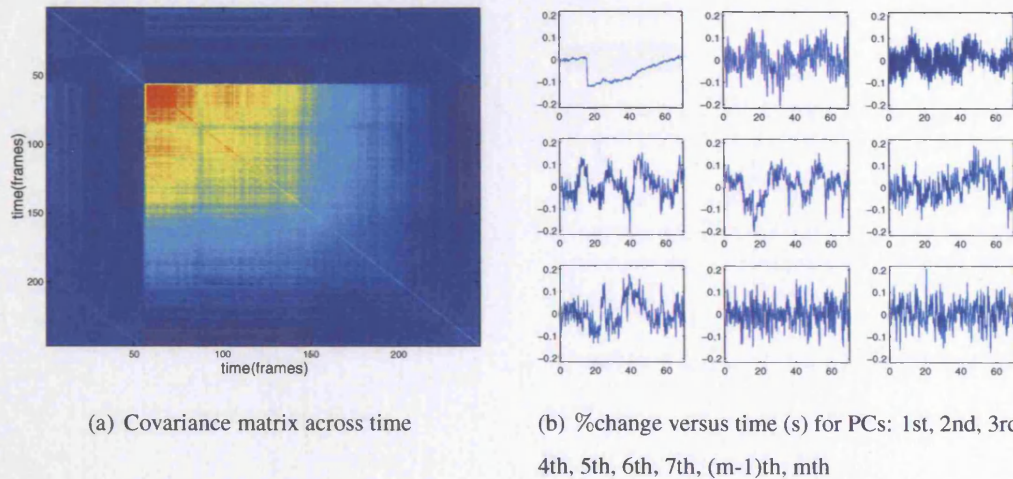


Figure 6.4: Neonatal data set 1 with SNR of around 10dB. a) Covariance matrix in time frames, where there were four frames a second; and b) PCs of the covariance with corresponding eigenvalues 1.5619, 0.0821, 0.0582, 0.0494, 0.0413, 0.0306, 0.0277, 0.0001, 0.0001. The first PC had most of the weight (high eigenvalue) and best represented the experimental paradigm while higher PCs represented other time courses that differ from it (red and blue correspond to high and low correlation, respectively).

ure 6.5) and had MPE of 23.8%. Thus, raw data (Figure 6.8(a)) was projected onto the second eigenvector leading to the second PC (Figure 6.8(a)).

6.3.3 Data and image comparison

I compared the data and the reconstructed conductivity SNR of the raw data and its first PCs.

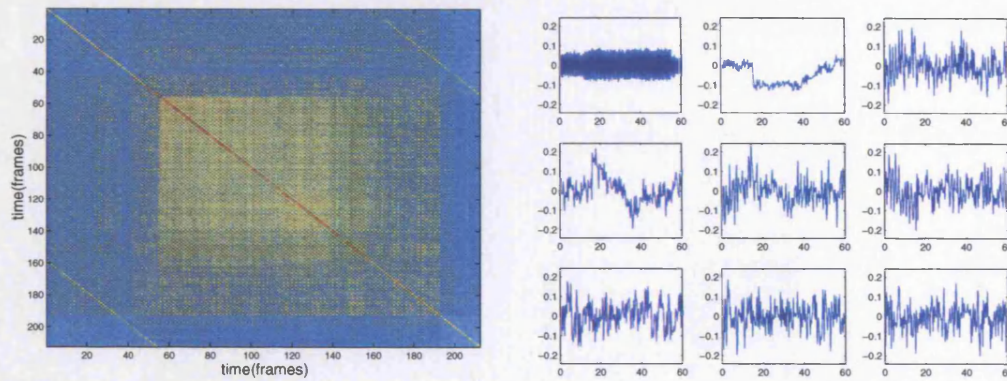
6.3.3.1 Data comparison

The SNR of the first PCs compared to the SNR of the raw data increased by 25dB for tank data and 15 to 20dB for neonatal data (Table 6.1).

For tank data, the first PC had a significant reduction of the baseline noise (Figure 6.6(b)) compared with the raw data (Figure 6.6(a)); the first PC removed also other type of signals during the stimulus period.

For the first neonatal data set, the first PC had a significant reduction of noise and a clearer signal and recovery (Figure 6.7(b)) than the raw data (Figure 6.7(a)).

For the second neonatal data set, the second PC reduced the noise and had a clear signal during the stimulus and recovery periods (Figure 6.8(b)) compared with the raw data (Figure 6.8(a)) that was excessively noisy.



(a) Covariance matrix in time

(b) %change versus time (s) for PCs: 1st, 2nd, 3rd, 4th, 5th, 6th, 7th, (m-1)th, mth

Figure 6.5: Neonatal data set 2 with SNR of around -5dB . a) Covariance matrix in time frames, where there were four frames a second; and b) PCs of the covariance with corresponding eigenvalues $0.3131, 0.1163, 0.0260, 0.0194, 0.0141, 0.0119, 0.0088, 0.9 \cdot 10^{-5}, 0.5 \cdot 10^{-5}$. The first PC had three times more weight (eigenvalue) than the second, however, it consisted of noise only. On the other hand, the 2nd PC best represented the experimental paradigm, and higher PCs corresponded to other time courses that differ from it (red and blue correspond to high and low correlation, respectively).

6.3.3.2 Image comparison

The SNR of the reconstructed first PCs compared to the reconstructed data SNR increased by 35dB for tank data and 15 to 20dB for neonatal data (Table 6.1).

For tank data, the first PC image SNR was higher but image quality did not improve significantly compared to reconstructed images of the raw data (Figures 6.9).

For the first neonatal data set, the first PC images were less dominated by artefacts both during the baseline and the stimulus periods compared to reconstructed images of the raw data (Figures 6.10).

For the second neonatal data set, the second PC had less artefacts during the baseline and higher SNR during the stimulus period compared to reconstructed images of the raw data (Figures 6.11). In fact, since the PC SNR was higher, the optimum regularisation parameter was smaller yielding an increase of SNR of the highest change in the image but with more artefacts, during the stimulus. Reconstructing the second PC where the first PC corresponded to high frequency noise had not only a significant improvement in image quality, but improved the SNR and consistency of the localisation during the stimulus period.

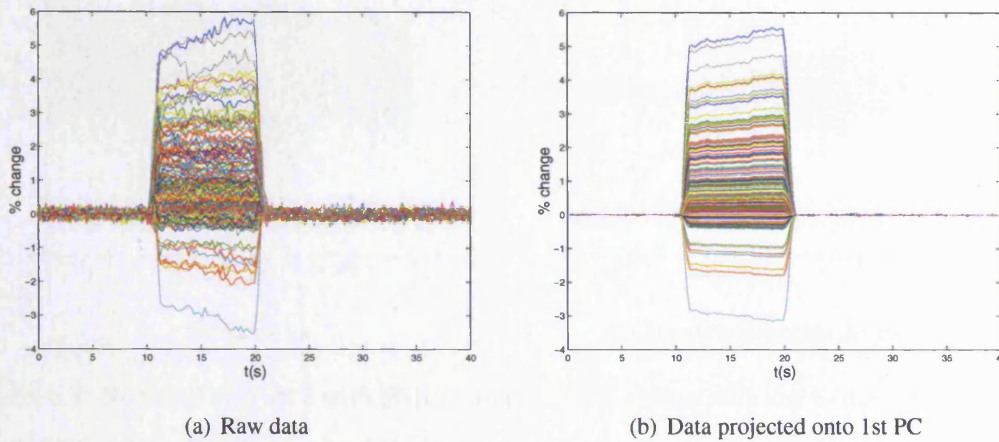


Figure 6.6: Data set of impedance measurements, of perspex in a saline head-shaped tank, for all 187 channels, measured four times a second following a paradigm of twenty seconds stimulus between two baselines of ten seconds each with no perspex on the tank. a) Raw data and b) data projected onto the 1st PC, which best represented the experimental paradigm, neglecting higher PCs.

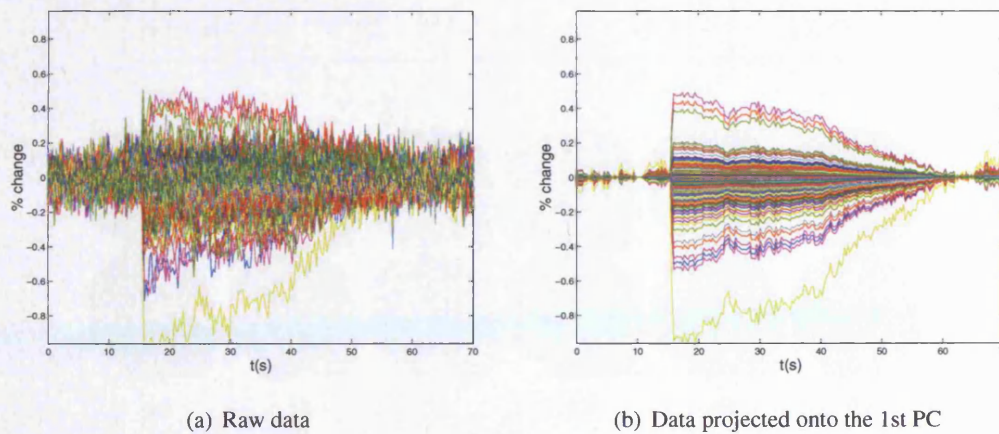


Figure 6.7: Neonatal data set 1 with SNR of around 10dB. a) Raw data and b) data projected onto the 1st PC, which best represented the experimental paradigm, neglecting higher PCs (stimulus from 15 to 40s).

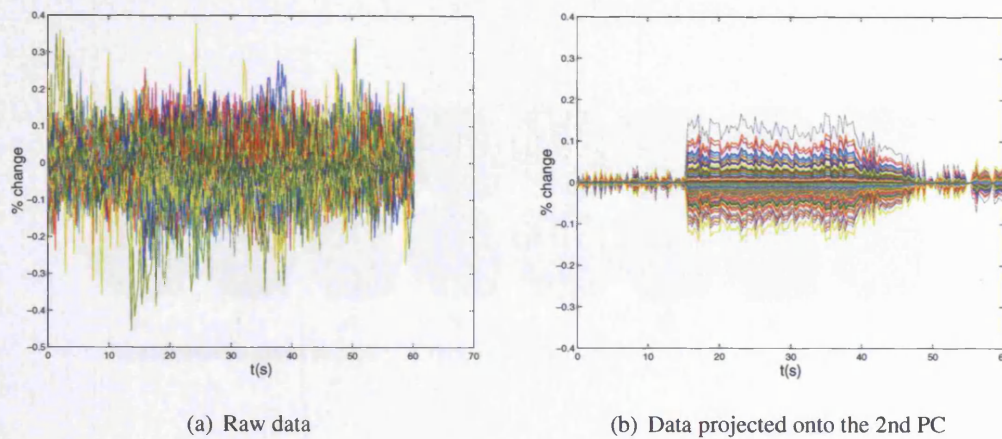


Figure 6.8: Neonatal data set 2 with SNR of around -5dB. a) Raw data and b) data projected onto the 2nd PC, which best represented the experimental paradigm, neglecting other PCs (stimulus from 15 to 40s).

Table 6.1: Data d and images x SNR, in decibels, before and after projecting the impedance measurements data onto the first principal components (PC), for perspex in a saline head-shaped tank and neonatal data during visual stimulation.

Data	$SNR(d)$	$SNR(d_{PC})$	$SNR(x)$	$SNR(x_{PC})$
Tank	16.24	39.53	5.62	39.53
Neonatal 1	0.33	18.86	-1.23	18.86
Neonatal 2	-5.32	11.32	-1.37	11.32

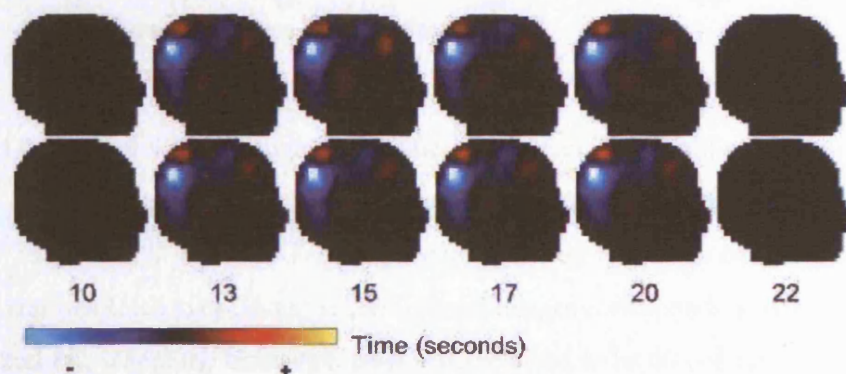


Figure 6.9: Sagittal view, through the middle of the head, of normalised reconstructed conductivity of perspex in a saline head-shaped tank where the stimulus was from 11 to 20s. Rows correspond to with (2nd row) and without (1st row) projecting onto the 1st PC

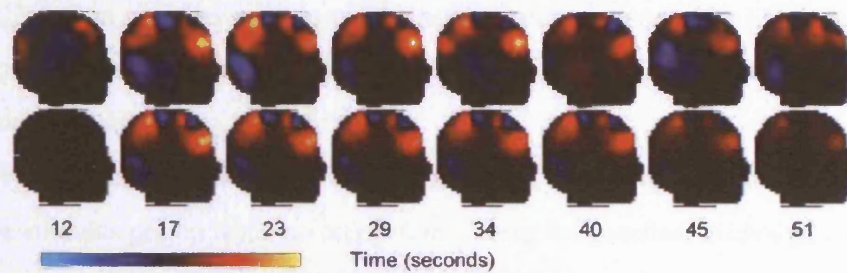


Figure 6.10: Sagittal view, through the middle of the head, of normalised reconstructed conductivity, for neonatal data set 1 (stimulus from 15 to 40s). Rows correspond to with (2nd row) and without (1st row) projecting onto the 1st PC

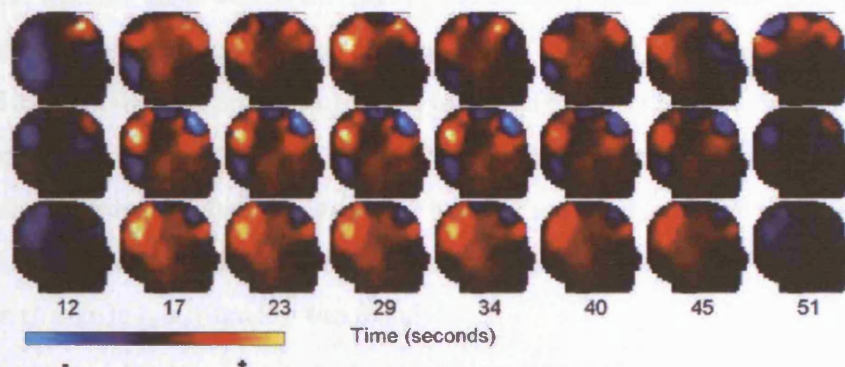


Figure 6.11: Sagittal view, through the middle of the head, of normalised reconstructed conductivity, for neonatal data set 2 (stimulus from 15 to 40s). Data has been reconstructed with Tikhonov and the GCV. First row are images corresponding to the raw data, where the truncation level was predicted to be 24 dof; second row are images corresponding to the data projected onto the 2nd PC, where the truncation level was predicted to be 60 dof since the SNR is now higher; and third row are images corresponding to the data projected onto the 2nd PC, reconstructed with a truncation level of 24 dof.

6.4 Discussion

The aim of this chapter was to improve the SNR of the data and reconstructed images by applying PCA and an optimum selection of the regularisation parameter for EIT of brain function on a saline head-shaped tank with Perspex as target and two neonatal data sets during visual stimulation paradigm.

Analysis of the covariance matrix in the saline tank data revealed high correlations in time during the stimulus period while no correlations during the baseline. Although correlations in channels existed, they were less obvious to identify; therefore, I computed only the PCs of the time covariance, and selected the first PCs that had a time response that best correlated with the stimulus paradigm.

The SNR of the first PCs compared to the SNR of the raw data increased by $25dB$ for tank data and 15 to $20dB$ for neonatal data; the first or the second PC decreased the noise significantly and yielded signals with less baseline noise and clearer responses during the stimulus and recovery periods. In both cases, an increase in conductivity was expected over the visual cortex, and such changes were apparent both in the uncorrected and corrected images; however, they were clearer in both cases after processing. There were also changes over the frontal lobes. It is unclear whether these were artefactual or due to unexpected additional changes in blood volume due to visual stimulation in the neonatal brain. The SNR of the reconstructed first PCs compared to the SNR of the reconstructed data increased by $35dB$ for tank data and 15 to $20dB$ for neonatal data. For neonatal data, improvement in image quality of the first or second PC was significant, reducing artefacts during the baseline and increasing the SNR of the highest change in the image. For tank data, for which the first PC represented the 99% of the data, no significant change in image quality was found.

In this work, I projected the data onto the first or second PC; as a consequence, I removed not only high frequency noise, but any PC whose signal did not have the expected time response paradigm, that is, baseline-stimulus-recovery-baseline. In general, one may project the data onto the first PCs, neglecting only higher PCs and including other changes given by secondary PCs. Nevertheless, selecting the second PC and neglecting other PCs, for one neonatal data set, changed image characteristics and improved the localisation and consistency of the highest change during the stimulus period, demonstrating the potential of imposing a priori knowledge about the time response to the PCs of the data.

In one case, I preferred the second to the first PC because while the first one corresponded to the largest variance of the data (the largest eigenvalue), it was high frequency noise that I aimed to eliminate from the data.

The methodology of this study aimed to impose the prior knowledge about the time response using the clear pattern of the time covariance, however, other ways of applying PCA are possible. I believe that using the channel covariance neglecting its last PCs would lead to similar results to neglecting the last PCs of the time covariance.

In this work, repetitions of experiments were averaged for obtaining a single experiment per subject. PCA has the potential for obtaining a single response instead of averaging; this has been previously applied for detecting a single EEG evoked response signal [87]. While averaging can be used for removing random noise, averaging several signals that are not random may distort the signal one is looking for. Besides, PCA can be used for detecting outliers in the data by looking at the last PCs of the data [84].

The advantages of this approach may be most clearly seen in the second neonatal data set where the stimulus related change in the raw data is obscured by noise. It is therefore somewhat surprising that the image quality is relatively good before the use of PCA. This is presumably because the chosen PC had the most relevant information of the image and the neglected PCs did not add relevant information. This raises the question as to whether the use of PCA on the raw data adds value or is a duplication of the effect of regularisation used for discarding uncorrelated noise in image reconstruction. In fact, it appears to add value, in that a larger number of singular values could be used for image reconstruction, and the eventual images contained less noise.

I have shown that analysing the time covariance matrix and its PCs provides a valuable technique for identification of different time responses in EIT of brain function. Furthermore, I demonstrated the feasibility of using time correlations to impose onto the PCs a priori knowledge about the time experimental paradigm. Thus, selecting the PCs that corresponded to the paradigm increased the SNR of the raw data and reconstructed images by at least fifteen decibels in all data sets; it also improved image quality where the effect was most significant for the noisiest neonatal data set and least significant for tank data. I therefore recommend reconstructing the principal components of the data together with an optimum selection of the regularisation parameter for linear EIT; besides, I also recommend to use PCA for obtaining a single response instead of averaging several experiments. The purpose of this work was to present the method and give some sample results. In future in my research group, we plan to use this approach to pre-process clinical data and establish its validity on larger clinical data sets.

Chapter 7

Validation of a finite element solution for an anisotropic medium

7.1 Introduction

It is well known that human tissues like bone, muscle, and brain white matter are anisotropic, and its modelling has been suggested for medical [54, 55] and geological [132] EIT; however, most applications have hitherto neglected anisotropy. Avoiding correction for anisotropy of both white matter and skull has been found to lead to errors of about 10% on the EEG forward solution and to be significantly relevant for inverse source localisation [182, 181], where the white matter anisotropic conductivity tensor was estimated from DTMRI [66][172, Chapter 5]. It seems plausible that modelling anisotropy is necessary to obtain an accurate forward solution for EIT of medical applications and that significant improvements in resulting image quality may result.

In an isotropic medium, Laplace's equation can be solved analytically for geometrically regular objects, for Neumann's boundary condition in a sphere using Green's functions [89], and for Dirichlet's boundary condition in an infinite plane by separation of variables [179]. EIT for geometrically complicated objects can be solved numerically using FEM with 3D-EIDORS [140]. The author is not aware of any published analytical solution for an anisotropic medium. A FEM solution that modified EIDORS to model anisotropic media has been presented [1].

An important concept when dealing with the conductivity tensor rather than with scalar conductivity is that the voltage $u(x)$ in the given domain Ω with conductivity $\sigma(x)$ is equal to a new voltage $\tilde{u}(\tilde{x})$ in the transformed domain $\tilde{\Omega}$ with a transformed conductivity $\tilde{\sigma}(\tilde{x})$, under a diffeomorphism Ψ , i.e. a smooth and invertible transformation $\Psi : \Omega \mapsto \tilde{\Omega}$, such that $\tilde{x} = \Psi(x)$, $\tilde{u}(\tilde{x}) = u(\Psi^{-1}(\tilde{x}))$, and $\tilde{\sigma}$ is given by

$$\tilde{\sigma}(\tilde{x}) = \left(\frac{\Psi' \sigma \Psi'^T}{|\det(\Psi')|} \right) (\Psi^{-1}(\tilde{x})), \quad (7.1)$$

where Ψ' is the Jacobian of the diffeomorphism Ψ defined as $\Psi' = \partial\tilde{x}/\partial x$. This can be shown by verifying that $S_{\tilde{\sigma}}(\tilde{u}, \tilde{v}) = S_{\sigma}(u, v)$ (3.9) holds for the above definition of $\tilde{\sigma}$ ¹.

The aim of this chapter is to expand and present a method for incorporation of anisotropy into a FEM forward solution originally presented in [1] and to validate this empirically. The convergence of the anisotropic FEM solution to an isotropic analytical solution was tested by applying a diffeomorphic transformation to the isotropic domain that converted it into an anisotropic one. The Dirichlet boundary value problem was assumed for simplicity where the starting domain was a cube with isotropic conductivity, for which an analytical solution can be obtained by separation of variables. Convergence was verified in two steps: first, by the equivalence of the FEM isotropic and anisotropic solutions, and then by the convergence of the isotropic FEM onto the analytical solution while increasing the mesh density. The results verified that the anisotropic FEM solution is accurate enough for modelling the forward problem in an anisotropic medium, which can be employed to study the influence of modelling anisotropy for EIT of the head, for which bone tissues like the skull and white matter are anisotropic.

7.2 Methods

7.2.1 Model

Let Ω be a homogeneous cubical domain of dimensions $-1 \leq x \leq 1$, $-1 \leq y \leq 1$, $0 \leq z \leq 2$, with isotropic conductivity $\sigma = \text{diag}(1, 1, 1)$. In this case, the generalized Laplace's equation (2.8) becomes Laplace's equation $[\partial_{xx} + \partial_{yy} + \partial_{zz}]u(x, y, z) = 0$. A Dirichlet boundary condition is assumed where the voltage is zero on the upper and side planes of the cube and one in the lower plane (Figure 7.1), that is,

$$u(\pm 1, y, z) = 0 \quad (7.2)$$

$$u(x, \pm 1, z) = 0 \quad (7.3)$$

$$u(x, y, 2) = 0 \quad (7.4)$$

$$u(x, y, 0) = 1, \quad |x| < 1, |y| < 1. \quad (7.5)$$

¹To remark that in this section the definition of Ψ i) is the inverse as the previous definition (3.4), and ii) does not fix the boundary. In fact, fixing the boundary leads to the non-injectivity of the forward problem (3.12), for anisotropic conductivity, and so this would also hold for that case; in this chapter, the emergence of anisotropy from a transformation seemed to be more comprehensible by transforming the whole domain than by fixing the boundary.

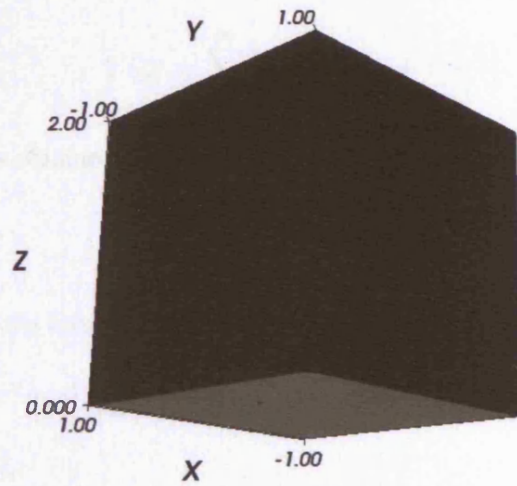


Figure 7.1: Imposed Dirichlet boundary condition: voltage $u = 1$ on the plane $z = 0$ for $|x| < 1, |y| < 1$ (grey), and $u = 0$ on the rest of the boundary (black), for the isotropic domain (mesh of 98843 elements).

7.2.2 Analytical solution

An analytical solution to the Dirichlet's value problem can be solved by separation of variables [179]

$$u(x, y, z) = X(x)Y(y)Z(z). \quad (7.6)$$

Thus, by substituting u in Laplace's equation for an isotropic medium and reordering

$$\frac{1}{X} \frac{d^2 X}{dx^2} = -\frac{1}{Y} \frac{d^2 Y}{dy^2} - \frac{1}{Z} \frac{d^2 Z}{dz^2} = -r^2, \quad (7.7)$$

where r is a constant. A solution to $X(x)$ can be expressed on the form

$$X(x) = A \cos(rx) + A' \sin(rx). \quad (7.8)$$

Since $u(\pm 1, y, z) = 0$ for all y and z , then $X(\pm 1) = 0$, leading to $A' = 0$ and $r = l\pi/2$, for $l = 1, 3, \dots$, which is equivalent to $r = (2\mu + 1)\pi/2$, for $\mu = 0, 1, \dots$. Therefore, the solution $X(x)$ is the linear combination

$$X(x) = \sum_{\mu=0}^{\infty} A_{\mu} \cos \left[(2\mu + 1) \frac{\pi x}{2} \right]. \quad (7.9)$$

Similarly for $Y(y)$, by reordering (7.7) for y

$$\frac{1}{Y} \frac{d^2 Y}{dy^2} = r^2 - \frac{1}{Z} \frac{d^2 Z}{dz^2} = -s^2, \quad (7.10)$$

and imposing boundary conditions $u(x, \pm 1, z) = 0$ for all x and z , then $Y(\pm 1) = 0$, leads to

$$Y(y) = \sum_{\nu=0}^{\infty} B_{\nu} \cos \left[(2\nu + 1) \frac{\pi y}{2} \right]. \quad (7.11)$$

A solution to $Z(z)$ is obtained by reordering (7.10) for z

$$\frac{1}{Z} \frac{d^2 Z}{dz^2} = r^2 + s^2 = t^2, \quad (7.12)$$

whose solution is of the form

$$Z(z) = C \exp(tz) + C' \exp(-tz), \quad (7.13)$$

where t is given by

$$t_{\mu\nu} = \frac{\pi}{2} \sqrt{(2\mu + 1)^2 + (2\nu + 1)^2}. \quad (7.14)$$

Applying the boundary conditions $u(x, y, 2) = 0$ and $u(x, y, 0) = 1$ for all x and y leads to

$$Z(z) = \frac{1}{1 - \exp(-4t_{\mu\nu})} (\exp(-t_{\mu\nu}z) - \exp(-t_{\mu\nu}(4 - z))) \quad (7.15)$$

The solution to Laplace's solution is written by combining the coefficients A_{μ} and B_{ν} with $D_{\mu\nu}$ as

$$u(x, y, z) = \sum_{\mu=0}^{\infty} \sum_{\nu=0}^{\infty} D_{\mu\nu} \cos \left[(2\mu + 1) \frac{\pi x}{2} \right] \cos \left[(2\nu + 1) \frac{\pi y}{2} \right] \quad (7.16)$$

$$\frac{1}{1 - \exp(-4t_{\mu\nu})} (\exp(-t_{\mu\nu}z) - \exp(-t_{\mu\nu}(4 - z))). \quad (7.17)$$

The coefficients $D_{\mu\nu}$ can be determined from the boundary condition $u(x, y, 0) = 1$,

$$u(x, y, 0) = \sum_{\mu=0}^{\infty} \sum_{\nu=0}^{\infty} D_{\mu\nu} \cos \left[(2\mu + 1) \frac{\pi x}{2} \right] \cos \left[(2\nu + 1) \frac{\pi y}{2} \right] = 1. \quad (7.18)$$

Finally, the potential u is given by

$$u(x, y, z) = \sum_{\mu=0}^{\infty} \sum_{\nu=0}^{\infty} \frac{16(-1)^{\mu}(-1)^{\nu}}{\pi^2(2\mu + 1)(2\nu + 1)} \cos \left[(2\mu + 1) \frac{\pi x}{2} \right] \cos \left[(2\nu + 1) \frac{\pi y}{2} \right] \frac{1}{1 - \exp(-4t_{\mu\nu})} (\exp(-t_{\mu\nu}z) - \exp(-t_{\mu\nu}(4 - z))). \quad (7.19)$$

7.2.3 Finite element solution

The weak formulation of the generalized Laplace's equation with a Dirichlet's boundary condition has zero current on the boundary, so the FEM formulation (8.1) becomes

$$\int_{\Omega} (\nabla \phi_i)^T \sigma \nabla u = \sum_j u_j \int_{\Omega} (\nabla \phi_i)^T \sigma \nabla \phi_j = 0, \quad (7.20)$$

which can be split into boundary $\partial\Omega$ and interior $\Omega \setminus \partial\Omega$ vertices,

$$\sum_{j \in \Omega \setminus \partial\Omega} u_j \int_{\Omega} (\nabla\phi_i)^T \sigma \nabla\phi_j = - \sum_{j \in \partial\Omega} u_j \int_{\Omega} (\nabla\phi_i)^T \sigma \nabla\phi_j. \quad (7.21)$$

It was computed as

$$Au = 0, \quad (7.22)$$

where A is the system matrix, computed using a modified version of 3D-EIDORS that models anisotropic objects without considering the electrode contact impedance [140, 1], and u is the potential on all vertices. Thus, by dividing the system matrix in blocks for the interior and exterior vertices

$$Au = \begin{pmatrix} A_{11} & A_{12} \\ A_{21} & A_{22} \end{pmatrix} \begin{pmatrix} u_{\Omega \setminus \partial\Omega} \\ u_{\partial\Omega} \end{pmatrix}. \quad (7.23)$$

Since $u_{\partial\Omega}$ are the boundary conditions, the interior potential was solved as

$$A_{11}u_{\Omega \setminus \partial\Omega} = -A_{12}u_{\partial\Omega}. \quad (7.24)$$

7.2.4 Convergence of the anisotropic FEM solution

7.2.4.1 Convergence of the analytical solution

For the computation of the analytical solution (7.19), one needs to select the maximum number of terms used to approximate an infinite series, given by $\mu\nu$ for the maximum number of μ and ν , which here is n . The convergence of the analytical solution was analysed by computing the difference between the analytical voltage (7.19) and the imposed boundary condition (7.5), on the plane $z = 0$ for $|x| < 1$ and $|y| < 1$, for which $u = 1$, as a function of the number of terms n . The rest of boundary conditions (7.2,7.3,7.4), for which $u = 0$, were clearly satisfied.

7.2.4.2 Comparison of isotropic and anisotropic FEM

The FEM solution $u^{\text{iso}}(x)$ in the isotropic domain Ω with conductivity σ , as given by 3D-EIDORS [140], was compared to the FEM solution $u^{\text{ani}}(\tilde{x})$ in the transformed domain $\tilde{\Omega}$ with conductivity $\tilde{\sigma}(\tilde{x})$ (7.1) by

$$e_i^{\text{ani}} = 100 \frac{|u_i^{\text{iso}}(x) - u_i^{\text{ani}}(\tilde{x})|}{|u_i^{\text{iso}}(x)|}, \quad \text{for } i = 1, \dots, n_I \quad (7.25)$$

where n_I is the number of interior vertices since in the FEM Dirichlet's boundary value problem the boundary potential is known (7.24).

A diffeomorphic transformation Ψ was applied to the domain Ω by mapping the mesh vertices onto a new mesh in $\tilde{\Omega}$. The same mesh was used for simplicity to test that 3D-EIDORS [140], and the modified version that models anisotropic objects [1], provided the same results;

they should agree as the mesh density is increased. Two nonlinear transformations of similar form differing only in the strength, which was measured by computing the determinant of the Jacobian of the transformation as a function of the domain, $|\det(\Psi')| = |\det(\tilde{\sigma})|$, were applied as:

$$\begin{cases} \tilde{x} = 1.2 \exp(x) + 0.7y + 0.4z \\ \tilde{y} = -0.2x + 1.5 \exp(y) + 0.3z \\ \tilde{z} = -0.3x - 0.2y + 1.2 \exp(z) \end{cases} \quad (7.26)$$

$$\begin{cases} \tilde{x} = 13.8 \exp(x) + 15.7y + 18.4z \\ \tilde{y} = -0.2x + 23.5 \exp(y) + 0.3z \\ \tilde{z} = -0.3x - 0.2y + 9.2 \exp(z) \end{cases} \quad (7.27)$$

The transformed conductivity $\tilde{\sigma}$ was computed elementwise by using (7.1) where Ψ' was calculated as follows. Let w be a vector in Ω , its transformed vector \tilde{w} in $\tilde{\Omega}$ is given by the push forward or Jacobian Ψ' as

$$\tilde{w} = \Psi' w. \quad (7.28)$$

In 3D, Ψ can be completely characterised by knowing the push forward of three independent vectors. Let $r_i = (x_i, y_i, z_i)^T$ be the coordinates of the four vertices of a tetrahedron Ω_k , for $i = 0, 1, 2, 3$, then taking r_0 as a reference, $W = [r_3 - r_0, r_2 - r_0, r_1 - r_0]$ is a 3-by-3 matrix whose columns are three independent vectors in Ω_k . Similarly, $\tilde{W} = [\tilde{r}_3 - \tilde{r}_0, \tilde{r}_2 - \tilde{r}_0, \tilde{r}_1 - \tilde{r}_0]$ is defined as a matrix whose columns are the transformed vectors in $\tilde{\Omega}_k$ where $\tilde{r}_i = (\tilde{x}_i, \tilde{y}_i, \tilde{z}_i)^T$. Thus, Ψ' was computed elementwise as

$$\dot{\Psi} = \tilde{W} W^{-1}. \quad (7.29)$$

7.2.4.3 Convergence of the FEM solution

Convergence of the FEM solution was studied by computing the discrepancy between the FEM and analytical solutions while increasing the mesh density. Two metrics were used for the comparison: the vertex relative error and the FEM error norm. Let u be the analytical solution and u^h the FEM solution, the percentage relative error was defined for each vertex as

$$e_i = 100 \left| \frac{u_i - u_i^h}{u_i} \right|. \quad (7.30)$$

The FEM error norm was approximated as

$$\|e\|_{\Omega} \simeq \left(\sum_{k=1}^N |e^{(k)}|^2 V_k \right)^{\frac{1}{2}}, \quad (7.31)$$

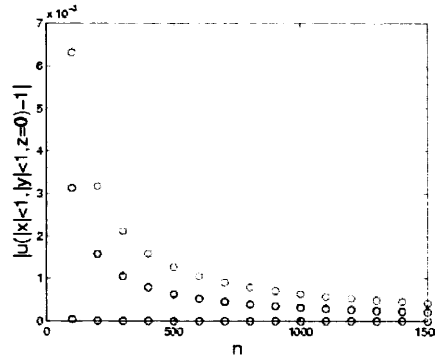


Figure 7.2: Convergence of the analytical solution (7.19), u , to the imposed boundary conditions $u(x, y, z) = 1$, for $z = 0$, $|x| < 1$, $|y| < 1$ (7.5), versus the maximum number of terms μ and ν equal to n used to approximate the infinite series, where the three different curves correspond to several points at the specified region of the boundary for a mesh of 384 elements.

where N is the number of tetrahedra, V_k is the tetrahedral volume, and $e^{(k)}$ is the absolute error of the k th-tetrahedral Ω_k computed as the vertex average

$$e^{(k)} = \frac{1}{4} \sum_{i \in \Omega_k} |u_i - u_i^h|. \quad (7.32)$$

Convergence was verified by studying the dependence of the FEM error on the element size h , which was given by the largest edge in the mesh; this reflects how much the FEM error decreased by consecutive refinement.

7.2.5 FEM mesh

The tetrahedral mesh for the FEM isotropic and anisotropic solutions comparison was generated using NETGEN (384 elements) [154]. For the comparison of the FEM with the analytical solution tetrahedral meshes of different mesh density were created by using Cubit (2001, Sandia Corporation, <http://cubit.sandia.gov/>).

7.3 Results

7.3.1 Convergence of the analytical solution

The analytical solution converged slowly to the imposed Dirichlet condition (7.5), on the plane $z = 0$ for $|x| < 1$ and $|y| < 1$, for which $u = 1$, because of the voltage jump from $u = 1$ to $u = 0$ for $|x| = 1$ and $|y| = 1$ (Figure 7.2). The difference was less than 0.01% for $n = 1000$, which was used for the rest of the analysis.

7.3.2 Comparison between the FEM isotropic and anisotropic solutions

The FEM anisotropic solution $u(\tilde{x})$ in the transformed domain $\tilde{\Omega}$ was verified to be equal (7.25), up to floating point accuracy, to the isotropic FEM solution $u(x)$ in Ω . The relative error is of

Table 7.1: FEM error norm $\% \|e\|_{\Omega}$ (7.31) by increasing the number of elements N , which yielded a relation $\|e\|_{\Omega} \propto h^{\alpha}$ (Figure 7.4), where h is the element size; and the maximum percentage relative vertex error $\max |e_i|$ (7.30).

N	$\% \max e_i $	$\ e\ _{\Omega}$	h
495	35.69	0.0326	0.88
2985	24.01	0.0228	0.52
8025	34.93	0.0170	0.37
13747	29.88	0.0135	0.32
35864	28.13	0.0099	0.26
55863	33.92	0.0087	0.24
98843	25.78	0.0060	0.21
353616	35.09	0.0051	0.14

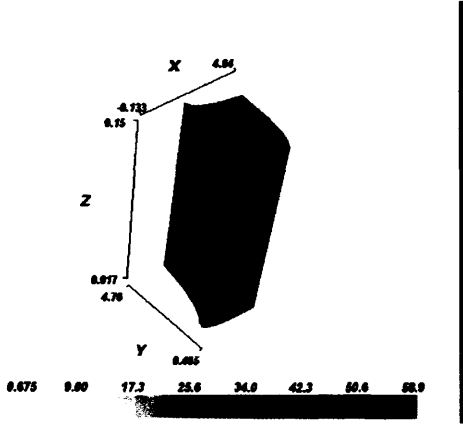
the order $10^{-13}\%$ for the nonlinear transformation (7.26) where errors were larger for those vertices for which the determinant of the Jacobian of the transformation $\det(\Psi')$ was larger (Figure 7.3(b)). Increasing the strength of the transformation (7.27), giving an increase of $\det(\Psi')$ of several orders of magnitude (Figure 7.3(c)) with respect to the previous one (Figure 7.3(a)), led to a relative error of the order $10^{-12}\%$ (Figure 7.3(d)).

7.3.3 Comparison of analytical and FEM solutions

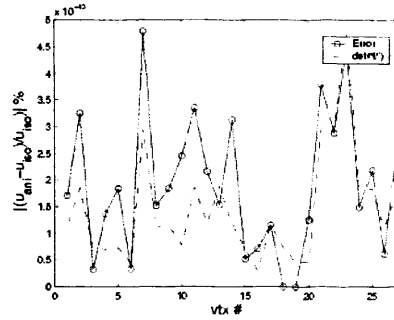
The FEM error norm $\|e\|_{\Omega}$ decreased proportionally to the element size h , as the number of elements increased, following the relation $\|e\|_{\Omega} \propto h^{\alpha}$, where α was between 0.22 and 0.99 (Table 7.1). A linear fit led to $\alpha = 1.1$ with $r = 0.98$ (Figure 7.4). The maximum percentage relative error at each vertex did not decrease, as the mesh density increased (Table 7.1), which may be due to the fact that the FEM solution cannot accurately model, for the given element size, the boundary conditions at the lower plane of the cube, at $z = 0$, where there is voltage jump from $u = 1$ to $u = 0$. However, the FEM error norm that measures the total error decreased linearly.

7.4 Discussion

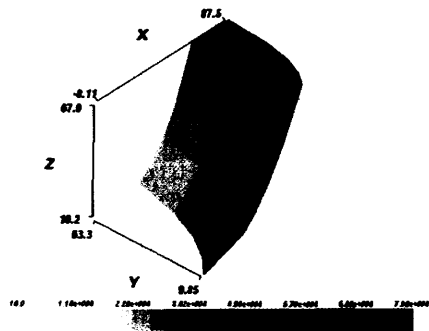
A method for an empirical validation of the FEM forward solution for the generalized Laplace's equation in an anisotropic medium has been presented. The convergence of the anisotropic FEM



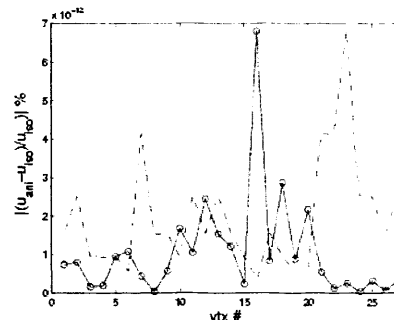
(a) Anisotropic domain given by the transformation (7.26)



(b) Relative voltage difference (7.25) for the interior vertices



(c) Anisotropic domain given by the transformation (7.27)



(d) Relative voltage difference (7.25) for the interior vertices

Figure 7.3: Percentage relative voltage difference e^{ani} (7.25), for the interior vertices, where $\text{vtx}\#$ is the number of interior vertices, between the FEM isotropic solution $u(x)$ in Ω for $\sigma = 1$, and the anisotropic FEM solution $u(\tilde{x})$ in the transformed domain $\tilde{\Omega}$ for $\tilde{\sigma}(\tilde{x}) = \hat{\Psi}\sigma(x)\hat{\Psi}^T / |\det(\hat{\Psi})|$ (7.1) under two nonlinear transformations given by a-b) (7.26), and c-d) (7.27), where $\det(\hat{\Psi})$ is the determinant of the Jacobian of the transformation (dash line, which was scaled as $|\det(\hat{\Psi})|(\max(e^{\text{ani}}) / \max(|\det(\hat{\Psi})|))$ to be plotted together with the relative error).

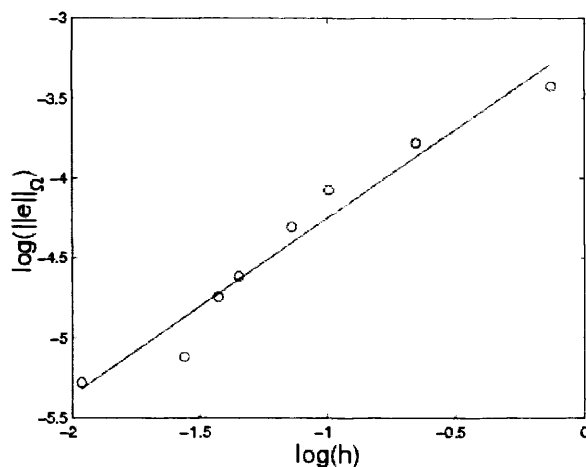


Figure 7.4: Loglog plot of the FEM error norm $\|e\|_{\Omega}$ (7.31) versus the element size h (the same as in table 7.1) and a linear fit $\|e\|_{\Omega} \propto h^{1.1}$ with correlation coefficient $r = 0.98$.

solution to an analytical solution was verified for the case of a homogeneous cube in terms of the relative vertex error and the FEM error norm. The isotropic solution in the given domain and the anisotropic solution in the transformed domain have been shown to be equivalent for a nonlinear transformation. The FEM error norm decreased proportionally to the tetrahedral size. On the contrary, the local relative vertex error did not decrease as the mesh density increased.

The goodness of the analytical solution was studied versus the number of basis functions in x and y used to approximate the infinite series. The error to fit the imposed boundary conditions was less than 0.01% when more than one thousand terms were employed. Since the number of terms in the series increases with the power of two of the number of basis functions, the analytical solution was approximated using one thousand basis functions. In addition, it presented a slow convergence because the imposed boundary conditions at $z = 0$ -plane had a voltage jump from one, in the interior of the plane, to zero, at the edges. The error of the analytical solution was significantly smaller than the error between the analytical and FEM solutions, so the analytical solution was accurate enough for testing the FEM solution.

The extension to the EIT problem from these results, that is, considering Neumann's boundary conditions together with the electrode contact impedance, can be done since in EIT formulation the conductivity tensor appears only in the main part of the system matrix, which has been tested here.

The convergence of the anisotropic FEM solution to the analytical solution was studied in two steps. First, the FEM solution in the isotropic domain was equal up to floating point accuracy to the anisotropic FEM solution in the transformed domain under a nonlinear transformation. Because the difference was larger for the more distorted elements and by increasing

the magnitude of the transformation, such that the determinant of the first derivatives of the transformation increased by several orders of magnitude, then the difference can be explained by the floating operations. Second, the FEM solution converged to the analytical solution with FEM error decreasing proportionally to the element size. However, the vertex error did not decrease accordingly, which could be due to the difficulty of the FEM solution to model the boundary conditions for the considered element sizes. From the decrease of the FEM error, it was concluded that the FEM solution converged to the analytical solution.

The results verified that the anisotropic FEM solution is accurate enough for modelling the forward problem in an anisotropic medium, which can be employed to study the influence of modelling anisotropy for EIT of the head, for which bone tissues like the skull and white matter are anisotropic.

Chapter 8

Recovery of the anisotropic conductivity tensor with known eigenvectors

8.1 Introduction

In this chapter, the interest is in the recovery of the anisotropic conductivity tensor in 3D. As it has been introduced earlier for an isotropic medium, the conductivity tensor can be represented as a scalar function multiplying the unit matrix (2.6). For the anisotropic case, it is represented by a 3-by-3 positive definite symmetric matrix with six independent values (2.7). Most important uniqueness results have been presented earlier (Section D.4.5). In brief, in an isotropic medium, with a known boundary and complete boundary data, one can uniquely recover a scalar conductivity [92, 93, 165]. However, in an anisotropic medium, the conductivity tensor has different representations in different coordinate systems. Therefore, given the boundary data, the conductivity tensor is uniquely defined only up to a diffeomorphic transformation (Appendix D.2); fixing the boundary selects one from an infinite number of possible diffeomorphisms [101]. Thus, while in the isotropic case there is one degree of freedom, which is uniquely defined by the boundary data, in the anisotropic case there are six degrees of freedom, for which it is necessary to select the diffeomorphism that fixes the coordinate system to uniquely define the conductivity tensor (Section D.4.5 and Appendix D.2).

Furthermore, uniqueness can be obtained by imposing a constraint onto the anisotropic conductivity tensor that determines the diffeomorphism. Uniqueness holds under these constraints: recovery of one eigenvalue [92, 93], that is, when eigenvectors and two eigenvalues are known and one aims to recover an unknown eigenvalue; multiple scalar to the tensor when eigenvectors and eigenvalue ratios are known and one aims to recover a multiple scalar [104]; and multiple function to the tensor [2, 48]. It has been suggested that providing information about eigenvectors, which, for example, in medical applications could be obtained from a structural imaging modality, and eigenvalues, could uniquely define the conductivity tensor [104]. In

addition, the existence of local orthogonal coordinates on 3D Riemannian manifolds (Appendix D.1) provides a natural coordinate system for which the metric is diagonal in all points of the manifold [36], and so the metric can be diagonalised by providing the right local coordinate system.

The finite element formulation for piecewise linear voltage and constant conductivity of the EIT forward problem is equivalent to the resistor network problem (Section 2.2.3), for which the conductance for resistors placed on the mesh edges can be expressed in terms of the element conductivity; in this case, the number of degrees of freedom in the forward problem is given by the number of edges that connect every two nodes, the node connectivity [106, 37, 35, 100]. A numerical study of the non-uniqueness for the finite element case suggested that fixing the mesh selected an arbitrary local coordinate system, fixing the extra degrees of freedom, which would lead to a unique meaningless solution in a fixed mesh; yet fixing the mesh did not fix the six degrees of freedom per element, which may have been due to the fact that, even for a fixed mesh, the mesh structure contains information that is not arbitrary, and so it may not specify all the information; it was found that one could recover between one and three times the number of elements [1].

An important usable constraint for EIT of medical applications is when the eigenvectors are known. The anisotropic structure of tissues like muscle, bone, and brain white matter can be approximated from a structural imaging modality or estimated directly from DT-MRI [172]. The eigenvalues, which are the conductivity along three orthogonal directions, are still unknown. Nonetheless, there is, to my knowledge, no theoretical proof of the uniqueness for this constraint.

The purpose of this chapter was to verify uniqueness for the recovery of a piecewise linear conductivity tensor with known eigenvectors from the complete NtoD data, that is, all possible boundary data, using a numerical approach. This was done in two steps, first, by studying the rank of the Jacobian, from which one could infer that the constrained problem is well conditioned, and second, by testing the convergence of the constrained inverse problem for several conductivity distribution simulations. The rank of the Jacobian for both linear conductivity and constant conductivity was computed; for linear conductivity, to verify that the Jacobian of the proposed constraint was well conditioned; for constant conductivity, to verify that the rank of the Jacobian for the discrete case is given by the number of edges in the finite element mesh. The linear conductivity tensor was nodal based and spanned by shape functions. Tensor distributions were simulated including diagonal and general tensors with two subgoals i) the recovery of smooth eigenvalues for a diagonal tensor that suggested theoretical unique-

ness, and ii) the recovery of eigenvalues for a piecewise smooth general tensor distribution that resembled physiological tissue like skull or brain white matter. Simulations included tensors whose eigenvectors and eigenvalues varied smoothly throughout the domain and a DTI sample of brain white matter. The inversion was performed by implementing a quasi-Newton method with linear search.

8.2 Methods

8.2.1 Forward solution

The forward problem in this chapter was given by the weak formulation of the generalized Laplace's equation (2.16) with Neumann boundary condition (2.9),

$$\sum_j u_j \int_{\Omega} (\nabla \phi_i)^T \sigma \nabla \phi_j = \int_{\partial\Omega} \phi_i \nu^T J, \quad (8.1)$$

where u is the voltage solution in a 3D domain Ω with conductivity σ , ν is the unit outwards normal to the domain surface $\partial\Omega$, J is the current density, and ϕ are linear shape functions (2.19).

8.2.1.1 Basis functions

Let ϕ_i be the shape function at the i th-node, with $i = 1, \dots, n$ where n is the number of nodes, (ϕ_1, \dots, ϕ_n) were used as the basis functions for both the voltage and the conductivity. In this basis, the voltage is

$$u = \sum_{j=1}^n u_j \phi_j, \quad (8.2)$$

and the conductivity tensor is

$$\sigma = \sum_{i=1}^n \sigma_i \phi_i, \quad (8.3)$$

so then both the voltage and conductivity are piecewise linear ¹.

For every point (x, y, z) in Ω , where σ is equivalent to a Riemannian metric in a manifold (section D.4.5), being represented by a 3-by-3 positive definite symmetric matrix in some coordinates, there is always an orthonormal transformation from the given coordinate system to a diagonal matrix [36]. Defining the local coordinate system by the tensor eigenvectors, σ can be represented as a diagonal matrix D in the local coordinate system (sections D.4.2 and A.2.1)

$$\sigma = V D V^T, \quad (8.4)$$

where $V = [v_1, v_2, v_3]$ is a matrix of orthonormal eigenvectors v_i and $D = \text{diag}(d_i)$ is a matrix of real positive eigenvalues. In the local coordinate system, the eigenvector corresponding to

¹In the rest of the thesis the conductivity is considered as piecewise constant; in this chapter, it is piecewise linear except in the rank analysis section where both of them are considered.

the largest eigenvalue defines the preferred direction of current flow. By providing the tensor eigenvectors at each node position r_i , the conductivity is spanned as

$$\sigma(x, y, z) = \sum_{i=1}^n \sigma(r_i) \phi_i = \sum_{i=1}^n \left(\sum_{j=1}^3 v_j(r_i) d_j(r_i) v_j^T(r_i) \right) \phi_i. \quad (8.5)$$

In some special cases, the tensor eigenvectors were aligned with the axis, which led to diagonal conductivity tensors

$$\sigma(x, y, z) = \sum_{i=1}^n \text{diag} (d_1(r_i), d_2(r_i), d_3(r_i)) \phi_i. \quad (8.6)$$

Hence, tensor distributions were simulated by providing eigenvectors and eigenvalues, $(d_1(r_i), d_2(r_i), d_3(r_i)) = (f_1(r_i), f_2(r_i), f_3(r_i))$, at each node r_i where f_i are some smooth spatial distributions.

Basis functions for injections and measurement patterns were the vectors $e_i \in \mathbb{R}^N$ perpendicular to ones (Figure 8.1(a)), since the Kernel of the NtoD map is a vector of constant elements (p. 67),

$$\begin{aligned} e_1 &= \left(1, \frac{-1}{N-1}, \dots, \frac{-1}{N-1} \right) \\ &\dots \\ e_N &= \left(\frac{-1}{N-1}, \dots, \frac{-1}{N-1}, 1 \right), \end{aligned} \quad (8.7)$$

where N is the number of boundary nodes, satisfying (2.12) for each injection. Thus, N current injections and N measurements for each injection yields N^2 boundary data. This provides the complete NtD map, that is, the current is injected and the voltage is measured everywhere on the surface.

8.2.1.2 System matrix

The system matrix for piecewise linear shape functions whose gradients $\partial_l \phi_i^{(k)}$ are constant in an element Ω_k and conductivities given by (8.3), was calculated as

$$\begin{aligned} S_{ij} &= \int_{\Omega} dr \partial_l \phi_i \sigma_{lm} \partial_m \phi_j = \\ &\sum_{k \in \text{supp}(i) \cap \text{supp}(j)} \partial_l \phi_i^{(k)} \left[\int_{\Omega_k} dr \sigma_{lm} \right] \partial_m \phi_j^{(k)} = \\ &\sum_{k \in \text{supp}(i) \cap \text{supp}(j)} \partial_l \phi_i^{(k)} \left[\int_{\Omega_k} dr \sum_{s=1}^4 \sigma_{lm}^{s(k)} \phi_s \right] \partial_m \phi_j^{(k)} = \\ &\sum_{k \in \text{supp}(i) \cap \text{supp}(j)} \partial_l \phi_i^{(k)} V_k \left[\frac{1}{4} \sum_{s=1}^4 \sigma_{lm}^{s(k)} \right] \partial_m \phi_j^{(k)} = \\ &\sum_{k \in \text{supp}(i) \cap \text{supp}(j)} V_k \sum_{l,m} \partial_l \phi_i^{(k)} \bar{\sigma}_{lm}^{(k)} \partial_m \phi_j^{(k)}, \end{aligned} \quad (8.8)$$

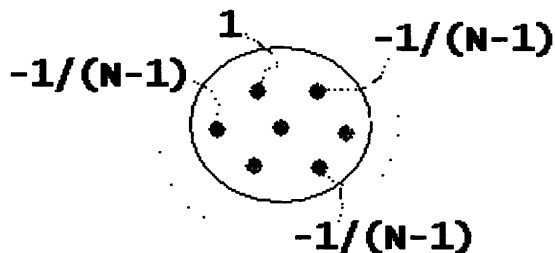


Figure 8.1: Representation of a current injection by a vector with value 1 at a given node and value $-1/(N - 1)$ at the rest of nodes, on the boundary, that is, $e_i = (-1/(N - 1), \dots, 1, \dots, -1/(N - 1))$, where N is the number of exterior nodes.

where $\text{supp}(i) \cap \text{supp}(j)$ is the support of the edge (i, j) , $\bar{\sigma}_{lm}^{(k)}$ is the average of the nodal values of the k th-element, and the integral of a shape function over an element is

$$\int_{\Omega_k} \phi_s = \frac{V_k}{4}, \quad (8.9)$$

where V_k is the volume of the k th-element. In EIDORS, the shape function gradients are computed in the reference element.

8.2.1.3 Uniqueness of the FP

Uniqueness needs to be imposed to the FP (p. 59); it was done as

$$\int_{\Omega} u = \sum_j u_j \int_{\Omega} \phi_j = \sum_j u_j \underbrace{\sum_{k \in \text{supp}(j)} \frac{V_k}{4}}_{C_j} = 0. \quad (8.10)$$

Thus, the FP was solved as

$$\begin{pmatrix} S \\ C_{1 \times n} \end{pmatrix} U = \begin{pmatrix} I \\ 0_{1 \times n} \end{pmatrix}, \quad (8.11)$$

where $U, I \in \mathbb{R}^{n \times N}$ for N current injections, $I = [I^{\partial\Omega^\perp} I^{\partial\Omega}]$ where $\partial\Omega$ is the boundary and $\partial\Omega^\perp$ is the interior, such that $I^{\partial\Omega^\perp} = 0$ and $I^{\partial\Omega} = [e_1, \dots, e_N]$, with n nodes and N exterior nodes.

8.2.1.4 Measurements

Let $U \in \mathbb{R}^{n \times N}$ be the forward solution, $U = [u_1, \dots, u_N]$, where u_i is the solution corresponding to the i th-current injection that can be separated in interior and boundary voltages as

$u_i = [u_i^{\partial\Omega^\perp}, u_i^{\partial\Omega}]$, then the N measurements for this injection in the basis (8.7) were computed as

$$\begin{aligned}\Lambda_{i1} &= \langle e_1, u_i^{\partial\Omega} \rangle \\ \Lambda_{i2} &= \langle e_2, u_i^{\partial\Omega} \rangle \\ &\dots \\ \Lambda_{iN} &= \langle e_N, u_i^{\partial\Omega} \rangle,\end{aligned}\tag{8.12}$$

where $i = 1, \dots, N$. Thus, the NtD map² is a map of the i th-current e_i into the (i,j) th-measurement Λ_{ij} as

$$e_i \mapsto \Lambda_{ij},\tag{8.13}$$

where $j = 1, \dots, N$.

8.2.2 Sensitivity matrix

The Jacobian was computed both by finite differences and by the product of measurement and current fields based on the derivation of the Jacobian for isotropic conductivity (3.13) [140]. Jacobians have been implemented with respect to the diagonal elements for a diagonal tensor and with respect to the eigenvalues for a general tensor.

8.2.2.1 By finite differences

The sensitivity of the measurement Λ_{ij} to a change of conductivity at the s th-node, σ_{ll}^s , was computed as

$$\frac{\partial\Lambda_{ij}}{\partial\sigma_{ll}^s} = \frac{\Lambda_{ij}(\sigma_{ll}^s + \Delta\sigma_{ll}^s) - \Lambda_{ij}(\sigma_{ll}^s)}{\Delta\sigma_{ll}^s},\tag{8.14}$$

where the conductivity increment was

$$\Delta\sigma_{ll}^s = \max(|\sigma_{ll}|)\sqrt{\text{eps}},\tag{8.15}$$

and eps was the floating point accuracy. In fact, σ_{ll}^s represents the diagonal elements for a diagonal tensor or the eigenvalues for a general tensor.

8.2.2.2 By product of measurements and current fields

The injection fields for the i th-current injection e_i were obtained by solving the forward problem $Su_i = e_i$, and the measurement fields were obtained by solving the forward problem $Su_j^* = e_j$ where e_j was the fictitious current corresponding to the j th-measurement.

For diagonal tensors, it was computed column by column where each column represented a nodal conductivity tensor coefficient. Let s be the s th-node and lm be the tensor coefficient

²Here, Λ represents the matrix or vector of boundary data for the NtoD map, while everywhere else in the thesis, Λ represents the DtoN map itself (section 3.1.1).

indices³, the sensitivity matrix integrated over the support of the s vertex was calculated as

$$\begin{aligned} \frac{\partial \Lambda_{ij}}{\partial \sigma_{lm}^s} &= - \int_{\Omega} dr \partial_l u_i \phi_s(r) \partial_m u_j^* = \\ &- \sum_{k \in \text{supp}(\phi_s)} \partial_l u_i^{(k)} \left(\int_{\Omega_k} dr \phi_s \right) \partial_m u_j^{*(k)} = \\ &- \sum_{k \in \text{supp}(\phi_s)} \frac{V_k}{4} \partial_l u_i^{(k)} \partial_m u_j^{*(k)}, \end{aligned} \quad (8.16)$$

where for each measurement (i, j) , the Jacobian with respect to the three diagonal entries at a given node was computed as $\hat{J}Q$ where $\hat{J} \in \mathbb{R}^{3 \times p}$ was given by $\hat{J} = [\hat{J}^{(1)}, \dots, \hat{J}^{(p)}]$ with $\hat{J}^{(k)} = -\frac{V_k}{4} \partial_l u_i^{(k)} \partial_l u_j^{*(k)}$ and p is the number of elements, and $Q \in \mathbb{R}^{p \times n}$ is a matrix that contains an entry one if an element contains a node and zero otherwise. In fact, \hat{J} is an elementwise Jacobian column and Q accounts for the nodal support yielding a nodal based Jacobian.

For a general tensor, by using the eigenvalue decomposition $\sigma = VDV^T$, the sensitivity matrix for each diagonal coefficient $D_{rr}^{(s)}$, where $r = 1, 2, 3$, at the s th-node, was given by

$$\begin{aligned} \frac{\partial \Lambda_{ij}}{\partial D_{rr}^{(s)}} &= - \int_{\Omega} \phi_s(r) \partial_l u_i V_{lr}^{(s)} V_{rm}^{(s)} \partial_m u_j^* = \\ &- \sum_{k \in \text{supp}(\phi_s)} \left(\int_{\Omega_k} dr \phi_s \right) \partial_l u_i^{(k)} V_{lr}^{(s)} V_{rm}^{(s)} \partial_m u_j^{*(k)} = \\ &- \sum_{k \in \text{supp}(\phi_s)} \frac{V_k}{4} (\nabla u_i^{(k)})^T (v_r v_r^T)^{(s)} (\nabla u_j^{*(k)}), \end{aligned} \quad (8.17)$$

where for each measurement (i, j) , it was computed by summing explicitly over all element contributions Ω_k for $r = 1, 2, 3$. Because the computational time for calculating the direct Jacobian for general tensors (8.17) was larger than the equivalent FD Jacobian, the latter was used for the simulations.

8.2.3 Finite element mesh

The finite element meshes used were spheres (148,309, and 807 elements) and cubes (495 elements); they were created with NETGEN [154].

8.2.4 Rank analysis

The study of the rank of the Jacobian aimed to test the numerical uniqueness in terms of having a well conditioned map between the conductivity and the boundary data. If the Jacobian was full-rank, then it was concluded that the data uniquely determined the unknowns and so the inverse reconstruction would be well defined. Full-rank was understood (section A.2.3) when

³The Jacobian was derived as the sensitivity of the measurements with respect to all tensor coefficients, yet only the diagonal elements σ_{ll} are needed.

the Jacobian singular values decayed smoothly and were not zero, where zero was defined when the i th-SV, s_i , was five orders of magnitude smaller than the first, that is,

$$\frac{s_i}{s_1} \leq 10^{-5}. \quad (8.18)$$

A second goal was to verify the hypothesis about the rank of the Jacobian for piecewise constant conductivity that says that the rank of the Jacobian is given by the nodal connectivity in the finite element mesh. As explained in Appendix D.4.5 (p. 237), the conductivity tensor can be recovered in a two step approach, first, by recovering the abstract manifold structure, and, second, by selecting the coordinate system. It is known that there is an arbitrary selection of coordinate systems; here the aim was to verify that the abstract manifold is given by the finite element nodal connectivity such that this number gives the maximum number of unknowns that one can recover, for piecewise constant conductivity. Besides, by constraining the eigenvectors for piecewise linear conductivity, the aim was to show that the number of unknowns for the proposed constraint is less than the mesh connectivity, given by the rank of the Jacobian for piecewise constant conductivity.

The idea is based on the equivalence between a finite element mesh and a resistor network, from which replacing edges by resistors and solving the equivalent resistor mesh, the system matrix is equivalent to the FE one (section 2.2.3) [106]. The nonzeros in the system matrix are given by the nodal connectivity where entries are zero only if nodes are not connected or in the case of a specific mesh, for example, with normal angles, for which the resistors conductance can be zero (Figure 8.2). Because of symmetry, one cannot expect to recover more unknowns than the number of nonzeros in the upper triangular submatrix of the system matrix, then the rank of the Jacobian is

$$\text{rank}(J) = \frac{\text{nz}(S) - n}{2}, \quad (8.19)$$

where $\text{nz}(S)$ is the number of nonzeros in the system matrix and n is the number of vertices, which accounts for the diagonal elements.

To test this hypothesis, the rank of two Jacobians was computed: a) with respect to the eigenvalues for piecewise linear conductivity (8.16,8.17), and b) with respect to the six independent tensor coefficients for piecewise constant conductivity given in [1]. The case a) aimed to verify that the Jacobian was full rank and so the constrained numerical inverse problem proposed here was well conditioned. The case b) aimed to estimate the mesh connectivity, that is, the maximum number of unknowns that are determined by the data, since the Jacobian with respect to the six tensor coefficients was expected to be rank deficient. It was done for a spherical and a cubical mesh.

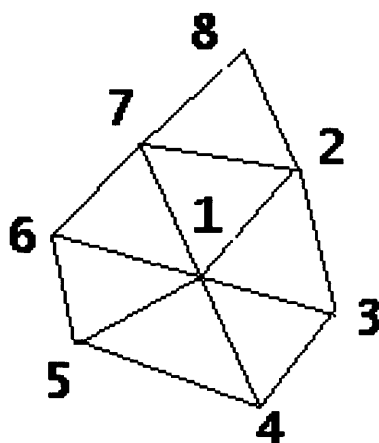


Figure 8.2: Mesh connectivity, in 2D, such that the system matrix is zero when nodes are not connected, that is, in this example the nonzero entries for node one are two to seven but not eight.

In a), the conductivity was a diagonal matrix with sinusoidal functions. In b), the conductivity was a constant general tensor in the domain defined elementwise equal to

$$\sigma = \begin{pmatrix} 1.1 & 0.1 & 0.2 \\ 0.1 & 1.2 & 0.3 \\ 0.2 & 0.3 & 1.3 \end{pmatrix}. \quad (8.20)$$

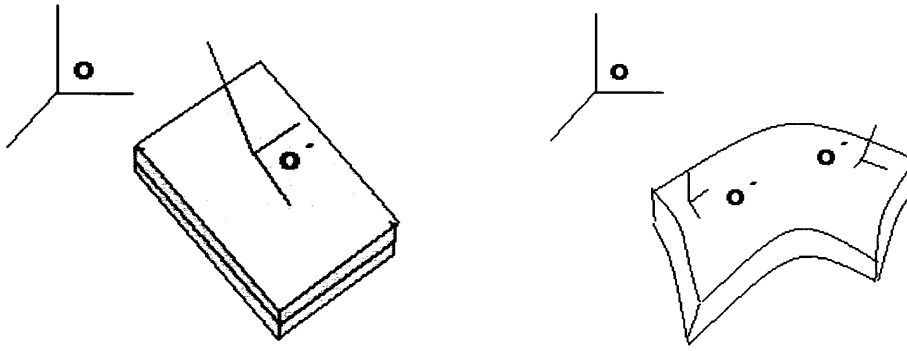
8.2.5 Simulated tensor distributions

Tensor distributions were simulated to test the feasibility of recovering piecewise linear eigenvalue distributions with known eigenvectors. In the simplest case, the tensor was diagonal

$$\sigma(x, y, z) = \text{diag}(d_x(x, y, z), d_y(x, y, z), d_z(x, y, z)), \quad (8.21)$$

where d_i provided the magnitude of the conductivity along each of the Cartesian axes. The assumption of a diagonal tensor is valid in 3D continuously differentiable Riemannian manifolds where there exist a local choice of orthogonal coordinates for which the Riemannian metric, equivalent to the conductivity (D.4.5), is diagonal [36]. Hence, given a general conductivity tensor there exists a diffeomorphism that transforms the metric to a diagonal matrix in the local coordinates. Let D be the diagonal conductivity tensor in local coordinates, there is a diffeomorphism Ψ that maps the global basis vectors $\{e_1, e_2, e_3\}$ into the local basis vectors $\{v_1, v_2, v_3\}$, such that the conductivity in global coordinates is given by

$$\sigma(x, y, z) = V(x, y, z)D(x, y, z)V^T(x, y, z), \quad (8.22)$$



(a) Eigenvectors that were equal for the whole domain

(b) Eigenvectors that changed throughout the domain

Figure 8.3: Example of two anisotropic domains, whose anisotropic structure is given at each point by the three orthonormal eigenvectors that form a local coordinate system \acute{O} whose axes did not coincide with axes in the global coordinate system O , where eigenvectors a) eigenvectors were constant in the domain, b) changed throughout the domain.

where V is the Jacobian of Ψ given by

$$V = [v_1, v_2, v_3]. \quad (8.23)$$

In fact, this is equivalent to the SVD of a matrix σ where V is the matrix of eigenvectors and D is the matrix of eigenvalues (sections D.4.2 and A.2.1)

$$D(x, y, z) = \text{diag}(d_1(x, y, z), d_2(x, y, z), d_3(x, y, z)). \quad (8.24)$$

General tensors were simulated using the eigenvalue decomposition (8.22) that allowed initialising them based on knowledge of the material structure, that is, eigenvectors v_i indicated the preferred directions of current flow, and eigenvalues d_i provided their magnitudes. Diagonal tensors were a simplification where eigenvectors coincide with the axes, yet, in general, eigenvectors had an orientation that did not coincide with the axes (Figure 8.3(a)), and $V = V(x, y, z)$ and $D = D(x, y, z)$ were a function of space and changed orientation throughout the domain (Figure 8.3(b)).

While eigenvectors provide the orientation, eigenvalues determine the shape of the physiological tissue by favouring one specific direction or plane. This leads to two basic structures, prolate and oblate (Figure 8.4(a)). In the prolate case, a dominant direction is described by a larger specific eigenvalue that determined a fibre type structure. In the oblate case, two equally dominant directions, with similar eigenvalues, defined a layered structure, where a third eigenvector is penalised by a lower eigenvalue.

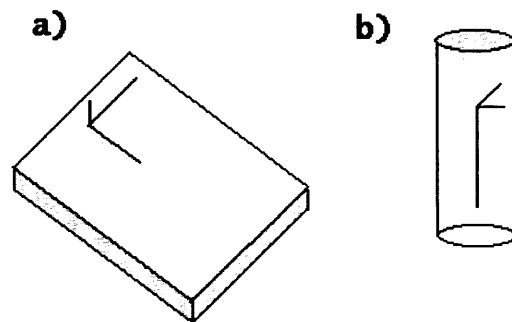


Figure 8.4: Main biological eigenvector orientation: a) oblate, of flattened structure like bone tissue; b) prolate, resembling fibre structure like brain white matter.

Several tensor distributions were simulated in terms of eigenvector orientation and eigenvalue distributions type. Eigenvectors were defined, at each node of the domain, using concepts of differential geometry that allowed description of three orthonormal vectors based on the velocity and normal vectors to a 3D curve (section D.3). Given the eigenvectors, at each point of the domain, eigenvalues determined two type of anisotropic structure: i) by assigning the velocity vector of a curve as the eigenvector with largest eigenvalue, and a plane perpendicular to the curve as the two eigenvectors with lowest eigenvalue, similar to a bunch of fibres (prolate case); ii) by assigning a surface changing throughout the domain as two eigenvectors with dominant eigenvalues, and a perpendicular vector to the plane as an eigenvector with smallest eigenvalue, similar to a layered structure (oblate case).

So far, only one tensor has been contemplated, however, real tissue comprises of a continuous mix of different tissue types, which can be modelled by a weighted sum of two different tensors accounting for an anisotropic structure with some extension that smoothly overlaps into the isotropic parts of the domain. This ideas have been applied for building phantoms resembling white matter fibre to test methods for the reconstruction of the diffusion tensor [102].

The last model was a diffusion tensor sample estimated from a DT-MRI sample of brain white matter.

In summary, there were five goals for the diverse tensor simulations: recovery of constant eigenvalues, to test the numerics; recovery of smooth eigenvalues for a diagonal tensor, to test the numerical convergence of the proposed constraint; recovery of eigenvalues for a general tensor, to test the feasibility for models resembling physiological structure; recovery of eigenvalues for a mix of two tensors, to test a more realistic case; recovery of eigenvalues of an

estimated DT of brain white matter, to test for realistic human tensor structure (Table 8.1).

In terms of the eigenvector orientation type there were six types: axial, spherical, polynomial, helical, mix of two different tensors, and the diffusion tensor, which were labelled as Model 1-6 (Table below).

Model label	Eigenvector orientation
Model 1	axial
Model 2	spherical
Model 3	polynomial
Model 4	helical
Model 5	mix of two tensors
Model 6	diffusion tensor (DT)

In terms of eigenvalue distribution type, five different types were simulated: constant, linear, sinusoidal, exponential, and smooth mix of two tensors, which were labelled as Model A-D (Table below).

Model label	Eigenvalue distribution
Model A	constant
Model B	linear
Model C	sinusoidal
Model D	exponential
Model E	mix of two tensors

Because of the diverse type of distributions, simulation labels and details are specified as the simulation number, model ID, objective of the simulation, eigenvector and eigenvalue type, geometry, and mesh; they are separated regarding their objective (Table 8.1).

Simulated eigenvalue distributions were intended to be recovered at the reconstruction stage, and so it was required to provide an initial estimate as a first step for the inversion. Below, eigenvectors and eigenvalue distribution and estimates for the simulated models are specified.

8.2.5.1 Model 1: axially orientated eigenvectors

In the case when the eigenvectors are orientated with the axis, $V = [e_1, e_2, e_3] = \mathbb{I}_{3 \times 3}$, then

$$\sigma = D = \text{diag}(d_1, d_2, d_3), \quad (8.25)$$

where $d_i = d_i(x, y, z)$ in general. Several smooth eigenvalue distributions d_i were simulated:

Table 8.1: Summary of simulations. Simulations are grouped regarding their purpose, the eigenvector (eigvec.) orientation and eigenvalue distribution type (eigvals.); they are labelled to be easily found in the text. Also the geometry (geom.) and number of elements of the mesh are given.

Model	Aim	Eigvec.	Eigval.	Geom.	Mesh
1A	constant	axis	constant	cube	495
1B	smooth eigvals.	axis	linear	sphere	807
1C	smooth eigvals.	axis	sinusoidal	sphere	807
2A	gen. eigvec.	spherical	constant	sphere	148
2D	gen. eigvec	spherical	exponential	sphere	148
2D	gen. eigvec.	spherical	exponential	sphere	309
3A	gen. eigvec.	polynomial	constant	cube	495
5 (1A & 3A)	mix two tensors	-	-	cube	495
5 (1B & 4)	mix two tensors	-	-	sphere	309
6	DTI	-	-	cube	495

- **Model 1A:** A constant distribution throughout the domain

$$\sigma = \text{diag}(\sqrt{3}, 1/\sqrt{3}, 1/\sqrt{3}) \quad \text{for all } x, y, z. \quad (8.26)$$

In this case, it resembled fibre type structure aligned with the x-axis favouring current flow in that direction, in a cubical domain (Figure 8.5). The conductivity estimate was $\sigma_{estimate} = \text{diag}(1, 1, 1)$.

- **Model 1B:** A linear distribution

$$\sigma = \text{diag}(3 + x + y + z, 3.2 + x + y + z, 3 + 1.2x + 1.4y + 0.8z). \quad (8.27)$$

In this case, these three linear functions were simulated in a spherical domain (Figures 8.14(a), 8.14(c), 8.14(e)). The conductivity estimate was $\sigma_{estimate} = \text{diag}(3, 3, 3)$.

- **Model 1C:** A sinusoidal distribution

$$\sigma = \text{diag}(3 + \cos(\pi x) + \cos(\pi y) + \cos(\pi z), 3, 3). \quad (8.28)$$

In this case, a sinusoidal function was simulated in a spherical domain (Figures 8.15(a), 8.15(c)). The conductivity estimate was $\sigma_{estimate} = \text{diag}(3, 3, 3)$.

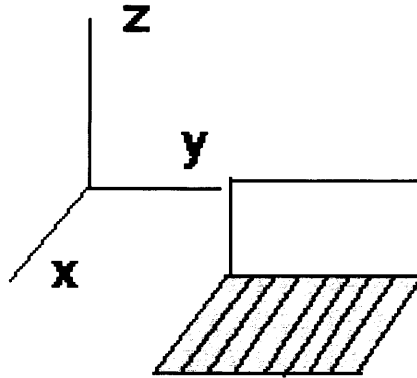


Figure 8.5: Model 1A: anisotropy structure with eigenvectors aligned with the axes in the given global coordinates such that conductivity is favoured in the x-direction resembling a fibre type material aligned with the x-axis. Since eigenvectors coincide with the axes, the conductivity tensor is diagonal, where diagonal elements weight the conductivity along each axis; the simulated conductivity was $\sigma = \text{diag}(\sqrt{3}, 1/\sqrt{3}, 1/\sqrt{3})$, constant in a cubical domain.

8.2.5.2 Model 2: Spherically orientated eigenvectors

Given the change of coordinates $\tilde{x} \mapsto x$ where $\tilde{x} = (\theta, \phi, r)$ are the local spherical coordinates, eigenvectors were defined as the local basis vectors $V = [e_\theta, e_\phi, e_r]$. Similarly, the same result is obtained by assuming a spherical surface of radius r , at each point (x, y, z) , such that each radius defined a spherical plane that can be represented by the two velocity vectors $v_1 = v_\theta$ and $v_2 = v_\phi$ tangential to the surface at the given point (section D.3), and the third eigenvector $v_3 = \nabla f$ is perpendicular to the surface $f = x^2 + y^2 + z^2$. The eigenvectors $V = V(\theta, \phi, r)$, where $\theta = \arctan(y/x)$ and $\phi = \arccos(z/r)$ were defined at each node as

$$\begin{aligned} v_1 &= (\cos \theta \cos \phi, \cos \theta \sin \phi, -\sin \theta)^T \\ v_2 &= (-\sin \theta \sin \phi, \sin \theta \cos \phi, 0)^T \\ v_3 &= (x, y, z)^T \end{aligned} \tag{8.29}$$

where v_i were normalised. In fact, this model presented a singularity in the center of the domain, $r = 0$ and $x = 0$ that was avoided because there was not a vertex at $(0, 0, 0)$. Thus, eigenvectors (v_θ, v_ϕ, v_r) were defined at each point of the volume (Figure 8.6).

Several smooth eigenvalue distribution d_i were simulated:

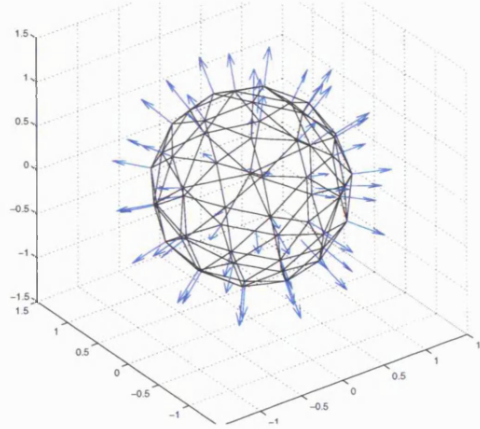


Figure 8.6: Model 2A for which eigenvectors are defined locally coinciding with the axes in spherical coordinates where the most important direction, the gradient direction, is shown.

- **Model 2A:** A constant distribution throughout the domain

$$D = \text{diag}(1, 1, 4) \quad \text{for all } x, y, z. \quad (8.30)$$

In this case, the conductivity is higher in the radial direction than perpendicular to it, so it resembled an anisotropic structure made of fibres that are born in the center and flow towards the surface. The conductivity estimate was $D_{\text{estimate}} = \text{diag}(1, 1, 1)$.

- **Model 2D:** An exponential distribution

$$D = \text{diag}(1, 1, \exp[-2(x^2 + y^2 + z^2)]). \quad (8.31)$$

In this case, the conductivity in the radial direction decays exponentially as it approaches to the center of the sphere. The conductivity estimate was $D = \text{diag}(1, 1, 1)$.

8.2.5.3 Model 3: Polynomially orientated eigenvectors

Based on the parametric curve

$$(x, y, z) = (x, t, at^2), \quad (8.32)$$

eigenvectors were based on the velocity vector, its derivative or normal, and their vectorial product or binormal (Appendix D.3), $V = [\hat{v}_t, \hat{a}_t, \hat{b}_t]$ (where $\hat{\cdot}$ represents the normalised version of a vector). For the simulation, the three vectors were simplified as

$$\begin{aligned} v_1 &= (0, 1, 2ay) \\ v_2 &= (0, -2ay, 1) \\ v_3 &= (1, 0, 0) \end{aligned} \quad (8.33)$$

where $a = 1/8$. This defined a layered structure where planes were formed by the eigenvectors v_1 and v_3 , the velocity vector to the curve and the x-axis, and v_2 was normal to the curve, such

that v_1 and v_2 were equal for $y = \text{const.}$ and smoothly vary with y , and v_3 was constant for the whole domain (Figure 8.7(a),8.7(b)).

Model 3A: Eigenvalues were defined as a constant distribution throughout the domain as

$$D = \text{diag}(\sqrt{3}, 1/\sqrt{3}, \sqrt{3}), \quad (8.34)$$

so the plane formed by the normal and the velocity vector, (v_1, v_3) , defines a layered structure of preferred current flow (Figure 8.7(a)). The conductivity estimate was set to $\text{diag}(1, 1, 1)$.

8.2.5.4 Model 4: helical orientated eigenvectors

Based on a helix function

$$(x, y, z) = (R \cos(\theta), R \sin(\theta), P\theta/\pi), \quad (8.35)$$

where R is the radius of the helix and P/π its velocity, were calculated as

$$\begin{aligned} v_\theta &= (-R \sin \theta, R \cos \theta, P/\pi) \\ a_\theta &= (-R \cos(\theta), -R \sin(\theta), 0) \\ b_\theta &= v_\theta \wedge a_\theta \end{aligned} \quad (8.36)$$

where v_θ was the velocity vector which defined the dominant direction, and a_θ and b_θ were the normal and binormal to the curve, respectively, that defined a perpendicular plane to the curve (Figure 8.8(a)). Eigenvectors $V = V(x, y, z) = V(\theta)$ were computed at each point of the finite discretisation. Thus, given z , θ was computed as

$$\theta = \theta(z) = \pi z/P, \quad (8.37)$$

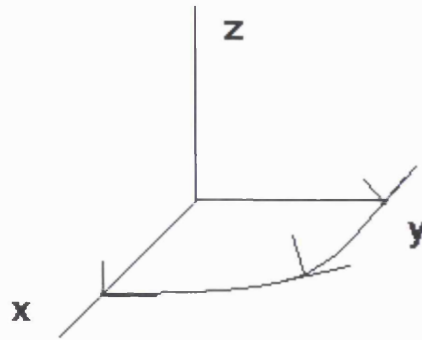
being equal for the xy -plane and changing smoothly with z . For example, for the plane $z = 0$, the x and y coordinates of the first eigenvector were $v_\theta \propto (0, 1)$; for $z = 1/4$, $v_\theta \propto (-1, 1)$. The helix parameters were $R = 0.5$ and $P = 1$ (Figure 8.9).

8.2.5.5 Model 5: mix of two tensors

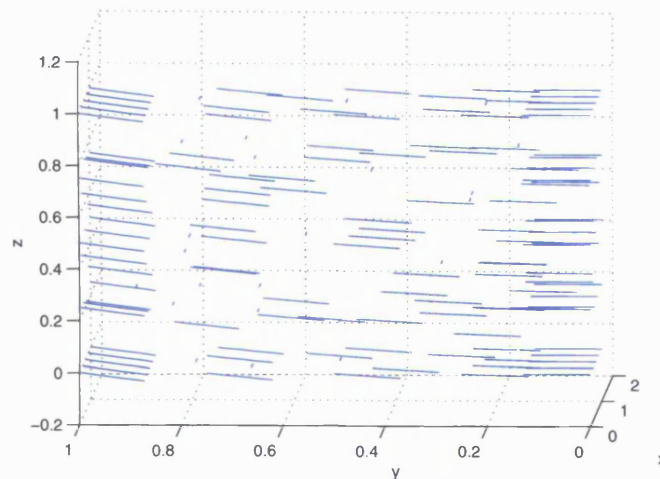
A piecewise smooth distribution of tensors with a smooth overlap of two regions of different tensor structure was simulated based on DT-MRI phantoms that resemble white matter fibre track [102]. The tensor distribution was defined by adding up a background diagonal tensor σ_1 with a general tensor σ_2 weighted by a smooth factor function $f(x, y, z)$ of the space as

$$\sigma = \sigma_1(x, y, z) + f(x, y, z)\sigma_2(x, y, z). \quad (8.38)$$

Eigenvalue distributions were simulated as follows.

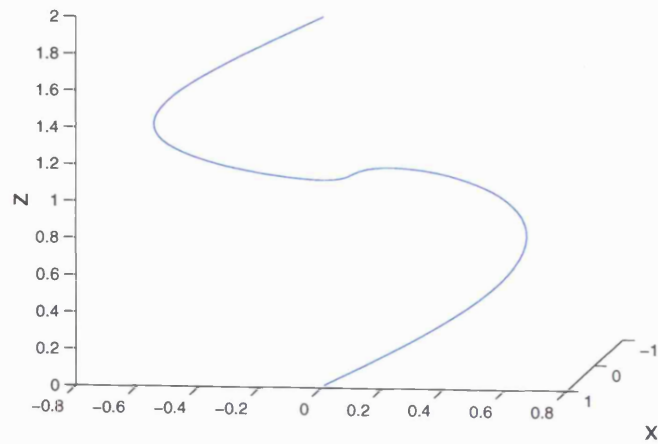


(a) First and second eigenvectors

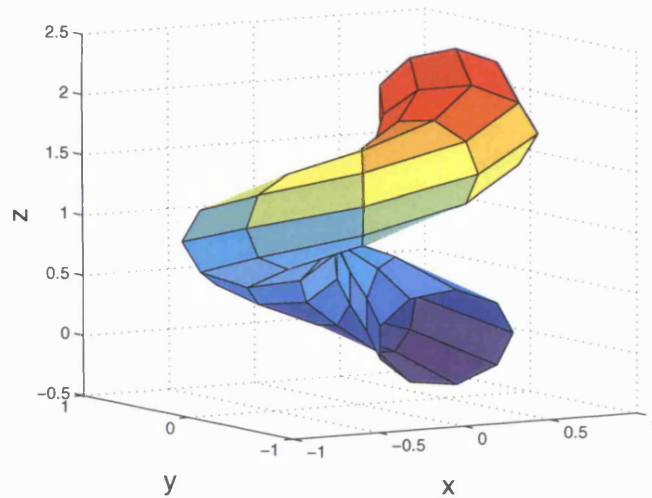


(b) Eigenvector corresponding to the largest eigenvalue

Figure 8.7: Model 3: anisotropic cubical domain (mesh of 495 elements) with eigenvectors changing along the y -direction, such that a) the first and second eigenvectors are the velocity and normal vectors to the curve $(x, y, z) = (x, t, at^2)$, for $a = 1/8$, that is, $v_1 = (0, 1, 2ay)$, $v_2 = (0, -2ay, 1)$, and $v_3 = (1, 0, 0)$ for the whole domain. Model 3A: eigenvalues weighting the conductivity along eigenvectors were $D = \text{diag}(\sqrt{3}, 1/\sqrt{3}, \sqrt{3})$, so that each plane $y = \text{const.}$ given by b) v_1 or v_3 defined a plane of preferred current flow, changing smoothly with y , and penalised the direction perpendicular to that plane given by v_2 .



(a) Helix (spring center)



(b) Spring surface

Figure 8.8: Model 4: anisotropic structure with preferred current flow along a helix and penalised along its perpendicular plane, defined in a spherical domain. a) Helix function, $(x, y, z) = (R \cos(\theta), R \sin(\theta), P\theta/\pi)$, along which the first eigenvector v_θ is defined as the velocity vector for every point of the domain being the predominant direction. b) Spring surface that represents the volume from defining a helix at each point, weighted with maximum weight in its center. Model 5(1B & 4): the conductivity was simulated by $\sigma = \text{diag}(0.5, 1.7, 0.5) + 1.3 \exp(-2r^2) V \text{diag}(1.7, 0.5, 0.5) V^T$ where r is the perpendicular distance from a point to the helix, where $V = [v_\theta, a_\theta, b_\theta]$, and $v_\theta = (-R \sin \theta, R \cos \theta, P/\pi)$, $a_\theta = (-R \cos(\theta), -R \sin(\theta), 0)$, $b_\theta = (0, 0, 1)$.

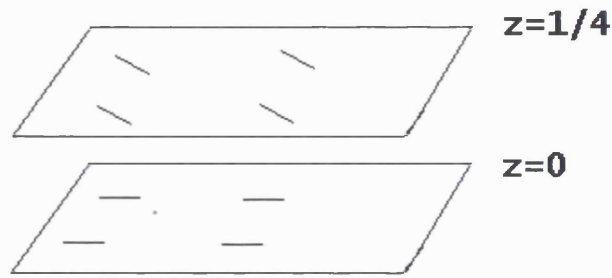


Figure 8.9: Model 4: Helix model where the first eigenvector is defined to be tangent to the helix. It is shown, here, projected in the plane $z = 0$ and $z = 1$ being constant for each plane $z = \text{const.}$ and varying smoothly with z .

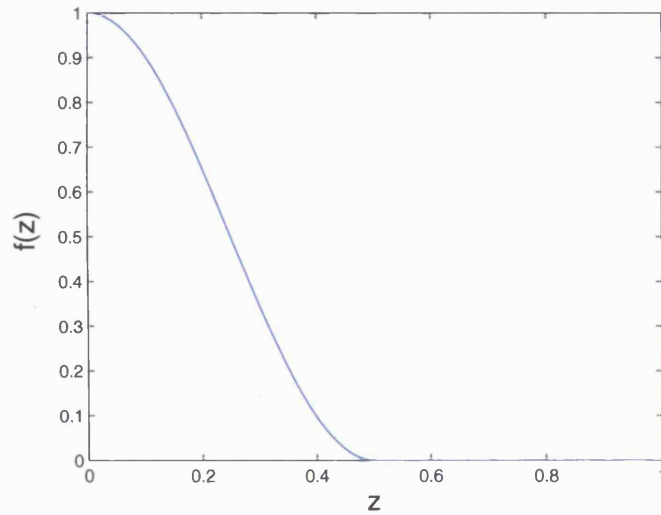


Figure 8.10: Weighting function $f(z) = 0.5(1 + \cos(2\pi z))$ used for adding up to tensor distributions in Model 5(1B & 4).

- **Model 5 mix of 1A and 3A:** The polynomial distribution of eigenvectors V of (8.33) within an isotropic background

$$\sigma = \text{diag}(1, 1, 1) + f(z)V\text{diag}(\sqrt{3}, 1/\sqrt{3}, \sqrt{3})V^T, \quad (8.39)$$

weighted by a sinusoidal function (8.10(a))

$$\begin{aligned} f(z) &= 0.5(1 + \cos(2\pi z)) & \text{for } z \leq 0.5 \\ f(z) &= 0 & \text{for } z > 0.5 \end{aligned} \quad (8.40)$$

such that the upper half plane of the cube was isotropic and the lower part changed smoothly into a layered structure.

- **Model 5 mix of 1A and 4A:** Based on a helix function

$$\sigma = \text{diag}(0.5, 1.7, 0.5) + 1.3 \exp(-2r^2) V \text{diag}(1.7, 0.5, 0.5) V^T, \quad (8.41)$$

where r is the distance from the given vertex to the helix curve and $V = [v_\theta, a_\theta, b_\theta]$. Based on a parametric helix (8.35), then the eigenvectors were the normalised vectors of (8.36). This structure aiming to be similar to white matter fibre defined a spring, or volumetric helix, where the helix indicated the dominant direction and its perpendicular plane defined the volume. It was also weighted where eigenvalues decreased exponentially from the center of the helix, so the tensor distribution smoothly mixed with the surrounding tensor. This aimed to approximate white matter phantoms that simulate a piecewise smooth tensor defined along a random walk such that it has the same properties as tissue: i) it has a non constant curvature, ii) it has an extension or volume, and iii) it mixes smoothly with the isotropic surrounding [102] (to note that i) was not intended to be modelled here).

8.2.5.6 Model 6: Diffusion tensor

Eigenvectors were computed from a Diffusion Tensor detail of brain white matter, of resolution 8-8-8 (2mm voxels). It was estimated following the procedure given in section 9.2.3.1: first, by estimating the DT, second, by interpolating the tensor coefficients, and finally by extrapolating them in a cubical mesh (495 elements), (Figure 8.22(a)-8.22(d)).

8.2.6 Inverse Problem

An iterative algorithm was applied to minimise the objective function

$$f(x_k) = \frac{1}{2} \|F(x_k) - d\|^2, \quad (8.42)$$

where $F(x_k)$ was the predicted boundary voltages for the conductivity x_k at step k , and d was the simulated data (real data in practice) for the true solution x_{true} , $d = F(x_{\text{true}})$.

The Quasi-Newton method BFGS was applied as indicated in (3.39), with the objective gradient was calculated as

$$\nabla f(x_k) = J_k^T (F(x_k) - d), \quad (8.43)$$

where J was the Jacobian (8.16 or 8.17).

8.3 Results

8.3.1 Rank analysis

The Jacobian with respect to the eigenvalues for piecewise linear conductivity (case i)) was full rank (Figure 8.11(b)). A comparison between the Jacobian computed by product of fields and by

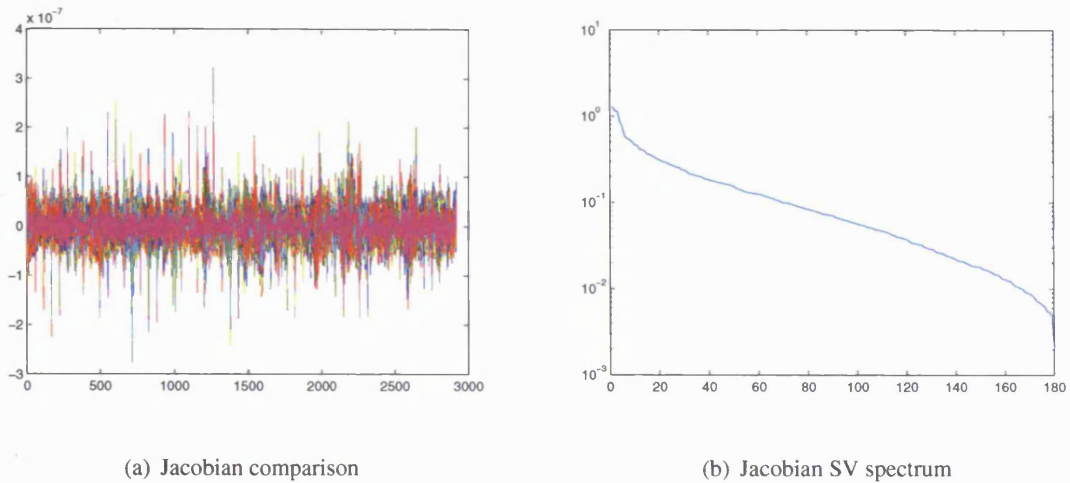


Figure 8.11: Rank analysis of the Jacobian with respect to the diagonal elements where a) is a comparison between the Jacobian computed by FD and product of fields, $(J^{\text{direct}} - J^{\text{FD}})$, and b) is the SV spectrum. The direct and finite difference Jacobians agreed up to the FD incremental step length $\Delta\sigma \simeq 10^{-8}$. It was full rank with conditioning $\text{cond}(J) = 59$. It corresponded to a sphere mesh of 148 elements with 2916 measurements and diagonal conductivity with sinusoidal diagonal elements.

FD was done to verify the numerics where the conductivity increment (8.15) was $\Delta\sigma_{ii} \simeq 10^{-8}$ (Figure 8.11(a)).

The rank of the Jacobian with respect to the six independent coefficients for piecewise constant conductivity (case ii) was verified to be given by the mesh connectivity. Besides, it was larger than the number of unknowns for the proposed inverse problem, three times the number of nodes, which agreed with the case i) being full-rank (Figure 8.12(b), Table 8.2). For example, for a spherical mesh with 148 elements and 60 nodes, the number of measurements was $n_s = 2916$ and the number of unknowns was $6n = 180$. The Jacobian $J \in \mathbb{R}^{2916 \times 888}$ had rank $r(J) = 259$ where $r < 6n_s$ yet $r > 3n$. Thus the proposed constrained problem with $3n$ unknowns had full rank Jacobian.

8.3.2 Recovery of eigenvalues

The objective function (8.42), its gradient (8.43), and the solution error is given for the ten simulations (Table 8.1). The solution error norm decreased less than 10% for a constant tensor distribution, (Model 1A, Figure 8.13(a)). The recovery of a smooth eigenvalue distribution pattern was possible: linear (Model 1B Figures 8.14(a)-8.14(f)), and sinusoidal (Model 1C Figures 8.15(a)-8.15(f)). The recovery of eigenvalues for generally orientated tensors was done

Table 8.2: Mesh parameters and rank results for the Jacobian J with respect to piecewise constant conductivity, for a general anisotropic tensor constant in the domain, where $J \in \mathbb{R}^{N^2 \times 6n_s}$ for # meas. = N^2 , the dof(E) is the number of nonzeros in the upper triangular part of the system matrix E , n_s is the number of elements, n is the number of nodes, N is the number of exterior nodes, and geom. is the geometry.

n_s	$6n_s$	n	$3n$	# meas.	rank(J)	dof(E)	geom.
148	888	60	180	2916	259	259	sphere
384	2304	125	375	9604	604	604	cube

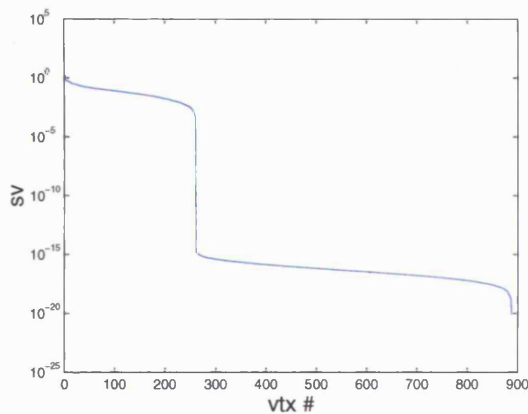
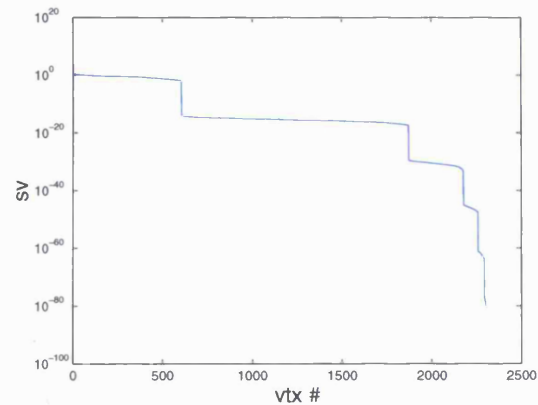
(a) J spectrum for a spherical mesh(b) J spectrum for a cubical mesh

Figure 8.12: Rank analysis of the Jacobian with respect to the six coefficients for piecewise constant conductivity, for the complete NtoD and current and measurement pattern given by vectors perpendicular to one (the only thing that changes with respect to the rest of the chapter is that the conductivity is piecewise constant instead of linear). SV spectrums for a) a spherical mesh (148 elements), and for b) a cubical mesh (384 elements).

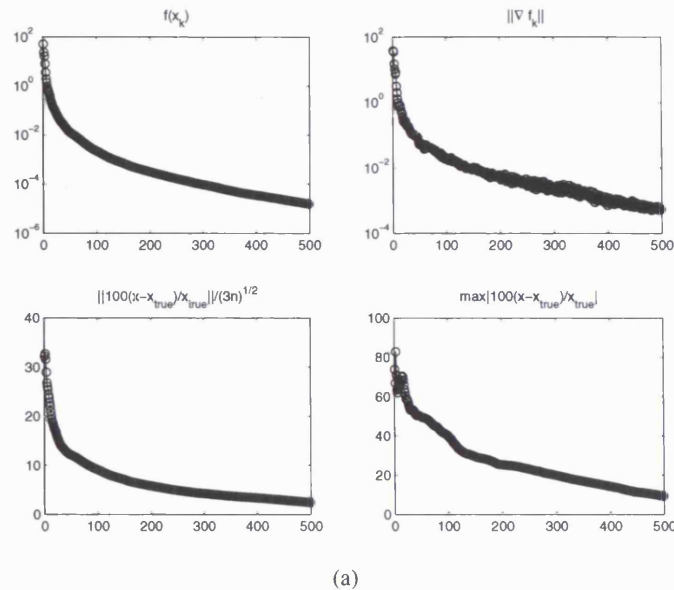


Figure 8.13: Model 1A. Results of the recovery of the eigenvalues for Model 1A, for which eigenvectors coincide with axis and conductivity was a constant distribution $\sigma = \text{diag}(\sqrt{3}, 1/\sqrt{3}, 1/\sqrt{3})$ in a cube of 495 elements. Objective function (top left), objective gradient (top right), relative error norm (bottom left), and max relative error (bottom right), versus the iteration number.

with error less than 10% (Models 2A-6, Figures 8.16(b)-8.22(f)).

8.4 Discussion

It has been verified numerically that it is possible to recover a piecewise linear conductivity tensor in a 3D anisotropic medium from the complete NtoD map for the constrained case with known eigenvectors. Simulations were done with two aims. First, the purpose of recovery of three piecewise linear eigenvalues was to verify numerical uniqueness for this constraint. The second was to demonstrate that the recovery of eigenvalues for general tensors with an eigenvector orientation that resembled physiological tissue was possible. Simulations included diagonal tensors with smooth eigenvalues, general tensors representing anisotropic structures of a fibre or layered type, piecewise tensor distributions varying smoothly along the domain, and a DTI sample of brain white matter. For the first case, a linear and a sinusoidal pattern were recovered for diagonal tensors. For the second case, eigenvalues for general tensors were recovered with an error below 10%. A rank analysis of the rank of the Jacobian of the complete NtoD map with respect to piecewise linear conductivity sampled on the vertices was full rank, for which the number of unknowns is three times the number of vertices, verifying that the inverse problem for this constraint is well conditioned. The rank of the Jacobian for piecewise

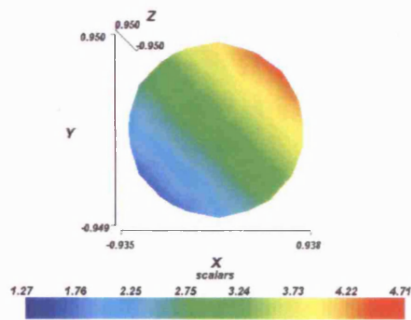
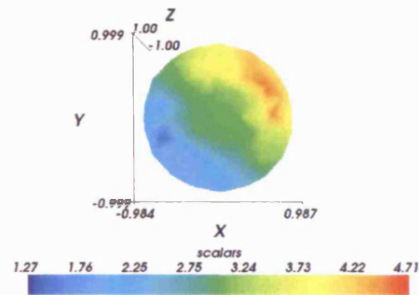
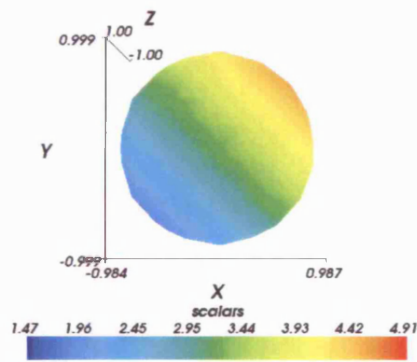
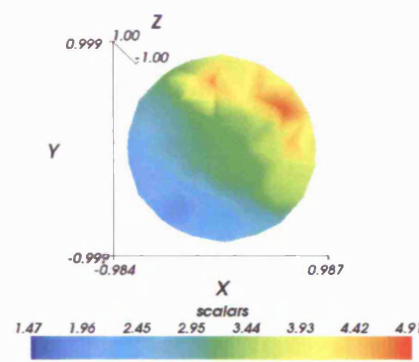
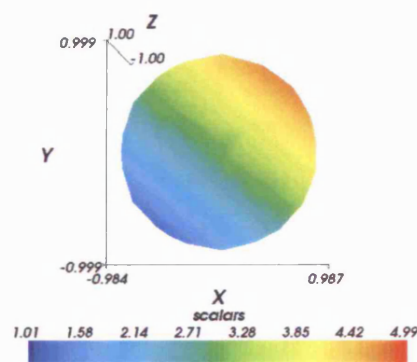
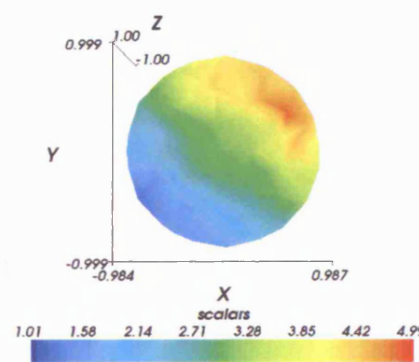
(a) Simulated σ_{xx} (b) Reconstructed σ_{xx} (c) Simulated σ_{yy} (d) Reconstructed σ_{yy} (e) Simulated σ_{zz} (f) Reconstructed σ_{zz}

Figure 8.14: Model 1B. Results of the recovery of the eigenvalues for Model 1B for a spherical mesh of 807 elements, for which eigenvectors coincide with axes and conductivity eigenvalues were three linear distributions. The simulated linear distributions were $\sigma_{xx} = 3 + x + y + z$, $\sigma_{yy} = 3.2 + x + y + z$, $\sigma_{zz} = 3 + 1.2x + 1.4y + 0.8z$, for a conductivity estimate $\sigma_{estimate} = \text{diag}(3, 3, 3)$. Cross sections centered at the origin for simulated (left) a) σ_{xx} , c) σ_{yy} , e) σ_{zz} and reconstructed (right) b) σ_{xx} , d) σ_{yy} , f) σ_{zz} eigenvalues.

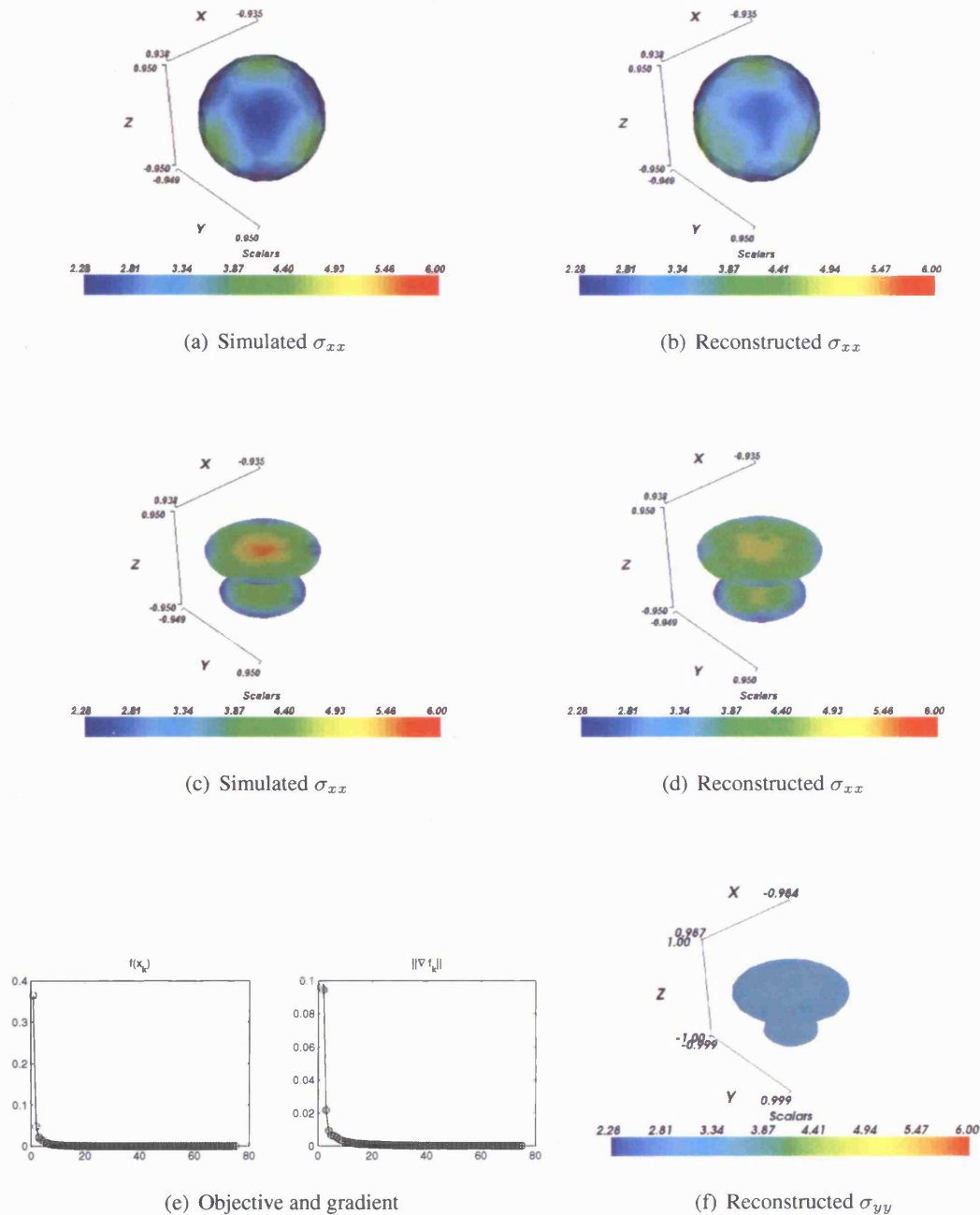
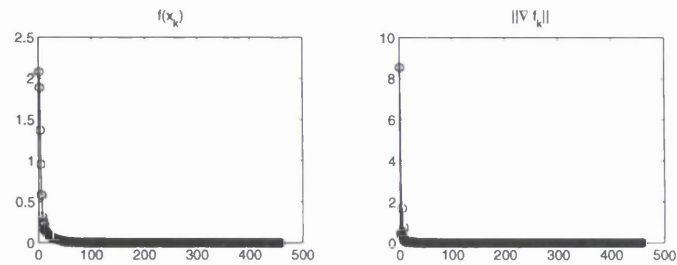
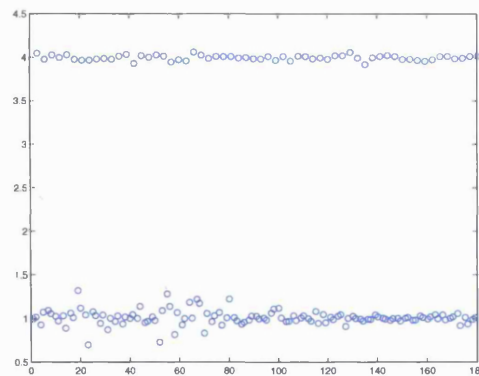


Figure 8.15: Model 1C. Results of the recovery of the eigenvalues for Model 1C for a spherical mesh of 807 elements, for which eigenvectors coincide with axis and conductivity was a cosine distribution for the first eigenvalue and constant for the other two. Simulated distributions were $\sigma_{xx} = 3 + \cos(\pi x) + \cos(\pi y) + \cos(\pi z)$, $\sigma_{yy} = 3$, $\sigma_{zz} = 3$, for a conductivity estimate $\sigma_{estimate} = 3$. Surface plot of the a) simulated and b) reconstructed σ_{xx} , cross sections of the c) simulated and d) reconstructed σ_{xx} , f) σ_{yy} , and e) objective function (left) and its gradient (right) are given versus the iteration number.



(a) Objective and its gradient



(b) Recovered eigenvalues

Figure 8.16: Model 2A. Results of the recovery of the eigenvalues for Model 2A for a spherical mesh of 148 elements, for which eigenvectors are defined locally coinciding with axes in spherical coordinates, and eigenvalues were constant in the domain. The conductivity tensor was given by $\sigma = VDV^T$, where $V = [v_\theta, v_\phi, v_r]$ and eigenvalues $D = \text{diag}(1, 1, 4)$, such that the radial was the preferred direction for current flow. a) Objective function (left) and its gradient (right), and b) the recovered eigenvalues are given.

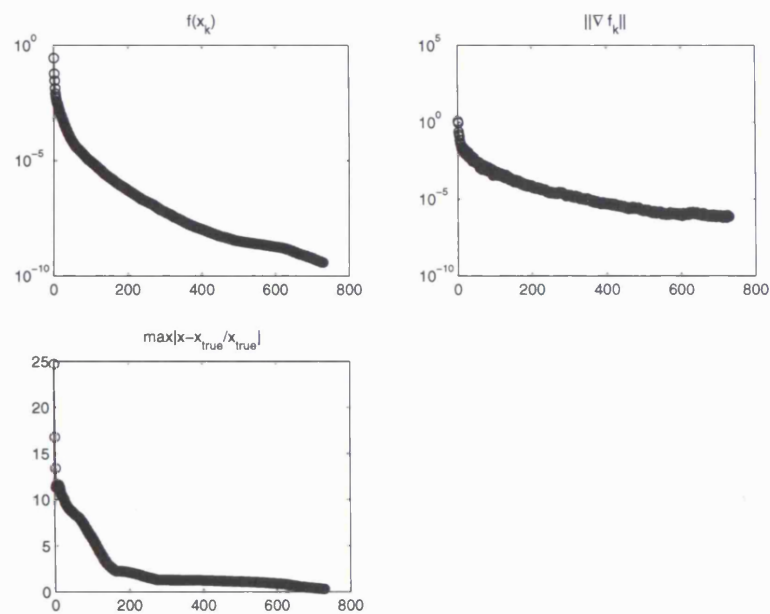
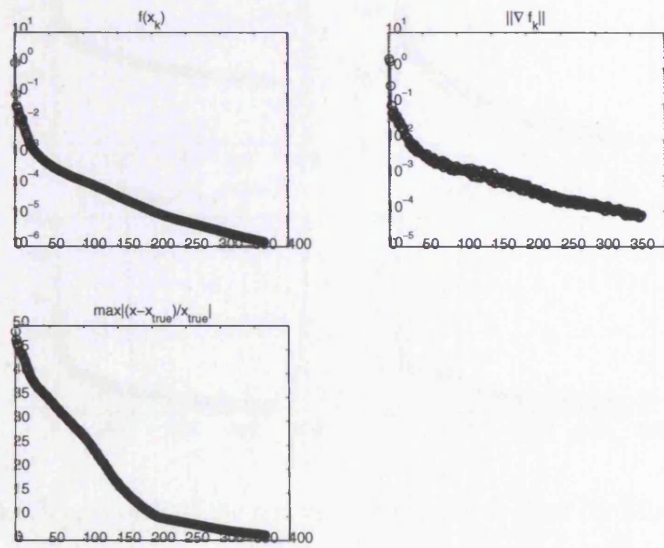


Figure 8.17: Model 2D. Results of the recovery of the eigenvalues for Model 2D for a spherical mesh of 148 elements, for which eigenvectors are defined locally coinciding with axes in spherical coordinates, and the first two eigenvalues were constant in the domain and the third one was exponentially decreasing towards the center. The conductivity tensor was given by $\sigma = VDV^T$, where $V = [v_\theta, v_\phi, v_r]$ and eigenvalues $D = \text{diag}(1, 1, \exp(-2(x^2 + y^2 + z^2)))$. Objective function (top left), objective gradient (top right), maximum relative error in percentage (bottom) are given versus the iteration number.



(a) Objective function, its gradient, and maximum solution error

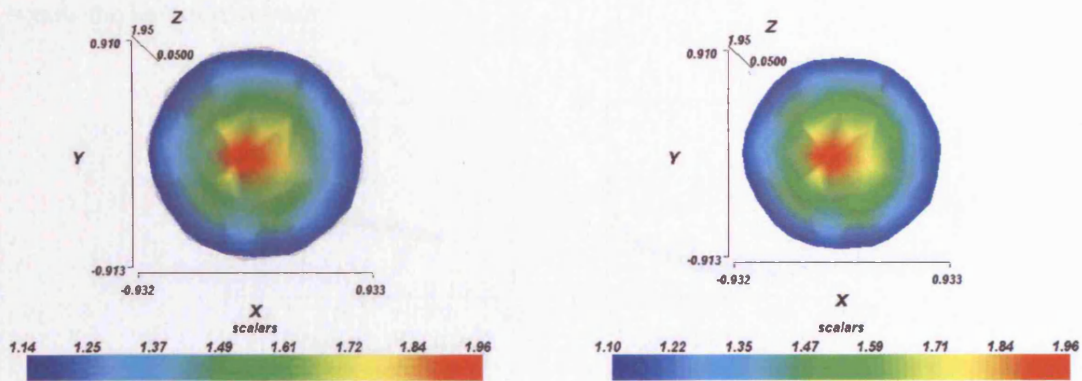
(b) Simulated σ_{zz} (c) Reconstructed σ_{zz}

Figure 8.18: Model 2D. Results of the recovery of the eigenvalues for Model 2D for a spherical mesh of 309 elements, for which eigenvectors are defined locally coinciding with axes in spherical coordinates, and the first two conductivity eigenvalues were constant in the domain and the third one was exponentially decreasing towards the center. The conductivity tensor was given by $\sigma = VDV^T$, where $V = [v_\theta, v_\phi, v_r]$ and eigenvalues $D = \text{diag}(1, 1, \exp(-2(x^2 + y^2 + z^2)))$. a) Objective function (top left), objective gradient (top right), maximum relative error in percentage (bottom) versus the iteration number; cross sections of the b) simulated and c) reconstructed third eigenvalue σ_{zz} .

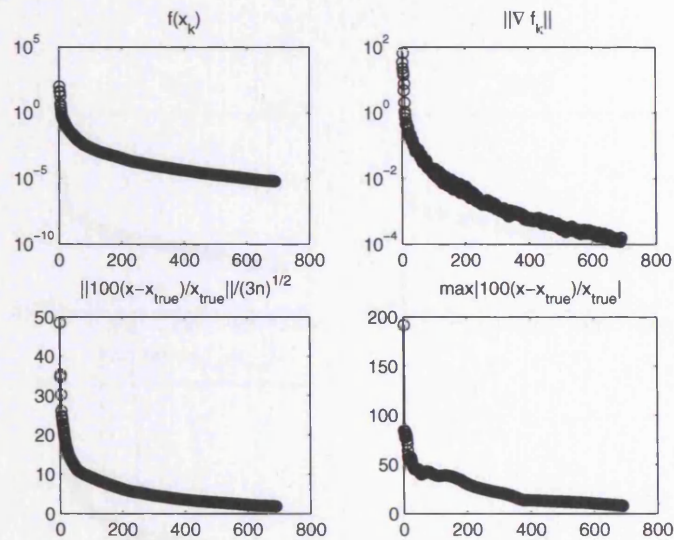
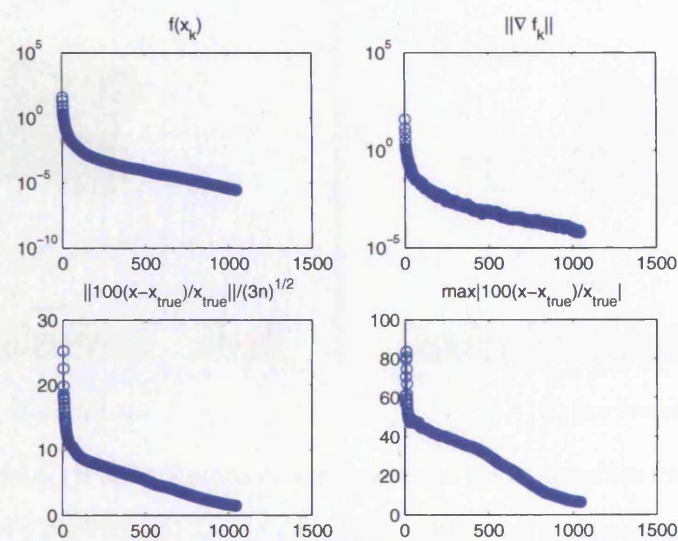
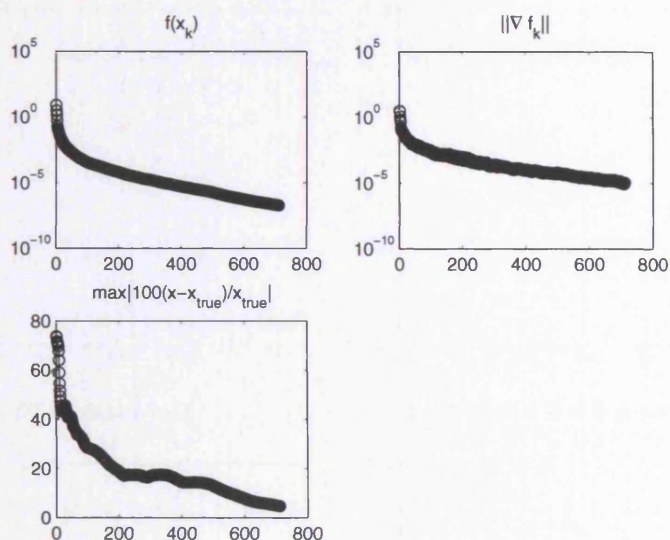


Figure 8.19: Model 3A. Results of the recovery of the eigenvalues for Model 3A for a cubical mesh of 495 elements, for which eigenvectors are defined locally parallel and perpendicular to a polynomial plane. Objective function (top left), objective gradient (top right), maximum percentage relative error norm (low left), and maximum percentage relative error (low right) versus the iteration number.

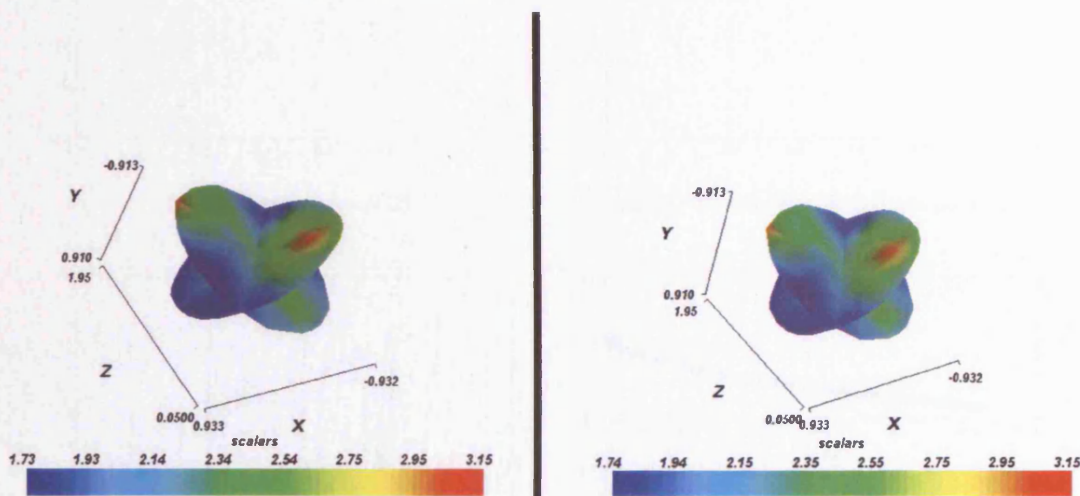


(a)

Figure 8.20: Model 5(1A & 3A). Results of the recovery of the eigenvalues for Model 5 (1A & 3A) for a cubical mesh of 495 elements, from a mix of two tensors that yield a smooth overlap between a tensor with eigenvectors defined locally parallel and perpendicular to a polynomial plane, and an isotropic background. Objective function (top left), objective gradient (top right), maximum percentage relative error norm (bottom left), and maximum percentage relative error (bottom right) are given versus the iteration number.



(a) Objective function (top left), its gradient (top right), and maximum solution error (bottom left)



(b) Simulated σ_{zz}

(c) Reconstructed σ_{zz}

Figure 8.21: Model 5(1B & 4). Results of the recovery of the eigenvalues for Model 5 (1B & 4), (spherical mesh of 309 elements), from a mix of two tensors that yield a smooth overlap between a tensor with eigenvectors defined locally parallel and plane perpendicular to a helix function, and an isotropic background, and with eigenvalues exponentially decaying towards the center of the helix. a) Objective function (top left), objective gradient (top right), maximum percentage relative error norm (bottom left), and maximum percentage relative error (bottom right) are given versus the iteration number, with cross sections of the b) simulated and c) reconstructed third eigenvalue σ_{zz} .

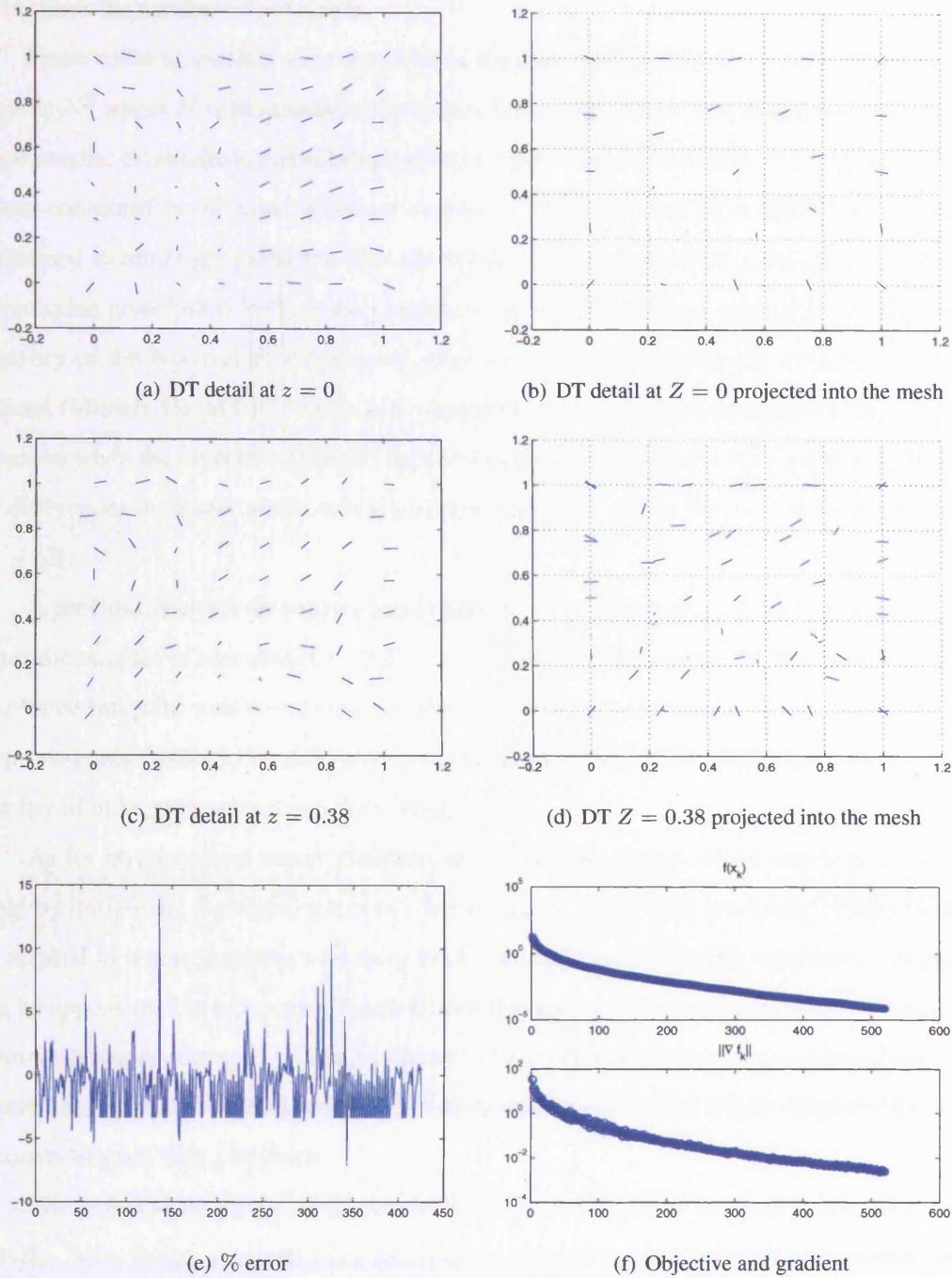


Figure 8.22: Model 6. Results of the recovery of the eigenvalues for Model 6 for a cubical mesh of 495 elements, for which eigenvectors were computed from a Diffusion Tensor (DT) detail, of resolution 8-8-8 (2mm voxels), by interpolating the tensor elements and extrapolating them in the mesh vertices. DT details at a) $z = 0$ and c) $z = 0.38$ and b,d) their projections into the mesh, respectively. e) Objective function (top) and objective gradient (bottom) are given versus the iteration number.

constant conductivity was verified to be given by the nodal connectivity and to be larger than three times the number of unknowns.

Finite element meshes were very coarse because considering all possible measurements grew as N^2 where N is the number of boundary nodes. Validation on a finer mesh would verify these results. Simulations considering general tensors used the Jacobian with respect to eigenvalues computed by FD since the direct Jacobian method was very slow; therefore, it should be vectorised to run larger problems. Because simulations took hundred of iterations to decrease the solution error below 10%, some simulations shown here were stopped before then, yet the recovery of the eigenvalues distribution was assumed by visualising the reconstructed distributions (Models 1B and 1C, linear and sinusoidal, respectively). Convergence was generally assumed when the objective gradient had decreased four or five orders of magnitude; however, no differences in image quality was significant when the solution error norm decreased below 10 – 5%.

A previous analysis showed the rank analysis of the Jacobian to be between one and three times the number of elements [1]. These results verified that the rank of the Jacobian is larger than three times the number of vertices, and so the numerical problem is well conditioned. In fact, one could expect to be able to recover higher order piecewise polynomials as long as the number of unknowns is less than the boundary data.

As for physiological tensor distributions, concentric spheres could represent the skull or scalp by initialising the eigenvectors in spherical coordinates. This encourages further study to be applied to a real phantom with anisotropic structure for which the eigenvector orientation can be approximately estimated. Theoretically, it is known that one can recover one eigenvalue from the boundary data, yet no result is known about recovering two or three eigenvalues. These results suggest that numerical uniqueness occurs when eigenvectors are provided and encourage theorists to study this constraint.

The practical relevance of this constraint is clear for EIT of medical applications where muscle, bone tissue, and white matter have a conductive preferred direction, which can be approximated from a structural imaging modality like MRI or directly estimated with DT-MRI.

Chapter 9

Influence of anisotropy on a realistic FEM model of the head

9.1 Introduction

It is well known that both the skull and white matter conductivities are anisotropic, however, for EIT of brain function they have been so far considered as isotropic.

9.1.1 Background

The white matter conductivity ratio normal:parallel to the fibres was found to be 1 : 9 [121]. The skull, which is comprised of two plates of hard bone tissue enclosing soft bone tissue of higher conductivity, could be represented as a layer with an effective conductivity ratio radial:tangential to the skull surface of 1 : 10 [146], which has been adopted as an upper bound ratio for studying the influence of anisotropy of the skull for EEG [182]. In vivo DTMRI measurements, the brain conductivity tensor can be estimated from the water self-diffusion tensor estimated by using the cross-property relation [173, 172], which relates the transport model for the two tensors with the underlying microstructure. A statistical analysis of the microstructure in terms of the intra- and extracellular space transport coefficients yields the conductivity and diffusion tensors sharing eigenvectors. Furthermore, at quasistatic frequencies where the current does not cross the intracellular space, there is a strong linear relationship between the diffusion and conductivity tensor eigenvalues. The scalp, which contains muscle tissue, can be estimated as being 1.5 more resistive in the radial than in the tangential direction at 50KHz [77]. A review of tissue impedances for the head tissues can be found in [77, chapter2].

The effect of anisotropic conductivity of muscle has been studied for absolute EIT of the heart by providing information about the tissue boundaries, obtained from MRI, and the anisotropic structure of muscle, assuming a cylindrical symmetry and a conductivity ratio tangential:normal to the muscle of 4.3:1, in 2D and 3D [54, 55]. The anisotropy of the my-

ocardium was not modelled because of the difficulty of estimating its anisotropic structure. In 3D, anisotropy of the muscle resulted in a shunting effect which influenced the measurements and reconstructed conductivity, yet did not dominate over other model parameters. The conductivity values tangential and normal to the muscle were reconstructed assuming that the conductivity was constant for each tissue.

The influence of anisotropy for EIT of the head has not been studied, but, it has been for EEG. A high resolution FEM model was used to study the influence of anisotropy of white matter for the EEG forward model, incorporating the brain conductivity tensors from DTMRI; from the results from the forward problem, it was suggested that the magnitude of the sources would be more affected than localisation and the effect would be greater when sources were deeper in the brain [66]. In contradiction with the previous result, a study in a 2D EEG forward model emphasized that looking at the correlation was not enough and found a high correlation yet more than 30% discrepancy in the relative error between model potentials for isotropy and anisotropic white matter estimated from DTMRI. From this result, it was concluded that anisotropy of white matter would influence source localisation because a previous analysis comparing a three-shell spherical with a realistic model yielded 5-10% relative error and an averaged 1.97cm localisation error [90].

A study that modelled anisotropy of the skull and white matter for the EEG forward problem analysed the effect of anisotropy by increasing the conductivity ratio of both tissues from one to ten, in terms of the Relative Difference Measure (RDM), which was described as a measure of the topographic error that compared the isotropic and anisotropic electrical fields [182]. For sources near the cortex, RDM was 11%, mainly affected by the skull anisotropy; for sources deeper in the brain: RDM was 10%, where now white matter anisotropy appeared most relevant. The effect of anisotropy for EEG source localisation reported a localisation error of up to 18mm, for superficial sources, being mainly sensitive to 1:10 skull anisotropy; and 6mm, for deeper sources [181, Chapter 7].

9.1.2 Objective and experimental design

The aim was to study the influence on the forward and inverse solutions of incorporation of anisotropy in a realistic numerical head model. This included four tissue types: scalp, skull, CSF, and brain [170], and anisotropy was included for all except the CSF. The forward solutions were compared in terms of i) the current norm, ii) the reduction of current that flows into the brain, which is relevant for the modelling studies, iii) the percentage error in the domain and on the boundary voltages by neglecting anisotropy, and iv) the percentage difference between boundary voltages corresponding to a model with and without a conductivity perturbation in

the brain. For the linear inverse solution subgoals were i) to study the effect of simulating data with the anisotropic model and reconstructing it with the isotropic model, and ii) to study the effect of simulating data with the anisotropic model and reconstructing it with the anisotropic model based on the assumption that the only possible conductivity change was a multiple scalar to a general anisotropic tensor. Previous to the head model, a preliminary analysis aimed to study the effect of anisotropy for simple cubic and a concentric spherical models in terms of the magnitudes used for the comparison for the head model: voltage and current density. For the cubical domain, the objective was to verify that the voltage decreased from the injection point equally in all directions and isopotential lines were semicircles with center at the injection point, for the isotropic model; and that isopotential lines redistributed from semicircles centered at the injection point to lines parallel to the predominant conductivity direction, for the anisotropic model. For the concentric spherical domain, for which the outer and inner shells were isotropic and the middle one resembled the anisotropy of the skull, the objective was to verify that the preferential current flow was tangential to the skull surface rather than into the inner shell.

A realistic FEM model of the head that discerned scalp, skull, CSF, and brain was created from the segmentation of a T1-MRI and tessellation in tetrahedra for the volume enclosed by the segmented surfaces. The selected isotropic conductivity values, obtained from [77], corresponded to a frequency of 50KHz that provided the largest conductivity change for epilepsy [44]. Before meshing, the T1-MRI was coregistered to the reference of the DT-MRI.

Three tissues were modelled as anisotropic: the scalp, the skull, and white matter. The anisotropic information for the brain was obtained in three steps. First, for a DT-MRI, of the same subject as the T1-MRI, the diffusion tensor coefficients were interpolated at the center of the brain tetrahedra. Second, the conductivity tensor was linearly related to the diffusion tensor by assuming both tensors shared eigenvectors and eigenvalues were linearly related. Third, the conductivity tensor trace was scaled to match the isotropic trace. The anisotropy for the scalp and skull was approximated by using the eigenvalue decomposition such that eigenvectors were two unit vectors parallel to the surface and one perpendicular to it. Eigenvalue tangential:normal ratios were 1.5:1 for the scalp [78] and 10:1 for the skull [182]. Also, the skull and scalp tensor trace was constrained to be equal to the equivalent isotropic trace.

The effect of anisotropy in the forward solution was studied qualitatively: first, by looking at the current density norm to verify that the current preferred direction of flow was tangential to the scalp and skull surfaces and along white matter fibres. This was done for meaningless isotropic conductivity values considering only the isotropy of the skull to isolate its effect; the same was done for the brain tissue. Second, both realistic isotropic and anisotropic models for

the scalp, skull, and brain of the head were compared in terms of the voltage, boundary voltages, and current density norm, with and without a local conductivity perturbation in the brain.

The effect of neglecting anisotropy in the reconstructed images was studied by simulating eight selected boundary voltages with the anisotropic model and recovering linearly the conductivity with the isotropic one, for a local perturbation at five positions in the brain: occipital to simulate stimulation of the visual cortex, temporal and hippocampus to simulate changes in epilepsy, and another two in the parietal and temporal lobe surrounded by white matter. In addition, all the simulated boundary voltages were reconstructed with the proposed linear reconstruction method for the recovery of a multiple scalar to a general conductivity tensor, assuming that tensor eigenvectors and eigenvalue ratios were known. Images were visualised and compared in terms of the localisation error.

9.2 Methods

9.2.1 Preliminaries: Voltage and current density in an anisotropic domain

The aim of this section was to visualise the effect that anisotropy had on voltage and the current density, magnitudes that were used to compare the effect of anisotropic conductivity for the head model, in two simplistic domains: a cube and a concentric sphere.

Given an anisotropic conductivity tensor σ in the domain, the forward problem was solved for one current injection, which provided the voltage u everywhere, then the electrical field $E = -\nabla u$ and current density vector $J = \sigma E$ were computed and visualised, where the σ was nodal based and current and measurement patterns were vectors perpendicular to ones to avoid the use of a pair electrodes for the injection (p. 135 in chapter 8). The corresponding isotropic model was also visualised for the comparison.

9.2.1.1 Cubic model

An anisotropic cubic domain with constant conductivity tensor was simulated with the conductivity in the x-direction being ten times larger than along its perpendicular plane, that is, $\sigma = \text{diag}(10, 1, 1)$ everywhere. The corresponding isotropic domain had conductivity $\sigma = \text{diag}(1, 1, 1)$.

9.2.1.2 Three-shell spherical model

The qualitative effect of the anisotropy of the skull was approximated using a three concentric spherical model (Figures 9.18(a) and 9.18(b)), where the inner and outer spheres were isotropic and the one in between was anisotropic with radial:tangential conductivity ratio 1:10. That is, $\sigma = \text{diag}(1, 1, 1)$ in the isotropic part and $\sigma = \alpha V D V^T$ with $D = \text{diag}(10, 10, 1)$ in the anisotropic part of the domain, where $V = [v_1, v_2, v_3]$, v_1 and v_2 represent two tangential

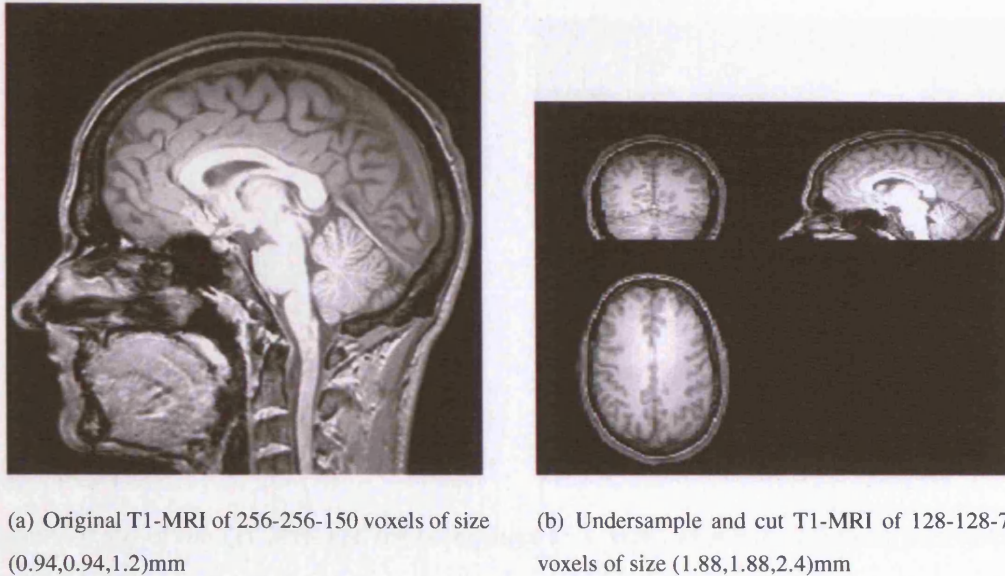


Figure 9.1: T1-MRI of a 24 year old male, acquired at 3T.

directions and v_3 represents the normal direction, and α is a constant factor to force the isotropic tensor to have the same trace as the isotropic one, $\text{trace}(\sigma) = \text{trace}(D) = 3$ (section E). Hence, $D = \text{diag}(1.493, 1.493, 0.15)$.

9.2.2 Head model: geometry and mesh

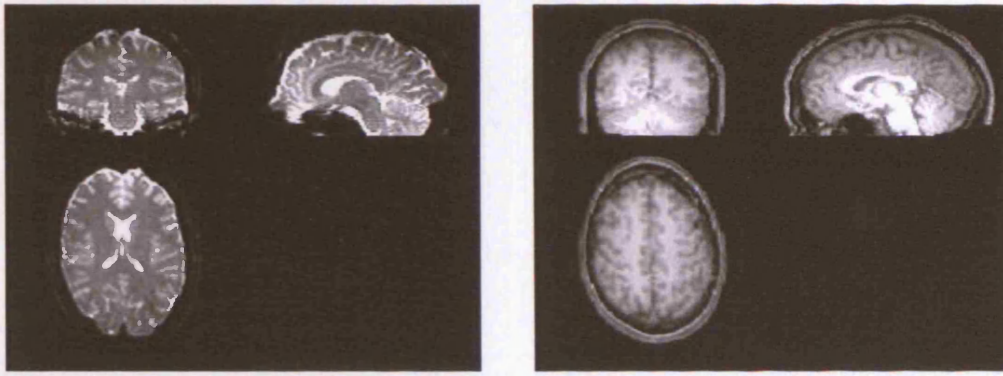
9.2.2.1 MRI and DT-MRI data sets and pre-processing

A T1-weighted MRI and diffusion weighted MRI of the same subject, a 24 year old male, were taken from the IXI-server at UCL (<http://ixiserv.cs.ucl.ac.uk/>). The DTI acquired at 3T, had 15 diffusion weighted images in different directions with $b = 1000s/mm^2$ and reference B0 ($b = 0$), with voxel resolution of $1.75 \times 1.75 \times 2mm$ and $128 \times 128 \times 64$ voxels (Figure 9.2(a) corresponds to the B0, i.e. zero diffusion). The T1-MRI acquired at 3T, had a voxel resolution of $0.94 \times 0.94 \times 1.2mm$ with $256 \times 256 \times 150$ voxels (Figure 9.1(a)).

Pre-processing of the T1-MRI was done because of its high resolution. First, the lower part of the head corresponding to the jaw was neglected since almost no current flows there; it would have lead to a excessively high density mesh [170]. It was cut below the brain using the VTK software (<http://www.vtk.org/Wiki/VTK>). Second, it was undersampled by half in three directions using MRicro (www.mricro.com) leading to a voxel size $1.88 \times 1.88 \times 2.4mm$ (Figure 9.1(b)).

9.2.2.2 Coregistration of MRI to the DT-MRI data

Previous to the coregistration, the T1-MRI and B0 of the DT-MRI were prealigned, and B0 slices corresponding to the blank spaces were increased to match those of the MRI



(a) B0 (DT-MRI) of 135-135-75 voxels of size (1.75,1.75,2)mm

(b) T1-MRI after being coregistered to the B0 of 135-135-75 voxels of size (1.75,1.75,2)mm

Figure 9.2: B0 of the DT-MRI and the coregistered T1, from which the FE mesh was obtained.

to avoid the MRI to be cut at the coregistration stage. Also MRICro, BrainSuite 2.0 (<http://brainsuite.usc.edu/>) [158], and (X)MedCon 0.9.9.0 (<http://xmedcon.sourceforge.net/>) [123] were used for visualising and converting among DICOM, analyze, and nifty formats (<http://www.sph.sc.edu/comd/rorden/micro.html>). The MRI was normalised and coregistered to the B0 and resliced after the coregistration using SPM2 (<http://www.fil.ion.ucl.ac.uk/spm/>) [47, 10]. If first applied an affine transformation followed by a nonlinear deformation that minimised a least squares functional based on maximum entropy (Figure 9.2(b),9.3,9.4).

9.2.2.3 Segmentation and meshing

The coregistered T1 was segmented and tessellated to a tetrahedral FEM mesh (procedure suggested by Raya Schindmes, Medical Physics, UCL [153, 152]). The segmentation and surface extraction of four tissues, brain, CSF, scalp, and skull, was done using BrainSuite [158, 39], and the meshing using Cubit (Figures 9.5(a), 9.5(b)). The mesh contained 311,727 tetrahedra for the whole head and 132,272 for the brain.

9.2.3 Head model: conductivity tensor estimate

9.2.3.1 Diffusion tensor estimation

The diffusion tensor was estimated from the DT-MRI data using the MATLAB tools provided by CMIC-wiki. Atkinson's *eshow* visualisation tool and other routines were used for displaying the DWI and reconstructing and visualising the diffusion tensor. Let DWI be the diffusion weighted images acquired at fifteen different directions, where g indicates the diffusion direction, the diffusion tensor D can be approximated by

$$DWI = B0\exp(-bg^T Dg). \quad (9.1)$$

Normalised Mutual Information Coregistration

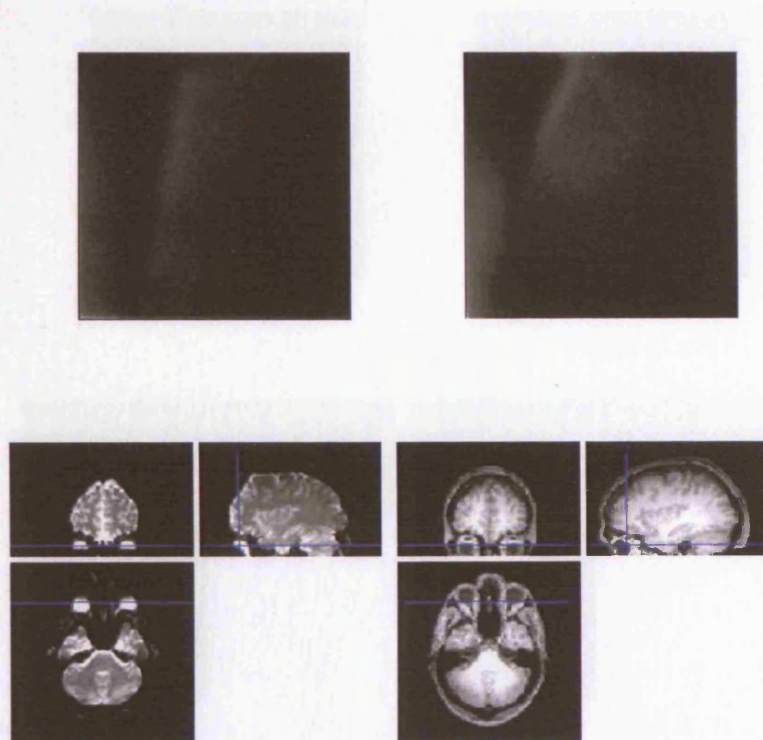


Figure 9.3: Results of the coregistration of T1-MRI to the B0 of the DT-MRI. Top) initial (left) and final (right) histograms, and bottom) target B0 (left) and coregistered T1 (right).

Normalised Mutual Information Coregistration

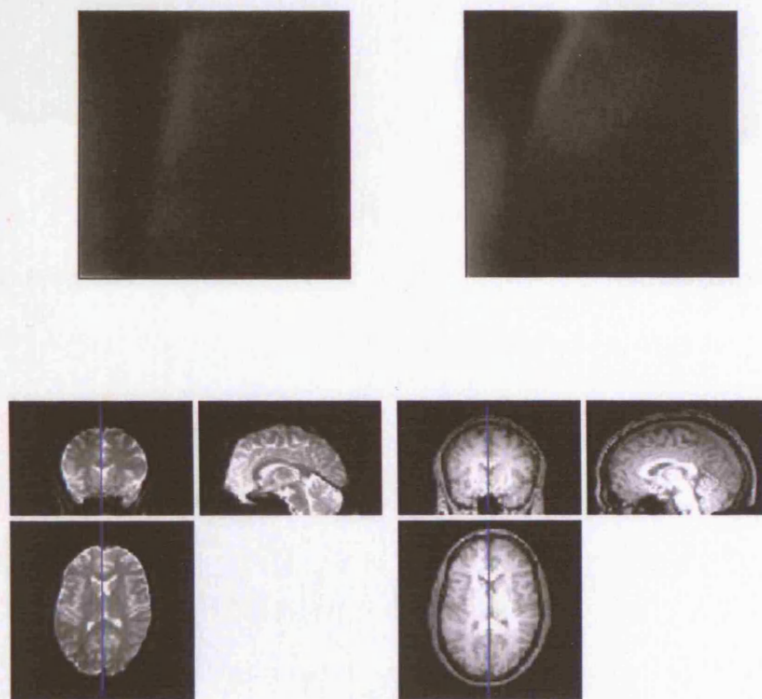
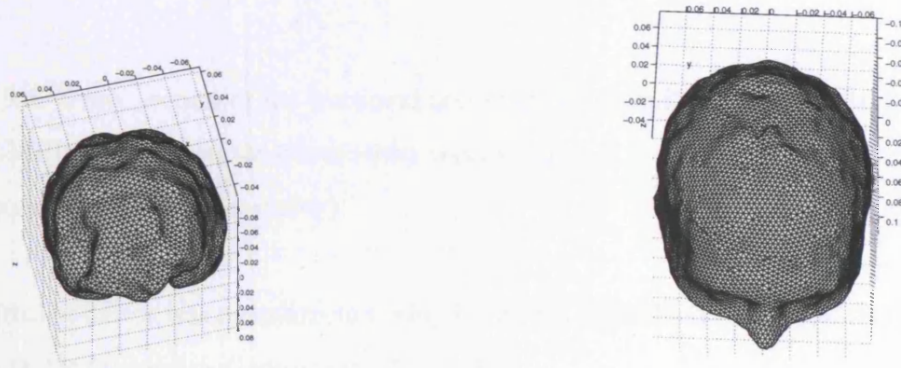
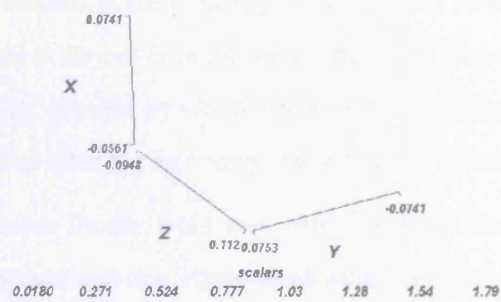


Figure 9.4: Second view of the results of the coregistration of T1-MRI to the B0 of the DT-MRI. Top) initial (left) and final (right) histograms, and bottom) target B0 (left) and coregistered T1 (right).



(a) Brain mesh

(b) Scalp mesh



(c) Conductivity values for the head model

Figure 9.5: Mesh from the coregistered T1-MRI, of 311,727 tetrahedral. a) Brain mesh, b) scalp mesh, c) conductivity model with isotropic conductivity values (S/m): brain 0.30, CSF 1.79, skull 0.018, scalp 0.44.

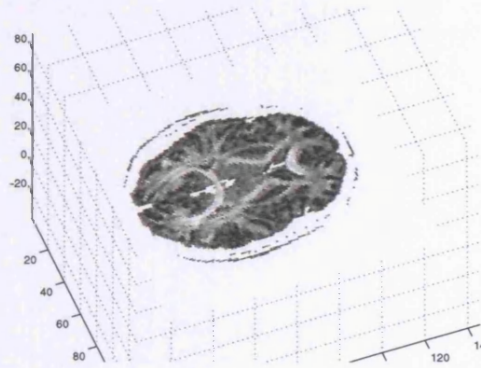


Figure 9.6: Cross section of the fractional anisotropy of the diffusion tensor estimated from the DT-MRI, on a grey scale where white correspond to $FA = 1$ (white matter) and black correspond to $FA = 0$ (grey matter).

The diffusion tensor was reconstructed using LS on the logarithmic version of (9.1) by using the MATLAB function *dwi2tensor* [14] (Figure 9.6).

9.2.3.2 Brain conductivity tensor

The DT was interpolated in the center of each tetrahedral element of the brain mesh and then the linear relationship between the CT and DT was applied. Thus, the DT coefficients T_{ij} , for $i, j = 1, 2, 3$ and $j < i$, defined in the regular grid of the MRI voxels, were interpolated using B-splines and extrapolated at the center of the brain tetrahedra. Before the interpolation, outside the brain the DT was set to isotropic by scaling its trace to the mean trace of the brain; after the extrapolation, the same was done for any nonpositive definite tensor.

The conductivity tensor for the brain was estimated from the diffusion tensor assuming that they shared eigenvectors, and that eigenvalues were proportional [173], $\sigma/T = 0.844 \pm 0.0545 Ss/mm^3$, where T is the diffusion tensor and σ is the conductivity tensor.

Three quantities were calculated and visualised to check the estimated conductivity tensor after the linear relation: the trace, the Fractional Anisotropy (FA) (see below), and main direction of the tensor.

The tensor trace had values around one, most between 0.9 and 1.6, with low and high values that may be caused by a mismatch from a not perfect segmentation or by an overlapping with the CSF tissue (Figure 9.7(a)-9.7(c)). Besides, a linear relation may have yielded a conductivity tensor with larger or smaller trace than the expected conductivity bounds. This was overcome by scaling the CT trace.

The FA, that differentiates the isotropic from the anisotropic tissue, $0 \leq FA \leq 1$, was

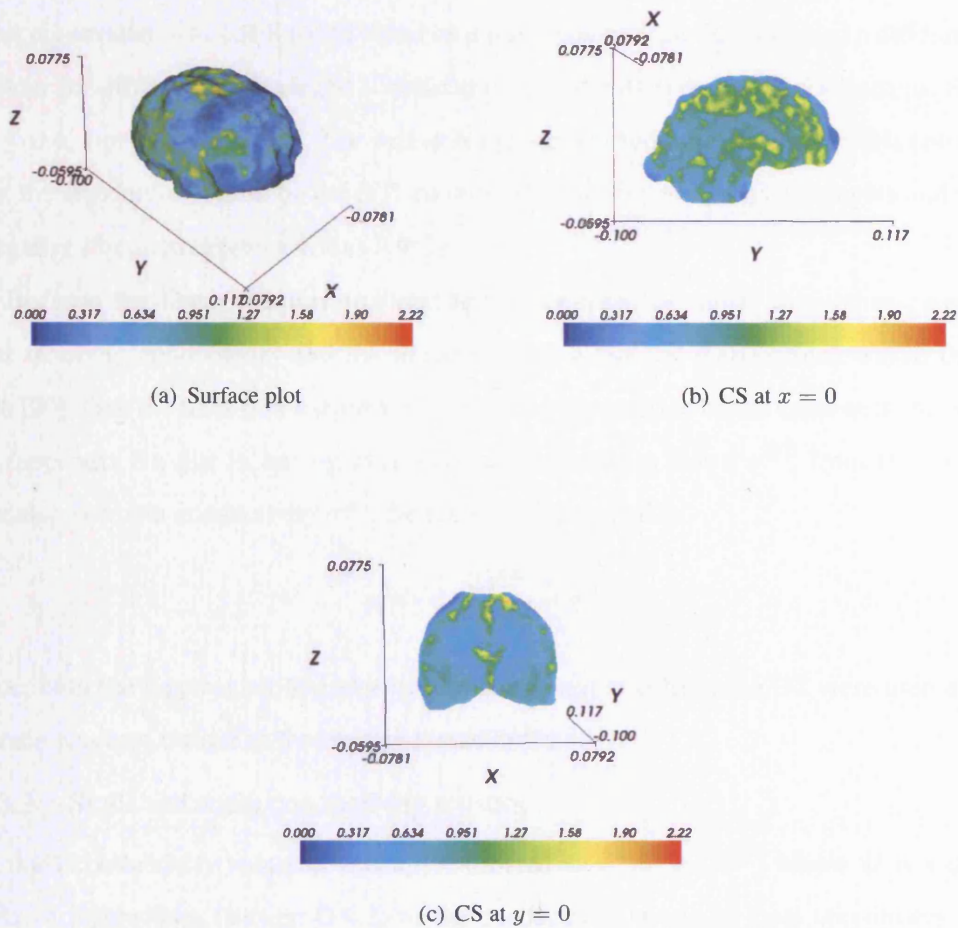


Figure 9.7: Conductivity trace a) surface and b-c) cross section (CS) of the brain conductivity tensor σ obtained from the diffusion tensor T by the linear relation $\sigma/T = 0.844 \pm 0.0545 Ss/mm^3$.

computed as

$$FA = \sqrt{\frac{3}{2}} \left(\frac{(D_{11} - \bar{T})^2 + (D_{22} - \bar{T})^2 + (D_{33} - \bar{T})^2}{D_{11}^2 + D_{22}^2 + D_{33}^2} \right)^{\frac{1}{2}}, \quad (9.2)$$

where $\bar{T} = \bar{D}$ is the mean trace or diffusivity (the bar indicates the mean) and D is the diagonal matrix of eigenvalues (Figures 9.8(a)-9.8(f)).

The main direction of the conductivity tensor was visualised to verify that the directions were well estimated. Thus, the main direction, given by the eigenvector corresponding to the largest eigenvalue, was color coded based on a three-colour scale that assigned a different value or colour for different predominant coordinates x , y , and z (0 or dark blue for isotropic tissue of $FA \leq 0.4$, 1 or light blue for x , 2 or yellow for y , and 3 or red for z). However, this colour code is not the standard one used by the DTI community and does not verify for angles and positive or negative direction (Figures 9.9(a)-9.9(f)).

Because the linear relation provided larger conductivity values than other tissues with larger isotropic conductivity and the linear relation is not yet well defined within the same tissue [90], then the trace of the conductivity tensor was scaled to be the same as in the isotropic case (appendix E); that is, having estimated the conductivity tensor σ^{DTI} from DTI and given the scalar isotropic conductivity σ^{iso} , the tensor σ was scaled as

$$\sigma \leftarrow \frac{3\sigma^{\text{iso}}}{\text{trace}(\sigma^{\text{DTI}})} \sigma^{\text{DTI}}. \quad (9.3)$$

Hence, both the eigenvector and eigenvalue ratios estimated from the DT were used and only the trace was constrained to the isotropic trace $3\sigma^{\text{iso}}$.

9.2.3.3 Skull and scalp conductivity tensors

The skull conductivity tensor σ was approximated as $\sigma = VDV^T$, where D is a diagonal matrix of eigenvalues (section D.4.2) or the conductivity tensor in local coordinates (section A.2.1), and V is a matrix whose columns are the eigenvectors or a linear transformation from the local to the global coordinates. Local coordinates were three orthonormal vectors $V = [v_1, v_2, v_3]$ where v_1 and v_2 spanned a tangential plane and v_3 a normal direction to the skull surface. Eigenvectors were computed for each element of the skull by defining the normal direction v_3 from the vectorial product of two out of three edges in a triangle element on the skull surface, and then by imposing orthonormality for the local basis $\{v_1, v_2, v_3\}$. This defined the eigenvectors for the skull surface; the eigenvectors for the skull volume were defined by assigning to each tetrahedron the same V as that of its closest surface element (Figures 9.10(a) and 9.10(b)).

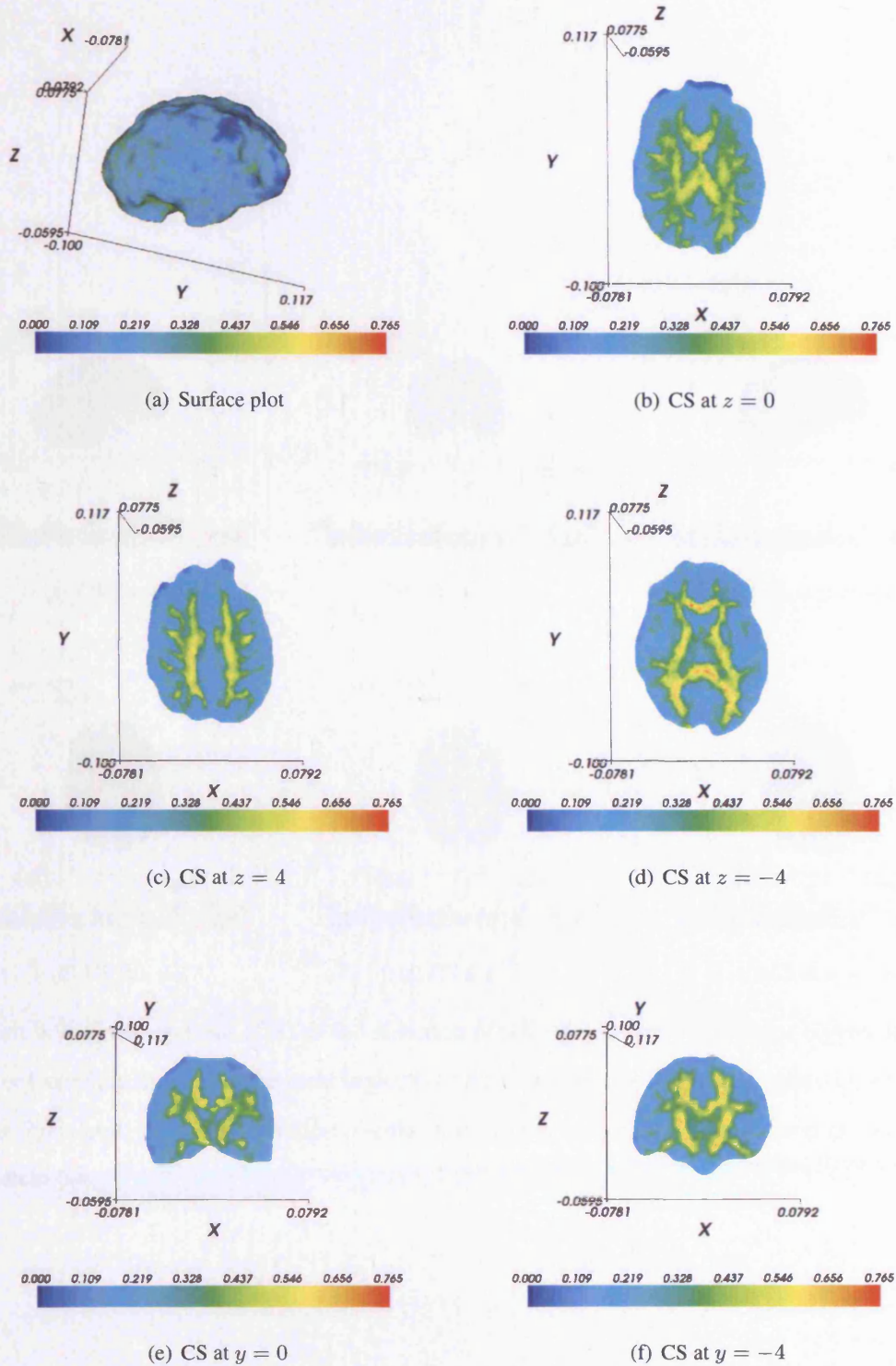


Figure 9.8: a) Surface and b-f) cross sections (CS) of fraction anisotropy of the conductivity tensor interpolated from the diffusion tensor by the linear relation in the brain finite elements.

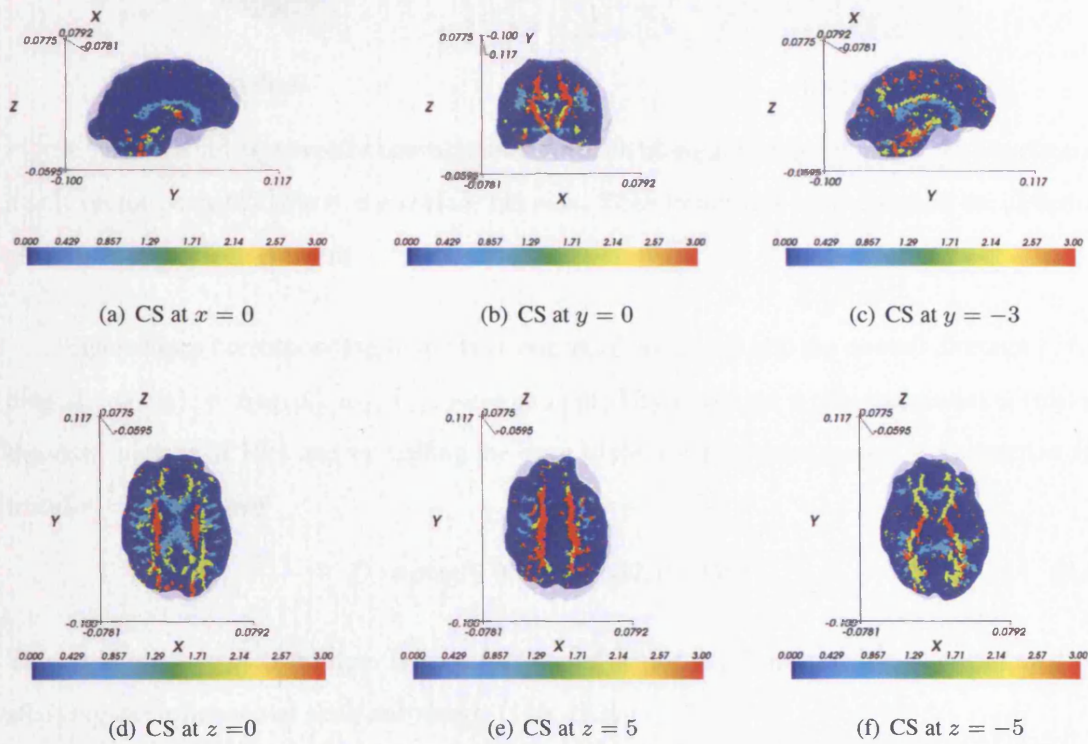


Figure 9.9: Cross sections (CS) of the direction of the eigenvector with largest eigenvalue on a tree colour scale indicating the most important direction among x (light blue, value 1), y (yellow, value 2), z (red, 3), where isotropic conductivity (blue, zero value) was defined as having FA less than 0.4.

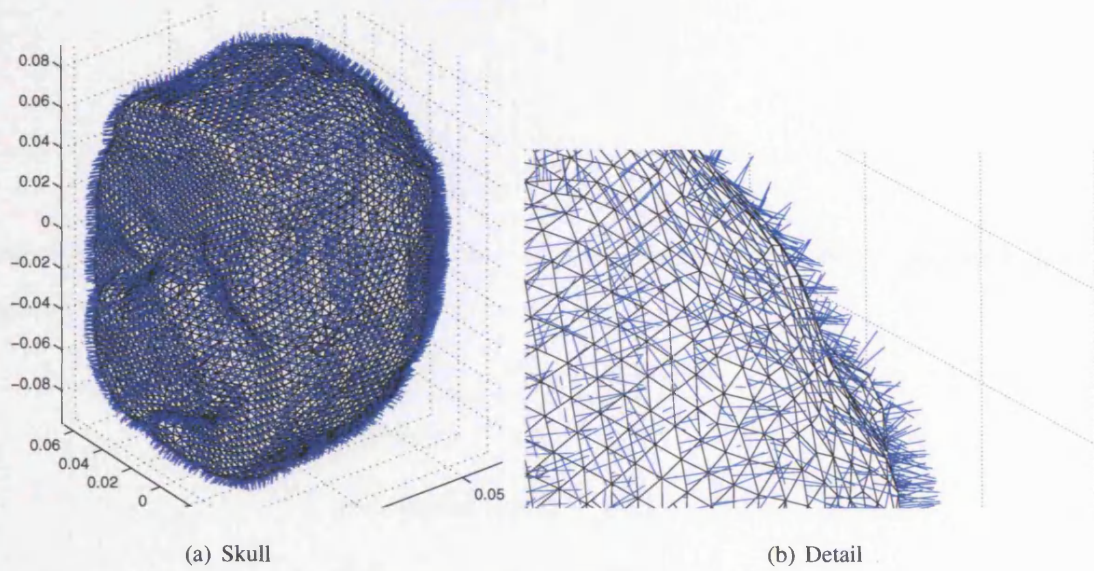


Figure 9.10: Radial eigenvector approximated for each triangular element on the skull surface as a unit vector perpendicular to the surface element. Then tetrahedra were assigned the direction of the closest surface element.

Eigenvalues corresponding to the two tangential directions and the normal direction, $D = \text{diag}(d_1, d_2, d_3) = \text{diag}(d_{tg}, d_{tg}, d_{\perp})$, were computed by imposing a ratio tangential:normal to the skull surface of 10:1 and by scaling the trace to the value of the isotropic trace (section E), $\text{trace}(\sigma) = 3\sigma^{\text{iso}}$, then

$$D = \text{diag}(0.0557, 0.0557, 0.00557). \quad (9.4)$$

Thus, the ratio considered here is an upper bound which has been previously considered for studying the influence of skull anisotropy [146, 182].

The anisotropy of the scalp, whose tensor was computed as in the case of the skull, had a ratio tangential:normal to the scalp surface of 1.5:1 that was approximated its the different tissues and contemplated anisotropy of muscle tissue at 50KHz [77].

9.2.3.4 Conductivity values for the head model

As a summary, for the isotropic tissue CSF, the conductivity tensor σ was defined as $\sigma = \sigma^{\text{iso}} \text{diag}(1, 1, 1)$; for the anisotropic tissues skull, scalp, and brain, the conductivity tensor trace was constrained to be the isotropic one as $\text{trace}(\sigma) = 3\sigma^{\text{iso}}$ (table 9.1). Thus, the trace of the CT in the head was the same for each tissue type (Figures 9.11(a)-9.11(c)).

The isotropic conductivity values used were selected from [77] corresponding to 50KHz that yielded the largest scalp voltages for epilepsy [44]: brain 0.30, CSF 1.79, skull 0.039, and scalp 0.44Sm^{-1} (Figure 9.5(c), Table 9.1).

Table 9.1: Tissues isotropic value σ^{iso} and tangential:normal conductivity ratio such that $\text{trace}(\sigma) = 3\sigma^{\text{iso}}$.

tissue	σ^{iso}	tg:normal
grey matter	0.30	DTI
white matter	0.30	DTI
skull	0.039	10:1
scalp	0.44	1.5:1
CSF	1.79	1:1

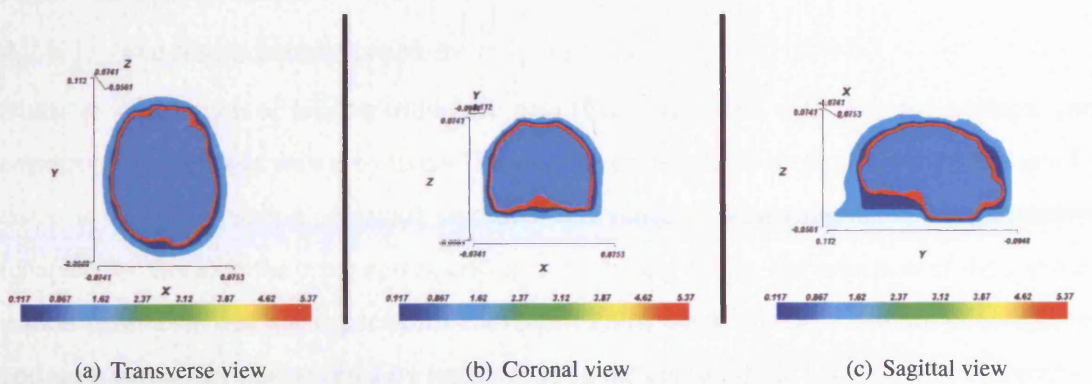


Figure 9.11: Three cross sections of the conductivity tensor trace for all head.

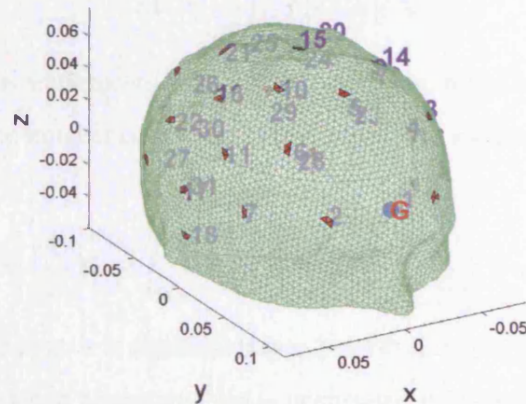


Figure 9.12: Electrode positions.

9.2.4 Forward solution

The voltage was solved everywhere using a modified version of 3D-EIDORS [140], piecewise linear for the voltages and constant for the conductivity, that models anisotropic media by accounting for a general tensor in the main compartment of the system matrix [1].

The 31-electrode position and protocol previously used at the UCL group [15] was implemented as given in section 5.2.5.2. Electrodes were approximating by using two triangle surface elements per electrode (Figure 9.12). The contact impedance accounting for skin and electrode impedance was set to $1K\Omega$ which is of the order of the measured values on human scalp [115]. The injected current was set to 5mA.

9.2.5 Inverse problem

9.2.5.1 The linear inverse problem

Scalar reconstruction of relative difference data (C.2), simulated with both the isotropic and anisotropic model, was solved by using Tikhonov as the inversion method and the GCV and L-curve as the regularisation parameter selection for a range of twenty regularisation parameters (chapter 5). Because the error corresponded to modelling errors, the selection of the regularisation parameter was not expected to converge. Thus, when the GCV did not converge, an optimum parameter was selected by approximating the corner of the L-curve. The reconstruction was constrained to the brain which reduced the Jacobian size and improved numerical stability.

In the isotropic case, as in chapters 5 and 6, the conductivity in the k th-finite element was represented as $\sigma^k = \beta^k \text{diag}(1, 1, 1)$, where β^k is a multiple scalar to the unit matrix. A change of conductivity, that leaves the conductivity isotropic, $\delta\sigma = \delta\beta \text{diag}(1, 1, 1)$, yields a change in

voltage δV which can be represented by the linear relation [140]

$$\delta V = - \int_{\Omega_k} \delta\beta (\nabla u)^T \nabla u^*. \quad (9.5)$$

Let V be one of the measurements on the scalp electrodes, then the Jacobian row, J^k for $k = 1, \dots, n$ where n is the number of elements, that relates that measurement to the element Ω_k is given by (3.13)

$$J^k = \frac{\delta V}{\delta\beta} = - \int_{\Omega_k} (\nabla u)^T \nabla u^* = - \int_{\Omega_k} \sum_{i=1}^3 (\nabla u)_i (\nabla u^*)_i. \quad (9.6)$$

In the anisotropic case, σ is a general tensor, yet, here, only a perturbation of the tensor that leaves the eigenvectors and eigenvalue ratios unchanged was considered. Let β be a multiple scalar to the tensor, such that $\sigma = \beta\sigma_0$, where σ_0 is a known tensor with $\det(\sigma_0) = 1$. Then, based on the Jacobian for a multiple scalar to an isotropic tensor (9.6), a change of conductivity, $\delta\sigma = (\delta\beta)\sigma_0$, was related to a change in voltage δV as

$$\delta V = - \int_{\Omega_k} \delta\beta (\nabla u)^T \sigma_0 \nabla u^*. \quad (9.7)$$

Hence, the Jacobian entry J^k that relates the measurement V to the element Ω_k is given by

$$J^k = \frac{\delta V}{\delta\beta} = - \sum_{i=1}^3 \sum_{j=1}^3 (\nabla u)_i (\sigma_0)_{ij} (\nabla u^*)_j, \quad (9.8)$$

which corresponds to the tensor product $\langle \nabla u, \nabla u^* \rangle_{\sigma_0}$ (A.9). In fact, by assigning $\sigma_0 = \text{diag}(1, 1, 1)$, one recovers the isotropic case.

The anisotropic Jacobian is different to the isotropic one, not only in the tensor product of the electrical fields given by σ_0 , but in the voltages u and u^* obtained by solving the forward problem for an anisotropic conductivity reference σ_{ref} . Previous to the inversion of the Jacobian, it was row normalised (section C.3) by providing a reference voltage $F(\sigma_{\text{ref}})$ where σ_{ref} was the reference conductivity.

9.2.6 Comparison of the forward solutions

First, the qualitative effects of anisotropy of the skull and white matter were studied separately for meaningless conductivity values, and then the global effect was analysed for a realistic conductivity model.

9.2.6.1 Qualitative comparison

To study the effect of the anisotropy of the skull, the anisotropic tensor for the skull (section 9.2.3.3) was scaled to have the same trace as the isotropic one, and the rest of the head was set to isotropic conductivity $\sigma = \text{diag}(1, 1, 1)$. The current density norm

$$\|J\| = \|\sigma E\| \quad (9.9)$$

for this model and the corresponding one for the isotropic model were compared. Similarly, the effect of anisotropy of white matter (section 9.2.3.2) was modelled.

9.2.6.2 Quantitative comparison

The isotropic and anisotropic models with the conductivity parameters from table 9.1 were compared in terms of the current density norm, the percentage voltage error in the domain and at the boundary by neglecting anisotropy, the absolute voltage difference for the inclusive conductivity perturbation in the anisotropic model and the reference conductivity in both the isotropic and anisotropic models, and the relative difference between the voltages for the reference conductivity and an inclusive conductivity perturbation for both the isotropic and anisotropic models.

9.2.7 Comparison of the reconstructed images

Three cases were considered for linear image reconstruction: i) data simulated with the isotropic model and scalar reconstruction for isotropic conductivity to test the inversion and set a bound for the best possible reconstruction, ii) data simulated with the anisotropic model and scalar reconstruction assuming isotropic conductivity to test the error by neglecting anisotropy, and iii) data simulated with the anisotropic model and scalar reconstruction for anisotropic conductivity to test the proposed method for recovering a multiple scalar to a general tensor. Images were visualised and compared in terms of the localisation error

$$LE = \|r_{\text{rec}} - r\| \quad (9.10)$$

where r was the location of the simulated conductivity change and r_{rec} was the location of the maximum peak near the region of interest of the reconstructed image. Thus, artefacts outside the region of interest, mainly near the surface of the brain, were not considered in defining the maximum peak. The location of the peak in the reconstructed images was obtained by manual selection of the coordinates in a 3D image created with the MayaVi visualisation toolkit [142]. The procedure was to smooth the reconstructed image, find the peak near the RoI by using a cross section view in three orthogonal directions, and maximisation of the image till the peak could be accurately selected.

In addition to the LE, images of the simulated and reconstructed conductivity changes were displayed as cross sections for orthonormal and sagittal views at the simulated locations and an isosurface 3D image for comparing artefacts in the whole brain. Images corresponding to simulated conductivity increase were displayed for a positive range only not showing negative values, to simplify the comparison.

9.2.8 Simulation of conductivity changes

A change in conductivity was simulated by multiplying the tensor σ by a scalar $\beta > 1$ for an increase in conductivity and $\beta < 1$ for a decrease in conductivity. Hence, it was assumed that the tensor structure did not change and simulated conductivity changes were placed in the grey matter. Eight simulations were done: four in the occipital lobe where one was the only simulation with the isotropic model and other one resembled stimulation of the visual cortex; two resembling epilepsy changes [44], one in the temporal lobe and one in the hippocampus; and two in the parietal and temporal lobes. In the occipital lobe (location A, Figures 9.13(a)-9.13(b)), three spherical conductivity changes of 35mm diameter and one of 17mm were simulated, three of them of 10% conductivity increase, and other of 1% increase simulating stimulation of the visual cortex. A 10% conductivity decrease located in the temporal lobe (location B, Figure 9.13(c)-9.13(e)) was simulated as a disc of 25mm radius and 10mm height, of 18cc (Figures 9.31(a),9.31(b),9.31(d)). A 10% conductivity decrease located in the hippocampus (location C, Figures 9.13(f)-9.13(c)) was simulated as a cylinder of 30mm length and 5.5mm radius, of 2.5cc (Figures 9.32(a),9.32(b),9.32(d)). Another two locations were chosen surrounded by white matter (locations D and E, Figures 9.14(a)-9.14(d)).

9.3 Results

9.3.1 Preliminaries: Voltage and current density in an anisotropic domain

9.3.1.1 Cubic model

In the isotropic domain, the voltage (Figure 9.15(a)) and current density norm (Figure 9.15(c)) propagated uniformly throughout the domain. The potential decreased uniformly, forming semicircular isopotential curves centred at the injection point. In the anisotropic domain, with the x-direction as preference for the conductivity, the current preferred to flow in the x-direction rather than in the y or z-direction, where the isopotential curves were parallel to the x-axis (Figures 9.15(c) and 9.15(d)) as was expected from an increase of the conductivity in the x-direction (Figure 9.16).

The electric field at each point was directed towards parts of the domain of lowest potential. In the isotropic domain, these pointed perpendicular to the semicircular isopotential curves (Figure 9.17(a)); in the anisotropic domain, these pointed perpendicular to the x-axis (Figure 9.17(c)). The current density vector, which depends on the electric field orientation and preferred conductivity direction, in the isotropic domain, coincided with the electric field flowing uniformly to points of lowest voltage, equally to high values in x and the y-direction (Figure 9.17(b)); in the anisotropic domain, it pointed to high values of y and low values of x (Figure

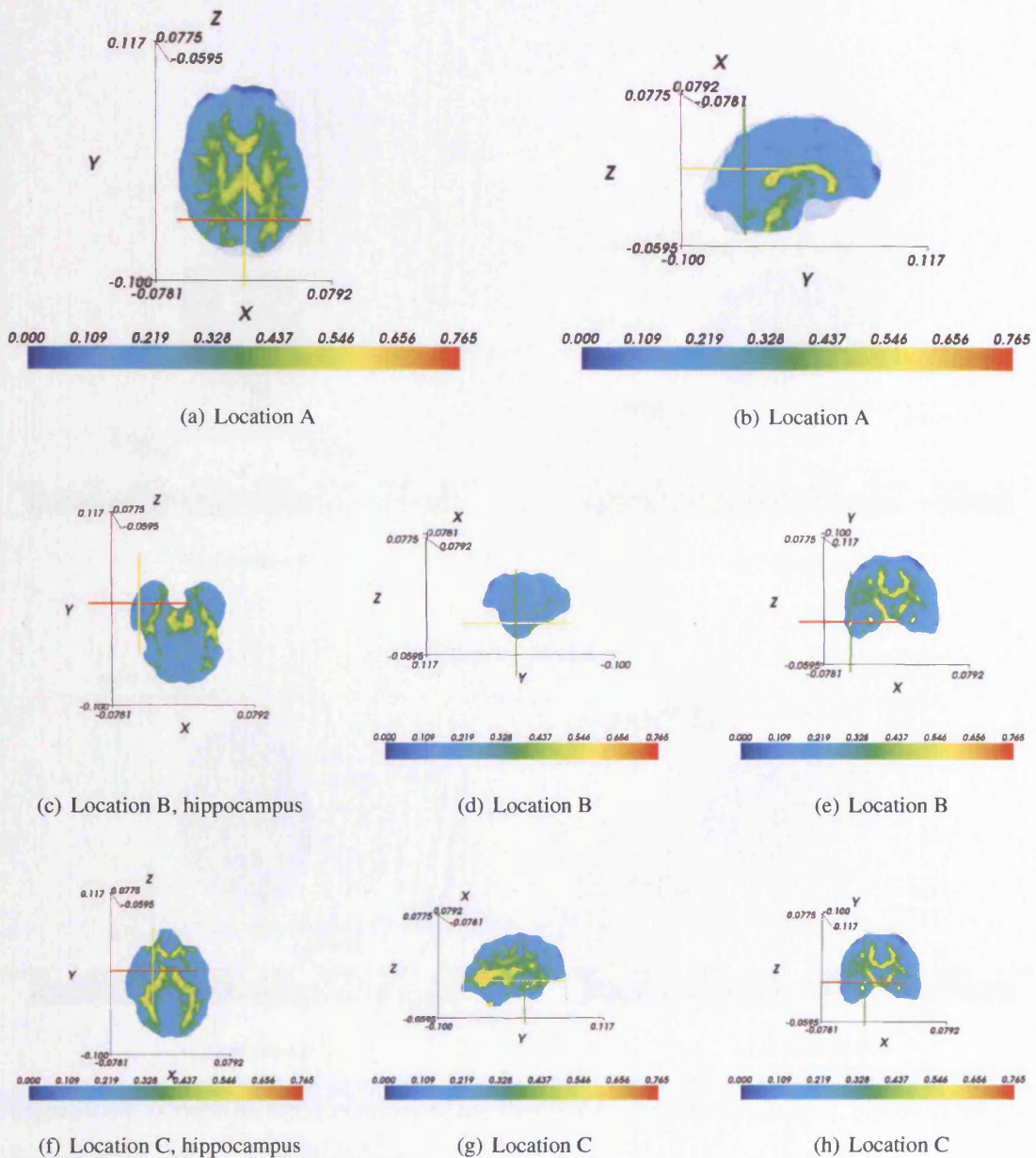
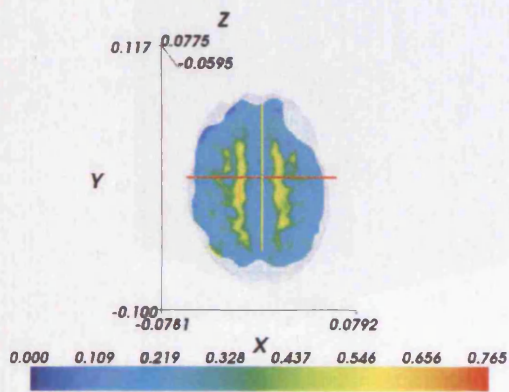
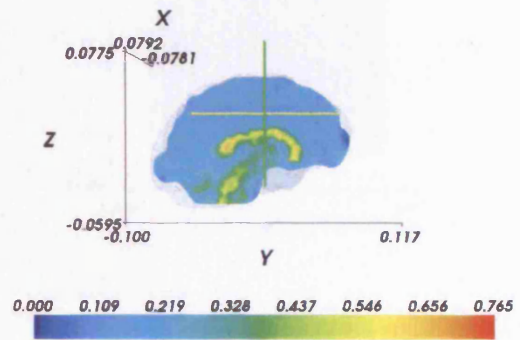


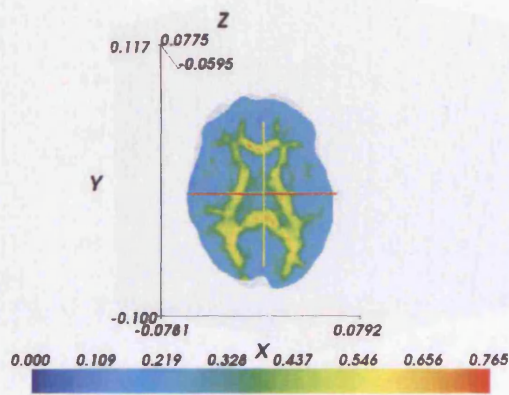
Figure 9.13: Locations of the simulated conductivity changes, placed in the grey matter, within FA in the background, in A) the occipital lobe to simulate stimulation of the visual cortex, and in B) the temporal lobe and C) the hippocampus to simulate changes in epilepsy.



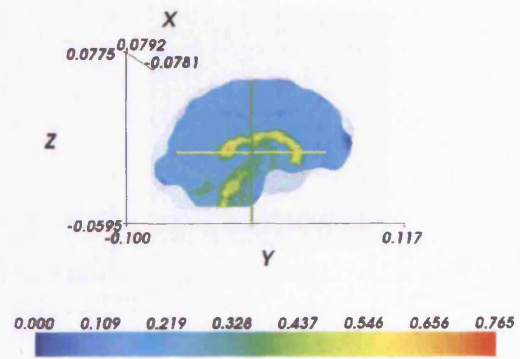
(a) Location D



(b) Location D

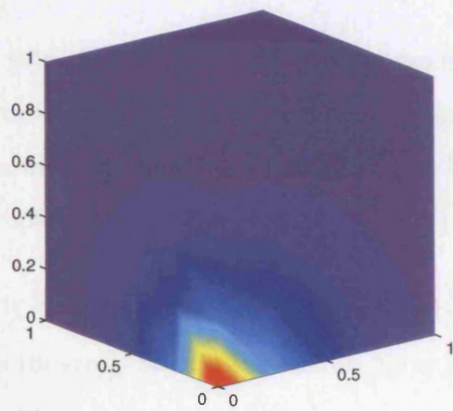


(c) Location E

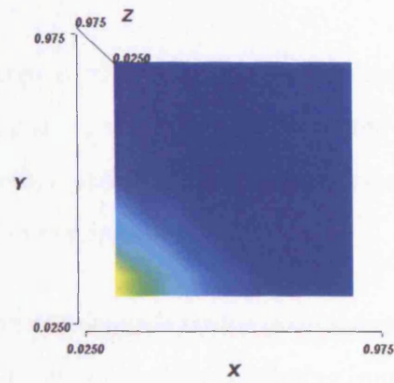


(d) Location E

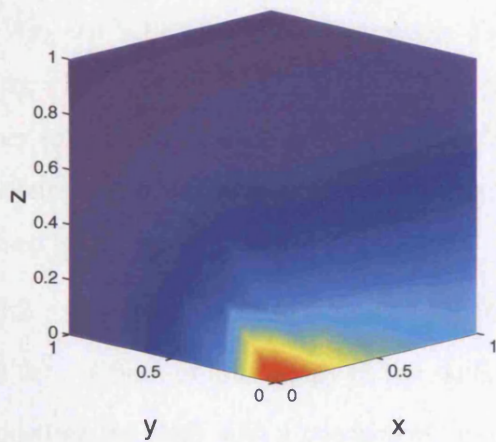
Figure 9.14: (Continuation) Locations of the simulated conductivity changes, placed in the grey matter, within FA in the background.



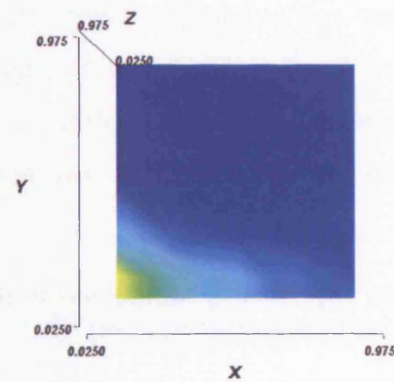
(a) Surface potential in the isotropic domain



(b) CS current density norm in the isotropic domain



(c) Surface potential in anisotropic domain



(d) CS current density norm in the anisotropic domain

Figure 9.15: Comparison of the surface potential (left) and current density norm (right) cross section (CS) at $z = 0.08$ (right), for a-b) an isotropic domain with $\sigma = \text{diag}(1, 1, 1)$ and c-d) an anisotropic domain with $\sigma = \text{diag}(10, 1, 1)$, for a current injection with value one at $(0, 0, 0)$ and zero elsewhere (current perpendicular to ones), using the nodal based conductivity model.

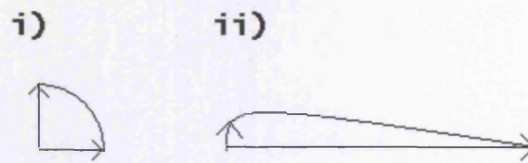


Figure 9.16: Sketch of the expected isopotential voltage in 2D for i) an isotropic domain and ii) anisotropic domain with ten times higher conductivity in the x-direction. While in the isotropic domain the isopotential is expected to be a semicircle centered at the injection point, in the anisotropic domain it is expected to become parallel to the main direction.

9.17(d)). Since the direction of the current density vector depends on the potential, and is not straight forwardly related to the conductivity tensor, it was not used for comparing isotropic and anisotropic domains; instead the current density norm was used.

9.3.1.2 Concentric sphere

In the isotropic domain, the current decreased uniformly from the injection point (Figures 9.19(a) and 9.19(b)). In the anisotropic domain, the current preferred to flow tangentially to the surface of the middle sphere with a significant decrease of current that flows into the inner sphere (Figures 9.19(a)-9.19(d)). In fact, a large difference between the isotropic and anisotropic domains was due to the thickness of the interior shell, and so a lesser effect is expected for the skull.

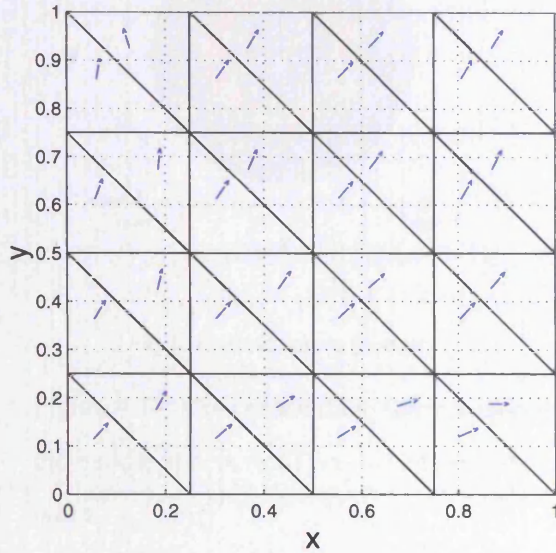
9.3.2 Qualitative comparison of the forward isotropic and anisotropic solutions

9.3.2.1 Effect of anisotropy of the skull

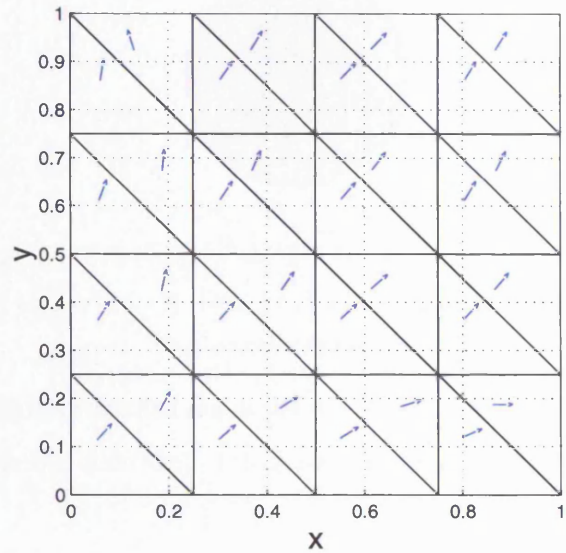
Modelling the skull with a conductivity ratio tangential:normal of 10:1 reduced the current density norm by half after crossing the skull layer (Figure 9.20(b)) while, in the isotropic model, it propagated uniformly (Figure 9.20(a)). The most relevant effect was to reduce the amount of current that penetrated into the brain; the field distribution still formed semicircles with larger radii after crossing the skull.

9.3.2.2 Effect of anisotropy of the white matter

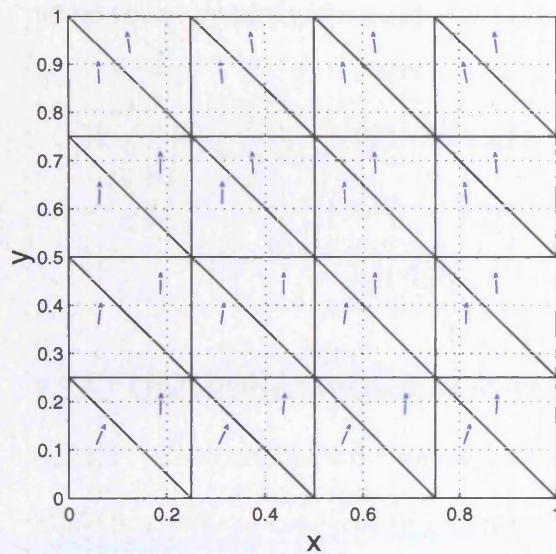
The anisotropy of the white matter changed the field distribution in the brain where the current propagated along the white matter fibres which were parallel to the current injection and was almost zero for those fibres that were aligned perpendicular to the injection field direction (Figures 9.21(b)-9.21(e)).



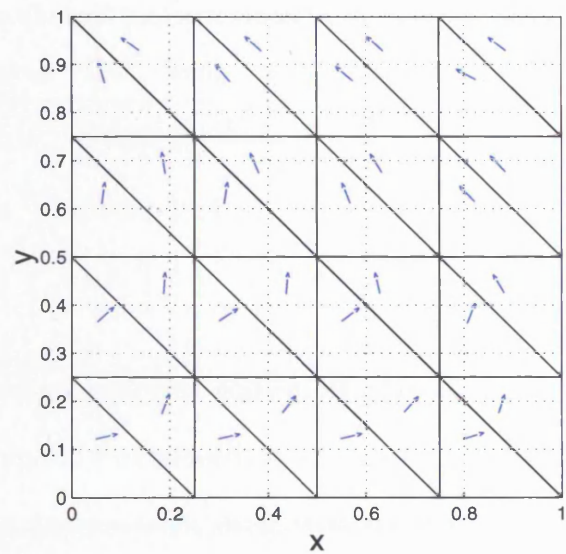
(a) Electrical field in the isotropic domain



(b) Current density in the isotropic domain



(c) Electrical field in the anisotropic domain



(d) Current density in the anisotropic domain

Figure 9.17: Cross sections, at $z = 0.08$, of the electrical field $E = -\nabla u$ (left) and normalised current density $J = \sigma E$ (right), for a-b) an isotropic domain with $\sigma = \text{diag}(1, 1, 1)$, and c-d) an anisotropic domain with $\sigma = \text{diag}(10, 1, 1)$.

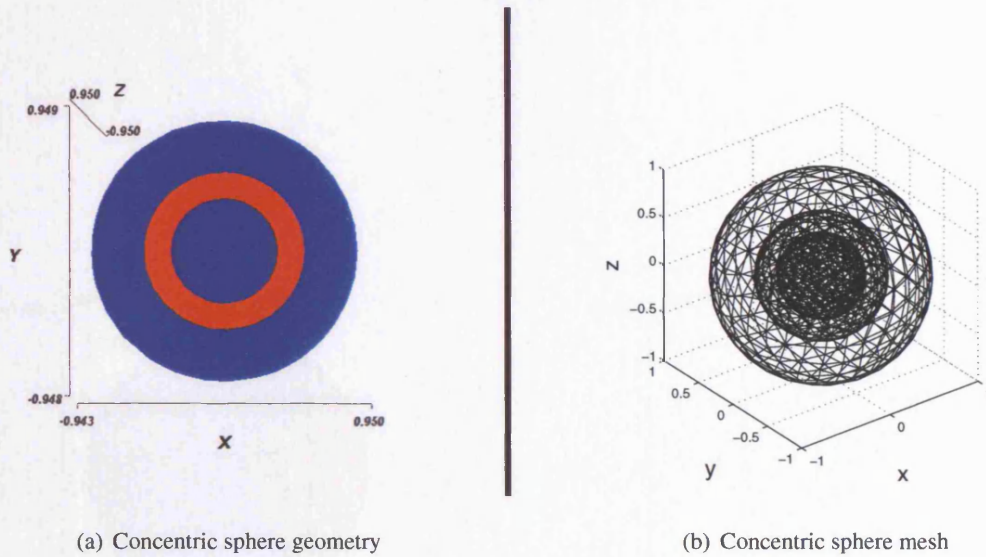


Figure 9.18: Concentric three spheres model with interior shell radius $0.4 \leq r \leq 0.6$, where a) the middle sphere (red) was anisotropic and inner and outer shells (blue) were isotropic, and b) mesh.

Table 9.2: Percentage current density norm at each shell, e.g. $100 \sum_{i \in \text{shell}} \|J_i\| / \sum_{i \in \text{head}} \|J_i\|$, where i corresponded to the tetrahedral elements, for both the isotropic and anisotropic models.

model	scalp	skull	CSF	brain
ISO	42.8	3.9	31.3	22
ANI	64.4	4	18.2	13.4
ANI/ISO	1.5	1	0.6	0.6

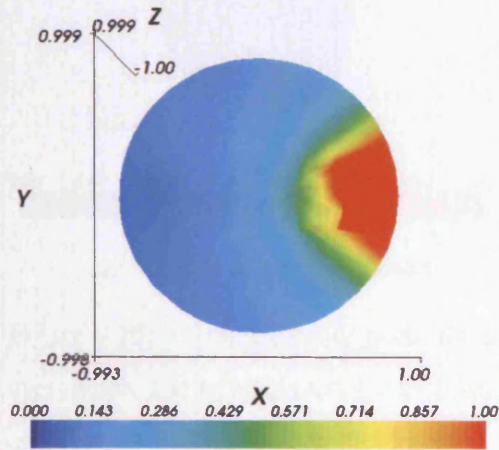
9.3.3 Quantitative comparison of the forward isotropic and anisotropic solutions

9.3.3.1 Comparison of the forward solutions for the conductivity reference

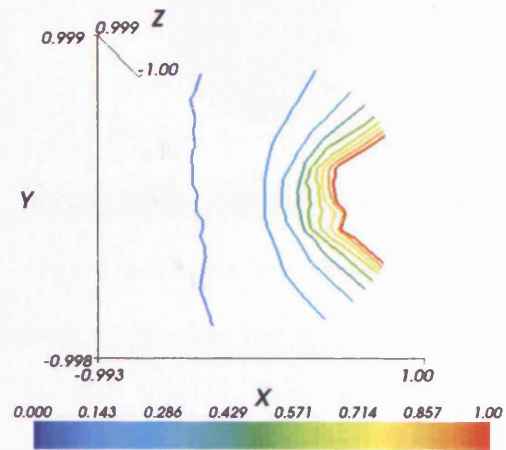
Modelling realistic conductivity parameters for the anisotropic head model (table 9.1), the current flowed tangential to the scalp and skull surfaces (Figure 9.22(b)) with respect to the isotropic model (Figure 9.22(a)), leading to a reduction by two of the total current that flows into the brain (table 9.2, Figures 9.22(c)-9.22(d)). The field distribution in the anisotropic brain indicated that the preferred direction was along the white matter fibres.

The effect of anisotropy on the voltage was the same effect as on the current norm (Figures 9.23(a)-9.23(b)). Thus, neglecting anisotropy led to a relative voltage error at the boundary of 53% (table 9.3, Figure 9.23(c)).

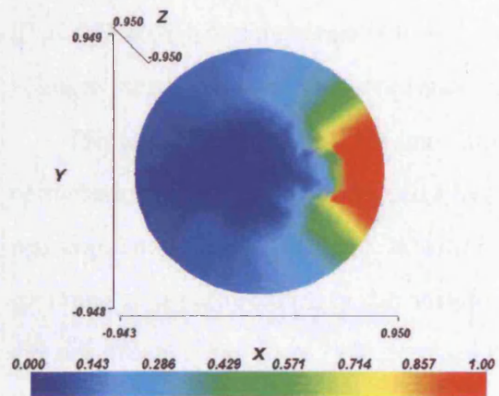
Modelling a local conductivity change of 10% (Figure 9.24) in the occipital part of the



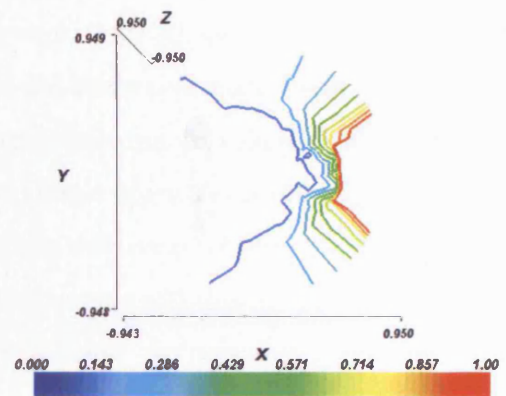
(a) Current density norm



(b) Current density norm (contour map)



(c) Current density norm



(d) Current density norm (contour map)

Figure 9.19: Cross section (left), at $z = 0$, and contour plot (right), for the current density of a-b) an isotropic domain with $\sigma = \text{diag}(1, 1, 1)$, and c-d) an anisotropic sphere with $\sigma = VDV^T$, where $D = \text{diag}(1.493, 1.493, 0.15)$ such that $\text{trace}(D) = 3$, in between inner and outer isotropic concentric spheres, for a nodal based conductivity and current pattern perpendicular to one.

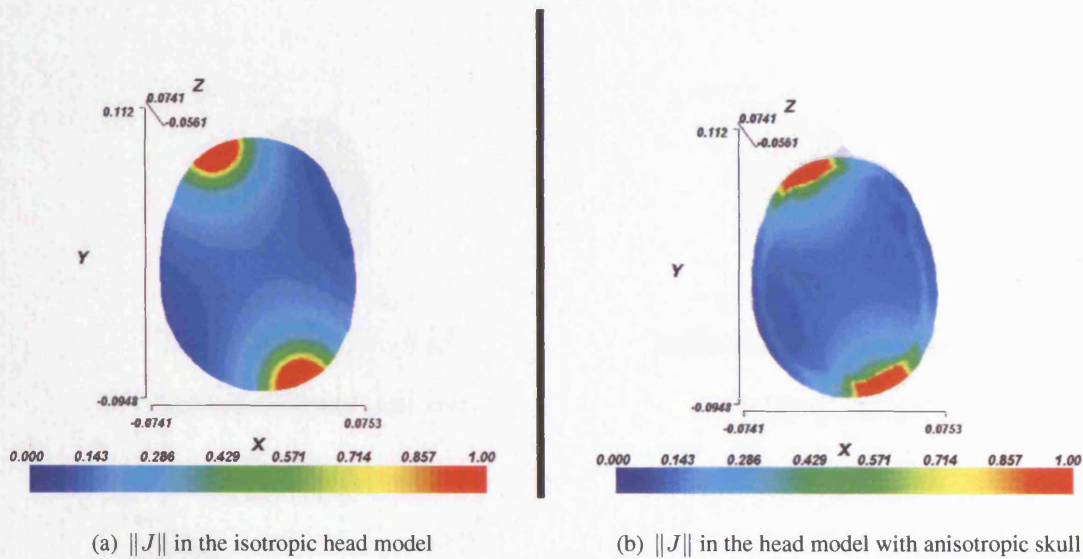


Figure 9.20: Current density norm for the a) isotropic head model with $\sigma = \text{diag}(1, 1, 1)$ everywhere and b) head model with anisotropic skull with $\sigma = VDV^T$ with eigenvalues $D = \text{diag}(1.43, 1.43, 0.14)$, such that $\text{trace}(\sigma) = 3$ for both the isotropic and the anisotropic head model.

brain led to a change of 0.0124% on the boundary voltage mean for the anisotropic model (Figure 9.26(a)), and a change of 0.06% for the isotropic model (Figure 9.26(b)); the boundary voltages mean was more than five times smaller for the anisotropic model (table 9.3).

The absolute difference, for one current injection, between the voltages with and without perturbation in the domain produced a local voltage change where the conductivity perturbation was simulated (Figure 9.25(a)); however, the absolute difference between the voltages corresponding to a perturbation in the anisotropic model and the reference in the isotropic model did not produce any local voltage change (Figure 9.25(b)). An important conclusion is that absolute imaging may be not possible without modelling anisotropy since the absolute voltage difference for a local perturbation was significantly smaller than the absolute difference between both models.

9.3.4 Effect of anisotropy on the linear image reconstruction of difference data

First, the reconstruction procedure was shown for a simulated change in the isotropic model, and then, the data was simulated in the anisotropic model and the comparison between the reconstructed images with the isotropic and anisotropic models was done (table 9.4).

9.3.4.1 Isotropic data and scalar isotropic reconstruction

As an example of the linear reconstruction procedure using Tikhonov and the GCV or the L-curve, the functionals used in chapter 5 are shown for the case of perturbation in the occipital

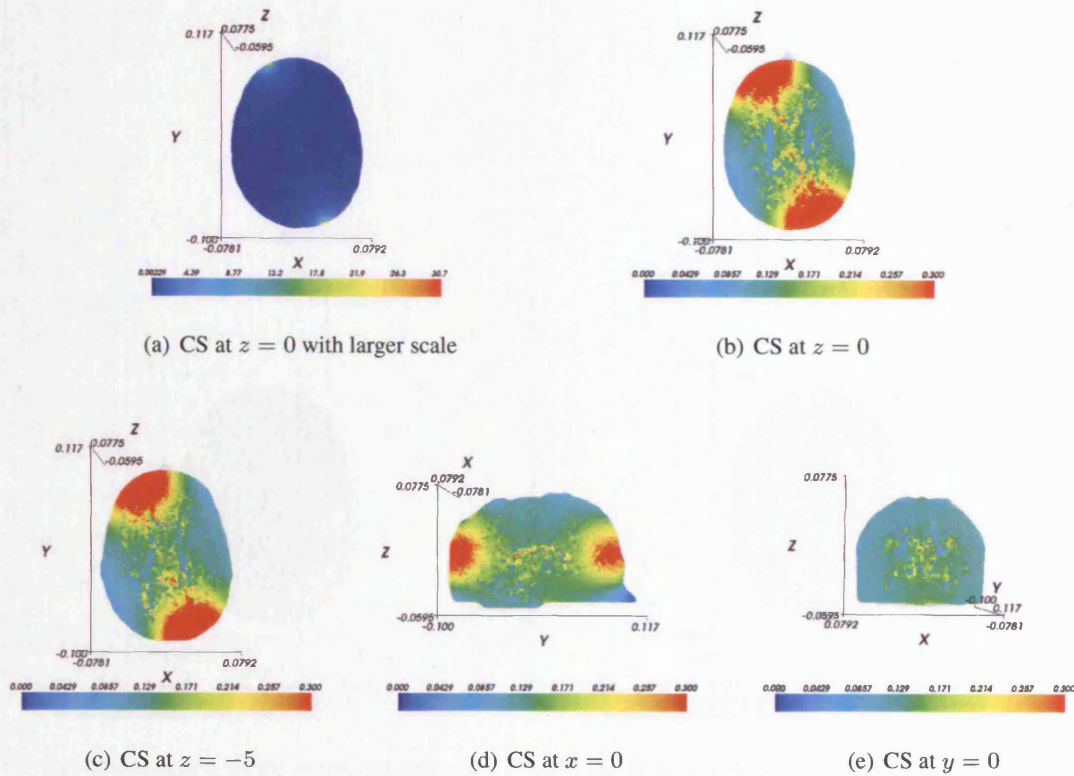
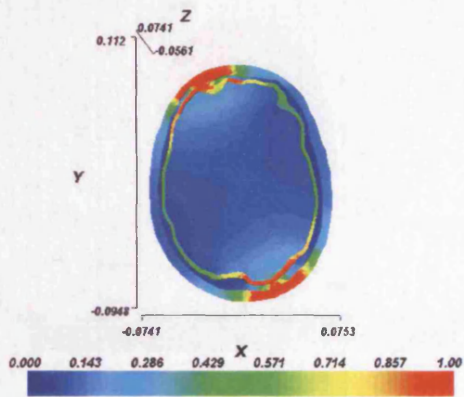


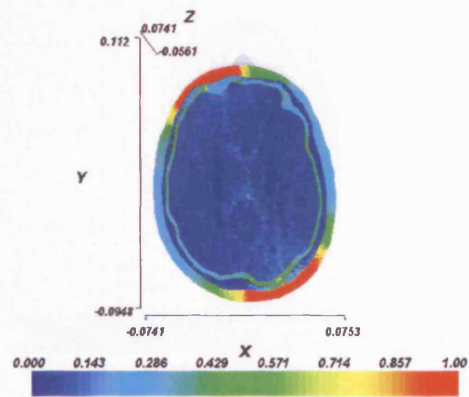
Figure 9.21: Cross sections (CS) of the current density norm $\|J\|$ for head model with anisotropic tensor for the brain estimated from DTI and scaled to $\text{trace}(\sigma) = 3$, where a) covers the whole range of values and b-e) covers a small range between two and three order of magnitude less for the current decrease because of the volume effect.

Table 9.3: Summary of scalp voltage comparisons between the isotropic and anisotropic models with and without a perturbation in the occipital lobe. First row - absolute relative difference (RD) between the anisotropic and isotropic boundary voltages for the reference conductivity: $RD = 100|(F(\sigma^{\text{ani}}) - F(\sigma^{\text{iso}}))/F(\sigma^{\text{ani}})|$, i.e. the error by neglecting anisotropy. Remaining rows - the relative difference between the boundary voltages with and without a conductivity perturbation, $RD = 100|(F(\sigma^{\text{inh}}) - F(\sigma^{\text{ref}}))/F(\sigma^{\text{ref}})|$, giving the mean (\bar{RD}) and standard error (SE), for the isotropic model and the anisotropic models, for a local perturbation where location, % change and size are specified.

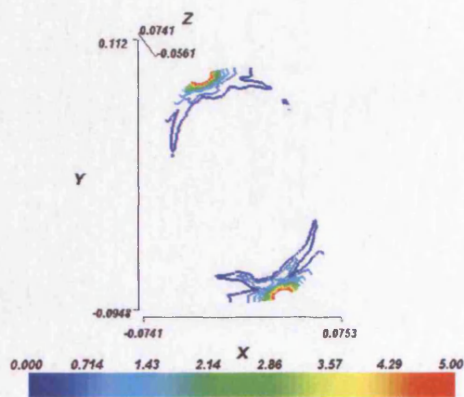
location	change	size(mm)	models	\bar{RD}	SE(RD)
-	-	-	ANI(REF) & ISO(REF)	53	0.32
occipital	10	35	ISO(INH) & ISO(REF)	0.061	0.004
occipital	10	35	ANI(INH) & ANI(REF)	0.0124	0.0001



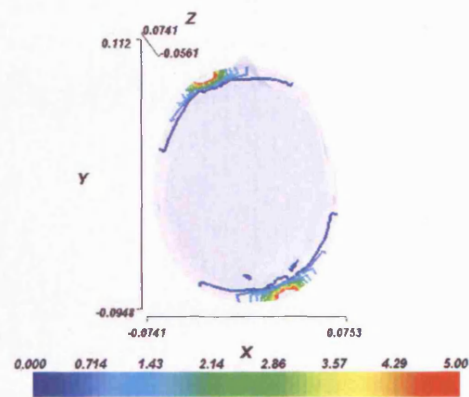
(a) Current norm for the isotropic head model



(b) Current norm for the anisotropic head model

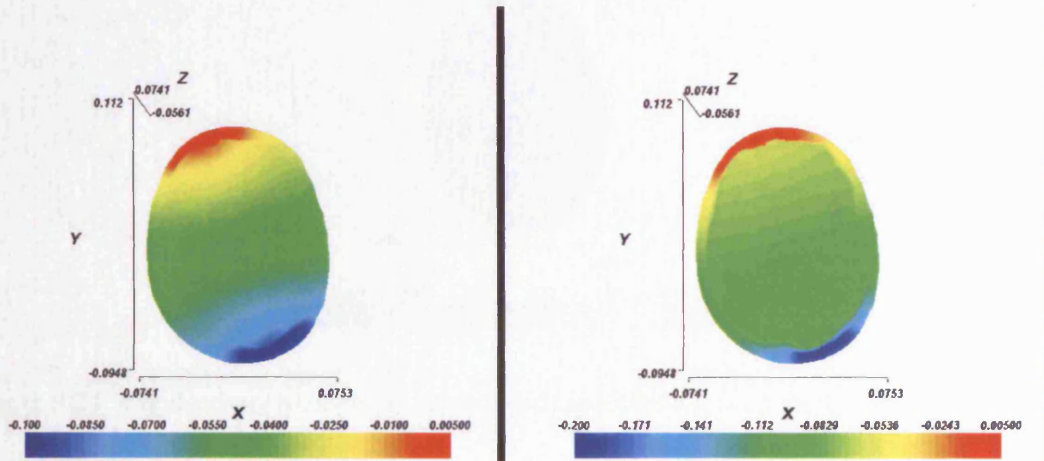


(c) Current norm contours for the isotropic model



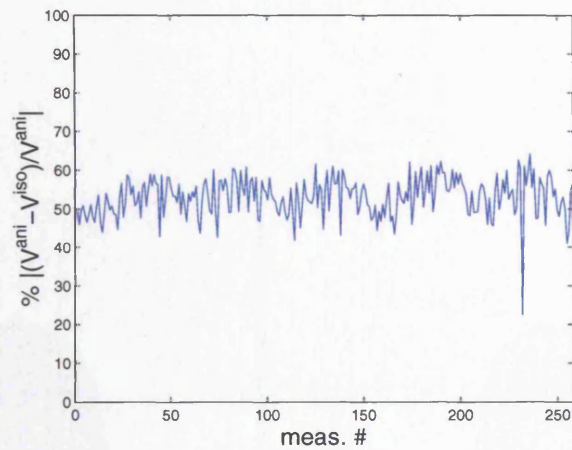
(d) Current norm contours for the anisotropic model

Figure 9.22: Current norm cross section for the a) isotropic and b) anisotropic head models. c-d) Same as a-b) but as contour maps.



(a) Isotropic head model

(b) Anisotropic head model



(c) Measurement voltage percentage difference

Figure 9.23: Cross sections of the voltage for the a) isotropic and b) anisotropic models, and c) Measurement voltage percentage error produced by considering the isotropic instead of the anisotropic model, $100|(V^{\text{ani}} - V^{\text{iso}})/V^{\text{ani}}|$ where V are the simulated measurement voltages with both models.

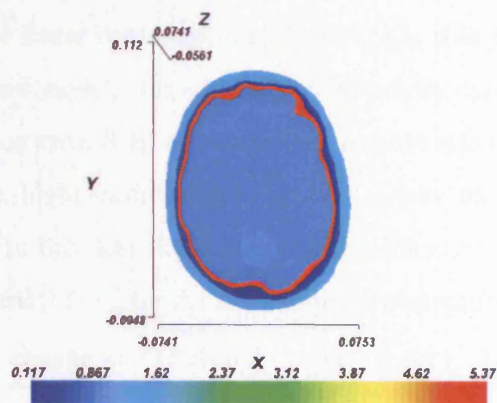


Figure 9.24: Conductivity trace in the anisotropic model for a local perturbation of 10% in the occipital lobe.

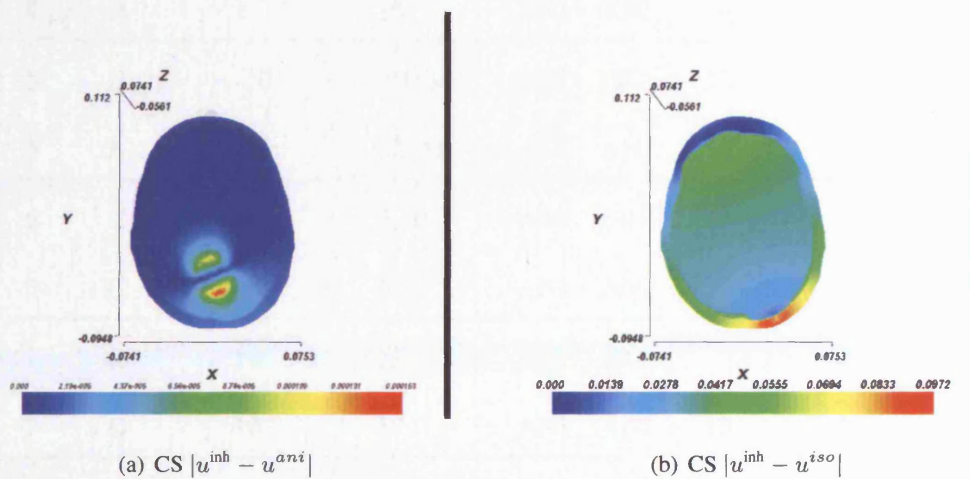
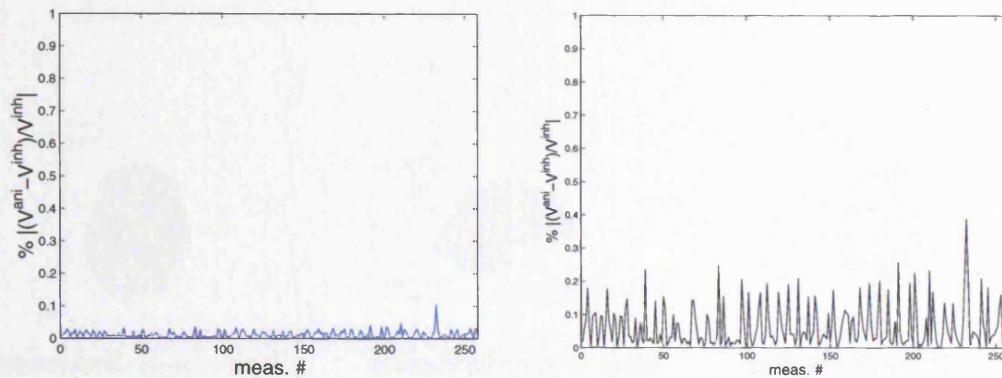


Figure 9.25: Cross section (CS) ($z = -4$) of the absolute voltage difference between the a) anisotropic models with and without perturbation, and b) anisotropic with perturbation and isotropic model, for one current injection.

Table 9.4: Results of the linear reconstruction of difference data for the isotropic (ISO) and anisotropic (ANI) data and models, for simulated conductivity changes in different locations, in terms of the localisation error (LE) and maximum reconstructed conductivity value (peak). Also the size (¹diameter, high) in millimeters is given, where the size of the head of the y-direction was 218mm. ²In this data there were two maximums. The LE was 15 ± 3 for the isotropic reconstruction and 13 ± 2 for the anisotropic reconstruction.

SIM	location	change %	size(mm)	data	model	LE(mm)	% peak
1	A	10	35	ISO	ISO	8	3.7
2	A	10	35	ANI	ISO	8	0.7
2	A	10	35	ANI	ANI	8	1.3
3	A	10	17	ANI	ISO	9	0.1
3	A	10	17	ANI	ANI	9	0.6
4	A	1	35	ANI	ISO	9	0.17
4	A	1	35	ANI	ANI	24	0.55
5	B	-10	¹ 50,10	ANI	ISO	20	-0.6
5	B	-10	50,10	ANI	ANI	16	-8.5
6	C	-10	6,30	ANI	ISO	24	-0.13
6	C	-10	6,30	ANI	ANI	7	-0.47
7	D	10	17	ANI	ISO	² 11,25	0.15,0.16
7	D	10	17	ANI	ANI	13	0.7
8	E	10	17	ANI	ISO	12	0.14
8	E	10	17	ANI	ANI	12	0.41



(a) Relative boundary voltages in the isotropic model

(b) Percentage change on scalp voltages for a perturbation in the brain (isotropic model)

Figure 9.26: Percentage change of scalp voltages for a local perturbation in the brain of 10% in the a) anisotropic model, b) isotropic model. Thus a local change of conductivity of 10% led to 0.02% change on the scalp for the anisotropic case and 0.1% in the isotropic case.

cortex, simulating the data and reconstructing it with the isotropic head model (Figures 9.28(a)-9.28(b)), for which the L-curve provided similar result as the GCV, so they seemed to converge also for the shell model even in absence of white noise.

The maximum reconstructed peak was 4% where the simulated (Figures 9.27(d)-9.27(f)) was 10% (Figures 9.28(c)-9.28(e)); the decrease may be due to the effect of regularisation. The localisation error was 8mm, which was set as a lower bound from the ill-posedness and regularisation.

9.3.4.2 Reconstruction of data simulated with the anisotropic model

Neglecting anisotropy did not have an effect in terms of localisation error, for conductivity changes in the occipital lobe, but a slight decrease in image quality was found when the spherical perturbation diameter was reduced from 35 (SIM 2, Figures 9.28(f)-9.28(h)) to 17mm diameter (SIM 3, Figures 9.29(d)-9.29(f)), and it worsened significantly when the conductivity change was reduced from 10 to 1% (SIM 4) which simulated stimulation of the visual cortex (SIM 4, Figures 9.30(d)-9.30(f)). For the epilepsy changes, a localisation error of 20mm was found in the temporal lobe (SIM 5, Figures 9.31(d)-9.31(f)), which may be due to shape of the simulated change, and 24 mm in the hippocampus (Figures 9.32(d)-9.32(f)), which was deep in the brain. For the other locations, surrounded by white matter and deep in the brain, the errors were 11-13mm and it had a significant effect in image quality (Figures 9.33(d)-9.33(f) for SIM 7, Figures 9.34(d)-9.34(f) for SIM 8). In general neglecting anisotropy affected image quality with the emergence of artefacts with higher change outside the region of interest mainly on the

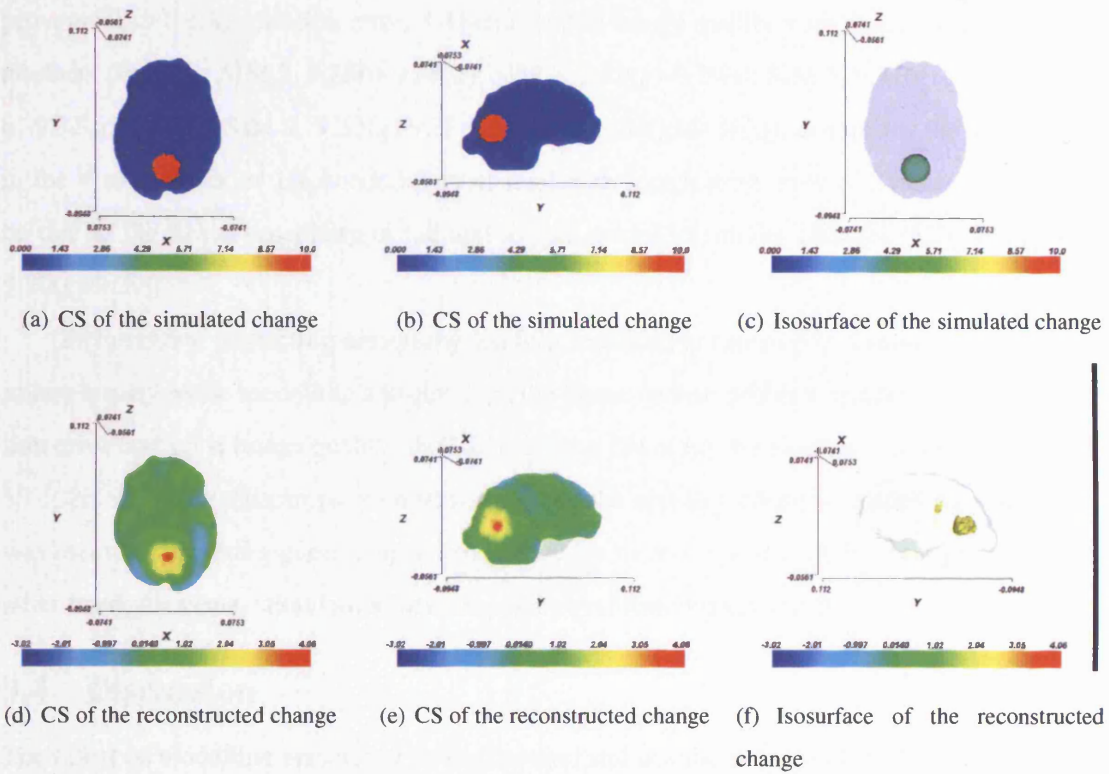
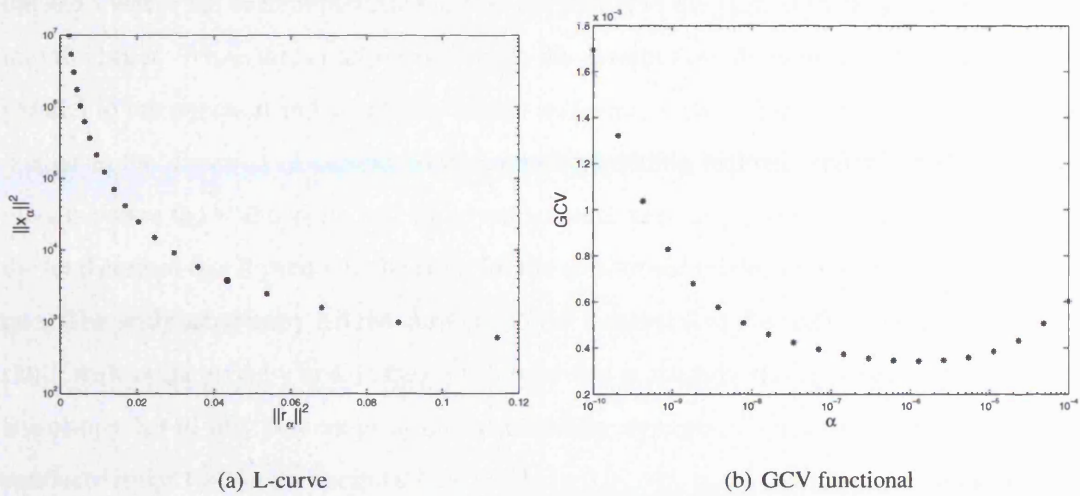


Figure 9.27: (SIM 1, location A) Cross sections (CS) (column 1 and 2) and isosurface (column 3) for linear reconstruction of isotropic data with d-f) an isotropic model for a-c) a local perturbation of 10% change in conductivity and of 16% diameter with respect to head size.



caption L-curve and GCV for the isotropic data and scalar isotropic reconstruction.

brain surface.

Modelling anisotropy in the linear reconstruction with the proposed method led to an improvement in the localisation error, 8-16mm, and in image quality with reduction of spurious artefacts (Figures: SIM 2, 9.28(i)-9.28(k); SIM 3, 9.29(g)-9.29(i); SIM 5, 9.31(g)-9.31(i); SIM 6, 9.32(g)-9.32(i); SIM 7, 9.33(g)-9.33(i); SIM 8, 9.34(g)-9.34(i)), except for the simulation in the visual cortex of 1% conductivity change with localisation error of 24mm, which may be due to the lower sensitivity in the anisotropic model to smaller changes (SIM 9, Figures 9.30(g)-9.30(i)).

In summary, neglecting anisotropy led to a localisation error up to 24mm and worsened image quality while modelling anisotropy in the linear inverse problem yielded lower localisation error and good image quality; the LE was $15 \pm 3mm$ for the isotropic reconstruction and $13 \pm 2mm$ for the anisotropic reconstruction. For the epilepsy changes, modelling anisotropy was essential to obtain good images and reduce by three times the localisation error; on the other hand, for visual stimulation there was not significant improvement.

9.4 Discussion

The effect of modelling anisotropy on the forward and inverse solutions for EIT of brain function has been presented.

9.4.1 Summary of results

First, a qualitative comparison analysed the redistribution of fields by modelling only the anisotropy of the skull in terms of the current norm; similarly, it was done for the white matter. Skull anisotropy had a shunting effect: the current norm decreased by two after crossing the skull where the current preferred to flow tangential to the skull surface rather than flowing into the brain. White matter anisotropy made the current flow through the white matter fibres parallel to the injection and avoid grey matter and white matter fibres whose path was perpendicular to the direction of current flow. Second, modelling realistic isotropic and anisotropic models where the scalp, skull, and white matter were anisotropic led to a reduction of two for the total current that flowed into the brain for the anisotropic model with respect to the isotropic one. The scalp anisotropy led the current to flow tangential to the scalp, as in the case of the skull, with an increase by two on the total current that propagates through the scalp. Neglecting anisotropy led to fifty percent error on the boundary voltages. Simulating a local increase of conductivity of 10% in the occipital lobe yielded a 0.0124% mean change in the boundary voltages in the anisotropic model; the same conductivity change modelled in the isotropic model yielded 0.061% mean on the boundary voltages. The absolute voltage difference, in the do-

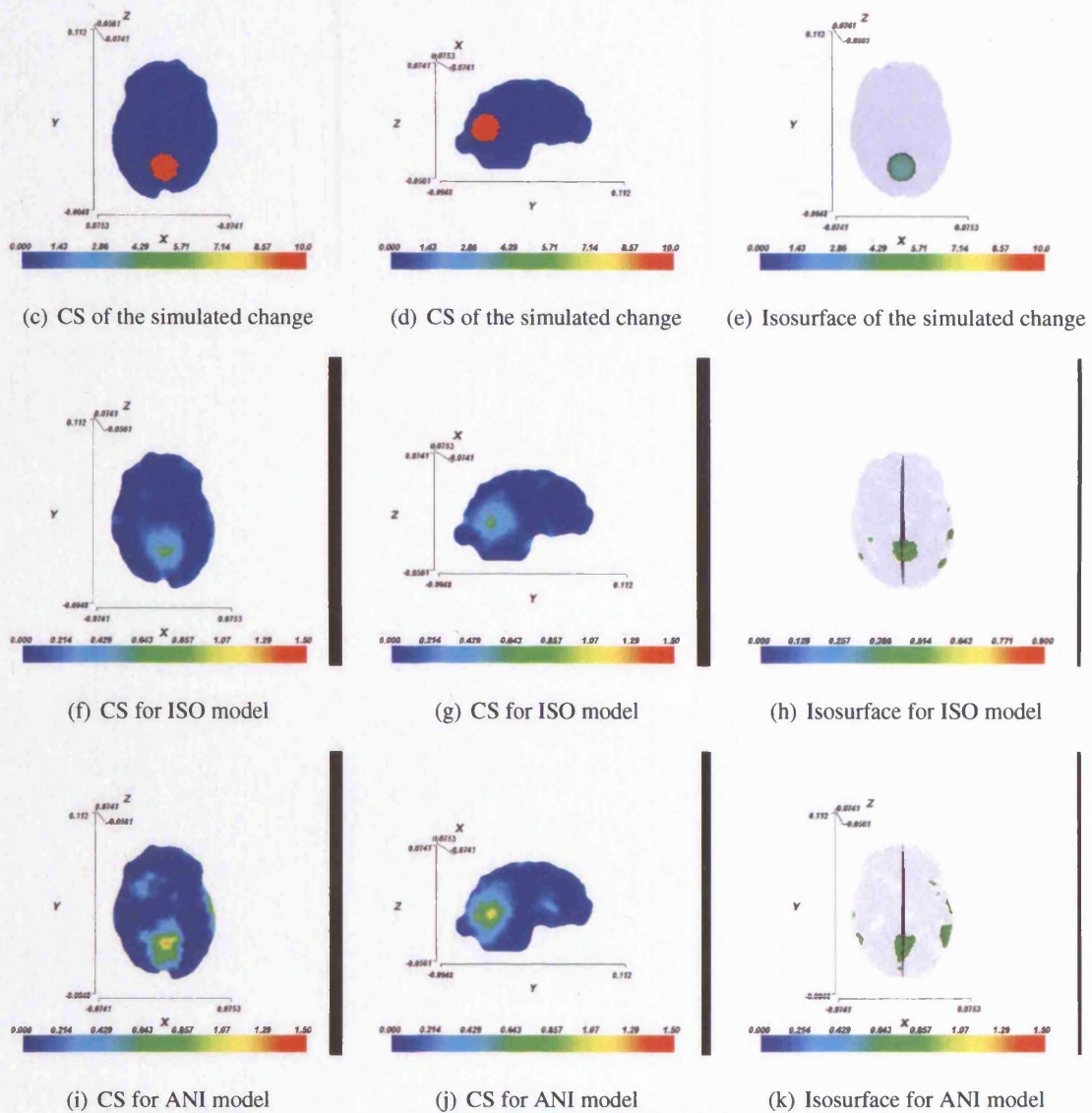


Figure 9.28: (SIM 2, location A) Cross sections (CS) (column 1 and 2) and isosurface (column 3) for linear reconstruction of anisotropic data with a-c) an isotropic (ISO) model and d-f) an anisotropic (ANI) model, for a local perturbation of 10% change in conductivity and of 16% diameter with respect to head size.

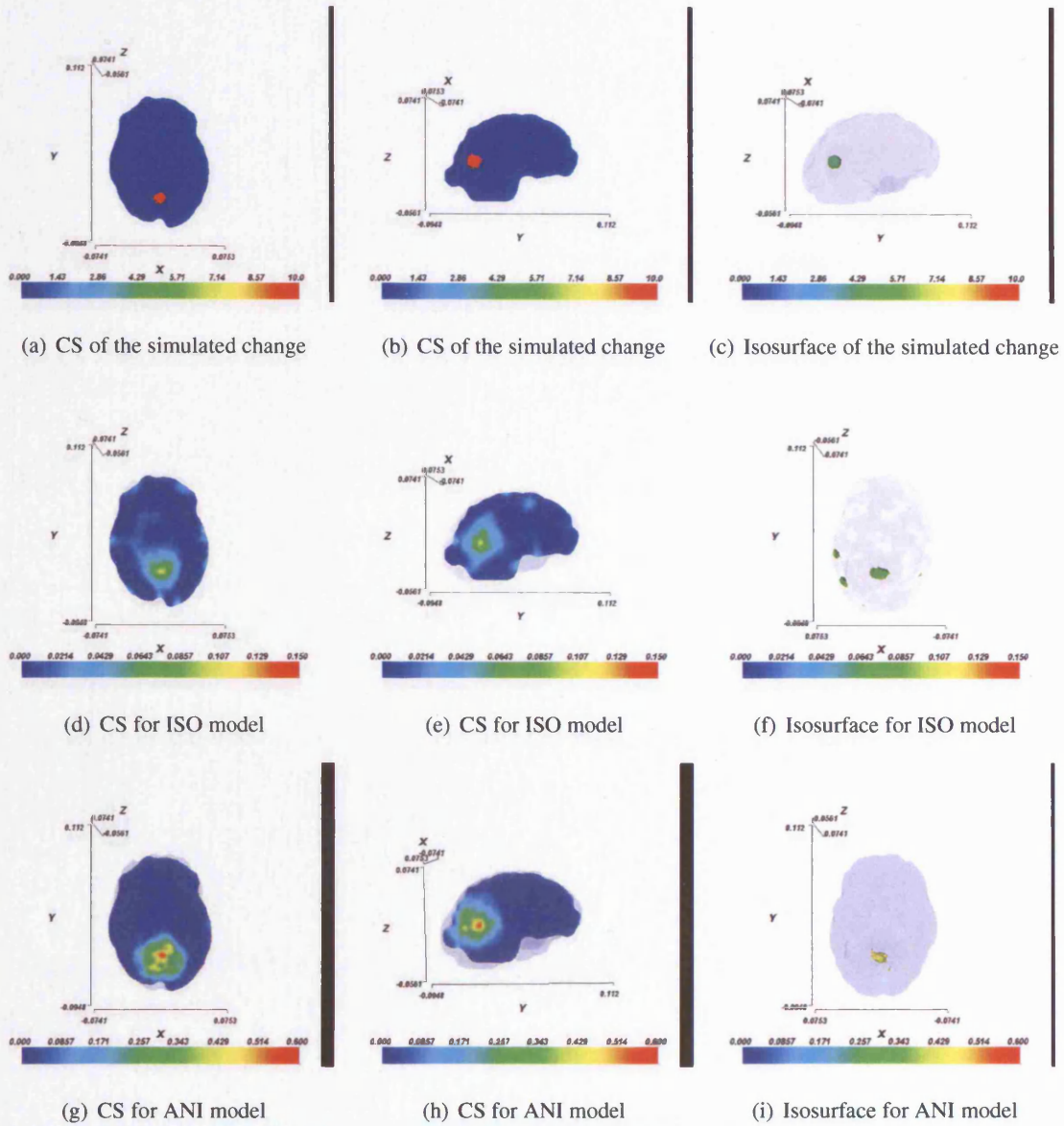


Figure 9.29: (SIM 3, location A) Cross sections (CS) (column 1 and 2) and isosurface (column 3) for linear reconstruction of anisotropic data with a-c) an isotropic (ISO) model and d-f) an anisotropic (ANI) model, for a local perturbation of 10% change in conductivity and of 8% diameter with respect to head size.

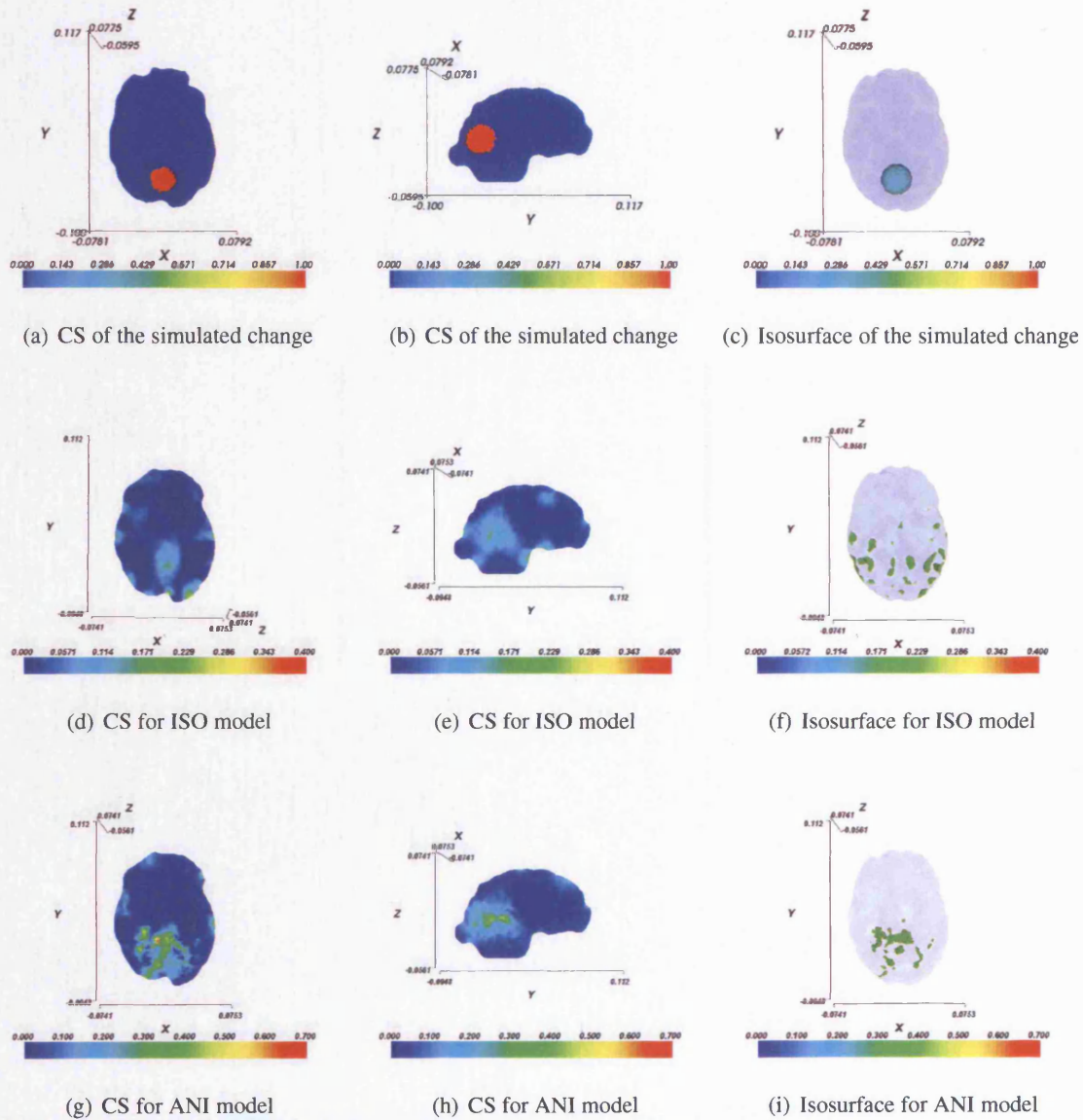


Figure 9.30: (SIM 4, location A) Cross sections (CS) (column 1 and 2) and isosurface (column 3) for linear reconstruction of anisotropic data with a-c) an isotropic (ISO) model and d-f) an anisotropic (ANI) model, for a local perturbation in the occipital lobe of 1% change in conductivity and of 16% diameter with respect to head size.

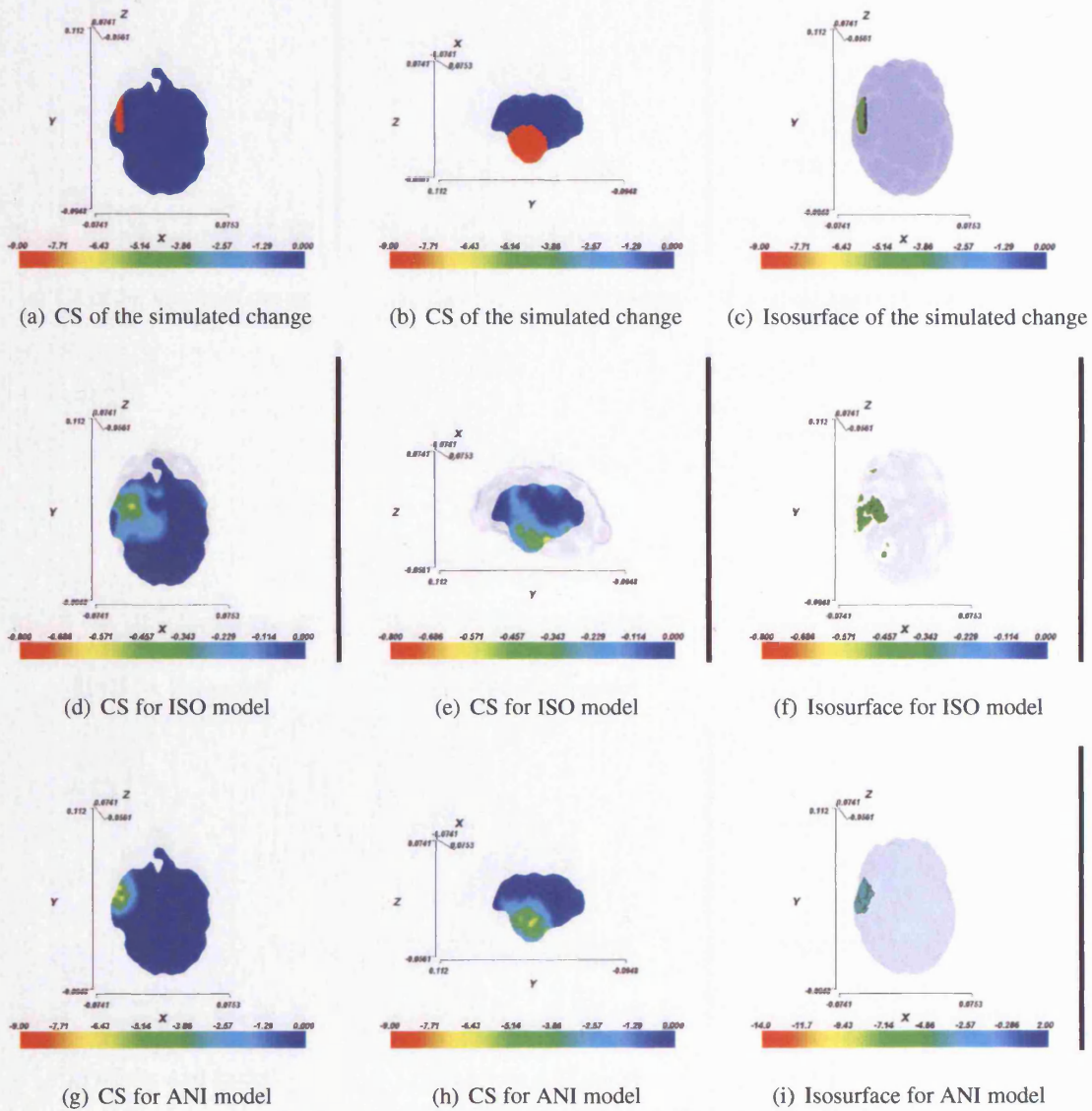


Figure 9.31: (SIM 5, location B) Cross sections (CS) (column 1 and 2) and isosurface (column 3) for linear reconstruction of anisotropic data corresponding to a-c) a simulated 9% decrease in conductivity on the temporal lobe, reconstructed with d-f) an isotropic (ISO) model and g-i) an anisotropic (ANI) model

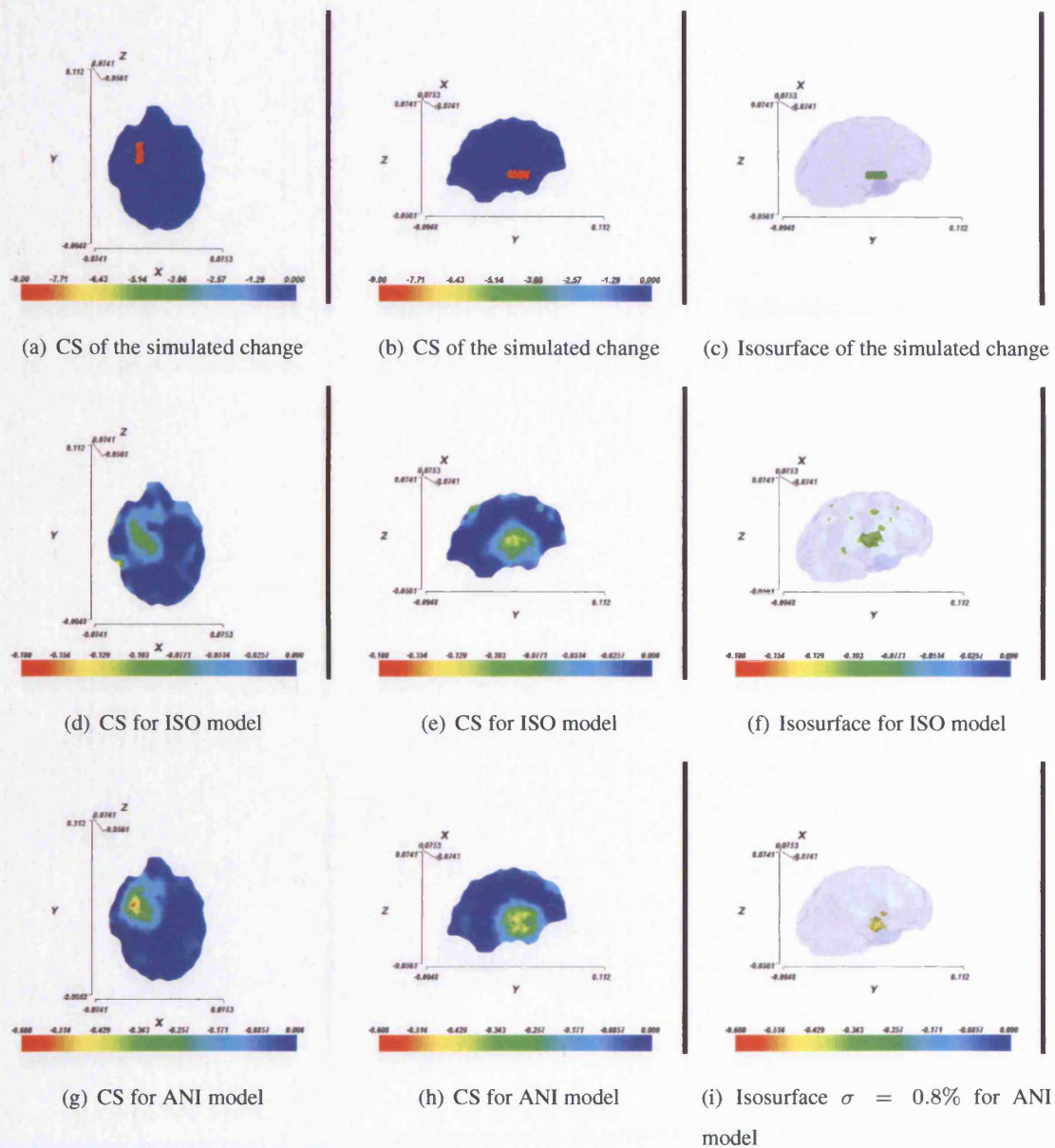


Figure 9.32: (SIM 6, location C) Cross sections (CS) (column 1 and 2) and isosurface (column 3) for linear reconstruction of anisotropic data corresponding to a-c) a simulated 9% decrease in conductivity on the hippocampus, reconstructed with d-f) an isotropic (ISO) model and g-i) an anisotropic (ANI) model

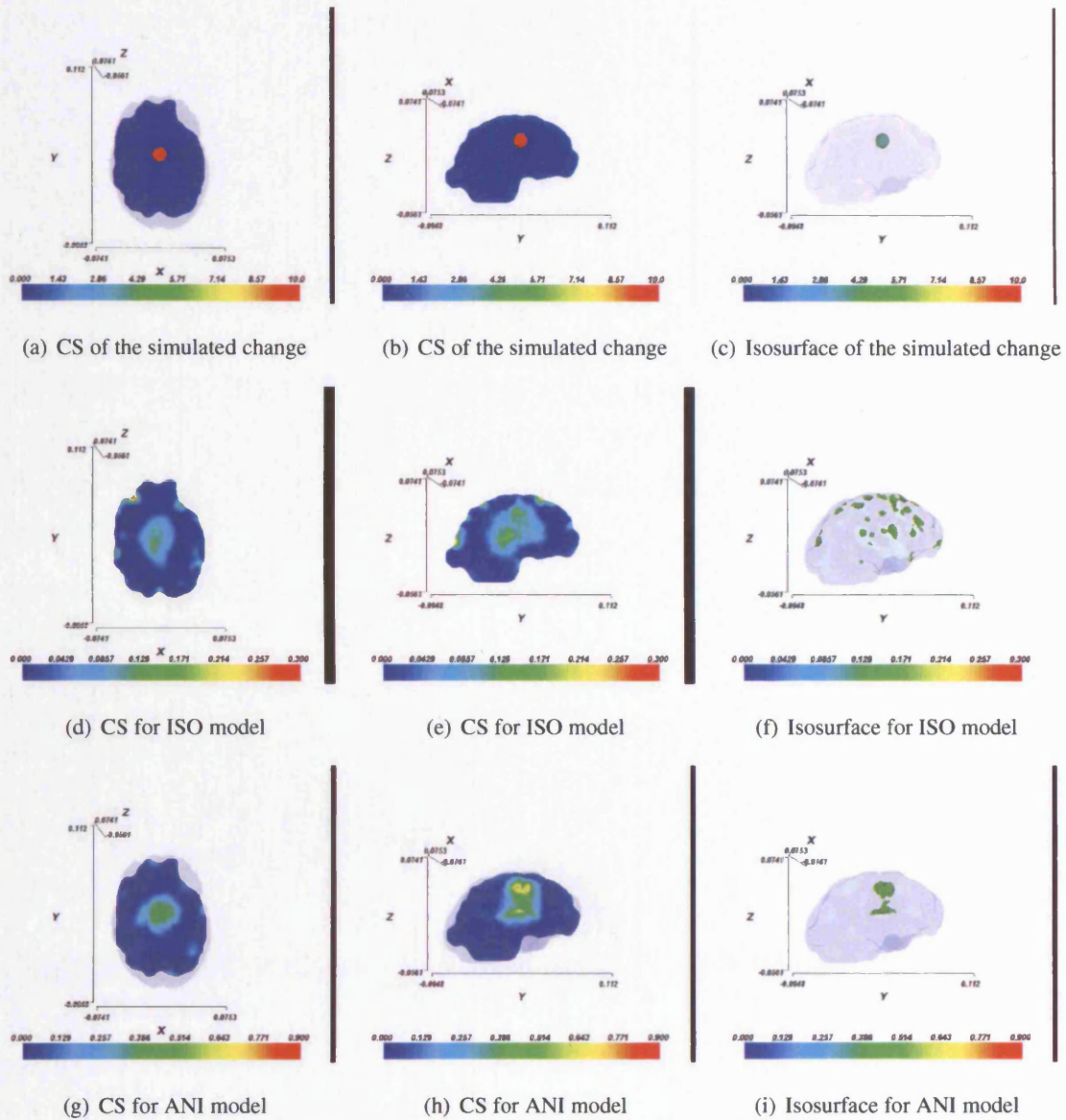


Figure 9.33: (SIM 7, location D) Cross sections (CS) (column 1 and 2) and isosurface (column 3) for linear reconstruction of anisotropic data with a-c) an isotropic (ISO) model and d-f) an anisotropic (ANI) model, for a local perturbation of 10% change in conductivity and of 8% diameter with respect to head size.

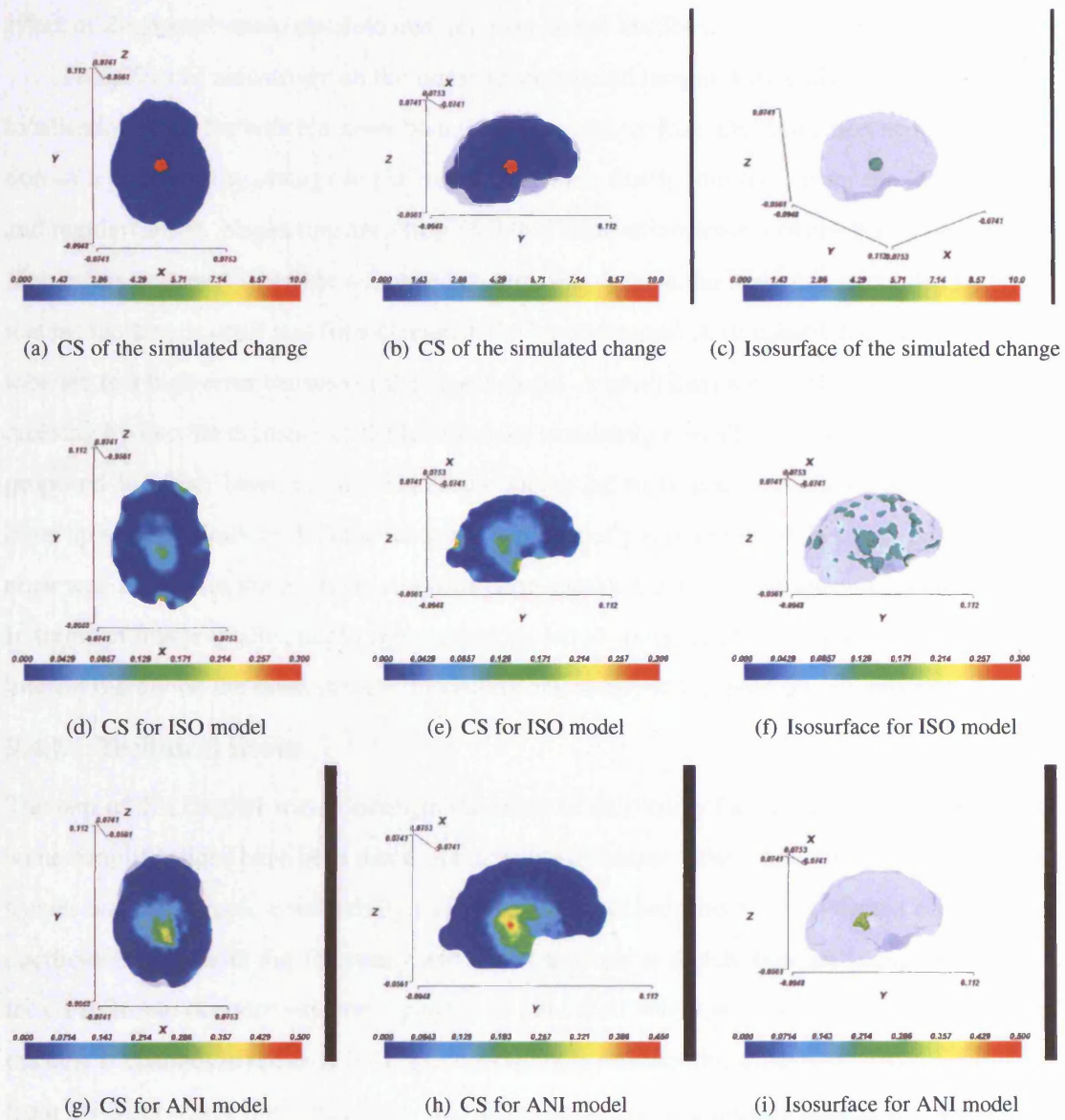


Figure 9.34: (SIM 8, location E) Cross sections (CS) (column 1 and 2) and isosurface (column 3) for linear reconstruction of anisotropic data with a-c) an isotropic (ISO) model and d-f) an anisotropic (ANI) model, for a local perturbation of 10% change in conductivity and of 8% diameter with respect to head size.

main, corresponding to the perturbation and the reference conductivity in the anisotropic model yielded a local voltage change while this was not the case for the difference corresponding to the perturbation in the anisotropic model and the reference in the isotropic model. Because of this and the fact that the voltage difference between models was significantly higher than the effect of the perturbation, absolute imaging may be not feasible.

The effect of anisotropy on the linear reconstructed images was analysed in terms of the localisation error, for which a lower bound of 8mm was set from the simulation and reconstruction of a conductivity change in the isotropic model; that is, the error from the ill-posedness and regularisation. Neglecting anisotropy led to a localisation error between 8-to-24mm where high errors occurred when the simulated change was deep in the brain or surrounded by white matter; the largest error was for a change in the hippocampus. A simulated disc in the temporal lobe led to a high error because of the object shape. A small increase of error was found for decreasing by two the diameter of the inclusion or simulating a smaller conductivity change. The proposed Jacobian based on the anisotropic model led to an improvement of the localisation error up to three times in the hippocampus, but generally it led to errors between 8-24mm; the error was 15 ± 3 for the isotropic reconstruction and 13 ± 2 for the anisotropic reconstruction. In terms of image quality, neglecting anisotropy led to spurious artefacts, outside the region of interest mainly on the brain surface; modelling anisotropy led to good quality images.

9.4.2 Technical issues

The aim of this chapter was to estimate the effect of anisotropy for a realistic model, however, some simplifications have been made. An accurate estimate of the conductivity for the different tissues and anisotropic conductivity ratios are not available where the published conductivity coefficients vary with the frequency and the conditions at which they are acquired. The selected isotropic conductivity corresponded to published values at 50KHz [77], which yielded the largest changes in epilepsy [44]. The conductivity ratio for the white matter was determined from DT-MRI where the conductivity and diffusion tensors are linearly related at low frequencies, that is, for frequencies no larger than 1 or 50KHz. In fact, the anisotropic tensor trace was constrained to be equal to the isotropic trace at 50KHz. A previous study also constrained the trace for the white matter tensor since while the conductivity and diffusion tensors are linearly related across different tissue types, there is not a strong linear relation within the same tissue [90]. The scalp anisotropy was approximated from the conductivity ratio tangential:normal to the scalp surface of 1.5:1 at 50kHz, determined from the scalp tissues contemplating the muscle anisotropy [77], which may be larger at other frequencies. The muscle conductivity was modelled with a ratio 4.3:1 in [54, 55]. The skull conductivity ratio tangential:normal to the skull

surface was chosen as 10:1 [146], which was the largest ratio discussed for the study of the influence of anisotropy for EEG [182], so it was selected as being an upper bound of the possible conductivity ratios to analyse the largest effect of neglecting anisotropy. Besides, it was found that the bone conductivity on the three orthogonal directions was constant up to 10KHz [144]. Therefore, modelling different conductivity values may vary slightly the results, yet this analysis aimed to provide relevance of the importance of anisotropy for EIT.

9.4.3 Comparison with previous results

Some results could be used to set a lower bound in the localisation error. A distortion of the MRI at the coregistration stage may lead to errors up to 5mm, yet they can be reduced to 1mm using specific methods [112, 170]. Also, the segmentation and boundaries extraction from the T1-MRI had 1-2mm error [39]. A limit of accuracy was set from modelling inaccuracies which would not be contemplated in practice. This included factors as the inhomogeneity of the skull; for 64 electrodes and 2% noise, this led to 10mm localisation error [127].

An assessment of the head-shell model for EIT of brain function was done on simulated, tank, and human data [11]. Localisation errors were (in millimeters), for simulated data from a homogeneous head-shaped model 21 ± 6 for head-shaped reconstruction and 24 ± 10 for spherical reconstruction; for homogeneous head tank data, 13 ± 7 for head-shaped reconstruction and 19 ± 8 for spherical reconstruction; and for head with skull tank data, 26 ± 8 for head-shaped reconstruction and 24 ± 8 for spherical reconstruction. For human data, an improvement in image quality was found. It was concluded that realistic conductivity values and accurate geometry led to slight improvements where improvements in image quality were more significant than localisation error and resolution.

From previous EEG results, modelling anisotropy for the skull and white matter, there seems to be a lower bound of 10mm error from mismodelling errors and upper bound of 30% in the forward solution and 18mm localisation error. The results presented here led to 50% on the forward solution, which suggests a significant influence of modelling the anisotropy of the scalp. While here the nonlinear problem has not been attempted, from the error on the forward solution the nonlinear inverse solution may be not possible. Linear reconstruction neglecting anisotropy led here to 24mm error, which compared with the 13-26mm error from the EIT studies on tank data, suggests that for linear reconstruction only for conductivity changes deep in the brain modelling anisotropy will improve results if mismodelling errors of the electrodes accounted in the EIT real studies are solved [11].

9.4.4 Conclusion and further work

In conclusion, neglecting anisotropy led to up to 50% error in the boundary voltages, which suggests that absolute reconstruction may not be feasible. The influence of anisotropy of the scalp and skull was apparent in the reduction by two of the total current flowing into the brain. For linear reconstruction, neglecting anisotropy led to an increase of localisation error by three times, up to 24 mm for inclusions deep in the brain, yet no difference was found for inclusions in the occipital cortex. Modelling anisotropy with the proposed method led to a significant improvement in the localisation error for some of the simulations and small improvement over all; it led to a significant improvement in image quality with large reduction of artefacts. Thus, modelling anisotropy is required to obtain an accurate forward solution and for absolute reconstruction, however, by neglecting anisotropy it was still possible to reconstruct linear changes of time difference data with an error of 24mm, so modelling anisotropy appears to be necessary for obtaining good quality images and low localisation error, especially if the imaged changes are deep in white matter. A more significant influence is likely to be for absolute imaging, for which the methodology proposed in chapter 9 for the recovery of the three eigenvalues could be applied here for the case of a wrong conductivity ratio estimate for the scalp, skull, and white matter. Further analysis of this constraint on real phantoms with anisotropic structure would set the relevance of anisotropy for many other EIT applications.

Chapter 10

Conclusions

10.1 Introduction

10.1.1 EIT of brain function

EIT may be applied for imaging brain function where changes of scalp impedance are related to changes of local brain impedance associated with slow neuronal activity like cell swelling during epilepsy and changes of blood volume during normal brain activity. EIT has the potential to become a technique for localising epileptic foci before surgery since it could image deep in the brain and be plugged into continuous recording in the telemetry unit [74]. Besides, EIT is portable and noninvasive, which make it highly attractive in comparison to the leading imaging techniques.

A major drawback of measuring scalp impedance is its low signal-to-noise ratio due to the shunting effect of the skull and the experimental sources of error. Local impedance changes in the brain related to slow brain activity were between 2-to-12% [42, 157, 41, 143, 76], and a decrease of one or two orders of magnitude is expected on scalp changes because of the attenuation by the skull [78]. Experimental errors have been classified in random noise, systematic changes, and physiological noise; as a general figure, noise could be decrease up to 1% [74, Chapter 1].

The main drawback of EIT is its low spatial resolution due to the fact that the image reconstruction problem is not well-posed, being highly sensitive to modelling and experimental errors, and data sampling is usually incomplete. In fact, the isotropic EIT problem is unique only if the boundary shape is perfectly known [105]. Other parameters that affect the solution are the contact impedance of the skin-electrode interface, modelling errors, and anisotropy. For example, one may recover simultaneously the electrode contact impedance and conductivity [175, 69], and boundary shape and conductivity [104, 160]. Also, modelling of errors has decreased the solution error [69].

In most clinical applications the approach to reduce some of the systematic errors has been linear reconstruction of difference data, that is, recovering a conductivity change from an impedance change, instead of doing static imaging where one aims to recover absolute conductivity.

In the last few years, some of those parameters have been modelled in studies into EIT of brain function. Some studies have shown the importance of an accurate model of the head, with representation in the model of scalp, skull, CSF, and brain, [167, 108, 16, 11, 170]. Moreover, electrode positions can be accurately obtained with a precision of a millimetre using photogrammetry [147]. However, modelling of the errors, contact impedance for each electrode, and anisotropy have not been modelled yet.

It is well known that human tissues like bone, muscle, and brain white matter are anisotropic, however, most medical applications have hitherto neglected anisotropy and its modelling has been suggested for medical [54, 55] and geological [132] applications. Avoiding anisotropy of both white matter and skull has been found to lead to errors of about 10% on EEG forward solution and to be significantly relevant for inverse source localisation [182, 181], where the white matter anisotropic conductivity tensor was estimated from diffusion tensor magnetic resonance imaging [66][172, Chapter 5].

10.1.2 Forward and inverse problem theory

Solving the forward problem implies obtaining the predicted boundary voltages for a conductivity estimate, modelled by Maxwell's equations, which at low frequency are given by Laplace's equation, and Neumann boundary conditions, which are modelled by the CEM, taken on account the electrode contact impedance, with an error of less than 0.1%. FEM provides a numerical formulation of the FP for general irregular geometries; besides, it can model anisotropy. This leads to a linear system of equations for the voltage and current injection, which can be efficiently solved by using PCG and multigrid.

The conductivity inverse problem has a unique solution for isotropic media [92, 93, 165]; however, uniqueness does not hold for anisotropic media [101] unless extra information is provided [104], where uniqueness can be recovered for some constraints: one eigenvalue and a scalar multiple to the tensor. The inverse problem is solved by minimising the difference between the experimental and the predicted data, and since it is ill-posed, as given by Hadamard's conditions, by applying some type of regularisation. A common choice is to assume that the solution follows a Gaussian distribution, which corresponds to Tikhonov regularisation. Reconstruction methods can be divided in linear and nonlinear and direct and iterative. Linear direct methods like TSVD and Tikhonov and nonlinear iterative like Newton's type are related to this

thesis.

Optimising the linear inverse problem requires selecting the regularisation parameter, which controls the amount of regularisation, and modelling the covariance of the noise of the data. The regularisation parameter can be chosen by several methods, which guarantee an optimum solution under a white noise assumption; otherwise, it is suggested to model the covariance of the noise. Unfortunately, EIT data is not white since measurements can have different variance and be correlated. In addition, estimating covariance from a low number of measurements leads to ill-posed covariance matrices. Some methods have dealt with modelling the covariance matrix [129, 130, 131, 21], and with rank-deficient covariance matrices [187]. An inverse solution that includes explicitly the covariance matrix and avoids its inversion is the Generalised-Tikhonov solution (4.51), which was the preferred solution in this work.

10.2 Summary of findings

The work in this thesis had four main goals. The first goal was to optimise linear reconstruction for EIT of brain function (chapter 5) by selecting an optimum regularisation parameter using Generalised Tikhonov reconstruction and four standard methods: L-Curve (LC), Generalised Cross Validation (GCV), Discrepancy Principle (DP), and Unbiased Predictive Risk Estimator (UPRE); and modelling a general covariance of the noise for simulated data and diagonal covariance for neonatal and tank data. Methods were tested on simulated data, saline head-shaped tank data with Perspex as test object, and scalp neonatal data during evoked response. The second goal was to apply Principal Component Analysis (PCA) on the raw data by projecting the data onto the first eigenvectors of the covariance (chapter 6). Goals three and four modelled a FEM forward solution for anisotropic media, which was, first, validated by its comparison with an analytical solution (chapter 7), were presenting and verifying numerically the uniqueness of a constrained anisotropic inverse solution (chapter 8), and studying the influence of modelling anisotropy of the scalp, skull, and brain white matter on the forward problem and on a linear reconstructed solution of a scalar multiple to a general tensor (chapter 7).

Selecting the truncation level minimised the solution error on simulated data, but no significant differences were found between the four selection methods. Modelling a general covariance of the noise significantly decreased the solution error. On tank data, LC and GCV were equally good while DP and UPRE failed to converge; modelling a diagonal covariance did not yield significant differences. On real data, the high variability among methods did not lead to significant differences. Overall, the LC and GCV with modelling the covariance were best, and results encourage a better estimation of the covariance, which proved to improve image quality

for a good estimate of the covariance. The recommendation for EIT of brain function is to apply LC or GCV and a fixed truncation level chosen experimentally when methods failed to converge.

Applying PCA, where time frames were considered as variables, significantly improved the signal-to-noise ratio by fifteen decibels on both tank and neonatal data. From these results, it is advised to apply PCA instead of averaging across repetitive experiments.

The FEM solution for Laplace's equation in an anisotropic medium was validated by studying its convergence to an analytical solution for the case of a cubic domain with a Dirichlet boundary condition. Convergence was verified by showing that the FEM error norm decreased proportionally to the tetrahedral size.

The feasibility of the recovery of a constrained anisotropic tensor with known eigenvectors was verified numerically by looking at the rank of the Jacobian and solving numerical examples for simple geometries with smooth eigenvalues and a general tensor whose eigenvectors varied smoothly throughout the domain. The practical relevance of this constraint is clear for medical applications where muscle, bone tissue, and white matter have a preferred direction for current flow, which can be approximated from a structural imaging modality like MRI or directly estimated with DT-MRI.

The effect of modelling anisotropy of the scalp, skull, and brain white matter on the forward and a linearised inverse solution was studied using a realistic FEM model of the head that distinguished four tissue types: scalp, skull, CSF, and brain, and approximated anisotropy for the skull and scalp from the geometrical boundaries and estimated anisotropy for the brain from DT-MRI. Neglecting anisotropy led to 50% error in the boundary voltages, which suggests that absolute reconstruction may not be feasible. The influence of anisotropy of the scalp and skull was apparent in the reduction by two of the total current flowing into the brain and by six on the boundary voltages for a simulated conductivity change on the occipital cortex in comparison with the equivalent isotropic model. For linear reconstruction, neglecting anisotropy led to an increase of localisation error by three times, up to 24 mm for inclusions deep in the brain, yet no difference was found for inclusions in the occipital cortex. Modelling anisotropy with the proposed method led to a significant improvement in the localisation error and in image quality with large reduction of artefacts. Thus, modelling anisotropy is required to obtain an accurate forward solution and for absolute reconstruction, however, by neglecting anisotropy it was still possible to reconstruct linear changes of time difference data with an error of 24mm, so while linear imaging is possible without modelling anisotropy, it is essential to obtain good quality images and low localisation error.

10.3 Suggestions for further research

As has been discussed, the EIT problem is highly sensitive to noise and parameters like boundary shape, electrode position, and electrode contact impedance. In addition, EIT of brain function boundary data has a low SNR because of the shunting effect by the skull.

The nonlinear reconstruction problem for EIT in general, from my point of view, is unlikely to be successful unless those parameters are accurately known; therefore, a possible approach could be to recover simultaneously with the conductivity all parameters that cannot be measured.

The linear reconstruction problem has been also verified to improved significantly when the noise was modelled. As with the nonlinear case, the uncertain parameters could be recovered to optimise the solution.

As for the preprocessing stage, increasing the SNR has been possible for neonatal data even in cases when the noise was larger than the signal of interest. Further research for discerning the signal of interest, in adults where the effect of the skull is larger than on neonates, and improving modelling of the covariance may be relevant.

Positive results found here for the recovery of a conductivity tensor with known eigenvectors suggest numerical uniqueness when eigenvectors are provided and encourage theorists to study this constraint. In addition, further study needs to be applied to test this constraint for real phantoms with anisotropic structure for which the eigenvector orientation can be approximately estimated.

Modelling anisotropy for the head has been shown to influence significantly the forward solution, however, the influence on the nonlinear reconstruction has not been assessed here. Therefore, analysis of its influence is desirable; in particular, to apply the proposed methodology for the recovery of the three eigenvalues of the conductivity tensor, for the case of a wrong conductivity ratio estimate for the scalp, skull, and white matter. In fact, testing this constraint for real data on phantoms with anisotropic structure will set the importance of this constraint for many other EIT applications.

Finally, I have developed three main improvements for image reconstruction in EIT: an automatic method for regularization in linear reconstruction, use of PCA to improve signal to noise, and the use of anisotropy in image reconstruction. Although I have undertaken validation on simulated, tank and example clinical data, their true advantages will only become apparent when used in earnest in clinical studies. They will all be used in studies in our research group into EIT in epilepsy, acute stroke, and functional activity, and I look forward to seeing how they can improve the image quality under these real-life conditions.

Appendix A

Miscellaneous mathematical definitions

A.1 Vector spaces

Let f be a function, defined in the domain $\Omega \in \mathbb{R}^n$, such that $f : \Omega \mapsto \mathbb{R}$.

A.1.1 Convex function

A function f is convex in a domain Ω if for any two points x and y in the domain and a parameter $t \in [0, 1]$ (http://en.wikipedia.org/wiki/Convex_function)

$$f(tx + (1 - t)y) \leq tf(x) + (1 - t)f(y). \quad (\text{A.1})$$

Thus, f must be continuous and differentiable everywhere, but at some points. As a test for convexity, if the second derivative of f is positive, then f is strictly convex.

A.1.2 Lipschitz continuity

A function f is Lipschitz continuous if there is a constant $C \geq 0$ such that

$$|f(x) - f(y)| \leq C|x - y|, \quad (\text{A.2})$$

where the Lipschitz constant C provides the largest value of the first derivative for functions with bounded first derivative.

A.1.3 Lebesgue integrable

The set of functions are said to be Lebesgue integrable, $\mathcal{L}_p(\Omega)$, if their Lebesgue integral is finite, that is,

$$\int_{\Omega} |f(x)^p| dx < \infty, \quad (\text{A.3})$$

where $p \in [1, \infty)$.

A.1.4 Generalised weak derivative

Let f be a generalised function, including distributions, the weak derivative D^α , where $\alpha = (\alpha_1, \dots, \alpha_n)$ and $|\alpha| = \alpha_1 + \dots + \alpha_n \leq k$ with $k \in \mathbb{Z}^+$, is defined as

$$\int_{\omega} (D^\alpha f(x))\psi(x)dx = (-1)^{|\alpha|} \int_{\Omega} f(x)(D^\alpha \psi(x))dx, \quad (\text{A.4})$$

where all derivatives of ψ are continuous.

A.1.5 Sobolev space

The Sobolev space of order k is defined as

$$W_p^k = \{f \in \mathcal{L}_p(\Omega) : D^\alpha f \in \mathcal{L}_p(\Omega), |\alpha| \leq k\}, \quad (\text{A.5})$$

where $p \in [1, \infty)$. The Sobolev norm is defined as

$$\|f\|_{W_p^k(\Omega)} = \left(\sum_{|\alpha| \leq k} \|D^\alpha f\|_{\mathcal{L}_p(\Omega)}^p \right)^{\frac{1}{p}} \quad (\text{A.6})$$

A.1.6 Hilbert space

The Hilbert space is a Sobolev space for the specific case when $p = 2$, that is $\mathcal{H}^k(\Omega) = W_2^k(\Omega)$.

For instance, the Hilbert space of order one is given by

$$H^1(\Omega) = \{f \in \mathcal{L}_p(\Omega) : \frac{\partial f}{\partial x_j} \in \mathcal{L}_p(\Omega), j = 1, \dots, n\}, \quad (\text{A.7})$$

with an associated norm

$$\|f\|_{H^1(\Omega)} = \left(\|f\|_{\mathcal{L}_p(\Omega)}^2 + \sum_{j=1}^n \left\| \frac{\partial f}{\partial x_j} \right\|_{\mathcal{L}_p(\Omega)}^2 \right)^{\frac{1}{2}}. \quad (\text{A.8})$$

A.1.7 G-norm

Let y be a vector that belong to a vector space with an inner product defined by a metric G , the associated norm is given in terms of the matrix operator G as

$$\|y\|_G^2 = y^T G y. \quad (\text{A.9})$$

In the case of the \mathcal{L}_2 -norm, $G = I$ and (A.9) becomes

$$\|y\|_2^2 = y^T y. \quad (\text{A.10})$$

A.1.8 Compact operators

Given an operator J , such that $J : H_1 \mapsto H_2$, is said to be bounded if

$$\|J\| = \sup \|Jx\|_{H_2}, \quad \text{for all } x, \text{ such that, } \|x\|_{H_1} = 1.$$

Any linear bounded operator with finite range is compact; matrix operators are compact [176].

It is also known that linear operators in \mathbb{R}^n are continuous.

A.1.9 Kernel

Given a function $f : \mathcal{S}_1 \mapsto \mathcal{S}_2$, the kernel or null space \mathcal{K} is a subset of \mathcal{S}_1 defined as

$$\mathcal{K}(f) = \{x \in \mathcal{S}_1 \text{ such that } f(x) = 0\}. \quad (\text{A.11})$$

A.1.10 Symmetric positive definite matrix

Let $A \in \mathbb{R}^{n \times n}$ be a positive definite matrix within the subspace of n -by- n matrices, and $x \in \mathbb{R}^n$, A is such that

$$x^T A x > 0. \quad (\text{A.12})$$

As a consequence, $|A| > 0$ and the eigenvalues of A are all positive (section A.2.1)

(<http://mathworld.wolfram.com/PositiveDefiniteMatrix.html>). Because of symmetry, $A_{ij} = A_{ji}$, only the elements of the upper triangular matrix of A are independent; for instance, in 3D, A is given by

$$A = \begin{pmatrix} A_{11} & A_{12} & A_{13} \\ A_{12} & A_{22} & A_{23} \\ A_{13} & A_{23} & A_{33} \end{pmatrix}, \quad (\text{A.13})$$

with only six independent coefficients.

A.2 Numerical tools

A.2.1 Eigenvalue decomposition

An introduction to the eigenvalue decomposition can be found in [56]. Let A be a $n \times n$ matrix, the eigenvalue problem is defined as finding the eigenvectors $v \in \mathbb{R}^n$ and eigenvalues λ , complex in general, that satisfy

$$Ax = \lambda x, \quad (\text{A.14})$$

which are given by solving $\det(A - \lambda \mathbb{I}) = 0$.

Let $A, D \in \mathbb{R}^{n \times n}$, it is said that there is a similarity transformation between A and D when there is an invertible matrix $V \in \mathbb{R}^{n \times n}$ such that

$$D = V^{-1}AV, \quad (\text{A.15})$$

where D is a diagonal matrix whose diagonal elements are the eigenvalues and V is a matrix whose columns are the eigenvectors. The relevance of similar matrices A and D are the following properties:

- A and D have the same eigenvalues λ .
- If x is an eigenvector of A corresponding to the eigenvalue λ , that is, $Ax = \lambda x$, then $V^{-1}x$ is an eigenvector of D corresponding to the eigenvalue λ , that is, $D(V^{-1}x) = \lambda(V^{-1}x)$.

For symmetric matrices $A \in \mathbb{R}^{n \times n}$, $A = A^T$, eigenvalues are real and eigenvectors are orthonormal. Thus, one can find an invertible orthogonal matrix $V \in \mathbb{R}^{n \times n}$, $V^{-1} = V^T$, such that

$$V^T A V = \text{diag}(\lambda_1, \dots, \lambda_n) = D. \quad (\text{A.16})$$

Accordingly, as given by the spectrum theorem, if A is a symmetric matrix corresponding to a linear operator, then it can be written as

$$A = \sum_{i=1}^n \lambda_i v_i v_i^T + \dots + \lambda_n v_n v_n^T = V D V^T, \quad (\text{A.17})$$

where $\lambda_1, \dots, \lambda_n$ is defined as the spectrum of A

(<http://en.wikipedia.org/wiki/Eigenvector>).

Linear operators can be visualised by how they act on vectors. In fact, given a linear transformation, eigenvectors provide the invariant directions by the transformation, and eigenvalues the scalar factor by which they are transformed.

Let A be a symmetric matrix representation of a linear operator, and $V D V^T$ be its eigenvalue decomposition, a symmetric matrix A , in 2D, maps the unit circle onto an ellipse such that the axes of the ellipse coincide with the direction of the eigenvectors and the length of the semi-axes is given by the eigenvalues (<http://en.wikipedia.org/wiki/Ellipse>). In 3D, a 3-by-3 symmetric matrix A maps the unit sphere into an ellipsoid (<http://en.wikipedia.org/wiki/Ellipsoid>). For instance, given a 2-by-2 symmetric matrix

$$A = \begin{pmatrix} 3 & 1 \\ 1 & 3 \end{pmatrix} = [v_1, v_2] \text{diag}(4, 2) [v_1, v_2]^T, \quad (\text{A.18})$$

where $v_1 = (\sqrt{2}/2, \sqrt{2}/2)$ and $v_2 = (-\sqrt{2}/2, \sqrt{2}/2)$, A maps the unit circle onto an ellipse where the main axes are given by the eigenvectors v_i and the semi-axes length given by the eigenvalues $\lambda_1 = 4$, $\lambda_2 = 2$ (Figure A.1). Besides, the action on the eigenvectors direction is invariant, $A(1, 1)^T = 4(1, 1)^T$, $A(-1, 1)^T = 2(-1, 1)^T$; the action on other vectors is not invariant, $A(1, 0)^T = (3, 1)^T$, $A(0, -1)^T = (-1, -3)^T$.

An example of a positive definite matrix is the conductivity matrix σ , defined as a mapping from the electrical field E to the current density field J , $J = \sigma E$. Let σ be the matrix given above (A.18), $\sigma = A$, then given an electrical vector as the vector defined above, one can calculate the direction of the current, which is invariant only along the directions given by the eigenvectors.

A.2.2 SVD

Let $J : \mathbb{R}^n \mapsto \mathbb{R}^m$ is a finite compact linear operator [176], then there is a singular system $\{u_j, s_j, v_j\}_{j=1}^r$, with the following properties:

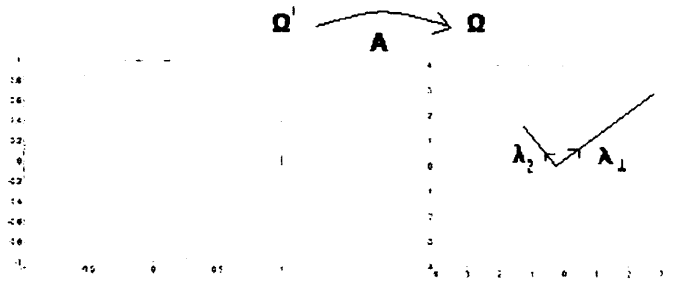


Figure A.1: A 2-by-2 symmetric matrix A (A.18) maps the unit circle onto an ellipse where the main axes are given by the eigenvectors v_i and the semiaxes length given by the eigenvalues $\lambda_1 = 4, \lambda_2 = 2$.

- i) the right singular vectors v_j form an orthonormal basis of $\mathcal{K}(J)^\perp$ for $j = 1, \dots, r$ and of $\mathcal{K}(J)$ for $j = r + 1, \dots, n$;
- ii) the left singular vectors u_j form an orthonormal basis of $\mathcal{R}(J)$ for $j = 1, \dots, r$ and of $\mathcal{R}(J)^\perp$ for $j = r + 1, \dots, m$;
- iii) the singular values s_j verify $s_1 \geq \dots \geq s_r > s_{r+1} = \dots = s_m = 0$ assuming $n > m$.

The following relations stand for the adjoint operator J^* : i) $\mathcal{R}(J^*) = \mathcal{K}(J)^\perp$; ii) $\mathcal{K}(J^*) = \mathcal{R}(J)^\perp$

Let J be a $m \times n$ matrix with a singular system $\{u_j, s_j, v_j\}_j$, then J has the singular value decomposition

$$J = USV^T, \tag{A.19}$$

where $U \in \mathbb{R}^{m \times m}$ and $V \in \mathbb{R}^{n \times n}$ are orthogonal matrices and $S = \text{diag}(s_1, \dots, s_m)$, with $n > m$. From the relations $JV = US$ and $J^T U = VS$, it follows that the pairs $\{u_j, s_j^2\}$ and $\{v_j, s_j^2\}$ are eigensolutions of the operators JJ^T and $J^T J$ respectively.

A.2.3 Rank

Let $J \in \mathbb{R}^{m \times n}$ be the matrix defined in section A.2.2, then with the given properties, the rank of J is

$$\text{rank}(J) = r, \tag{A.20}$$

where r (section A.2.2) is the number of singular values s of J , such that, $s_i \neq 0$ for $i = 1, \dots, r$ and $s_i = 0$ for $i = r + 1, \dots, m$ with $m \leq n$. That is, r is the number of SV different to zero. In practice, because SV decay slowly to zero, a SV is said to be zero when it has decayed several order of magnitude. Also a jump usually occurs in the SV spectrum such that the SV

corresponding to the $r + 1$ SV is few order of magnitude smaller than the r -th SV; in this case, the rank is considered as r . A full-rank matrix is defined as that matrix whose SV decay smoothly with no jump along its SV spectrum.

A.2.4 Pseudo-inverse

Let J be a $m \times n$ matrix with SVD $J = USV^T$, the pseudo-inverse of J [56] is defined as

$$J^\dagger = VS^{-1}U^T, \quad (\text{A.21})$$

where $S^{-1} = \text{diag}(s_1^{-1}, \dots, s_m^{-1})$.

An important property of the pseudo-inverse is its relation to the LS problem. Let d be the observable data, and x the solution, if $d \in \mathcal{R}(J) + \mathcal{R}(J)^\perp$, then the least square solution to the problem

$$\min\{\|Jx - d\|_2^2\}, \quad (\text{A.22})$$

is given in terms of the pseudo-inverse as

$$x_{LS} = J^\dagger d. \quad (\text{A.23})$$

A.2.5 Condition number

Let J be $m \times n$ matrix, the SVD (A.19) gives the condition number as

$$\text{cond}(J) = \frac{s_1}{s_m}, \quad (\text{A.24})$$

where s_1 is the largest singular value and s_m is the smallest one. If J represents the system matrix of linear system of equations, a very high condition number implies ill-posedness because of relatively small singular values, such that a singular matrix would have infinite condition number. On the other hand, the highest condition number is $\text{cond} = 1$ for scalar matrices.

A.2.6 Differentiation

I introduce definitions and notation for the partial and directional derivatives, gradient, and Jacobian. Then, I describe the usual formulation for calculating gradient and Jacobian.

Given a function $F : \mathbb{R}^n \mapsto \mathbb{R}$, its gradient is defined as the operator $\nabla : \mathbb{R} \mapsto \mathbb{R}^n$, such that

$$\nabla F = (\partial_1 F, \dots, \partial_n F)^T, \quad \text{where} \quad \partial_i = \frac{\partial}{\partial x^i}.$$

The partial derivative of F with respect to the i th-coordinate is the linear function $\partial_i : \mathbb{R}^n \mapsto \mathbb{R}$ described from the gradient as

$$\partial_i F(x) = (\nabla F(x))^T e_i,$$

where e_i is the i th-basis vector.

From the definition of partial derivative, the directional derivative of F along the direction given by the vector $v \in \mathbb{R}^n$ is

$$\partial_v F(x) = (\nabla F(x))^T v,$$

where by making $v = e_i$ one gets back the partial derivative.

An analogous to the first derivative for multivariate functions, $F : \mathbb{R}^n \mapsto \mathbb{R}^m$, is given by the Frechét derivative $F'(x)$ defined as

$$F(x + h) = F(x) + F'(x)h + o(\|h\|), \quad \text{where} \quad \|h\| \rightarrow 0.$$

The Jacobian can be define as the operator composed of n gradients as $J : \mathbb{R}^n \mapsto \mathbb{R}^m$

$$J = \frac{\partial(F_1, \dots, F_m)}{\partial(x^1, \dots, x^n)} = (\nabla F_1, \dots, \nabla F_m)^T,$$

where each row $J_i = \nabla F_i$ can be computed by finite differences as

$$J_i = \frac{F(x + h) - F(x)}{h}. \quad (\text{A.25})$$

The Jacobian is usually expressed as a $m \times n$ matrix with entries

$$J_{ij} = \frac{\partial F_i}{\partial x^j}.$$

From J , the directional derivative $\partial_v F$ can be explain as

$$\partial_v F = Jv,$$

where the partial derivative is given for $v = e_i$ as

$$\partial_i F = J e_i.$$

The gradient and Jacobian can be computed from the definition of the Lie-derivative or directional derivative

$$\frac{d}{d\tau} F(x + \tau h)|_{\tau=0} = F'(x)h,$$

where both the gradient and Jacobian my be represented as $F'(x)$.

Appendix B

Statistical background

This chapter contains the statistical background and notation necessary for understanding the linear model, LS solutions, regularisation and priors for inverse problems, covariance estimation, and PCA.

First, general concepts are introduced where multivariate analysis, joint distribution, moments, and Bayes theorem are the most important. Then, relevant results that are referred in the thesis like maximum likelihood estimation, MAP estimation, best linear predictor, and PCA are introduced.

B.1 General concepts

The framework of multivariate linear analysis assumes a linear model and more than one dependent variable. General concepts on multivariate statistics can be found in [32, 91].

Let $X = (X_1, \dots, X_m)$ be a vector representing a multivariate distribution of m discrete random variables where each variable X_i is a function from a sample space S_i to the real numbers, that is $X_i : S_i \mapsto \mathbb{R}$; and $x = (x_1, \dots, x_m)$ be a realisation, or sample, of X ; and $P(X_i = x_i)$, where $0 \leq P \leq 1$, be the probability of the variable X_i to take the value x_i .

A random variable X_i is characterised by its distribution function $F(X_i)$, which represents the accumulative probability of being less or equal to a value x_i , that is $F(X_i) = P(X_i \leq x_i)$. For a set of random variables, a joint distribution function represents the simultaneous realisation of all variables, that is

$$F(x) = P(X_1 \leq x_1, \dots, X_m \leq x_m), \quad (\text{B.1})$$

such that, when all $x_i \rightarrow \infty$, then $F(x)=1$. The probability of an event is defined by a joint frequency function

$$f(x_1, \dots, x_m) = P(X_1 = x_1, \dots, X_m = x_m), \quad (\text{B.2})$$

such that

$$F(x) = \sum_{t \leq x} f(t). \quad (\text{B.3})$$

Treating several variables yield defining independent variables as those whose joint distribution can be separated onto the product of the variable distributions, i.e. X_1, \dots, X_m are independent if

$$f(x_1, \dots, x_m) = \prod_{i=1}^m f(x_i). \quad (\text{B.4})$$

Non independent variables means that given the realisation of a variable X_i , the probability of the realisation of a variable X_j depends on the $P(X_i)$. Thus, conditional probability is defined as

$$P(X_j|X_i) = \frac{P(X_i, X_j)}{P(X_i)}. \quad (\text{B.5})$$

Otherwise, independent variables comply

$$P(X_j|X_i) = P(X_j). \quad (\text{B.6})$$

B.1.1 First and second moments

Among all types of distribution, the focus here is on Gaussian distributions, which can be defined by the first and second moments. The first moment or expected value is defined as

$$\mu = (\mu_1, \dots, \mu_m) = (E[x_1], \dots, E[x_m]), \quad (\text{B.7})$$

which is a measure of the centre of mass of the distribution.

The second moment or covariance of two variables x_i and x_j is given by

$$C_{ij} = \text{cov}(x_i, x_j) = E[(x_i - \mu_i)(x_j - \mu_j)] = E[x_i x_j] - \mu_i \mu_j, \quad (\text{B.8})$$

which is measure of the linear dependence between the variables. Thus, $C_{ij} = 0$ for independent variables. A normalised measure of correlation between variables is given by the correlation matrix, whose elements are given by

$$\text{corr}(x_i, x_j) = \frac{\text{cov}(x_i, x_j)}{\sigma_i \sigma_j}, \quad (\text{B.9})$$

where $\sigma_i^2 = \text{cov}(x_i, x_i)$ is the variance of x_i , and σ is the STandard Deviation (STD).

B.1.2 Bayes theorem

Let X and Y be two random set of variables jointly distributed, where Y is the observed variable function of X , the posterior probability or Maximum A Posteriori (MAP) estimator is given by

$$P(X|Y) = \frac{P(Y|X)}{P(Y)} P(X), \quad (\text{B.10})$$

where $P(X)$ is the a priori density function or prior, and $P(Y|X)$ is the likelihood density function.

B.1.3 Gaussian distribution

Let $X = (X_1, \dots, X_m)$ be a multivariate standard Gaussian, Normal, distribution with mean zero and unit covariance matrix, indicated as $X \sim N(0, I)$ and read as ' η follows a Normal distribution of mean zero and covariance I '. Its joint frequency function is given by

$$f(x) = \frac{1}{(2\pi)^{\frac{m}{2}}} \exp\left(-\frac{1}{2}x^T x\right). \quad (\text{B.11})$$

Now, by applying a transformation $Y = \mu + Bx$, Y becomes a Gaussian distribution with mean μ and covariance matrix $C = BB^T$, i.e. $Y \sim N(\mu, C)$, with the joint frequency function given by

$$f(y) = \frac{1}{(2\pi)^{\frac{m}{2}} |\det(C)|^{\frac{1}{2}}} \exp\left(-\frac{1}{2}(y - \mu)^T C^{-1}(y - \mu)\right), \quad (\text{B.12})$$

assuming that B^{-1} exists. In fact, standard variables X_i assume an equal variance domain, described by ones in the covariance diagonal, and no correlation, explained by off diagonals of C being zero. However, in general, variables may differ in variance and be correlated, which is modelled by the Normal variables Y_i having a general covariance matrix C .

B.2 Maximum Likelihood Estimate

Given a set of variables $Y \in \mathbb{R}^m$ and unknown parameters $\theta = \theta_1, \dots, \theta_r$, the joint frequency function, also called likelihood $\mathcal{L}(\theta)$, can be used for estimating θ . The Maximum Likelihood Estimate (MLE) maximises $\ln \mathcal{L}(\theta)$ with respect all parameters θ as

$$\frac{\partial}{\partial \theta_k} \ln \mathcal{L}(\theta) = 0, \quad k = 1, \dots, r. \quad (\text{B.13})$$

Relevant MLEs from a Gaussian distribution are the linear LS solution estimations, mean, and variance, however, since variance MLE is biased, it is common used an unbiased estimate of the covariance.

B.3 Estimation of the first and second moments

Being μ the population mean, and C the population covariance matrix, they can be estimated from an experiment of n observations by applying MLE, however, the MLE of the covariance is a biased estimate. Given a parameter θ , the bias of the estimator $\hat{\theta}$ is defined by $\text{bias} = E[\hat{\theta}] - \theta$; therefore, the unbiased estimator has bias equal zero.

B.3.1 Mean estimation

The expectation for the variable x_i is computed as

$$E[x_i] = \frac{1}{m} \sum_{k=1}^n x_{ik}. \quad (\text{B.14})$$

B.3.2 Unbiased estimate of the covariance

The unbiased estimate of the covariance is given by

$$C_{ij} = \text{cov}(x_i, x_j) = \frac{1}{n-1} [(x_i - E[x_i])(x_j - E[x_j])], \quad (\text{B.15})$$

where $E[x_i]$ is given by (B.14).

As the number of variables, m , increases, the computation of C using (B.14) becomes impracticable since the number of observations must be equal to the number of parameters to be determined, given by (4.35). Therefore, if the number of observations n is less than (4.35), then the covariance will not be completely determined and may be ill-posed; besides, if $n < m$, then the covariance will be rank-deficient.

A possible solution for determining C from a low number of observations is imposing constraints to it. There are several ways for constraining the covariance [98] where the most explicit is applying conditional independence to variables that are not directly dependent. This is employed in Geophysics for spatial data where entries for the concentration matrix, C^{-1} , are set to zero for conditional independent variables that are, for example, far apart. For EIT of the head, it is not obvious how to define conditional independence where channel variables correspond to injection from two diametric positions. However, other constraints could be imposed.

B.4 Best linear predictors

Given a set of observable variables y , one is interested in obtaining the best predictor based on a new set of variables x . However, while the best predictor requires the frequency distribution, the Best Linear Predictor (BLP), provides a linear approximation $f(x)$ [32], based on the first and second moments, minimising

$$E[(y - f(x))^T (y - f(x))]. \quad (\text{B.16})$$

B.4.1 Principal Component Analysis

Principal Component Analysis (PCA), known as the oldest multivariate analysis technique [32], provides a new set of variables defining the Principal Components (PCs), which are BLP of the original data.

PCA to high dimensionality data for reducing the dimensionality to few uncorrelated components that retain most of the information of the original data. Therefore, if there is high correlation, then the first PCs will contain most of the information.

Originally, given the data $y \in \mathbb{R}^m$ and vector basis $a_i \in \mathbb{R}^m$, PCs $a_i^T y$ were derived such that $a_i^T y$ has maximum variance, and they are orthogonal in the sense

$$\text{cov}(a_i^T y, a_j^T y) = a_i^T C a_j, \quad (\text{B.17})$$

where $C = \text{cov}(y)$ [84, 32].

Using Lagrange multipliers, the first PC is obtained by maximising its variance, subject to normalisation, that is,

$$\max_{a_1} \{a_1^T C a_1 - \lambda_1 (a_1^T a_1)\}, \quad (\text{B.18})$$

which becomes

$$(C - \lambda_1 I) a_1 = 0. \quad (\text{B.19})$$

Higher order components are calculated on the same way by imposing orthogonality.

The new basis a_i are the eigenvectors of C with eigenvalue λ_i ; the PCs of the data are the projections of the eigenvectors onto the data, i.e. $a_i^T y$.

Note, the variance, eigenvalue, of the PCs tend to decrease for higher components [84]. Thus, approximating the data from the first PCs when the covariance matrix has been estimated from a low number of observations, is appealing since last PCs are estimated with lower precision.

In the case where the covariance is rank deficient, if there are q redundant variables, then $\text{rank}(C) = m - q$, and one can reduce from m to $m - q$ variables without loss of information [84].

Appendix C

Derivation of linear approaches

Difference imaging results can be improved by reconstructing relative difference data rather than difference data [74, Chapter 4] requiring also a normalisation in the Jacobian, called row normalisation. Here, the linear LS problem is derived from the nonlinear LS problem for the case of relative difference data.

Let V be the measured voltage and V_{ref} be the measured reference voltage; $F(x)$ be the model predicted voltages, or forward solution, for a given conductivity distribution x ; and $F(x_{\text{ref}})$ be the predicted reference voltage, for a reference conductivity x_{ref} . For a small conductivity change $\Delta x = x - x_0$ around x_0 , the predicted voltage $F(x)$ can be approximated around the predicted reference voltage $F(x_0)$ using Taylor's expansion as

$$F(x) \simeq F(x_0) + J(x_0)\Delta x, \quad (\text{C.1})$$

where changes of order $(\Delta x)^2$ are neglected, and $J(x_0)$ is the Jacobian of the forward mapping F at x_0 .

Relative data is obtained by dividing the measured data V by its measured reference data V_{ref} , that is,

$$\frac{V}{V_{\text{ref}}}, \quad (\text{C.2})$$

relative difference data d by

$$d = \frac{V - V_{\text{ref}}}{V_{\text{ref}}}. \quad (\text{C.3})$$

C.1 Nonlinear least squares problem

The nonlinear LS problem seeks an approximated solution to the nonlinear system of equations $F(x) = V$ as

$$\min_x \{\|V - F(x)\|^2\}. \quad (\text{C.4})$$

Now, dealing with relative voltages $F(x)/F(x_{\text{ref}}) = V/V_{\text{ref}}$, the LS problem becomes

$$\min_x \left\{ \left\| \frac{V}{V_{\text{ref}}} - \frac{F(x)}{F(x_{\text{ref}})} \right\|^2 \right\}. \quad (\text{C.5})$$

C.2 Linear least squares problem

Substituting Taylor's approximation in (C.1) into the nonlinear LS problem (C.5),

$$\left\| \frac{V}{V_{\text{ref}}} - \frac{F(x_0)}{F(x_{\text{ref}})} + \frac{V_{\text{ref}}}{F(x_{\text{ref}})} - J(x_0)\Delta x \right\|^2, \quad (\text{C.6})$$

and assuming $x_{\text{ref}} = x_0$, the linear LS problem is given by

$$\min_x \left\{ \left\| \frac{V - V_{\text{ref}}}{V_{\text{ref}}} - \frac{J(x_0)\Delta x}{F(x_0)} \right\|^2 \right\}, \quad (\text{C.7})$$

which can be expressed in terms of d (C.3) as

$$\min_x \left\{ \left\| d - \frac{1}{F(x_0)} J(x_0)\Delta x \right\|^2 \right\}, \quad (\text{C.8})$$

whose solution estimates a conductivity change Δx_{LS} for relative difference data d as

$$\Delta x_{LS} = \left(\frac{1}{F(x_0)} J(x_0) \right)^\dagger d, \quad (\text{C.9})$$

where \dagger denotes the pseudo-inverse.

However, in practice it seems that using the term Jx_0 instead of $F(x_0)$ for the row normalisation (section C.3) yields better results.

C.3 Row normalisation

Defining the row normalisation matrix as

$$R = \text{diag}(F_1(x_0)^{-1}, \dots, F_m(x_0)^{-1}), \quad (\text{C.10})$$

where each row of the Jacobian is scaled by the corresponding predicted voltage, for a total number of m predicted voltages. Because each entry of the voltage difference (C.2) has been scaled by the reference voltage, the same operation must be done to the Jacobian. Therefore, row normalisation must be applied when reconstructing relative difference data.

Denoting the normalised Jacobian as

$$J_n = RJ, \quad (\text{C.11})$$

the linear LS problem (C.8) becomes

$$\min_x \left\{ \left\| d - J_n \Delta x \right\|^2 \right\}, \quad (\text{C.12})$$

and the solution to (C.8) is given by

$$\Delta x_{LS} = J_n^\dagger d. \quad (\text{C.13})$$

In fact, for obtaining relative difference conductivity in percentage change one needs to divide the solution (C.13) by the reference conductivity

$$100 * \frac{\Delta x}{x_0}. \quad (\text{C.14})$$

Row normalisation can be derived in a more practical way. Given that the Jacobian maps a change of conductivity Δx into a change of voltage ΔV , that is, $J : \Delta x \mapsto \Delta V$, where $\Delta x = x - x_0$ and $\Delta V = V - V_0$, the relative difference data can be approximated as

$$\frac{\Delta V}{V_0} \simeq \frac{J\Delta x}{F(x_0)}, \quad (\text{C.15})$$

the conductivity change is then obtained as

$$\Delta x = J_n^{-1} \frac{\Delta V}{V_0}. \quad (\text{C.16})$$

Row normalisation for EIT has been studied in [108], however, it is still not very clear the best approach to row normalisation. In practice, it seems that results by using the row normalisation (C.10) are better if $F(x_0)$ is approximated by $b = Jx_0$, that is, defining R as

$$R = \text{diag}(b_1^{-1}, \dots, b_m^{-1}). \quad (\text{C.17})$$

Nevertheless, since it has been pointed out that row normalisation [108] increases the conditioning of the Jacobian (Figure C.1), it would be more efficient to apply the normalisation to d , such that, the problem becomes

$$J\Delta x = (Jx_0)d. \quad (\text{C.18})$$

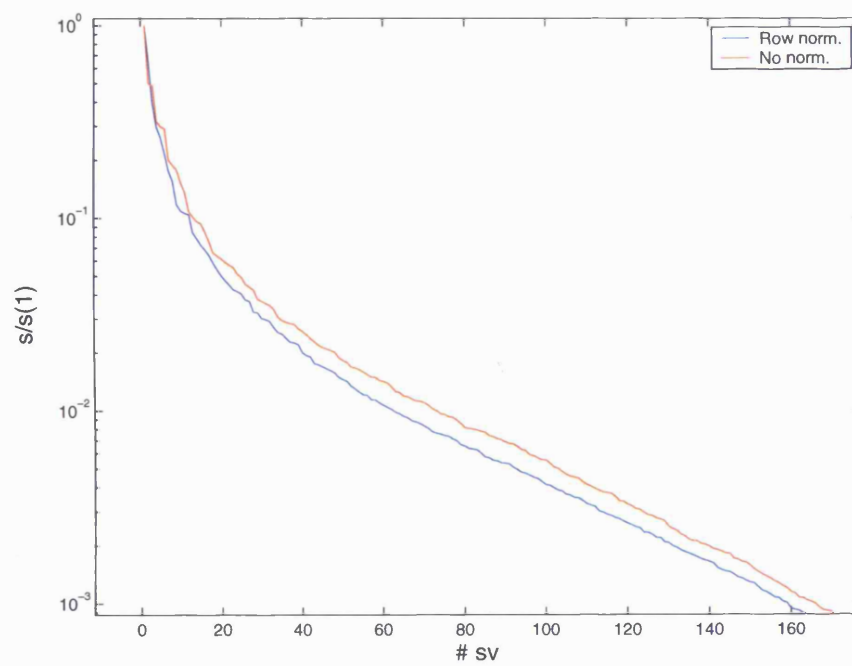


Figure C.1: Relative singular values of the Jacobian with and without row normalisation.

Appendix D

Concepts of differential geometry

An introduction to classic differential geometry can be found in [124].

D.1 Diffeomorphism on manifolds

A smooth manifold can be described as a set of points with a neighbourhood called 'local charts' such that there is a one-to-one correspondence between each chart and an open region of \mathbb{R}^3 , which induces local coordinates on each chart. Examples of manifolds are a region of the Euclidean space or a surface with non-singular points.

A diffeomorphism Ψ can be defined as a one-to-one function where both the function and its inverse are smooth. Thus, one can define a class of diffeomorphically equivalent manifolds \mathcal{M} if there exist a diffeomorphic transformation among the manifolds, $\Psi : \tilde{\mathcal{M}} \mapsto \mathcal{M}$, given by smooth functions f_i

$$\begin{aligned}x &= f_1(\tilde{x}, \tilde{y}, \tilde{z}) \\y &= f_2(\tilde{x}, \tilde{y}, \tilde{z}) , \\z &= f_3(\tilde{x}, \tilde{y}, \tilde{z})\end{aligned}\tag{D.1}$$

such that its Jacobian $\Psi' = \partial(f_1, f_2, f_3)/\partial(\tilde{x}, \tilde{y}, \tilde{z})$ has nonzero determinant, that is, $|\Psi'| \neq 0$.

It includes affine transformations, nonlinear smooth transformations, and infinitesimal perturbations. Affine are linear transformations together with translation that preserved lines and parallelism but not angles and lengths; therefore, they are considered as linear diffeomorphism acting on linear manifolds by (adding) a constant vector to each point of the manifold.

D.2 Invariance up to a diffeomorphism

An interesting idea from general relativity, that indirectly provides physical intuition to the non-unique anisotropic inverse problem, explains a diffeomorphism as a type of transformation such that physical events are independent of the choice of coordinates (Math Pages, <http://www.mathpages.com/rr/s9-02/9-02.htm>). This type of transformation extended the previous transformation that in special relativity defined the class of inertial systems to a more gen-

eral choice of transformation that relates systems of coordinates to describe events in general relativity. Thus, a one-to-one smooth transformation with differentiable inverse left invariant physical laws, such that the physical description of events did not depend on the choice of coordinates. This type of transformation is called diffeomorphism and two sets of an event are said to be equivalent up to a diffeomorphism if there exist a diffeomorphic transformation between them.

D.3 Curves and surfaces in 3D manifolds

A 3D curve in parametric form is defined as

$$x = f_1(t), y = f_2(t), z = f_3(t), \quad (\text{D.2})$$

with curve length

$$dl = |v_t|dt, \quad (\text{D.3})$$

where v_t is the tangent or velocity vector to the curve at every point, given by

$$v(t) = \left(\frac{df_1}{dt}, \frac{df_2}{dt}, \frac{df_3}{dt} \right) = v_i e_i,^1 \quad (\text{D.4})$$

where v_i are the vector components defined as

$$v_i = \frac{df_i}{dt}, \quad (\text{D.5})$$

and e_i are the vectors tangent to the coordinate grid, given by

$$e_i = \frac{\partial}{\partial x_i}. \quad (\text{D.6})$$

Curve natural coordinates are defined in terms of the natural parameter t such that $|v_t| = 1$; in this case, a normal to the curve is

$$\nu = \frac{dv_t}{dt} \quad \text{where} \quad v \perp \nu = \frac{dv}{dt} \quad \text{since} \quad v \frac{dv}{dt} = 0. \quad (\text{D.7})$$

Three vectors are needed to uniquely describe a curve in 3D, v, ν, b , where the third vector b , called the binormal, can be defined by vectorial product as

$$b = v \wedge \nu. \quad (\text{D.8})$$

In fact, these concepts defined the extrinsic geometry of a curve.

A nonsingular surface in 3D is defined by

$$F(x, y, z) = \text{const.} \quad \text{where} \quad \nabla F \neq 0. \quad (\text{D.9})$$

¹Summation is understood over repeated indices.

From the definition (D.9) the gradient to the surface is given by

$$\nabla F(x, y, z) = \left(\frac{\partial F}{\partial x}, \frac{\partial F}{\partial y}, \frac{\partial F}{\partial z} \right) = \sum_{i=1}^3 \frac{\partial F}{\partial x_i} e_i. \quad (\text{D.10})$$

Given a curve (D.2) and a function $g(x, y, z)$ defined at each point on the curve, $g = g(f_1(t), f_2(t), f_3(t))$, the function derivative is given by the projection of the function gradient onto the curve velocity vector

$$\frac{dg}{dt} = \nabla g \cdot v_t = \frac{\partial g}{\partial x_i} \frac{dx_i}{dt}. \quad (\text{D.11})$$

D.4 Tensors and transformation of coordinates

In this section, a distinction between up and lower indices is used to define contravariant and covariant components of a tensor and their transformation rules. A tensor is introduced as a generalisation of scalar, vector, and matrix, which are defined as rank zero, one, and two tensors. Here, only up to two rank tensors are considered. A zero rank tensor is a scalar, which is invariant under any transformation. A one rank tensor is a vector v , which can be described in terms of contravariant components v^i , with upper index, or in terms of covariant components v_i , with lower index. A two rank tensor can have two contravariant indices as v^{ij} , two covariant indices as v_{ij} , or mixed as v_j^i . Tensor components are defined by their transformation rules under a change of coordinates [163].

Given the coordinates x^i in terms of the coordinates \hat{x}^j as

$$x^i = x^i(\hat{x}^j), \quad (\text{D.12})$$

the Jacobian of the transformation can be defined as

$$A_j^i = \frac{\partial x^i}{\partial \hat{x}^j}, \quad (\text{D.13})$$

or in matrix form as

$$A = \frac{\partial(x^1, x^2, x^3)}{\partial(\hat{x}^1, \hat{x}^2, \hat{x}^3)} = \begin{pmatrix} \frac{\partial x^1}{\partial \hat{x}^1} & \frac{\partial x^1}{\partial \hat{x}^2} & \frac{\partial x^1}{\partial \hat{x}^3} \\ \frac{\partial x^2}{\partial \hat{x}^1} & \frac{\partial x^2}{\partial \hat{x}^2} & \frac{\partial x^2}{\partial \hat{x}^3} \\ \frac{\partial x^3}{\partial \hat{x}^1} & \frac{\partial x^3}{\partial \hat{x}^2} & \frac{\partial x^3}{\partial \hat{x}^3} \end{pmatrix}. \quad (\text{D.14})$$

Similarly, if the Jacobian determinant is non zero, $|\partial x^i / \partial \hat{x}^j| \neq 0$, then there exists an inverse relation $\hat{x} = \hat{x}(x)$, so the inverse of the Jacobian A is given by

$$B_j^i = \frac{\partial \hat{x}^i}{\partial x^j}, \quad (\text{D.15})$$

that is, $B = A^{-1}$. The effect of the transformation in the differential volume $dx^1 dx^2 dx^3$ is given by the determinant of the transformation $|A|$ by

$$dx^1 dx^2 dx^3 = |A| d\hat{x}^1 d\hat{x}^2 d\hat{x}^3, \quad (\text{D.16})$$

such that the volume increases when $|A|$ is larger than one.

D.4.1 Rank one tensor: Vector components

The contravariant component of a vector, v^i , change as

$$v^i = \frac{\partial x^i}{\partial \hat{x}^j} \hat{v}^j = A_j^i \hat{v}^j \quad (\text{D.17})$$

$$\hat{v}^i = \frac{\partial \hat{x}^i}{\partial x^j} v^j = B_j^i v^j, \quad (\text{D.18})$$

or in matrix form as

$$(v^c) = A(\hat{v}^c) \quad (\text{D.19})$$

$$(\hat{v}^c) = A^{-1}(v^c) = B(v^c), \quad (\text{D.20})$$

where c indicates that the component is contravariant, and $(v^c) = (v^1, v^2, v^3)^T$.

The covariant component of a vector, v_i , change as

$$\hat{v}_i = \frac{\partial x^j}{\partial \hat{x}^i} v_j = A_i^j v_j \quad (\text{D.21})$$

$$v_i = \frac{\partial \hat{x}^j}{\partial x^i} \hat{v}_j = B_i^j \hat{v}_j, \quad (\text{D.22})$$

or in matrix form as

$$(\hat{v}_c) = A^T(v_c) \quad (\text{D.23})$$

$$(v_c) = B^T(\hat{v}_c) \quad (\text{D.24})$$

where $_c$ indicates that the component is covariant, and the transpose is introduced because the upper index of a matrix, as in (D.21,D.22), is 'on the top left' (the lower index 'on the bottom right') considered as row (column), and so it must be transposed to agree with the matrix multiplication.

An example of covariant vector is the coordinate vector $e_i = \partial_i$, being parallel to the coordinates lines; examples of contravariant vectors are the differential form dx^i and the velocity vector $v^i = dx^i/dt$, being perpendicular to the coordinates lines. Note that the differential forms dx^i have a direct integration x^i .

D.4.2 Two rank tensor: Conductivity tensor

A two rank tensor with two contravariant components like the conductivity tensor σ^{ij} , which is represented as a two-by-two matrix in some coordinates, follows the transformation rule

$$\sigma^{ij} = \frac{\partial x^i}{\partial \hat{x}^k} \sigma^{kl} \frac{\partial x^j}{\partial \hat{x}^l} = A_k^i \sigma^{kl} (A^T)_l^j \quad (\text{D.25})$$

$$\sigma^{ij} = \frac{\partial \hat{x}^i}{\partial x^k} \sigma^{kl} \frac{\partial \hat{x}^j}{\partial x^l} = (A^{-1})_k^i \sigma^{kl} (A^{-T})_l^j = B_k^i \sigma^{kl} (B^T)_l^j \quad (\text{D.26})$$

where in matrix form

$$(\sigma) = A(\hat{\sigma})A^T \quad (\text{D.27})$$

$$(\hat{\sigma}) = A^{-1}(\sigma)A^{-T} = B\sigma B^T \quad (\text{D.28})$$

In fact, given an orthogonal transformation $x = x(\hat{x})$ [36], where x is considered the given global coordinate system, and \hat{x} the local coordinate system, for which $\hat{\sigma}$ is diagonal, σ can be also defined by the eigenvalue decomposition as

$$\sigma = VDV^T, \quad (\text{D.29})$$

where the eigenvalue matrix D can be understood as the conductivity tensor in the local coordinate system, $V = [v_1, v_2, v_3]$ with v_i the eigenvectors and σ as the conductivity tensor in the global coordinate system, which agrees with the transformation rules $A = [\acute{e}_1, \acute{e}_2, \acute{e}_3]$ for $\acute{e}_i = \partial x / \partial \hat{x}^i = v_i$ (section A.2.1).

D.4.3 Two tensor: Riemannian metric tensor

D.4.4 Riemannian metric tensor

Let $x = (x_1, x_2, x_3)$ be the Cartesian coordinates in the Euclidean space, the scalar product induces a norm for the velocity vector $v = dx/dt$

$$\|v\|^2 = \left\| \frac{dx}{dt} \right\|^2 = \sum_{i=1}^3 \left(\frac{dx^i}{dt} \right)^2 = \frac{dx^k}{dt} \delta_{kl} \frac{dx^l}{dt}, \quad (\text{D.30})$$

where δ_{ij} is the Euclidean metric given by the unit matrix. By defining $z^i = \hat{x}^i$ as the old coordinate system, such that $x^i = x^i(z^i)$, and by applying the transformation rule for covariant coordinates (D.20)

$$\|v\|^2 = \frac{dz^i}{dt} \frac{\partial x^k}{\partial z^i} \delta_{kl} \frac{\partial x^l}{\partial z^j} \frac{dz^j}{dt} = \frac{dz^i}{dt} A_i^k \delta_{kl} A_j^l \frac{dz^j}{dt}. \quad (\text{D.31})$$

Now, since a Riemannian metric \acute{g} is a positive definite quadratic form that leaves invariant the scalar product (D.30) in the new coordinates, then

$$\|v\|^2 = \left\| \frac{dz}{dt} \right\|^2 = \frac{dz^i}{dt} \acute{g}_{ij} \frac{dz^j}{dt}, \quad (\text{D.32})$$

and so the new metric is

$$\acute{g}_{ij} = A_i^k \delta_{kl} A_j^l. \quad (\text{D.33})$$

In fact, in the Euclidean space $g = \mathbb{I}$, and then, in matrix form, a metric \acute{G} in the old coordinate system is given with respect to the new metric G by

$$\acute{G} = A^T G A, \quad (\text{D.34})$$

which is equivalent to the transformation rule for covariant two rank tensors.

Let v, w be two vectors in \mathbb{R}^3 , the Riemannian metric can be defined, by tangent vectors, vectors in contravariant coordinates, at every point of the manifold and depending smoothly on the choice of local coordinates, as a positive definite symmetric bilinear function $g : \mathbb{R}^3 \times \mathbb{R}^3 \mapsto \mathbb{R}^+$. That defines a scalar product for each point P of a manifold \mathcal{M} , being locally smooth, as

$$v \cdot w = u^i g_{ij} w^j, \quad (\text{D.35})$$

with an induced norm or distance (D.30). Thus, the metric is defined by

(http://en.wikipedia.org/wiki/Metric_tensor)

$$g_{ij} = \left\langle \frac{\partial}{\partial x^i}, \frac{\partial}{\partial x^j} \right\rangle = \langle e_i, e_j \rangle. \quad (\text{D.36})$$

The length between the points a and b is defined as

$$L = \int_a^b (dx^i g_{ij} dx^j)^{\frac{1}{2}}. \quad (\text{D.37})$$

D.4.5 Relation conductivity-metric

A relation between the conductivity and the metric in Riemannian manifolds can be done in terms of modern differential geometry [104, 174]. Let \mathcal{M} be a connected manifold with compact boundary $\partial\mathcal{M}$ and g the Riemannian metric such that $ds^2 = g_{ij} dx^i dx^j$.

Given the conductivity tensor σ , in 3D, there is a metric g for which the conductivity equation becomes the Laplace Beltrami equation

$$\frac{1}{\sqrt{|g|}} \frac{\partial}{\partial x^i} \left(\sqrt{|g|} g^{ij} \frac{\partial u}{\partial x^j} \right) = 0, \quad (\text{D.38})$$

where the metric is given uniquely by the conductivity

$$g^{ij} = \frac{1}{|\sigma^{kl}|} \sigma^{ij}. \quad (\text{D.39})$$

Note that g^{ij} is the inverse of g_{ij} . With this relation, the EIT problem is equivalent to determine the Riemannian metric from the NtoD map $\Lambda_g = \Lambda_\sigma$. Because given two metrics g and \tilde{g} related by a diffeomorphism that fixes the boundary, then $\Lambda_g = \Lambda_{\tilde{g}}$, and so the metric can be

determined in two steps [174]: i) determining the abstract manifold that corresponds to the conductivity, ii) selecting an appropriate embedding of the abstract manifold in \mathbb{R}^3 . While the step ii) is not uniquely defined, providing extra information can make it unique.

As an example, given $\sigma^{ij} = \text{diag}(2, 1, 1)$, $g^{ij} = \text{diag}(1, 0.5, 0.5)$, and then $g_{ij} = \text{diag}(1, 2, 2)$, which leads to a differential length $ds^2 = (dx)^2 + 2(dy)^2 + 2(dz)^2$.

D.4.6 Example: spherical coordinates

Given the change of coordinates $(\hat{x}, \hat{y}, \hat{z}) = (r, \theta, \phi) \mapsto (x, y, z)$, (e_r, e_θ, e_ϕ) are given by the transformation rule (D.24), for example,

$$e_r = \frac{\partial x^j}{\partial x^r} e_j = \frac{\partial x}{\partial r} e_x + \frac{\partial y}{\partial r} e_y + \frac{\partial z}{\partial r} e_z. \quad (\text{D.40})$$

Given the conductivity tensor $\hat{\sigma} = \hat{\sigma}(r, \theta, \phi)$, that is, initialised in spherical coordinates, then in the new coordinates it is given by

$$\sigma = A \hat{\sigma} A^T, \quad (\text{D.41})$$

where A is given by

$$\begin{aligned} A &= \frac{\partial(x, y, z)}{\partial(r, \theta, \phi)} = [e_r, e_\theta, e_\phi] \\ &= \begin{pmatrix} \sin \theta \cos \phi & r \cos \theta \cos \phi & -r \sin \theta \sin \phi \\ \sin \theta \sin \phi & r \cos \theta \sin \phi & r \sin \theta \cos \phi \\ \cos \theta & -r \sin \theta & 0 \end{pmatrix}. \end{aligned} \quad (\text{D.42})$$

An analogy with the eigenvalue decomposition can be defined as $\sigma = V D V^T$ by defining $V = A$ and $D = \hat{\sigma}$.

Let $f = f(x, y, z) = x^2 + y^2 + z^2 = \text{const.}$ be a 3D spherical surface, with gradient given by

$$\nabla f = \sum_i \frac{\partial f}{\partial x^i} e_i = (2x, 2y, 2z), \quad (\text{D.43})$$

the derivative with respect to θ is

$$\frac{df}{d\theta} = \left\langle \nabla f, \frac{dx}{d\theta} \right\rangle = \sum_i \frac{\partial f}{\partial x^i} \frac{dx^i}{d\theta} = 0, \quad (\text{D.44})$$

such that f is constant along the curve θ ; the same applies to ϕ . The same applies to r that yields the obvious result

$$\frac{df}{dr} = (2x, 2y, 2z) \cdot \left(\frac{x}{r}, \frac{y}{r}, \frac{z}{r} \right) = 2r. \quad (\text{D.45})$$

D.4.7 Tangent and cotangent space

Differential geometry defining vectors and tensors on manifolds provides an intuitive understanding of the concepts of vectors and tensors. Here, the interest is on smooth manifolds and diffeomorphic transformations between them.

Given a manifold M , the tangent space $T_p M$ is defined as the space composed of all tangent vectors for every point p . The vector position of p is given, in 3D, as $v_p = (x^1, x^2, x^3) = (x^1 - 0, x^2 - 0, x^3 - 0)$, $v \in T_p M$, where x^i are the coordinates; therefore, the tangent vectors correspond to the usual vectors. Let $F : M \mapsto N$ be a diffeomorphism, the push forward F_* is defined as a linear map from the tangent space of M to the tangent space on N (http://en.wikipedia.org/wiki/Push_forward)

$$F_* : T_p M \mapsto T_{F(p)} N, \quad (\text{D.46})$$

then the push forward maps vectors to vectors, and so a linear map can be defined on how it acts on vectors. If F_* is defined as matrix, then the push forward corresponds to the Jacobian of the transformation $J = \partial x / \partial x'$, where x' are the coordinates in M and x are the coordinates in N , such that the push forward of the vector v' is $Jv' = v$.

The cotangent space $T_p^* M$ is defined as the dual space to the tangent space $T_p M$, composed of linear functions or tensors $f \in T_p^* M$ that map vectors onto numbers

$$f : T_p M \mapsto \mathbb{R}. \quad (\text{D.47})$$

For example, the projection of any vector v onto w can be defined as a tensor $f_w(v) = w \cdot v$. The pull back of tensors is defined as a linear map from the cotangent space $T_p^* M$ to the cotangent space on $T_p^* N$

$$F^* : T_{F(p)}^* N \mapsto T_p^* M, \quad (\text{D.48})$$

that is, it map backs tensors (<http://en.wikipedia.org/wiki/Pullback>). This is clear when expressed for the previous example of a projection

$$(F^* f)(v) = f(F(v)) = f(w), \quad (\text{D.49})$$

where the action of the pull back F^* on the tensor f is given by the tensor f acting on tensor $w \in T_p^* N$. Let A be the matrix representing the push forward F_* , then since the pull back acts in reverse direction, it can be proven that the transpose matrix A^T represents the pull back F^* .

In conclusion, given a diffeomorphism $F : M \mapsto N$, the push forward is a linear map $F_* : T_p M \mapsto T_{F(p)} N$ represented by a matrix A that pushes forward vectors (vectors in contravariant coordinates) as $Av' = v$, which agrees with the previous definition (D.20), and the

pull back is a linear map $F^* : T_{F(p)}^* N \mapsto T_p^* M$ represented by A^T that pulls back tensors (vectors in covariant coordinates) as $A^T f = f'$, which agrees with the previous definition (D.24).

One rank tensors or vectors can be defined by both covariant and contravariant components, which are related by defining a metric on the manifold. Position vectors are given in contravariant coordinates and belong to the tangent space; linear functions are given by covariant components and belong to the cotangent space. Linear functions are also called covectors and one-forms.

Appendix E

Conductivity tensor scaling

The aim of this chapter is to analyse the effect of constraining (scaling) the conductivity tensor in terms of the current norm, tensor trace, and determinant, for two constraints that have been previously applied in EEG: i) scaling of the tensor trace [90] and ii) Wang's constraint [182].

It is assumed there is an electrical field with equal components $E_i = E$. Let $\sigma = \sigma_{sc} \text{diag}(1, 1, 1)$ be the isotropic conductivity tensor where σ_{sc} is the scalar isotropic conductivity. The trace is $\text{trace}(\sigma) = 3\sigma_{sc}$. The current density is

$$\|J\|^2 = \sigma_{xx}^2 E_x^2 + \sigma_{yy}^2 E_y^2 + \sigma_{zz}^2 E_z^2 = 3\sigma_{sc}^2 E^2, \quad (\text{E.1})$$

so $\|J\| = \sqrt{3}\sigma_{sc}E$. The determinant is $|\sigma_{sc}^3|$.

Now, given a scalar anisotropic tensor, whose conductivity in the x and y-direction, the x-y plane, is ten times larger than in the z-direction, $\sigma_{xx} = \sigma_{yy} = 10\sigma_{zz}$, the effect of scaling the tensor is compared to the isotropic case.

Scaling the trace to be equal to the isotropic one

$$\text{trace}(\sigma) = 3\sigma_{sc} = 21\sigma_{zz}, \quad (\text{E.2})$$

then $\sigma_{zz} = (3/21)\sigma_{sc}$ and $\sigma_{xx} = \sigma_{yy} = 10(3/21)\sigma_{sc}$. The current norm is

$$\|J\| = \sqrt{201} \frac{3}{21} \sigma_{sc} E = 2.03 \sigma_{sc} E. \quad (\text{E.3})$$

The determinant is

$$|\sigma| = 10^2 \left(\frac{3}{21} \right)^3 \sigma_{sc}^3 = 0.29 \sigma_{sc}^3. \quad (\text{E.4})$$

Imposing Wang's constraint

$$\sigma_{xx}\sigma_{zz} = \sigma_{sc}^2 = 10\sigma_{zz}^2, \quad (\text{E.5})$$

then $\sigma_{xx} = \sigma_{yy} = \sqrt{10}\sigma_{sc}$ and $\sigma_{zz} = \sigma_{sc}/\sqrt{10}$. The trace is

$$\text{trace}(\sigma) = \left(2\sqrt{10} + 1/\sqrt{10} \right) \sigma_{sc} = 6.64 \sigma_{sc}. \quad (\text{E.6})$$

The current norm is

$$\|J\| = \sqrt{20 + 0.1}\sigma_{sc}E = 4.48\sigma_{sc}E. \quad (\text{E.7})$$

The determinant is

$$|\sigma| = \frac{10}{\sqrt{10}}\sigma_{sc}^3 = 3.16\sigma_{sc}^3. \quad (\text{E.8})$$

Wang's constraint yields twice the trace and current norm than the isotropic case while scaling the trace yields same trace and similar current norm. The determinant is different for both of them by a factor of three. Larger effects were found using a volume constraint [182], which constrained the product of the three eigenvalues to be equal to the equivalent product for the isotropic conductivity, than Wang's constraint. Here, both Wang's constraint and scaling the trace were used yet the latter was preferred for studying the effect of anisotropy of the head.

Bibliography

- [1] J. F. P.-J. Abascal and W. R. B. Lionheart. Rank analysis of the anisotropic inverse conductivity problem. In *Proc. ICEBI XII-EIT V*, pages 511–514, Gdansk, Poland, 2004.
- [2] G. Alessandrini and R. Gaburro. Determining conductivity with special anisotropy by boundary measurements. *SIAM J. Math. Anal.*, 33(1):153–171, 2001.
- [3] D. C. Alexander, G. J. Barker, and S. R. Arridge. Detection and modeling of non-gaussian apparent diffusion coefficient profiles in human brain data. *Magnetic Resonance in Medicine*, 48:331–340, 2002.
- [4] D. C. Alexander, C. Pierpaoli, P. J. Basser, and J. C. Gee. Spatial transformations of Diffusion Tensor Magnetic Resonance Imaging. *IEEE Trans. Medical Imaging*, 20:1131–1139, 2001.
- [5] A. W. Anderson, R. Marois, E. R. Colson, B. S. Peterson, C. C. Duncan, R. A. Ehrenkranz, K. C. Schneider, J. C. Gore, and L. R. Ment. Neonatal auditory activation detected by functional magnetic resonance imaging. *Magnetic Resonance Imaging*, 19:1–5, 2001.
- [6] J. M. M. Anderson, B. A. Mair, M. Rao, and C.-H. Wu. Weighted least-squares reconstruction methods for positron emission tomography. *IEEE Trans. Medical Imaging*, 16:159–166, 1997.
- [7] T. J. Andrews, S. D. Halpern, and D. Purves. Correlated size variations in human visual cortex, lateral geniculate nucleus, and optic tract. *The Journal of Neuroscience*, 17(8):2859–2868, 1997.
- [8] S. R. Arridge. Optical tomography in medical imaging. *Inv. Problems*, 15:R41–R93, 1999.
- [9] S. R. Arridge and M. Schweiger. A gradient-based optimisation scheme for optical tomography. *Optics Express*, 2(6):213–226, 1998.

- [10] J. Ashburner, P. Neelin, D. L. Collins, and A. C. E. K. J. Friston. Incorporating prior knowledge into image registration. *NeuroImage*, 6:344–352, 1997.
- [11] A. P. Bagshaw, A. D. Liston, R. H. Bayford, A. Tizzard, A. P. Gibson, A. T. Tidswell, M. K. Sparkes, H. Dehghani, C. D. Binnie, and D. S. Holder. Electrical impedance tomography of human brain function using reconstruction algorithms based on the finite element method. *NeuroImage*, 20:752–764, 2003.
- [12] D. C. Barber and B. H. Brown. Applied potential tomography. *J. Phys. E: Sci. Instrum.*, 17:723–733, 1984.
- [13] D. C. Barber and A. D. Seagar. Fast reconstruction of resistance images. *Clin. Phys. Physiol. Meas.*, 8:47–54, 1987.
- [14] P. G. Batchelor, D. Atkinson, D. L. Hill, F. Calamante, and A. Connelly. Anisotropic noise propagation in diffusion tensor mri sampling schemes. *Magn. Reson. Med.*, 49(6):1143–51, 2003.
- [15] R. H. Bayford, K. G. Boone, Y. Hanquan, and D. S. Holder. Improvement of the positional accuracy of EIT images of the head using a Lagrange multiplier reconstruction algorithm with diametric excitation. *Physiol. Meas.*, 17:A49–A57, 1996.
- [16] R. H. Bayford, A. Gibson, A. Tizzard, A. T. Tidswell, and D. S. Holder. Solving the forward problem for the human head using IDEAS (Integrated Design Engineering Analysis Software) a finite element modelling tool. *Physiol. Meas.*, 22:55–63, 2001.
- [17] C. Beaulieu. The basis of anisotropic water diffusion in the nervous system - a technical review. *NMR in Biomedicine*, 15:435–455, 2002.
- [18] C. A. Berenstein and E. C. Tarabusi. Integral geometry in hyperbolic spaces and electrical impedance tomography. *SIAM J. Appl. Math.*, 56:755–764, 1996.
- [19] D. L. Bihan, J.-F. Mangin, C. Poupon, C. A. Clark, S. Pappata, N. Molko, and H. Chabriet. Diffusion Tensor Imaging: concepts and applications. *Journal of Magnetic Resonance Imaging*, 13:534–546, 2001.
- [20] C. Binnie, A. Rowan, and T. Gutter. *The 10-20 system*. Cambridge University Press, Cambridge, UK, 1982.
- [21] A. Bjorck. *Numerical methods for least squares methods*. Society for Industrial and Applied Mathematics, Philadelphia, PA, USA, 1990.

- [22] R. S. Blue, D. Isaacson, and J. C. Newell. Real-time three-dimensional electrical impedance tomography. *Physiol. Meas.*, 21:15–26, 2000.
- [23] M. Bonnet and A. Constantinescu. Inverse problems in elasticity. *Inv. Problems*, 21:R1–R50, 2005.
- [24] L. Borcea. Electrical impedance tomography. *Inv. Problems*, 18:R99–R136, 2002.
- [25] B. Borden. Mathematical problems in radar inverse scattering. *Inv. Problems*, 18:R1–R28, 2002.
- [26] A. Borsic. *Imaging from Electrical Measurements*. PhD thesis, Oxford Brookes University, Oxford, 2002.
- [27] A. Borsic, W. R. B. Lionheart, and C. McLeod. Generation of anisotropic-smoothness regularisation filters for EIT. *IEEE Trans. Medical Imaging*, 21:579–587, 2002.
- [28] I. Bouchouev and V. Isakov. Uniqueness and stability for inverse problems that arise in financial markets. *Inv. Problems*, 15:R95–R116, 1999.
- [29] D. Braess. *Finite Elements*. Cambridge University Press, Cambridge, UK, 1997.
- [30] B. H. Brown. Medical impedance tomography and process impedance tomography: a brief review. *Meas. Sci. Technol.*, 12:991–996, 2001.
- [31] M. Cheney, D. Isaacson, and J. C. Newell. Electrical impedance tomography. *SIAM Review*, 41(1):85–101, 1999.
- [32] R. Christensen. *Advanced linear modeling*. Springer-Verlag, New York, 2001.
- [33] R. D. Cook, G. J. Saulnier, D. G. Gisser, J. C. Goble, J. C. Newell, and D. Isaacson. Act3: A a high-speed, high-precision electrical impedance tomograph. *IEEE Trans. Biomed. Eng.*, 41(8):713–, 1994.
- [34] K. Curran. *Diffusion Tensor matching for Image Registration*. PhD thesis, UCL, London, England, 2005.
- [35] E. B. Curtis and J. A. Morrow. Determining the resistors in a network. *SIAM J. Appl. Math.*, 50(3):918–930, 1990.
- [36] D. M. Deturck and D. Yang. Existence of elastic deformations with prescribed principal strains and triply orthogonal systems. *Duke Mathematical Journal*, 51(2):243–260, 1984.

- [37] K. A. Dines and R. J. Lytle. Analysis of electrical conductivity imaging. *Geophysics*, 46(7):1025–1036, 1981.
- [38] D. C. Dobson and F. Santosa. An image enhancement technique for electrical impedance tomography. *Inv. Problems*, 10:317–34, 1994.
- [39] B. Dogdas, D. W. Shattuck, and R. M. Leahy. Segmentation of skull in 3d human mr images using mathematical morphology. *Progr. biomed. opt. imaging*, 3(22):1553–1562, 2002.
- [40] O. Dorn. Shape reconstruction in scattering media with voids using a transport model and level sets. *Canad. Appl. Math. Quart.*, 10(2):239–275, 2002.
- [41] Z. Elazar, R. T. Hado, and Adey. Impedance changes during epileptic seizures. *Epilepsia*, 7(4):291–307, 1966.
- [42] Z. Elazar, R. T. Kado, and W. R. Adey. Impedance changes during epileptic seizures. *Epilepsia*, 1:291–307, 1966.
- [43] S. N. Evans and P. B. Stark. Inverse problems as statistics. *Inv. Problems*, 18:R55–R97, 2002.
- [44] L. Fabrizi, L. Horesh, A. McEwan, and D. Holder. A feasibility study for imaging of epileptic seizures by eit using a realistic FEM of the head. In *Proc. of 7th conference on biomedical applications of electrical impedance tomography*, pages 45–48, Korea, 2006. Kyung Hee University and COEX.
- [45] L. Fabrizi, M. Sparkes, L. Horesh, J. F. P.-J. Abascal, A. McEwan, R. H. Bayford, R. Elwes, C. D. Binnie, and D. S. Holder. Factors limiting the application of electrical impedance tomography for identification of regional conductivity changes using scalp electrodes during epileptic seizures in humans. *Physiol. Meas.*, 27:S163–S174, 2006.
- [46] R. P. Feynman, R. B. Leighton, and M. Sands. *Feynman Lectures on Physics, mainly electromagnetism and matter, volume II*. Addison Wesley, Reading, Massachusetts, USA, 1964.
- [47] K. J. Friston, J. Ashburner, C. D. Frith, and J.-B. Poline. Spatial registration and normalization of images. *Human Brain Mapping*, 2:165–189, 1995.
- [48] R. Gaburro. *Anisotropic conductivity inverse boundary value problems*. PhD thesis, The University of Manchester, 2003.

- [49] L. A. Geddes and L. E. Baker. The specific resistance of biological material—a compendium of data for the biomedical engineer and physiologist. *Med. Biol. Eng.*, 5(3):271–293, 1967.
- [50] A. Ghahary and J. G. Webster. Electrical safety for an electrical impedance tomograph. In *Proc. of the 11th conference of the IEEE engineering in medicine & Biology*, volume 2, pages 461–462, 1989.
- [51] O. Gilad, G. M. Ahadzi, R. H. Bayford, and D. S. Holder. Near DC conductivity change measurement of fast neuronal activity during human VEP. In *Proc. ICEBI XII-EIT V*, pages 279–282, Gdansk, Poland, 2004.
- [52] O. Gilad, L. Horesh, G. M. Ahadzi, R. H. Bayford, and D. S. Holder. Could synchronized neuronal activity be imaged using Low Frequency Electrical Impedance Tomography (LFEIT)? In *6th Conference on Biomedical Applications of Electrical Impedance Tomography*, London, UK, 2005.
- [53] D. G. Gisser, D. Isaacson, and J. C. Newell. Theory and performance of an adaptive current tomography system. *Clin. Phys. Physiol. Meas.*, 9(Suppl. A):35–41, 1988.
- [54] M. Glidewell and K. T. Ng. Anatomically constrained electrical-impedance tomography for anisotropic bodies via a two-step approach. *IEEE Trans. Medical Imaging*, 14:498–503, 1995.
- [55] M. Glidewell and K. T. Ng. Anatomically constrained electrical impedance tomography for three-dimensional anisotropic bodies. *IEEE Trans. Medical Imaging*, 16(5):572–80, 1997.
- [56] G. H. Golub and C. F. V. Loan. *Matrix Computations*. North Oxford Academic, London, 1986.
- [57] A. R. Hampshire, R. H. Smallwood, B. H. Brown, and R. A. Primhak. Multifrequency and parametric EIT images of neonatal lungs. *Physiol. Meas.*, 16:A175–A189, 1995.
- [58] M. Hanke. Limitations of the L-curve in ill-posed problems. *BIT*, 36:287–301, 1996.
- [59] M. Hanke and P. C. Hansen. Regularization methods for large-scale problems. *Surv. Math. Ind.*, 3:253–315, 1993.
- [60] P. C. Hansen. Analysis of discrete ill-posed problems by means of the L-curve. *SIAM Rev.*, 34(4):561–580, 1992.

- [61] P. C. Hansen. Numerical tools for analysis and solution of Fredholm integral equations of the first kind. *Inv. Problems*, 8:849–872, 1992.
- [62] P. C. Hansen. *Rank-deficient and discrete ill-posed problems*. Society for Industrial and Applied Mathematics, Philadelphia, PA, USA, 1998.
- [63] P. C. Hansen and D. P. O’Leary. The use of the L-curve in the regularisation of discrete ill-posed problems. *SIAM J. Sci. Statist. Comput.*, 14:1487–1503, 1993.
- [64] A. V. Harreveld and J. P. Schadé. Changes in the electrical conductivity of cerebral cortex during seizure activity. *Experimental Neurology*, 5:383–400, 1962.
- [65] N. D. Harris, A. J. Suggett, D. C. Barber, and B. H. Brown. Applied potential tomography: a new technique for monitoring pulmonary function. *Clin. Phys. Physiol. Meas.*, 9(Suppl. A):79–85, 1988.
- [66] J. Haueisen, D. S. Tuch, C. Ramon, P. H. Schimpf, V. J. Wedeen, J. S. George, and J. W. Belliveau. The influence of brain tissue anisotropy on human eeg and meg. *NeuroImage*, 15(1):159–66, 2002.
- [67] J. C. Hebden, A. Gibson, R. Yusof, N. Everdell, E. M. C. Hillman, D. T. Delpy, S. R. Arridge, T. Austin, J. H. Meek, and J. S. Wyatt. Three-dimensional optical tomography of the premature infant brain. *Phys. Med. Biol.*, 47:4155–4166, 2002.
- [68] D. J. Heeger and D. Ress. What does fMRI tell us about neuronal activity? *Nature*, 3:142–151, 2002.
- [69] L. M. Heikkinen, T. Vilhunen, R. M. West, and M. Vauhkonen. Simultaneous reconstruction of electrode contact impedances and internal electrical properties: II. Laboratory experiments. *Meas. Sci. Technol.*, 13(12):1855–1861, 2002.
- [70] J. Heino, E. Somersalo, and J. P. Kaipio. Compensation for geometric mismodelling by anisotropies in optical tomography. *Optics Express*, 13(1):296–308, 2005.
- [71] M. R. Hestenes. *Conjugate direction methods in optimization*. Springer-Verlag, Berlin, 1980.
- [72] D. S. Holder. Detection of cerebral ischaemia in the anaesthetised rat by impedance measurement with scalp electrodes: implications for non-invasive imaging of stroke by electrical impedance tomography. *Clin. Phys. Physiol. Meas.*, 13(1):63–75, 1992.

- [73] D. S. Holder. Electrical impedance tomography with cortical or scalp electrodes during global cerebral ischaemia in the anaesthetised rat. *Clin. Phys. Physiol. Meas.*, 13(1):87–98, 1992.
- [74] D. S. Holder. *Clinical and Physiological Applications of EIT*. UCL Press, London, UK, 1993.
- [75] D. S. Holder. *Electrical Impedance Tomography*. IOP, London, UK, 2005.
- [76] D. S. Holder, A. Rao, and Y. Hanquan. Imaging of physiologically evoked responses by electrical impedance tomography with cortical electrodes in the anaesthetized rabbit. *Physiol. Meas.*, 17(Suppl. A):A179–A186, 1996.
- [77] L. Horesh. *Some novel approaches in modelling and image reconstruction for multi-frequency electrical impedance tomography of the human brain*. PhD thesis, University College London, London, UK, 2006.
- [78] L. Horesh, O. Gilad, A. Romsauerova, S. R. Arridge, and D. S. Holder. Stroke type by Multi-Frequency Electrical Impedance Tomography (MFEIT)-a feasibility study. In *6th Conference on Biomedical Applications of Electrical Impedance Tomography*, London, UK, 2005. UCL.
- [79] L. Horesh, A. Romsauerova, L. Fabrizi, A. McEwan, S. R. Arridge, and D. S. Holder. Review of the dielectric properties of human head pathophysiology for Multi-Frequency Electrical Impedance Tomography (MFEIT). *Paper in preparation*, 2007.
- [80] A. L. Hyaric and M. K. Pidcock. A one step image reconstruction algorithm for electrical impedance tomography in three dimensions. *Physiol. Meas.*, 21:95–98, 2000.
- [81] D. Isaacson and E. L. Isaacson. Comment on calderón’s paper: on an inverse boundary value problem. *Math. Comp.*, 52(186):553–559, 1989.
- [82] D. Isaacson, J. Newell, S. Simske, and J. Goble. NOSER: An algorithm for solving the inverse conductivity problem. *Internat. J. Imaging Systems and Technol.*, 2:66–75, 1990.
- [83] V. Isakov. Uniqueness and stability in multi-dimensional inverse problems. *Inv. Problems*, 9:579–621, 1993.
- [84] I. T. Jolliffe. *Principal component analysis*. Springer-Verlag, New York, 1986.

- [85] J. P. Kaipio, V. Kolehmainen, E. Somersalo, and M. Vauhkonen. Statistical inversion and Monte Carlo sampling methods in electrical impedance tomography. *Inv. Problems*, 316:1487–1522, 2000.
- [86] M. G. Kang and A. K. Katsaggelos. General choice of the regularisation functional in regularised image restoration. *IEEE Trans. Image Processing*, 4(5), 1995.
- [87] P. A. Karjalainen, J. P. Kaipio, A. S. Koistinen, and M. Vauhkonen. Subspace regularization method for the single-trial estimation of evoked potentials. *IEEE Trans. Biomed. Eng.*, 46(7):849–860, 1999.
- [88] L. Kaufman and A. Neumaier. PET regularisation by envelope guided conjugate gradient. *IEEE Trans. Medical Imaging*, 15:385–389, 1996.
- [89] J. Kevorkian. *Partial differential equations: analytical solution techniques*. Springer-Verlag, New York, 2000.
- [90] S. Kim, T.-S. Kim, Y. Zhou, and M. Singh. Influence of conductivity tensors in the finite element model of the head on the forward solution of EEG. *IEEE Trans. Nuclear Science*, 50:133–139, 2003.
- [91] K. knight. *Mathematical statistics*. Chapman & Hall/CRC, EEUU, 2000.
- [92] R. V. Kohn and M. Vogelius. Determining conductivity by boundary measurements, interior results II. *Commun. Pure Appl. Math.*, 37:281–298, 1984.
- [93] R. V. Kohn and M. Vogelius. Determining conductivity by boundary measurements, interior results II. *Commun. Pure Appl. Math.*, 38:643–667, 1985.
- [94] V. Kolehmainen. *Novel approaches to image reconstruction in diffusion tomography*. PhD thesis, Kuopio University, 2001.
- [95] V. Kolehmainen, S. R. Arridge, W. R. B. Lionheart, M. Vauhkonen, and J. P. Kaipio. Recovery of region boundaries of piecewise constant coefficients of an elliptic PDE from boundary data. *Inv. Problems*, 15:1375–1391, 1999.
- [96] V. Kolehmainen, M. Lassas, and P. Ola. The inverse conductivity problem with an imperfectly known boundary. *SIAM J. Appl. Math.*, 66(2):365–383, 2005.
- [97] V. Kolehmainen, M. Vauhkonen, P. A. Karjalainen, and J. P. Kaipio. Assessment of errors in static electrical impedance tomography with adjacent and trigonometric current patterns. *Physiol. Meas.*, 18:289–303, 1997.

- [98] W. J. Krzanowoski and F. H. C. Marriott. *Multivariate analysis. Part2. Classification, covariance structures and repeated measurements*. Edward Arnold, London, UK, 1994.
- [99] K. K. Kwong, J. W. Belliveau, D. A. Chesler, I. E. Goldberg, R. M. Weisskoff, B. P. Poncelet, D. N. Kennedy, B. E. Hoppel, M. S. Cohen, R. Turner, H.-M. Cheng, T. J. Brady, and B. R. Rosen. Dynamic magnetic resonance imaging of human brain activity during primary sensory stimulation. In *Proc. Natl. Acad. Sci. USA*, volume 89, pages 5675–5679, 1992.
- [100] R. Lazarovitch, D. Rittel, and I. Bucher. Experimental crack identification using electrical impedance tomography. *NDT&E International, Elsevier*, 35:301–316, 2002.
- [101] J. M. Lee and G. Uhlmann. Determining anisotropic real-analytical conductivities by boundary measurements. *Commun. Pure Appl. Math.*, 38:643–667, 1989.
- [102] A. Leemans, J. Sijbers, M. Verhoye, V. der Linden, and D. V. Dyck. A simulated phantom for diffusion tensor MRI fiber tracking. In *Proc. of Acivs (Advanced Concepts for Intelligent Vision Systems)*, pages 2–5, 2003.
- [103] H. Lester and S. R. Arridge. A survey of hierarchical non-linear medical image registration. *Pattern Recognition*, 32:129–149, 1999.
- [104] W. R. B. Lionheart. Conformal uniqueness results in anisotropic electrical impedance imaging. *Inv. Problems*, 13:125–34, 1997.
- [105] W. R. B. Lionheart. Boundary shape and electrical impedance tomography. *Inv. Problems*, 14:139–147, 1998.
- [106] W. R. B. Lionheart. EIT reconstruction algorithms: pitfalls, challenges and recent developments. *Physiol. Meas.*, 25:125–142, 2004.
- [107] W. R. B. Lionheart, J. Kaipio, and C. N. McLeod. Generalized optimal current patterns and electrical safety in EIT. *Physiol. Meas.*, 22:85–90, 2001.
- [108] A. D. Liston. *Models and image reconstruction in electrical impedance tomography of brain function*. PhD thesis, UCL, London, England, 2003.
- [109] H. D. Lux, U. Heinemann, and I. Dietzel. Ionic changes and alterations in the size of the extracellular space during epileptic activity. *Advances in neurology*, 44:619–939, 1986.

- [110] J. B. A. Maintz and M. A. Viergever. A survey of medical image registration. *Medical Image Analysis*, 2(1):1–36, 1998.
- [111] Y. F. Mangall, A. Baxter, R. Avill, N. Bird, B. Brown, B. D, A. Seager, and A. Johnson. Applied potential tomography: a new non-invasive technique for assessing gastric function. *Clin. Phys. Physiol. Meas.*, 8:119–129, 1987.
- [112] C. R. J. Maurer, G. B. Aboutanos, B. M. Dawant, S. Gadamsetty, R. A. Margolin, R. J. Maciunas, and J. M. Fitzpatrick. Effect of geometrical distortion correction in MR on image registration accuracy. *J. Comput. Assist. Tomogr.*, 20(4):666–79, 1996.
- [113] J. C. Mazziotta and M. E. Phelps. Human sensory stimulation and deprivation: positron emission tomographic results and strategies. *Ann. Neurol.*, 15(Suppl.):S50–S60, 1984.
- [114] F. J. McArdle, B. H. Brown, R. G. Pearse, and D. C. Barber. The effect of the skull of low-birthweight neonates on applied potential tomography imaging of centralised resistivity changes. *Clin. Phys. Physiol. Meas.*, 9(Suppl. A):55–60, 1988.
- [115] A. McEwan, A. Romsauerova, R. Yerworth, L. Horesh, R. Bayford, and D. Holder. Design and calibration of a compact multi-frequency EIT system for acute stroke imaging. *Physiol. Meas.*, 27:S199–S210, 2006.
- [116] A. McEwan, R. Yerworth, R. Bayford, and D. Holder. Specification and calibration of a multi-frequency MEIT system for stroke. In *6th Conference on Biomedical Applications of Electrical Impedance Tomography*, London, UK, 2005.
- [117] P. Metherall, D. C. Barber, R. H. Smallwood, and B. H. Brown. Three-dimensional electrical impedance tomography. *Nature*, 380:509–512, 1996.
- [118] A. Nachman. Global Uniqueness for a two-dimensional inverse Boundary Value Problem. *Annals of Math.*, 143:71–96, 1996.
- [119] F. Natterer. *The mathematics of computerized tomography*. Society for Industrial and Applied Mathematics, Philadelphia, PA, USA, 2001.
- [120] J. C. Newell, R. S. Blue, D. Isaacson, G. J. Saulnier, and A. S. Ross. Phasic three-dimensional impedance imaging of cardiac activity. *Physiol. Meas.*, 23:203–209, 2002.
- [121] P. W. Nicholson. Specific impedance of cerebral white matter. *Experimental Neurology*, 13:386–401, 1965.

- [122] J. Nocedal and S. J. . Wright. *Numerical optimization*. Springer-Verlag, New York, 1999.
- [123] E. Nolf. XMedCon - An open-source medical image conversion toolkit. *European Journal of Nuclear Medicine*, 30(2):S246, 2003.
- [124] S. P. Novikov. *Basic elements of differential geometry and topology*. Kluwer Academic Publishers, Dordrecht,Boston, 1990.
- [125] N. A. of Engineering. Greatest engineering achievements of the 20th century, 2005. <http://www.greatachievements.org>.
- [126] S. H. Oh, J. Y. Han, S. Y. Lee, M. H. Cho, B. I. Lee, and E. J. Woo. Electrical conductivity imaging by Magnetic Resonance Electrical Impedance Tomography (MREIT). *Magnetic Resonance in Medicine*, 50:875–878, 2003.
- [127] J. O. Ollikainen, M. Vauhkonen, P. A. Karjalainen, and J. P. Kaipio. Effects of local skull inhomogeneities on eeg source estimation. *Med. Eng. Phys.*, 21(3):143–54, 1999.
- [128] K. S. Ostermana, T. E. Kerner, D. B. Williams, A. Hartov, S. P. Poplack, and K. D. Paulsen. Multifrequency electrical impedance imaging: preliminary in vivo experience in breast. *Physiol. Meas.*, 21:99–109, 2000.
- [129] C. C. Paige. Computer solution and perturbation analysis of generalised linear least squares problems. *Math. Comp.*, 33:171–183, 1979.
- [130] C. C. Paige. Fast numerically stable computations for generalised least squares problems. *SIAM J. Numer. Anal.*, 16:165–171, 1979.
- [131] C. C. Paige. The general linear model and the generalised singular value decomposition. *Linear Algebra Appl.*, 70:269–284, 1985.
- [132] C. C. Pain, J. V. Herwanger, J. H. Saunders, M. H. Worthington, and Cassiano R E de Oliviera. Anisotropic and the art of resistivity tomography. *Inv. Problems*, 19:1081–1111, 2003.
- [133] A. Pang and P. M. Matthews. FMRIB, 2002. http://www.fmrib.ox.ac.uk/fmri_intro/.
- [134] R. D. Pascual-Marqui. Standardized low resolution brain electromagnetic tomography (sloreta): technical details. *Methods and Findings in Experimental and Clinical Pharmacology*, 24D:5–12, 2002.

- [135] K. Paulson, W. Breckon, and M. Pidcock. Electrode modelling in electrical impedance tomography. *SIAM J. Appl. Math.*, 52:1012–1022, 1992.
- [136] N. Petrick, A. O. H. III, N. H. Clinthorne, W. L. Rogers, and J. M. Slosar. Least squares arrival time estimators for single and piled up scintillation pulses. *IEEE Trans. Nuclear Science*, 40(4):1026–1030, 1993.
- [137] M. E. Phelps. Molecular imaging with positron emission tomography. *Annu. Rev. Nucl. Part. Sci.*, 52:303–338, 2002.
- [138] C. Phillips, J. Mattout, M. D. Rugg, P. Maquet, and K. J. Friston. An empirical bayesian solution to the source reconstruction problem in eeg. *NeuroImage*, 24:997–1011, 2005.
- [139] N. Polydorides. *Image reconstruction algorithms for soft-field tomography*. PhD thesis, UMIST, Manchester, England, 2002.
- [140] N. Polydorides and W. R. B. Lionheart. A Matlab toolkit for three-dimensional electrical impedance Tomography: a contribution to the Electrical Impedance and Diffuse Optical Reconstruction Software project. *Meas. Sci. Technol.*, 13:1871–1883, 2002.
- [141] N. Polydorides and W. R. B. Lionheart. Krylov Subspace Iterative Techniques: On the Detection of brain activity with electrical impedance tomography. *IEEE Trans. Medical Imaging*, 21:596–603, 2002.
- [142] P. Ramachandran. The MayaVi Data Visualizer, 2002. <http://oldwww.rug.nl/hpc/VTK/vtk.htm>.
- [143] A. Rao. *Electrical impedance tomography of brain activity: studies into its accuracy and physiological mechanisms*. PhD thesis, UCL, London, England, 2000.
- [144] G. N. Reddy and S. Saha. Electrical and dielectrical properties of wet bone as a function of frequency. *IEEE Trans. Biomed. Eng.*, 31(3):296–302, 1984.
- [145] A. Romsauerova, A. M. Ewan, L. Horesh, R. Yerworth, R. H. Bayford, and D. S. Holder. Multi-frequency electrical impedance tomography (EIT) of the adult human head: initial findings in brain tumours, arteriovenous malformations and chronic stroke, development of an analysis method and calibration. *Physiol. Meas.*, 27(5):S147–S161, 2006.
- [146] S. Rush and D. Driscoll. Current distribution in the brain from surface electrodes. *Anaesthesia and analgetica*, 47(6):717–723, 1968.

- [147] G. S. Russell, K. J. Eriksen, P. Poolman, P. Luu, and D. M. Tucker. Geodesic photogrammetry for localizing sensor positions in dense-array EEG. *Clinical Neurophysiology*, 116:1130–1140, 2005.
- [148] O. Sacks. *The man who mistook his wife for a hat*. Picador, London, Uk, 1986.
- [149] R. J. Sadleir and R. A. Fox. Detection and quantification of intraperitoneal fluid using Electrical Impedance Tomography. *IEEE Trans. Biomed. Eng.*, 48(4):484–491, 2001.
- [150] S. Saha. Electric and dielectric properties of wet human cortical bone as a function of frequency. *IEEE Trans. Biomed. Eng.*, 39(12):1298–1304, 1992.
- [151] F. Santosa and M. Vogelius. A backprojection algorithm for electrical impedance imaging. *SIAM J. Appl. Math.*, 50(1):216–243, 1990.
- [152] R. Schindmes, L. Horesh, and D. S. Holder. The effect of using patient specific finite element meshes for modelling and image reconstruction of electrical impedance tomography of the human head, 2007. In progress.
- [153] R. Schindmes, L. Horesh, and D. S. Holder. Technical report - generation of patient specific finite element meshes of the human head for electrical impedance tomography, 2007. In progress.
- [154] J. Schoberl. NETGEN: a three-dimensional mesh generation software, 1999. <http://www.hpfem.jku.at/netgen/>.
- [155] M. Schweiger and S. R. Arridge. Newton-Krylov solver for non-linear reconstruction in diffusive optical tomography. *Internal Report. UCL. London*, 2004.
- [156] J. K. Seo, O. Kwon, and E. J. Woo. Anisotropic conductivity image reconstruction problem in B_z -based MREIT. In *Proc. ICEBI XII-EIT V*, pages 531–534, Gdansk, Poland, 2004.
- [157] M. N. Shalit. The effect of metrazol on the hemodynamics and impedance of the cat's brain cortex. *Neuropathol Exp. Neurol.*, 24:75–84, 1965.
- [158] D. W. Shattuck and R. M. Leahy. BrainSuite: an automated cortical surface identification tool. *Med. Image. Anal.*, 6(2):129–42, 2002.
- [159] M. Soleimani. *Image and shape reconstruction methods in Magnetic Induction and Electrical Impedance Tomography*. PhD thesis, University of Manchester, Manchester, England, 2005.

- [160] M. Soleimani, J. F. P.-J. Abascal, and W. R. B. Lionheart. Simultaneous reconstruction of the boundary shape and conductivity in 3d electrical impedance tomography. In *Proc. ICEBI XII-EIT V*, pages 475–478, Gdansk, Poland, 2004.
- [161] E. Somersalo, M. Cheney, and D. Isaacson. Existence and uniqueness for electrode models for electric current computed tomography. *SIAM J. Appl. Math.*, 52(4):1023–1040, 1992.
- [162] E. Somersalo, M. Cheney, D. Isaacson, and E. Isaacson. Layer stripping: a direct numerical method for impedance tomography. *Inv. Problems*, 7(6):899–926, 1991.
- [163] M. R. Spiegel. *Schaum's outline of theory and problems of vector analysis : and an introduction to tensor analysis*. Mc Graw-Hill, London, UK, 1974.
- [164] J. W. Stayman and J. A. Fessler. Efficient calculation of resolution and covariance for penalised-likelihood reconstruction in fully 3-D SPECT. *IEEE Trans. Medical Imaging*, 23:1543–1556, 2004.
- [165] J. Sylvester and G. Uhlmann. A global uniqueness theorem for an inverse boundary value problem. *Annals of Math.*, 125:153–169, 1987.
- [166] T. Tidswell. *Functional Electrical Impedance Tomography of adult and neonatal brain function*. PhD thesis, UCL, London, England, 2002.
- [167] T. Tidswell, A. Gibson, R. H. Bayford, and D. S. Holder. Validation of a 3D reconstruction algorithm for EIT of human brain function in a realistic head-shaped tank. *Physiol. Meas.*, 22:177–185, 2000.
- [168] T. Tidswell, A. Gibson, R. H. Bayford, and D. S. Holder. Three-Dimensional Electrical Impedance Tomography of Human Brain Activity. *NeuroImage*, 13:283–294, 2001.
- [169] P. A. Tipler. *Physics for scientists and engineers*. W H Freeman & Co Ltd, New York, 1999.
- [170] A. Tizzard, L. Horesh, R. J. Yerworth, D. S. Holder, and R. H. Bayford. Generating accurate finite element meshes for the forward model of the human head in EIT. *Physiol. Meas.*, 26:S251–S261, 2005.
- [171] N. J. Trujillo-Barreto, E. Aubert-Vázquez, and P. A. Valdés-Sosa. Bayesian model averaging in EEG/MEG imaging. *NeuroImage*, 21:1300–1319, 2004.

- [172] D. S. Tuch. *Diffusion MRI of complex tissue structure*. PhD thesis, Massachusetts Institute of Technology, Massachusetts, 2002.
- [173] D. S. Tuch, V. J. Wedeen, A. M. Dale, J. S. George, and J. W. Belliveau. Conductivity tensor mapping of the human brain using diffusion tensor mri. *Proc. Natl. Acad. Sci. USA*, 98(20):11697–701, 2001.
- [174] G. Uhlmann. Recent progress in the anisotropic electrical impedance problem. *J. Diff. Eq.*, 6:303–311, 2001.
- [175] T. Vilhunen, J. P. Kaipio, P. J. Vauhkonen, T. Savolainen, and M. Vauhkonen. Simultaneous reconstruction of electrode contact impedances and internal electrical properties: I. Theory. *Meas. Sci. Technol.*, 13(12):1848–1854, 2002.
- [176] C. R. Vogel. *Computational methods for inverse problems*. Society for Industrial and Applied Mathematics, Philadelphia, PA, USA, 2002.
- [177] G. Wahba. Practical approximate solutions to linear operator equations when the data are noisy. *SIAM J. Numer. Anal.*, 14:651–667, 1977.
- [178] M. Wang, T. F. Jones, and R. A. Williams. Visualization of asymmetric solids distribution in horizontal swirling flows using electrical resistance tomography. *Chemical Engineering Research and Design*, 81(A8):854–861, 2003.
- [179] H. J. Weber and G. B. Arfken. *Essential mathematical methods for physicists*. Elsevier Academic Press, London, UK, 2004.
- [180] A. J. Wilson, P. Milnes, A. R. Waterworth, R. H. Smallwood, and B. H. Brown. Mk3.5: a modular, multi-frequency successor to the Mk3a EIS/EIT system. *Physiol. Meas.*, 22:49–54, 2001.
- [181] C. H. Wolters. *Influence of tissue conductivity inhomogeneity and anisotropy on EEG/EMG based source localization in the human brain*. PhD thesis, University of Leipzig, Leipzig, Germany, 2003.
- [182] C. H. Wolters, A. Anwander, X. Tricoche, D. Weinstein, M. A. Koch, and R. S. MacLeod. Influence of tissue conductivity anisotropy on EEG/EMG field and return current computation in a realistic head model: A simulation and visualization study using high-resolution finite element modeling. *NeuroImage*, 30(3):813–826, 2006.

- [183] K. J. Worsley, S. MArrett, P. Neelin, and A. C. Evans. Searching scale space for activation in PET images. *Human Brain Mapping*, 4:74–90, 1996.
- [184] P. Xu. Truncated SVD methods for discrete linear ill-posed problems. *Geophys. J. Int.*, 135:505–514, 1998.
- [185] R. J. Yerworth, R. H. Bayford, G. Cusick, M. Conway, and D. S. Holder. Design and performance of the UCLH Mark 1b 64 channel electrical impedance tomography (EIT) system, optimized for imaging brain function. *Physiol. Meas.*, 23:149–158, 2002.
- [186] B. N. Zakhariev and V. M. Chabanov. New situation in quantum mechanics (wonderful potentials from the inverse problem). *Inv. Problems*, 13:R47–R79, 1997.
- [187] H. Zha and P. C. Hansen. Regularization and the general Gauss-Markov linear model. *Math. Comp.*, 55:613–624, 1990.

Index

- additive noise, 78
- Anisotropy (see conductivity), 68
- CEM, 59
- Conductivity tensor, 58, 67, 68, 173, 175, 178, 235, 236, 240
- Covariance, 78, 83
- Diffeomorphism, 68, 69, 132, 231, 238
- Diffusion tensor, 151, 169, 173
- Dirichlet-to-Neumann, 67, 137
- Discrepancy Principle, 84, 99
- Eigenvalue decomposition, 217
- Forward problem, 52
- Generalised Cross Validation, 85, 99
- Generalised least squares, 79
- Generalised SVD, 82
- Hadamard's conditions, 71
- ill-conditioned, 79
- Ill-posedness, 71, 79
- inverse problem, 70
- Jacobian, 70, 78, 137, 181, 221, 238
- L-curve, 85, 99
- Least Squares, 220
- linear model, 78
- Linear Regularisation, 80
- Mark 1b UCLH EIT system, 96
- Matched filtering theorem, 82
- Optimisation, 73
- Predictive error norm, 84, 99
- Principal Component Analysis, 107, 225
- Pseudo-inverse, 79, 220
- rank, 138, 219
- regularisation, 71
- Regularisation parameter, 84, 90
- Sensitivity matrix (see Jacobian), 70
- Smoothing, 82
- Solution error norm, 84, 99
- SVD, 218
- System matrix, 61, 62, 135, 180
- Tikhonov, 81, 82
- trace constraint, 173, 178, 240
- Truncated SVD, 80
- Unbiased Predictive Risk Estimator, 85, 99
- Uniqueness, 67, 69, 132